THESE

Pour l'obtention du Grade de

DOCTEUR DE L'UNIVERSITE DE POITIERS

Faculté des Sciences Fondamentales et Appliquées

Diplôme National - Arrêté du 7 août 2006

Ecole Doctorale Sciences et Ingénierie en Matériaux, Mécanique, Energétique et Aéronautique

Secteur de Recherche : Milieux Denses, Matériaux et Composants

Présentée par :

Guo-Ping BEI

Synthesis, microstructural characterization and mechanical properties of nanolaminated $Ti_3Al_xSn_{(1-x)}C_2$ MAX phases

---

Directeurs de Thèse :

Sylvain DUBOIS
Véronique BRUNET

Soutenue le 7 Juillet 2011 devant la Commission d'Examen

JURY

G. DIRRAS	Professeur des Universités, LSPM, Paris XIII	Rapporteur
F. BERNARD	Professeur des Universités, ICB, Dijon	Rapporteur
D. VREL	Chargé de recherches CNRS, LSPM, Paris XIII	Examinateur
C. TROMAS	Maître de conférences, Institut Pprime, Poitiers	Examinateur
S. DUBOIS	Professeur des Universités, Institut Pprime, Poitiers	Examinateur
V. BRUNET	Maître de conférences, Institut Pprime, Poitiers	Examinateur

Content

General Introduction

MAX phases are a class of ternary nitrides and carbides, with the general formula $M_{n+1}AX_n$ (n=1 to 3), where M is a transition metal, A is an A group element, and X is either carbon or nitrogen[1] . Up to now, more than 60 MAX phases have been indentified. These phases have a hexagonal crystal structure that consists of edge-sharing $[M_6X]$ octahedron interleaved with A layers; they are thus considered as nanolaminated-layered materials. Strong M-X bonds, weaker M-A bonds associated with the nanolayered nature of the structure endow these solids a unique combination of metal and ceramic properties[1]. For example, they are resistant to oxidation and corrosion, elastically stiff, but at the same time, they also demonstrate high thermal and electrical conductivities and they are machinable. Furthermore, according to previous theoretical and experimental studies, MAX phases can form a large number of isostructural solid solutions; substitutions being possible at each site. In such a context, it is of interest to better understand the role of "chemistry" in order to control the physical and/or mechanical properties of MAX phases. Hence, MAX phases and MAX phase solid solutions have aroused great interests among the scientists in physics, chemistry, and material science.

As a relatively new member of MAX phases in the Ti-Al-C system, Ti_3AlC_2 has typical merits of the MAX phases. It is lightweight (4.25 g/cm^3), good electrical and thermal conductor, elastically stiff, resistant to thermal shock, tolerant to damage, readily machinable; it also has a low hardness, high flexural and compressive strength. Because of the narrow existence domain of Ti_3AlC_2, it is quite difficult to synthesize highly pure and dense Ti_3AlC_2 bulk materials. Hence, up to now, most of the research work on Ti_3AlC_2 is mainly focused on the synthesis of such a phase. Only a few papers report the remarkable properties, especially the mechanical response of Ti_3AlC_2.

Concerning the Ti-Sn-C system, only the 211 phase, Ti_2SnC, was investigated. No 312 and 413 bulk MAX phases have been reported in the literature.

MAX phase solid solutions obtained by substitution on the A site mostly concern Ti-Al-Si-C and Ti-Si-Ge-C systems. $Ti_3Al_xSn_{(1-x)}C_2$ solid solutions have not been synthesized and investigated, although some studies on the optimization of Ti_3AlC_2 synthesis using Sn as

an additive have been reported[2, 3].

In such a context, the main objectives of this thesis will focus on the synthesis and on the mechanical properties investigation of new MAX phases and related solid solutions in the Ti-Al-Sn-C system.

The first objective will concern:

- the production of a new 312 MAX phase, Ti_3SnC_2,
- the optimization of the process for producing highly pure and dense Ti_3AlC_2 bulk material,
- the synthesis of a set of new solid solutions, $Ti_3Al_xSn_{(1-x)}C_2$.

The second point will consist in studying the hardness and the elastic modulus of Ti_3AlC_2, Ti_3SnC_2 and $Ti_3Al_xSn_{(1-x)}C_2$ solid solutions as a function of the Al content. The plastic behavior of Ti_3AlC_2 and selected $Ti_3Al_xSn_{(1-x)}C_2$ solid solutions will be investigated by performing uniaxial compression tests, compression tests under confining gas pressure and nanoindentation tests. The different experimental set-ups will be used to study the deformation mechanisms at macroscopic and microscopic scales.

According to this outline of the research objectives, this thesis is divided into six chapters:

- Chapter I gives a general introduction on MAX phases. It also describes the studies about Ti_3AlC_2 and MAX phase solid solutions synthesis that have been reported in the literature and some of the mechanical properties of MAX phases we will further evaluate.
- Chapter II describes the experimental details relative to the different techniques that have been used in this thesis, to produce, to characterize and to measure some of the mechanical properties of MAX phases.
- Chapter III describes the processing route and the reactions mechanisms leading to the formation of the new Ti_3SnC_2 MAX phase. The second part of this chapter consists in the measure of some mechanical properties (hardness, elastic modulus) of well-characterized multi-phased Ti_3SnC_2 samples by using nanoindentation tests.

- Chapter IV deals with the synthesis and the microstructural characterization of highly pure and dense Ti_3AlC_2 bulk material. Some of the mechanical properties such as the hardness (comparison between nano and microhardness), the elastic modulus and the compressive behavior resulting from macroscopic or microscopic deformation at room temperature will be studied. The Kinking Non-linear Elastic (KNE) model established by Barsoum *et al.* [4,5] will be successfully applied to the Ti_3AlC_2 sample deformed by cyclic compression tests at room temperature.
- Chapter V firstly demonstrates the possibility to produce a set of $Ti_3Al_xSn_{(1-x)}C_2$ solid solutions. The second part of this chapter concerns the measure of the hardness and elastic modulus of $Ti_3Al_xSn_{(1-x)}C_2$ solid solutions as a function of the Al content. The compressive behavior resulting from macroscopic or microscopic deformation at room temperature of the $Ti_3Al_{0.8}Sn_{0.2}C_2$ solid solution will be studied and discussed in terms of KNE solid.
- Finally, some general conclusions and some possible perspectives will be described.

Chapter I

Bibliography

I-1. MAX phases: definition, structure, existing phases and characteristic properties

MAX phases are a family of nanolaminated ternary nitrides and carbides, with the general formula $M_{n+1}AX_n$ (n=1 to 3), where M is an early transition metal, A is an A group element, and X is either carbon or nitrogen [1] (see Figure 1). These carbides and nitrides were firstly synthesized by Jeitschko and Nowotny in the sixties [6-10]. They found that these phases owned a $P6_3/mmc$ space group and a hexagonal crystal structure.

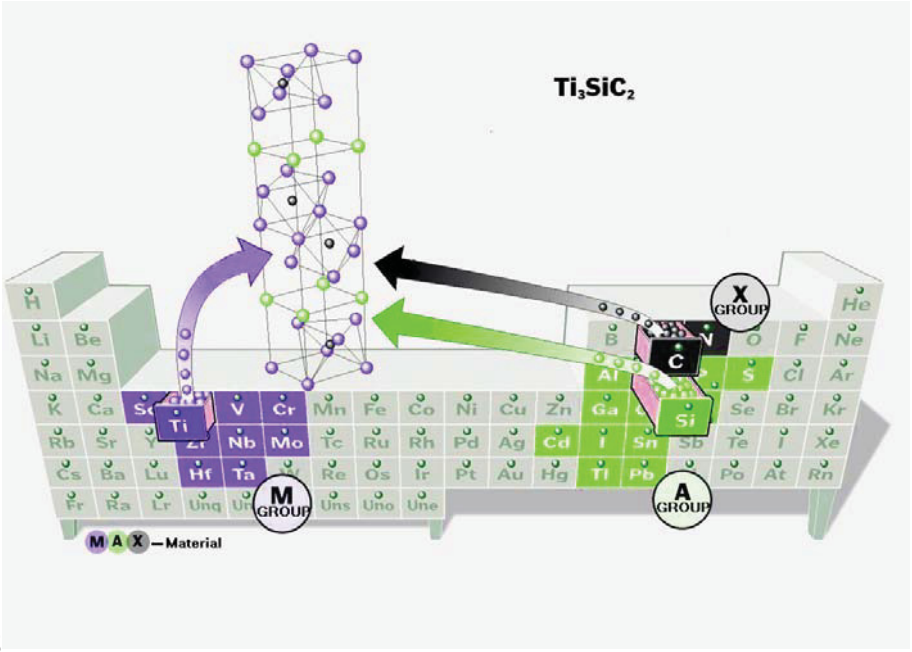

8

Figure 1: Location of the elements of $M_{n+1}AX_n$ ternary nitrides and carbides in the periodic table (Picture from http://www.ltu.se).

The unit cells of M_2AX, M_3AX_2 and M_4AX_3 phases are shown in Figure 2 (a). One can note that each structure consists of edge-sharing $[M_6X]$ octahedra interleaved with A layers. In the M_2AX or 211's phases, every third layer is an A layer; in the M_3AX_2 or 312's, every fourth layer, and in the M_4AX_3 or 413's, every fifth layer. Furthermore, a high-resolution transmission electron microscopy (HRTEM) image of the classical Ti_3SiC_2 structure is displayed in Figure 2(b). Ti_3SiC_2 structure consists of two adjacent covalent chains of Ti-C-Ti-C-Ti (Ti_3C_2 or $TiC_{0.667}$) sharing one Si atom. It can also be considered as a layer of two-dimensional close packed Si periodically intercalated into the twin boundary of TiC [1, 11]. MAX phases are thus considered as nanolaminated-layered materials.

Up to now, it exists more than 60 MAX phases and solid solutions. From Figure 3,

established by Barsoum's group in 2001 [11], one can see that most of the phases belong to the 211 family (so-called H- or Hägg phases). Only three 312 phases and one 413 phase were found at that time. However, the members of this family have continuously increased in the last several years by using different synthesis methods. Ta_3AlC_2 [12,13], Ti_3GaC_2 [14] and Ti_3SnC_2[15] were successfully synthesized to extend the 312 family. Furthermore, Ta_4AlC_3 [13,16-18], Nb_4AlC_3 [19], Ti_4SiC_3 [20], Ti_4GeC_3 [20,21], Ti_4GaC_3 [22], V_4AlC_3 [23] were complementary to the 413 class.

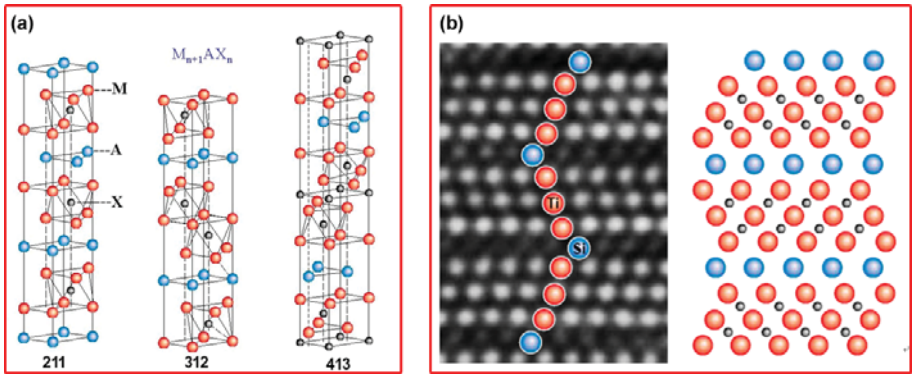

Figure 2[11]*: (a) The unit cells of the MAX phases for 211, 312 and 413 classes. (b) A HRTEM micrograph of the cross section of the Ti_3SiC_2 structure (Projection of atoms on (110) plane).*

211	Ti_2AlC^*	Ti_2AlN^*	Hf_2PbC^*	Cr_2GaC	V_2AsC	Ti_2InN
	Nb_2AlC^*	$(Nb,Ti)_2AlC^*$	$Ti_2AlN_{0.5}C_{0.5}^*$	Nb_2GaC	Nb_2AsC	Zr_2InN
	Ti_2GeC^*	Cr_2AlC	Zr_2SC	Mo_2GaC	Ti_2CdC	Hf_2InN
	Zr_2SnC^*	Ta_2AlC	Ti_2SC	Ta_2GaC^*	Sc_2InC	Hf_2SnN
	Hf_2SnC^*	V_2AlC	Nb_2SC	Ti_2GaN	Ti_2InC	Ti_2TlC
	Ti_2SnC^*	V_2PC	Hf_2SC	Cr_2GaN	Zr_2InC	Zr_2TlC
	Nb_2SnC^*	Nb_2PC	Ti_2GaC	V_2GaN	Nb_2InC	Hf_2TlC
	Zr_2PbC^*	Ti_2PbC^*	V_2GaC	V_2GeC	Hf_2InC	Zr_2TlN
312	$Ti_3AlC_2^*$	$Ti_3GeC_2^*$				
	$Ti_3SiC_2^*$					
413	$Ti_4AlN_3^*$					

Figure 3[11]*: A table of the existing MAX phases reported by Barsoum in 2001. Phases with star have been synthesized by his group.*

MAX phases possess a remarkable set of properties which derive from their nanolayered structure through the strong covalent M-X bonds which are interleaved with A layers through weak M-A bonds. Indeed, MAX phases exhibit a combination of the merits of both metals and ceramics. For example, like metals, they are readily machinable, relatively soft (1-5GPa), damage tolerant, thermally and electrically conductive, resistant to thermal shock and they

deform plastically at elevated temperature. Like ceramics, they are oxidation resistant, quite stiff, resistant to chemical attack, and have relatively low thermal expansion coefficients [1,11,24-50]. Some of the best properties of typical MAX phases are summarized in Table 1.

Properties	Ti_4AlN_3	Ti_3SiC_2	Ti_3AlC_2	Ti_2AlC	Cr_2AlC
Lattice Parameters (Å) [1]	*a*=2.988 *c*=23.37	*a*=3.06 *c*=17.67	*a*=3.07 *c*=18.578	*a*=3.051 *c*=13.637	*a*=2.86 *c*=12.8
Density (g/cm^3)	4.76[34]	4.5[24]	4.25[36]	4.11[25]	5.24[44,47,49]
Vickers hardness (GPa)	2.5[34]	4[24]	3.5 [36]	5.5[25] / 4.5[31]	5.5[44]/3.5[47]/5.2[49]
Young's modulus (GPa)	310[32]	339[32]/343[46]	297[36]	277 [31]	278[47] / 288[49]
Shear modulus (GPa)	127 [32]	139[32]/143[46]	124[36]	118[31]	116 [47]
Poisson's ratio	0.22[32]	0.20[32]	0.20[36]	0.19[31] 0.169[46]	0.2 [47]
Flexural strength (MPa)	330-600[34]	600[30] (FG) 330[30](CG)	375[36]	384[50]	378 [47] 483 [49]
Compressive strength (MPa)	475[34]	1050[30] (FG) 720[30] (CG)	560[36]	393[25,31] 540[31]	1159[49]
Electrical resistivity (μΩ·m)	2.61[45]	0.227[45]	0.39[45]	0.36[25,31,50]	0.74[45]
Debye temperature (K)	779[1]	715[1]	764[36]	735[31]	644[42]/ 774 [43]
Thermal Conductivity (W/m·K) (at 300K)	12[45]	34[45]	40[45]	33[45]	23[45]
Thermal expansion coefficient ($10^{-6}K^{-1}$)	9.7[45]	9.1[45]	9.0[45]	8.2[31] 8.8[45]	12[45]

Table 1: Characteristic properties of some typical MAX phases (FG: fine-grained, CG: coarse-grained).

I-2. Ti_3AlC_2: synthesis and microstructural characterization

A part of the work of this thesis will focus on the synthesis and characterization of Ti_3AlC_2 bulk samples. As a consequence, a short review concerning what has been done in the literature in terms of synthesis and characterization on this 312 MAX phase will be given in this section.

Ti_3AlC_2 is a relatively new member of the MAX phase family. It has been identified by Pietzka and Schuster *et al.* in 1994 when they investigated the Ti-Al-C ternary phase diagram[51]. However, it has not received much attention until Tzenov and Barsoum *et al*.

synthesized highly pure Ti_3AlC_2 (bulk samples) and reported its unique physical, chemical and mechanical properties[36]. In their work, a 12Ti:Al_4C_3:5C reactant mixture was sintered at 1400°C for 16h under a pressure of 70MPa using a reactive Hot Isostatic Pressing (HIPing) process. Ti_3AlC_2 lamellas, with a grain size of 20-30μm, were observed by Scanning Electron Microscopy (SEM). About 4 vol.% of Al_2O_3 was detected by Energy Dispersive X-ray Spectroscopy (EDXS). Tzenov and Barsoum *et al.*[36] have demonstrated that Ti_3AlC_2 is isostructural with Ti_3SiC_2 and possesses a serious of salient properties, such as low density (4.25g/cm^3) and hardness (3.5GPa), high Young's modulus (297 GPa), self-lubricant, easy machinability, high thermal and electrical conductivity and excellent mechanical response. Since this pioneering work on Ti_3AlC_2, a variety of processing techniques have been used to prepare either Ti_3AlC_2 bulk material or powder material due to its remarkable properties. Most of the processing techniques as well as some microstructural characterizations of final products are summarized in Table 2.

As shown in Table 2, besides the reactive HIPing technique [36], reactive Hot Pressing (HPing)[52-57], Spark Plasma Sintering (SPS)[58,59] or Pulse Discharge Sintering (PDS)[60-64], pressureless sintering[2,3,65], mechanically activated sintering technique[66] and combustion or mechanically activated self-propagating high-temperature synthesis technique(MASHS)[67-71] were used to synthesize Ti_3AlC_2. Moreover, different initial reactant mixtures, such as Ti:Al_4C_3:C[36,54,58], Ti:Al:C[2,52,53,56,58,60,66-71], Ti:Al:TiC[3,55,58,61,65], TiH_2:Al:TiC[63], TiH_2: Al: C[64], Ti:Al_4C_3:TiC[62], TiC_x:Al[57], Ti:TiAl:C[68] and Ti:Al:C:TiC[69,71] were used as the starting materials in the former studies. In most cases, the heat treatment was in the 1200-1600°C temperature range. However, due to the narrow existence domain of Ti_3AlC_2 in the Ti-Al-C phase diagram[51], impurities such as Al_2O_3[2,36], TiC[55,57-59,64,66-71], or the 211 MAX phase, Ti_2AlC[2,56-58,64,65], often co-exist with Ti_3AlC_2. Especially, the presence of TiC invariably deteriorates the high electrical conductivity and machinability of Ti_3AlC_2. So, several sintering additives such as Sn[2,3], Si[55,58] and B_2O_3[65] are introduced during synthesis to avoid the impurities formation and to get the Ti_3AlC_2 single phase. Although the former research works by Ai *et al.*[2] and Li *et al.* [3] have proved that Sn is an efficient additive which may favor $Ti_3Al(Sn)C_2$ solid solution formation and inhibit the presence of

TiC impurity, no further investigations were performed to confirm the formation of such solid solutions. It is important to note that the Ti_3AlC_2 grain size indicated in Table 2 is most of the time a mean grain size, likely measured in the basal plane. The grain size along the c axis is not mentioned.

Processing methods	Starting Materials (at.%)	Heat treatment conditions	XRD results (phase identification)	Results from SEM observations and EDXS analyses	Reference
Hot Isostatic Pressing (HIP)	12Ti:Al_4C_3:5C	1400°C/70MPa/16h	Ti_3AlC_2	Layered structure Ti_3AlC_2, GS:20-30 µm 4 vol .% Al_2O_3	[36]
Hot Pressing (HP)	3Ti:1.1Al:1.8C	1500°C/25MPa/5min then 1200°C/20min	Ti_3AlC_2	Ti_3AlC_2 plate-like grains GS:Diameters:20-50µm, Thickness: 5-8µm	[52,53]
	3Ti:0.3Al_4C_3:1.1C	1400°C/25MPa with different soaking time	Ti_3AlC_2 Ti_2AlC, TiC	Ti_3AlC_2 Ti_2AlC, TiC Ti_3AlC_2 GS:10-20µm	[54]
	3Ti:1.1Al:2C	1425°C/25MPa/30min	Ti_3AlC_2 Ti_2AlC	Ti_3AlC_2 plate-like grains GS:20µm	[56]
	Ti:1.2Al:2TiC	1200-1400°C/30MPa/2h	Ti_3AlC_2 , TiC	-	[55]
	Ti:Al:0.2Si:2TiC	1400-1500°C/30MPa/2h	$Ti_3(Al, Si)C_2$	Ti_3AlC_2 plate-like grains GS:5µm in thickness and 15µm in longitudinal direction	
	Ti:1.2Al:2TiC	1400-1500°C/30MPa/2h	Ti_3AlC_2 , TiC		
	3$TiC_{0.6}$:1.1Al	800-1600°C/25MPa with various holding time	Ti_3AlC_2 Ti_2AlC, $TiC_{0.6}$	Typical Ti_3AlC_2 laminated grains, GS:5µm at 1300°C	[57]
		1400°C/25MPa/60min	Ti_3AlC_2	GS: 20-30µm	
Spark Plasma Sintering (SPS)	Ti_3AlC_2 and Ti_2AlC from SHS a mixture of 2Ti:Al:C	1250°C/22MPa/5min	Ti_3AlC_2 Ti_2AlC	Layered nano-structure	[58]
	3Ti:0.3Al_4C_3:1.1C	1250°C/22MPa/5min	Ti_3AlC_2 Ti_2AlC, TiC	Layered nano-structure	
	2TiC:Ti:Al 2TiC:Ti:1.2Al	1250°C/30MPa/8min	Ti_3AlC_2, TiC	Layered nano-structure	[59]
	Ti:Al:2TiC:0.2Si	1200-1250°C/30MPa/8min	$Ti_3(Al, Si)C_2$	Plate-like grains GS: 2-5µm in width and 10-25µm in length.	
Pulse Discharge Sintering (PDS)	7Ti:Al_4C_3:3TiC	1400°C/50MPa/15min	Ti_3AlC_2	Plate-like grains GS: 5-10µm in width and more than 50µm in length	[62]
	3Ti:1.1Al:1.8C	1250-1350°C/50MPa/15min and 1300°C/50MPa/15-60min	Ti_3AlC_2	Plate-like grains GS: 2-10µm in width and 5-140µm in length	[60]
	2Ti:2Al:3TiC	1300°C/50MPa/15min	Ti_3AlC_2	Plate-like grains GS: 3-5µm in width and 20-50µm in length	[61]
	TiH_2:Al:1.8TiC	1350-1400°C/50MPa/ 20min	Ti_3AlC_2		[63]

				Plate-like grains GS: 3-6μm in width and 20-50μm in length at 1350°C/10 min 10-20μm in width and more than 50μm in length at 1400°C/20min	
	$3TiH_2$:1.1Al:1.8C	1250-1500°C/50MPa/ 20min	Ti_3AlC_2 Ti_2AlC TiC	Ti_3AlC_2, Ti_2AlC and TiC Ti_3AlC_2 GS: 2-5μm in width and 5-10μm in length at 1300°C	[64]
Pressureless Sintering	2TiC:Al:Ti	1300-1400°C/15-30min	97%Ti_3AlC_2 and 3%TiC	GS: less than 5μm with a hexagonal shape	[65]
	3Ti:1.1Al:1.8C	1450-1500°C/5min	Ti_3AlC_2	powders	[2]
	3Ti:Al:1.8C:0.2Sn	1350-1500°C/5min	97%Ti_3AlC_2 3%Al_2O_3	powders	
	Ti:Al:TiC:0.1Sn	1350-1500°C/10min	Ti_3AlC_2	Platelet shape, GS: 4-6μm	[3]
Mechanically Activated Sintering	3Ti:Al:2C	Co-milling CR=20:1/4h or CR=50:1/1.5h +sintering at 1350°C/1h	Ti_3AlC_2 TiC	powders	[66]
Combustion or MASHS	2Ti:Al:C	Ignited in vacuum	Ti_3AlC_2, Ti_2AlC, TiC	Layered nano-structure	[67]
	3Ti:Al:2C	Ignited in Ar atmosphere	Ti_3AlC_2,TiC,Al_4C_3	-	[68]
	2Ti:TiAl:2C	Ignited in Ar atmosphere	Ti_3AlC_2,TiC	-	
	1.5Ti:Al:C	Ignited in vacuum (2.33Pa)	TiC, Al, Ti_3AlC_2	Layered structure + equiaxed grain	[69]
	2Ti:Al:C		Ti_3AlC_2, Ti_2AlC, TiC	Layered structure	
	2Ti:1.5Al:C		Ti_3AlC_2, $TiAl_3$, TiC	Layered structure	
	2Ti:2Al:C		Ti_3AlC_2, $TiAl_3$, TiC	Layered structure	
	3Ti:Al:2C		Ti_3AlC_2, Al, TiC	-	
	3Ti:Al:2C-20%wt.TiC		Ti_3AlC, TiC	-	
	3Ti:Al:2C-30%wt.TiC		Ti_3AlC, TiC	-	
	3Ti:Al:2C	Ignited in Ar atmosphere	Ti_3AlC_2, TiC	Laminated grains and terraced structure	[70]
	3Ti:Al:2C	Ignited in high purity Ar atmosphere	Ti_3AlC_2, Ti_2AlC, TiC	Plate-like, GS:5-10μm	[71]
	(3-x)Ti:Al:(2-x)C:xTiC X=(0.25-1.25)		Ti_3AlC_2, Ti_2AlC, TiC	Plate-Like GS: 5-10μm	

Table 2: Summary of the recent studies on synthesis and microstructural characterization of Ti_3AlC_2 (Grain size marked as GS in the table)

I-3. MAX phase solid solutions

Another important part of this thesis consists in synthesizing and characterizing a set of $Ti_3Al_xSn_{(1-x)}C_2$ solid solutions. In this section, a description of the MAX phase solid solutions reported in the literature will be given, as a function of the substitution's site.

From the periodic table (Figure 1), it is worth noting that, in MAX phases, M, A and X elements either belong to same group or are closed to each other. This means that the physical and chemical properties of elements of each site are similar to each other. In such a case, an easy formation of the solid solutions, at each site, may be expected. Hence, in a first part, we will give a review on the theoretical investigation on the MAX phase solid solutions. In a second part, we will describe the experimental studies that have been reported, in literature, on the synthesis and microstructural characterization of MAX phase solid solutions. As solid solutions synthesized in this thesis are focused on the A substitution site, the description will be specially emphasized on these solid solutions.

I-3.1.Theoretical investigation of MAX phase solid solutions

First-principles electronic calculations have demonstrated the interest in studying the important characteristics of Ti_3SiC_2 [72,73] and Ti_3AlC_2[74] materials. For example, the equilibrium geometrical parameters were well-reproduced [72,73] and the mechanisms of mechanical stability under high pressure was exhibited [66]. Therefore, first principle studies were performed to get a better understanding of the structure/property relationship and to theoretically check the possibility to tune the properties of MAX phase solid solutions.

I-3.1.1. Substitutions at M site

In 2003, Sun *et al.*[75] have performed *ab initio* total energy calculations of the solubility within $(M_xM'_{2-x})AlC$ solid solutions, M and M' being Ti, V and Cr. The calculated values of the equilibrium volume as a function of the substitution contents of the second transition-metal is shown in Figure 4 (a). It is demonstrated that the volume varies linearly with the substitution content. Moreover, equilibrium volume and c/a ratios are in good agreement with experimental results[76]. Sun and co-authors also suggest that, except for the $(Cr,Ti)_2AlC$ system, the other solid solutions investigated show solubility. The variation of

$(M_xM'_{2-x})AlC$ theoretical bulk modulus is shown, as a function of x, in Figure 4(b). It can vary by 36% from 166 to 226 GPa as x increases from 0 to 2. Such a result is supposed to be explained by the filling of the p-d hybridized bonding states. This result has been further refined, in 2004, by Wang and Zhou[77]. Indeed, Wang and Zhou[77] have investigated the elastic stiffness and band structures of $(M_xM'_{2-x})AlC$ (M and M'=Ti, V and Cr) solid solutions by means of the *ab initio* pseudo-potential total energy method.

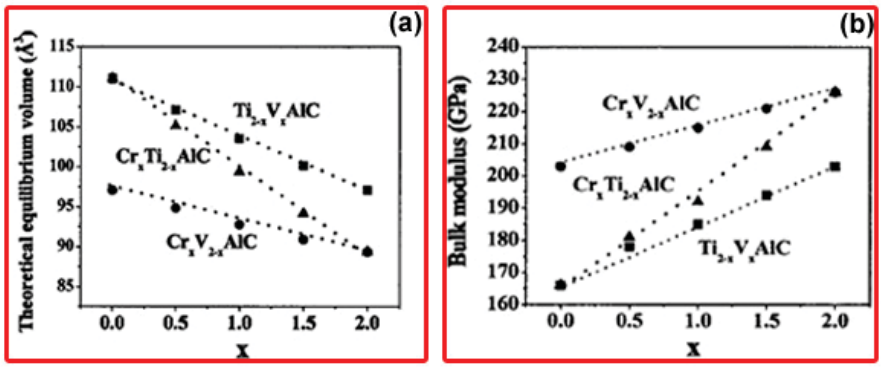

Figure 4 [75]: (a) Calculated values of equilibrium volume as a function of the solid solution content "x" for $(M_xM'_{2-x})AlC$, with M and M'=Ti, V, and Cr. (b) Theoretical bulk modulus of $(M_xM'_{2-x})AlC$ as a function of solid solution content x.

The theoretical bulk modulus of the $[M_xM'_{(2-x)}]AlC$ phases as a function of the Valence Electron Concentration (VEC) is plotted in Figure 5(a). The dashed lines represent the weighted average value of the bulk modulus of the two end-members M_2AlC and M'_2AlC: $B([M_xM'_{(2-x)}]AlC) = x.B(M_2AlC)+(2-x).B(M'_2AlC)$. One can notice that the bulk modulus of $[M_xM'_{(2-x)}]AlC$ is close, in magnitude, to the weighted average value. Such a result indicates that the bulk modulus of $[M_xM'_{(2-x)}]AlC$ systems is well related to the substitution content x and to the VEC; it further indicates that the bulk modulus is predictable when tuning the chemical content in the solid solutions. The solid solution bulk modulus increases monotonically as VEC increases and the improvement is larger when going from Ti_2AlC to V_2AlC than from V_2AlC to Cr_2AlC. The authors have also examined the computed variation of the shear modulus c_{44} as a function of the VEC for the $[M_xM'_{(2-x)}]AlC$ solid solutions; such a variation is shown in Figure 5(b). Figure 5(b) shows that the shear modulus c_{44} saturates to a maximum value for VEC in the range 8.4-8.6. A similar trend was observed for transition metal carbonitrides, in which the c_{44} and microhardness simultaneously reach a maximum at

the VEC value of about 8.4[78]. If the rules for transition metal carbonitrides, are applicable to the studied compounds, this class of ternary carbides would exhibit maximal hardness for VEC in the appropriate range; in other words, solid solution hardening might be operative in $[M_xM'_{(2-x)}]AlC$ for VEC in a certain range. To understand the trends in elastic moduli, common to all these materials on a fundamental level, the characteristics of the electronic band structure of $[M_xM'_{(2-x)}]AlC$ were examined. The authors intend to interpret the trends in elastic stiffness by illustrating the occupation of additional valence electrons in certain electronic states. They show that the bonding states related to the M(M')-C dp interactions are located far above the Fermi level (see Figure 6) and are slightly disturbed as VEC varies.

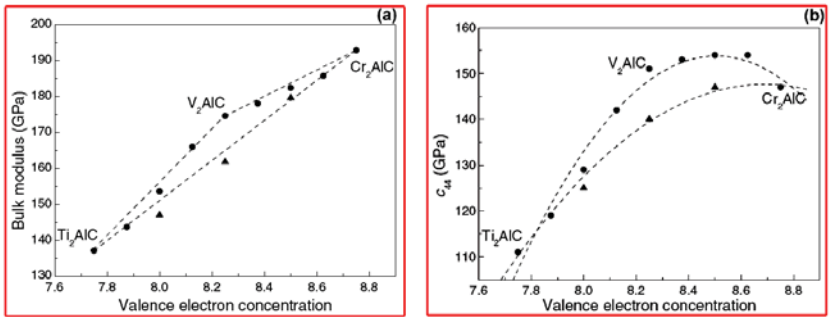

Figure 5[77]*: Theoretical (a) Bulk modulus, (b) shear modulus c_{44} of $[M_xM'_{(2-x)}]AlC$ as a function of Valence electron concentration. Full circles represent the results of $[Ti_xV_{(2-x)}]AlC$ and $[V_xCr_{(2-x)}]AlC$, triangles represent the data of $[Ti_xCr_{(2-x)}]AlC$.*

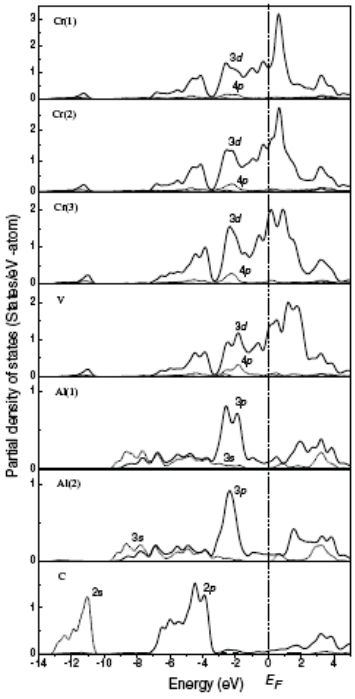

Figure 6 [77]*: Site and angular momentum projection of the electronic density of states of $V_{0.5}Cr_{1.5}AlC$.*

I-3.1.2. Substitutions at A site

In 2003, Wang *et al.*[79] and later Xu *et al.*[80] have studied $Ti_3Si_{1-x}Al_xC_2$ solid solutions using first-principle calculations. All first-principle calculations were performed using a plan-wave pseudo-potential method based on Density Functional Theory (DFT). The crystal structure of $Ti_3Si_{1-x}Al_xC_2$ are built based on the crystal structure of Ti_3SiC_2 using the supercell method. Although synthesized $Ti_3Si_{1-x}Al_xC_2$ solid solutions do not form ordered supercells, Wang *et al.*[79] have shown that the structure calculated based on a supercell is well consistent with the one of the solid solution. In previous investigations performed on MAX phases, Ti atom positions were typically indexed with Ti_I and Ti_{II} owing to the structurally non equivalent positions [1]. However, Zhang *et al.*[81] defined the Ti atom position with four notations, $Ti_{I,1}$, $Ti_{I,2}$, $Ti_{II,1}$, $Ti_{II,2}$, corresponding to the different coordinating environments with C, Si and Al atoms.

The lattice parameters calculated by Xu *et al.* are plotted in Figure 7[80]. It is shown that lattice parameters of $Ti_3Si_{1-x}Al_xC_2$ increase linearly with Al content; it follows Vegard's law which is valid for ideal solid solution. By replacing Si with Al in the solid solution, they found that the structure becomes unstable both energetically and geometrically. Such a result has also been demonstrated by Wang *et al.*[79].

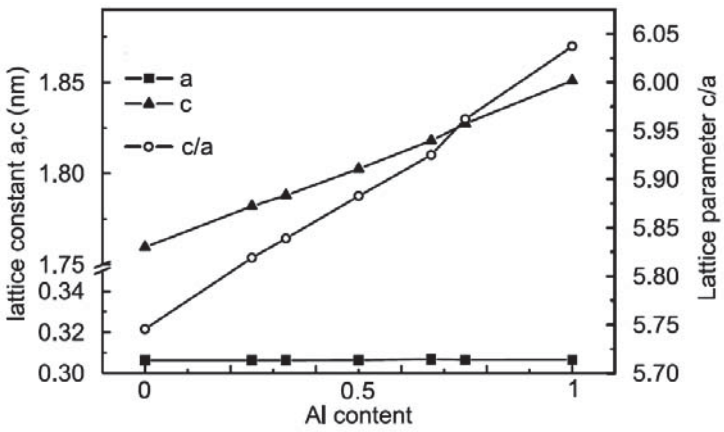

Figure 7 [80]: Crystal structure parameters of $Ti_3Si_{1-x}Al_xC_2$ (x=0, 0.25, 0.33, 0.5, 0.67, 0.75, 1) as a function of Al content "x".

Indeed, the fundamental structural element in Ti_3AC_2 layered ternary carbides was the edge-shared Ti_6C octahedron. Investigation of the geometry of Ti_6C octahedrons show that the octahedrons distort anisotropically in $Ti_3Si_{0.75}Al_{0.25}C_2$ compared to those in Ti_3AlC_2. The

distortions are accommodated by expansion, contraction and rotation of Ti-C bonds in different levels. Two types of deformation for Ti_6C octahedrons are observed. The first one, for which the edge atoms of the octahedron are composed of Ti_I and $Ti_{II,2}$ atoms, is accomplished by $Ti_{I,2}$-C_{II} bond expansion and $Ti_{II,2}$-C_{II} bond contraction. The second type occurs for the octahedron in which edge atoms are composed of Ti_I, $Ti_{II,2}$ and $Ti_{II,1}$. Besides the first distortion mode, it is also accompanied by inclination of the $Ti_{II,2}$ and $Ti_{II,1}$ close packed-plane, which is induced by expansion and rotation of Ti-C bonds.

With increasing Al content in the solid solution, the strength of the chemical bonding is reduced. More precisely, Wang and Zhou have demonstrated that the degrees of covalency of Ti-Si and Ti-Al bonds in $Ti_3Si_{0.75}Al_{0.25}C_2$ is remarkably reduced compared with those in Ti_3SiC_2 and Ti_3AlC_2 compounds[79]. Such a result may imply that $Ti_3Si_{0.75}Al_{0.25}C_2$ has a better oxidation resistance than the end-members as Al atoms can easily escape from the structure to form a protective Al_2O_3 scale. Moreover, the decrease of chemical bonding upon Al content increase implies that the melting point, Vickers hardness, Young's modulus, compressive and tensile strengths of $Ti_3Si_{1-x}Al_xC_2$ are decreased compared to the ones of Ti_3SiC_2.

In summary, theoretical investigations realized on $Ti_3Si_{1-x}Al_xC_2$ MAX phase solid solutions show that:

- *a linear variation of the lattice parameters is expected,*
- *an anisotropic contraction of the Ti_6C octahedrons is expected (it may be accommodated by contraction, expansion and/or rotation of the Ti-C bonds),*
- *replacing the Si by Al atoms in the solid solution reduces the structure stability,*
- *the degree of covalency of the Ti-Si and Ti-Al bonds is reduced compared to the one of the two end-members.*

I-3.1.3. Substitutions at X site

Du *et al.*[82] have performed first principal calculations based on the DFT to predict elastic and thermal properties of $Ti_2AlC_{0.5}N_{0.5}$. The total energies were calculated by using the full-potential linearized augmented plane-wave method plus local orbital as implemented in WIEN2k code[83]. The calculated values of the lattice constants as well as the corresponding

experimental results [84] are plotted in Figure 8. The computed structural parameters agree quite well with experimental data; the deviations for the lattice constants and cell volume are 0.6% and 1.8%, respectively. The *a* parameter varies linearly with the N content and thus follows the Vegard's law valid for ideal solid solution, while the *c*-parameter remains essentially unchanged. In contrast, when Si is replaced by Al as in $Ti_3Si_{0.75}Al_{0.25}C_2$, the *c* values are more affected than the *a* values (see Figure 7). This result suggests that *c*-value is more dependent on the M-A bonds than on the M-X bonds.

Like most other Ti-containing MAX phases, the states in the vicinity of the Fermi level are mainly occupied by Ti 3d. The calculated density of states at the Fermi level are 2.59, 4.82 and 3.93 states/(eV unit cell) for Ti_2AlC, $Ti_2AlC_{0.5}N_{0.5}$ and Ti_2AlN, respectively. These high values explain the metallic behavior of these compounds.

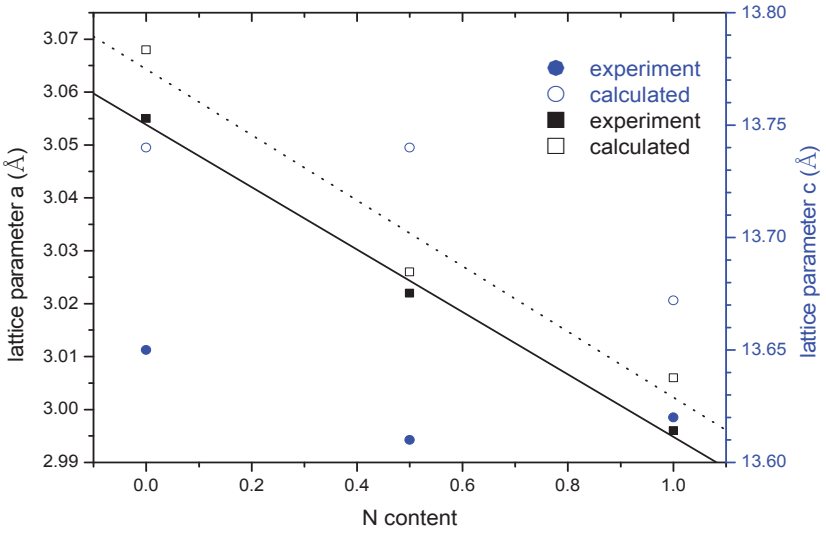

Figure 8 [82,84]: Lattice parameters of $Ti_2AlC_{1-x}N_x$ (x=0, 0.5, 1) as a function of N content "x".

I-3.2. Synthesis and microstructural characterization of selected MAX phase solid solutions

I-3.2.1. Substitutions at the M site

Table 3 lists the synthesis conditions and some microstructural characterizations of several $(M_xM'_{1-x})_{n+1}AX_n$ solid solutions. As shown in Table 3, $(Ti_xNb_{1-x})_2AlC$, $(Ti_xV_{1-x})_2AlC$, $(Ti_xHf_{1-x})_2InC$, $(Ti_xZr_{1-x})_2InC$, $(V_xCr_{1-x})_2GeC$, $(V_xCr_{1-x})_2AlC$ have been produced. These solid solutions are mostly synthesized by HPing[85-88] or HIPing[85,89-95] techniques in the 1180°C-1600°C temperature range. Some impurities such as A-oxide [85,89-92], MC binary

phase[85,88-91,93-95] and pure A element[93-95], are detected in the final products. In this table, also, the MAX phase solid solution grain size is most of the time a mean grain size, probably measured in the basal plane. The grain size along the c axis is not mentioned. This remark is valid for the other solid solutions (substitutions on A and X sites) further described in Tables 4 and 5.

MAX phases solid solutions	Starting materials	Synthesis conditions	XRD results	SEM/EDXS results	Reference
$(Ti_{0.5}Nb_{0.5})_2AlC$	Ti:Nb:Al_4C_3:C stoichiometric proportions	HIP 1600°C/8h/100MPa HP 1450°C/24h/100MPa	Predominately single phase *a*=3.077 Å c=13.79 Å	98vol.% $(Ti_{0.5}Nb_{0.5})_2AlC$ GS: 45µm at 1600°C GS: 15µm at 1450°C < 1 vol.% Al_2O_3 ≈ 1 vol.% Nb-Ti carbides and aluminides	[85,89-91]
$(Ti_{0.5}V_{0.5})_2AlC$	Ti:V:Al:C stoichiometric proportions	HIP 1600°C/8h/70MPa	Single phase	$(Ti_{0.5}V_{0.5})_2AlC$ GS: 25±10 µm < 2 vol.% Al_2O_3, some grains deficient in Al	[92]
$(Ti_x,V_{1-x})_2AlC$ (x=0.05-0.2)	Ti:V:Al:C	HP 1450°C/1h/20MPa	Single phase *a* and *c* changes linearly with x	GS for all the samples: 39 µm in diameter 19 µm in thickness	[86]
$(Ti_{0.5}Hf_{0.5})_2InC$	Ti:Hf:In:C stoichiometric proportions	Pressure less sintering 650°C/10h/vacuum + HIP 1300°C/12h/70MPa	Single phase	96 vol.% $(Ti_{0.5}Hf_{0.5})_2InC$ GS: 25±5µm 2 vol.% TiC_x and HfC_x 2 vol.% In	[93-95]
$(Ti_{0.5}Zr_{0.5})_2InC$	Ti:Zr:In:C stoichiometric proportions	Pressure less sintering 650°C/10h/vacuum +HIP 1300°C/12h/70 MPa	Single phase	95 vol.% $(Ti_{0.5}Zr_{0.5})_2InC$ GS: 8±5µm 2 vol.%: ZrC_x≈TiC_x≈In	[93,94]
$(Cr_{0.5}V_{0.5})_2GeC$	Cr:V:Al:C stoichiometric proportions	HP 1180°C/8h/1.5GPa	96 vol.% $(Cr_{0.5}V_{0.5})_2GeC$ a=2.773Å c=12.161Å <3vol.% Ge <1vol.% GeO_2	EPMA $Cr_{25.8}V_{25.0}Ge_{26.2}$ GS: 4-5 µm	[87]
$(V_{1-x}Cr_x)_{n+1}AlC_n$	1Cr:1V:1.1Al:C 1.5Cr:1.5V:1.1Al:2C 2Cr:2V:1.1Al:3C	HP 1400-1600°C/1h/30 MPa Ar	x ≈0 or 1 211 +V_{1-x} Cr_xC x≈0.5 or T>1500°C: 211+new phases $(V_{0.5}Cr_{0.5})_3AlC_2$ and $(V_{0.5}Cr_{0.5})_4AlC_3$	-	[88]

Table 3: Summary of the recent studies on synthesis and microstructural characterization of MAX phase solid solutions on the M site (GS: grain size).

I-3.2.2. Substitutions at the A site

Table 4 summarizes the synthesis conditions and some microstructural characterizations of $M_{n+1}[A_{1-x}A'_x]C_n$ solid solutions. As shown in Table 4, in the Ti-Si-Ge-C system, the synthesis and characterization of $Ti_3(Si_xGe_{1-x})C_2$ (x=0.5, 0.75) was first reported by Ganguly *et al.* and Barsoum *et al.*[96-98]. They fabricated coarse-grained $Ti_3(Si_xGe_{1-x})C_2$ (x=0.5, 0.75) solid solutions by HIPing a Ti:Ge:SiC:C reactant mixture with stoichometric proportions at 1600°C for 8h under a pressure of 172MPa. The as-synthesized $Ti_3Si_{0.5}Ge_{0.5}C_2$ solid solution is predominantly single phase with about 2 vol. % of TiC and 3 vol. % of titanium silicides. $Ti_3Si_{0.5}Ge_{0.5}C_2$ grain size is 40±30µm. As-synthesized coarse-grained (70±56µm) $Ti_3Si_{0.75}Ge_{0.25}C_2$ solid solution contains about 3 vol. % of TiC. The fine-grained (7±3µm) $Ti_3Si_{0.5}Ge_{0.5}C_2$ solid solution has been synthesized at a lower temperature, 1450°C, the other parameters being constant. The solid solution contains about 4 vol.% of TiC. The calculated *a* and *c* lattice parameters of $Ti_3Si_{0.5}Ge_{0.5}C_2$ are 3.082±0.001 Å and 17.751±0.006 Å, while the $Ti_3Si_{0.75}Ge_{0.25}C_2$ ones are 3.074±0.002 Å and 17.747±0.004 Å. The lattice parameters of the solid solutions lie in between the ones of the two end-members.

A set of $Ti_3(Al_{1-x}Si_x)C_2$ ($x \leq 0.25$) solid solutions were fabricated by Zhou *et al.* and Chen *et al.* using a solid-liquid synthesis reaction and simultaneous in situ hot pressing method[99-101]. A Ti:Al:Si:C reactant mixture with proper mol. ratio was heated at 1500°C for 1h under a pressure of 30MPa to yield the desired solid solutions. From X-Ray Diffraction (XRD) patterns, only $Ti_3(Al_{1-x}Si_x)C_2$ solid solutions were detected. The *a* and *c* lattice parameters of $Ti_3(Al_{1-x}Si_x)C_2$ solid solutions are plotted, in Figure 9, as a function of Si content. Figure 9 allows demonstrating that the Si content increase leads to a drastic decrease of the *c* lattice parameter whereas the *a* lattice parameter remains almost unchanged. Furthermore, the microstructures of the as-synthesized $Ti_3(Al_{1-x}Si_x)C_2$ solid solutions were almost the same; the mean grain size given by the authors is 20µm.

Radovic *et al.*[46] synthesized the $Ti_3Si_{0.5}Al_{0.5}C_2$ solid solution by HIPing a Ti:SiC:Al:C reactant mixture at 1400°C for 10h under a pressure of 100MPa. A consecutive annealing treatment was performed at 1400°C for 48h under an Ar atmosphere to reduce the TiC_x content. The as-synthesized $Ti_3Si_{0.5}Al_{0.5}C_2$ sample contains about 6 vol.% of TiC_x. The mean

$Ti_3Si_{0.5}Al_{0.5}C_2$ grain size is 15±5µm.

On the other hand, substitution of Si by Al to form $Ti_3(Si_{1-x}Al_x)C_2$ (x=0.01-0.15) solid solutions was used to improve the purity of Ti_3SiC_2[81,102]. To prepare the desired sample, 3Ti:1.2($Si_{1-x}Al_x$):2C reactant mixtures were heated at 1550°C for 5 min, and then annealed at 1400°C for 1h under a pressure of 40MPa. For x in the 0.01-0.04 range, as-synthesized $Ti_3(Si_{1-x}Al_x)C_2$ samples contain TiC and SiC as the secondary phases. For x in the 0.05-0.1 range, pure $Ti_3(Si_{1-x}Al_x)C_2$ samples are obtained. For x higher than 0.1, TiC appears once more in the $Ti_3(Si_{1-x}Al_x)C_2$ sample

MAX phases solid solutions	Starting materials	Synthesis conditions	XRD results	SEM/EDXS results	Reference
$Ti_3(Si_{0.5}Ge_{0.5})C_2$	Ti:Ge:SiC:C stoichometric proportions	HIP 1600°C/8h/172MPa	Calculation of the lattice parameters	95 vol.% $Ti_3(Si_{0.5}Ge_{0.5})C_2$ GS:40±30 µm 2 vol.% TiC 3 vol.% Si-Ti liquid phase	[96-98]
		HIP 1450°C/8h/172MPa		96 vol.% $Ti_3(Si_{0.5}Ge_{0.5})C_2$ GS: 7 ±3 µm 4 vol.% TiC	
$Ti_3(Si_{0.75}Ge_{0.25})C_2$		HIP 1600°C/8h/172MPa	Calculation of the lattice parameters	97 vol.% $Ti_3(Si_{0.75}Ge_{0.25})C_2$ GS: 70±56 µm 3 vol.% TiC	
$Ti_3(Al_{1-x}Si_x)C_2$ (x≤0.25)	Ti:Al:Si:C with proper ratio	HP 1500°C/1h/30MPa	Pure Calculation of the lattice parameters	Pure GS: 20 µm	[99-101]
$Ti_3(Al_{0.5}Si_{0.5})C_2$	Ti:SiC:Al:C	HIP 1400°C/10h/100MPa + Annealing 1400°C/48h/Ar	94 vol.% $Ti_3Al_{0.5}Si_{0.5}C_2$ 6 vol.% TiC	GS: 15±5µm	[46]
$Ti_3(Si_{1-x}Al_x)C_2$ (x=0.01-0.15)	3Ti:1.2($Si_{1-x}Al_x$):2C	HP 1550°C/5 min + Annealing 1400°C/1h/40MPa	x=0.01-0.04 $Ti_3(Al_{1-x}Si_x)C_2$ TiC and SiC x=0.05-0.1 pure $Ti_3(Al_{1-x}Si_x)C_2$ x> 0.1 $Ti_3(Al_{1-x}Si_x)C_2$ and TiC	-	[81,102]

Table 4: Summary of the recent studies on synthesis and microstructural characterization of $M_{n+1}[A_{1-x}A'_x]C_n$ solid solutions. (GS: grain size).

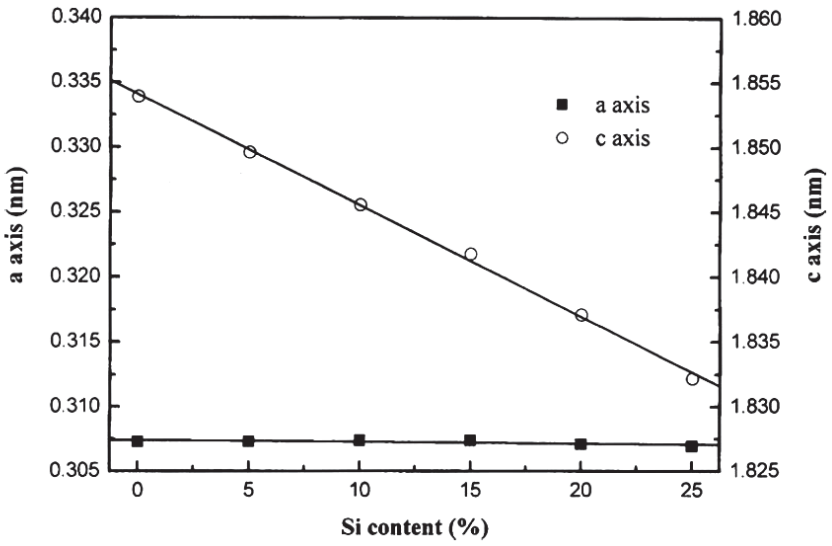

Figure 9 [99]*: Lattice parameters of* $Ti_3(Al_{1-x}Si_x)C_2$ *solid solutions calculated from Rietveld refinement method.*

In summary, substitutions on the A site are possible, using different A group elements, to form MAX phase solid solutions. Either HIPing [46,96-98] *or HPing*[81,99-102] *techniques have been adopted to synthesize these solid solutions in the 1450-1600°C temperature range. Furthermore, minor impurities such as carbides (TiC or SiC)*[46,81,93-95,102] *and intermetallics (titaniumsilicide phases)*[96-98] *can coexist with as-synthesized MAX phase solid solutions.*

I-3.2.3. Substitutions at the X site

In MAX phase, only two elements, C and N, correspond to X site. To date, only two solid solutions, $Ti_2AlC_{0.5}N_{0.5}$ and Ti_3AlCN, have been reported at the X substitution site [31,84,103]. Table 5 gives the reported synthesis methods and some microstructural characterizations of $Ti_{n+1}Al[C_{1-x}N_x]_n$ solid solutions.

$Ti_2AlC_{0.5}N_{0.5}$ solid solution was firstly synthesized by Barsoum *et al.* using HIPing process in 1999[31]. As-synthesized $Ti_2AlC_{0.5}N_{0.5}$ solid solution was predominately single phase with 4 vol.% of Al_2O_3 and Ti_3P as the secondary phases. The mean $Ti_2AlC_{0.5}N_{0.5}$ grain size is 25µm. More recently, Ti_3AlCN was synthesized by Manoun *et al.* using HIPing process [103]. From XRD analyses and SEM observations, the authors show that as-synthesized Ti_3AlCN solid solution is predominately single phase with 2 vol.% of TiC and 3 vol.% of Al_2O_3 as the secondary phases. The Ti_3AlCN mean grain size is 25±15µm.

MAX phases solid solutions	Starting materials	Synthesis conditions	XRD results	SEM/EDXS results	Reference
$Ti_2AlC_{0.5}N_{0.5}$	Ti:Al_4C_3:C:AlN stoichometric proportions	HIP 1300°C/15h/40MPa	Predominately pure Calculation of the lattice parameters	96 vol.% $Ti_2AlC_{0.5}N_{0.5}$ GS: 25µm 4 vol.%Al_2O_3 and Ti_3P	[31,84,103]
$Ti_3Al(C_{0.5}N_{0.5})_2$	Ti:AlN:C proper stoichiometric	HIP 1400°C/10h/100MPa	Predominately pure Calculation of the lattice parameters	95 vol.% $Ti_3Al(C_{0.5}N_{0.5})_2$ GS: 25±15µm 2 vol.% TiC 3 vol.% Al_2O_3	[31,84,103]

Table 5: Summary of the recent studies on synthesis and microstructural characterization of $Ti_{n+1}Al[C_{1-x}N_x]_n$ solid solutions (GS: grain size).

I-4. Some selected mechanical properties of MAX phases and solid solutions

As mentioned above, MAX phases own a combination of excellent properties of metals and ceramics. In this part, some of the mechanical properties of the MAX phases studied in the literature will be reported; mechanical properties that we will further study in the frame of this thesis. The mechanical properties investigated are the hardness (using nanoindentation tests), the elastic properties (room temperature and temperature dependence) and the compression behavior. As MAX phase mechanical properties depend on grain size, fine-grained (noted FG) and coarse-grained (noted CG) microstructures will be further compared and discussed.

I-4.1. Elastic properties

I-4.1.1. Temperature dependency of elastic properties

In general, MAX phases are relatively stiff and lightweight, which can be deduced from theoretical and experimental investigations. One of the most efficient method to evaluate the temperature dependence of elastic properties is the pulse-echo ultrasonic technique or the Resonant Ultrasound Spectroscopy (RUS)[1,32,43,46,84,98,104,105]. From the measure of the longitudinal and shear velocities (V_l and V_s respectively) by RUS technique, the Young's modulus (E), shear modulus (G), and Poisson's ratio (υ) can be deduced using Navier's equations:

$$E = V_s^2 \rho \frac{(3V_l^2 - 4V_s^2)}{(V_l^2 - V_s^2)} \quad (1)$$

$$G = V_s^2 \rho \quad (2)$$

$$v = \frac{E}{2G} - 1 \quad (3)$$

where ρ is the density of the sample.

At temperature lower than the Brittle-to-Ductile Transition Temperature (BDTT), the elastic modulus variations with temperature can be well-fitted assuming [32]:

$$\frac{E}{E_{RT}} = \frac{d(E/E_{RT})}{dT}(T - 298) \quad (4)$$

$$\frac{G}{G_{RT}} = \frac{d(G/G_{RT})}{dT}(T - 298) \quad (5)$$

In such a case, the temperature dependencies of elastic constants of different MAX phases were investigated in different temperature ranges:

- ✧ ***Low temperature dependency***: Finkel *et al.*[32,104] have investigated the elastic properties of Ti_4AlN_3, Ti_3AlC_2 and Ti_3SiC_2 in the 90-300K temperature range. As shown in Figures 10 (a) and (b), they found that, for the three MAX phases and in the 125-300K temperature range, E and G slightly decrease with increasing temperature. Elastic moduli of Ti_3SiC_2 are larger than the ones of Ti_4AlN_3 which are larger than the ones of Ti_3AlC_2. In addition, comparing E and G for CG (100-200μm) and FG(3-5μm) Ti_3SiC_2 samples, they found that there is no obvious difference between elastic moduli of the two type of sample with different grain size.
- ✧ ***Room temperature to high temperature range dependency***: The temperature dependence of elastic constants of Ti_3SiC_2, Ti_3GeC_2, $Ti_3Si_{0.5}Al_{0.5}C_2$ and Ti_2AlC MAX phases were investigated by Radovic *et al.* [46] in the 300-1573K temperature range. As shown in Figures 11 (a) and (b), E and G decrease gradually and linearly with increasing temperature for the four studied MAX phases. Elastic moduli of the different MAX phases investigated can be classified as follows: Ti_2AlC < Ti_3GeC_2 <

$Ti_3Si_{0.5}Al_{0.5}C_2 < Ti_3SiC_2$.

✧ **The *room temperature*** (RT) elastic constants of some MAX phases, measured by RUS technique, are summarized in Table 6. It is shown that the RT Young's modulus E of selected MAX phases ranges between 245 and 347GPa. The corresponding shear modulus G values range between 105 and 145GPa. The Poisson's ratio is in the 0.16-0.22 range. Moreover, compared to the 312 and 413 phases, the 211 phases are significantly less stiff due to the small fraction of M-X bonds in the structure. Another important factor which may affect the elastic properties is the solid solution effect. A solid solution strengthening is observed in Ti-Al-C-N system [84] but not in the Ti-Al-Si-C[46] and Ti-Si-Ge-C[98] systems. Compared to the end-members, E and G of Ti_3AlCN[84] and $Ti_2AlC_{0.5}N_{0.5}$[84] are higher than the ones of Ti_3AlC_2[32] and Ti_4AlN_3[32] (Ti_3AlN_2 does not exist) and Ti_2AlN[84] and Ti_2AlC[43,46], respectively. However, in the Ti-Al-Si-C system [46], E and G seem to vary linearly from Ti_3AlC_2 to Ti_3SiC_2. In the Ti-Si-Ge-C system[98], E and G of $Ti_3Si_{0.5}Ge_{0.5}C_2$ are smaller than the ones of Ti_3SiC_2[32] and Ti_3GeC_2[46]. A solid solution softening is thus observed in the Ti-Si-Ge-C system.

MAX phases		ρ (g/cm^3)	V_l (m/s)	V_s (m/s)	E (GPa)	G (GPa)	υ	Reference
413 phase	Ti_4AlN_3	4.7	8685	5201	310	127	0.22	[32]
312 phase	Ti_3AlCN	4.5	9092	5514	330	137	0.21	[84]
	Ti_3AlC_2	4.2	8880	5440	297	124	0.2	[32]
	$Ti_3Al_{0.5}Si_{0.5}C_2$	4.35	9015	5650	322	136.8	0.176	[46]
	FG Ti_3SiC_2	4.47	9100	5570	333	139	0.2	[32]
	CG Ti_3SiC_2	4.5	9142	5613	339	142	0.2	[32]
	$Ti_3Si_{0.5}Ge_{0.5}C_2$	5.02	8262	5096	310	130	0.2	[98]
	Ti_3GeC_2	5.29	8242	5182	347	145	0.196	[46]
211 phase	Ti_2AlC	4.0	8509	5423	277	118.8	0.19	[43,46]
	$Ti_2AlC_{0.5}N_{0.5}$	4.2	8670	5407	290	123	0.18	[84]
	$Ti_2AlN_{0.996}$	4.25	8553	5328	285	120.5	0.18	[84]
	Cr_2AlC	5.24	7215	4450	245	105	0.20	[43]
	Nb_2AlC	6.34	7125	4306	286	117	0.21	[43]
	V_2AlC	4.81	7898	4913	277	127	0.20	[43]
	Ti_2SC	4.59	8200	5200	290	125	0.16	[105]

Table 6: Young's modulus (E), shear modulus (G) and Poisson's ratio (υ) of some MAX phases, measured by RUS technique at room temperature.

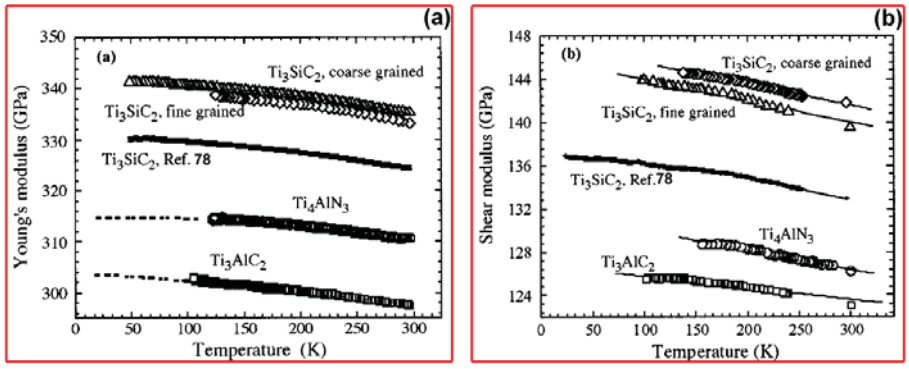

Figure 10 [32]*: Temperature dependencies, in the 30-300K temperature range, of (a) Young's modulus, (b) shear modulus of Ti_4AlN_3, Ti_3AlC_2 and Ti_3SiC_2.*

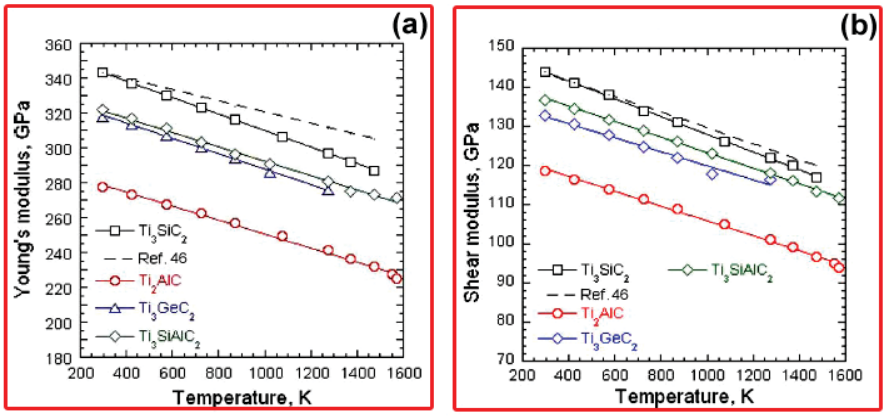

Figure 11 [46]*: Temperature dependencies, in the 300-1600K temperature range, of (a) Young's modulus, (b) shear modulus of Ti_3SiC_2, Ti_3GeC_2, $Ti_3Si_{0.5}Al_{0.5}C_2$ and Ti_2AlC.*

I-4.1.2. Elastic modulus (E) determined by nanoindentation tests

Another conventional way to determine the elastic modulus of the material is using load-penetration depth curves obtained from nanoindentation tests. Table 7 lists some research work on the elastic modulus measurement of MAX phases by nanoindentation tests. As shown in Table 7, the elastic modulus of Ti_3SiC_2, measured with two different types of indenter[106,107], is similar and also close to the one measured by RUS technique[32]. In both studies, the authors demonstrate that the elastic modulus of Ti_3SiC_2 is independent on the grain orientation. Nevertheless, using a Berkovich indenter, Kooi *et al.*[106] have found that Ti_3SiC_2 elastic modulus slightly varies along different orientations. They explain that such a difference is not caused by the elastic modulus anisotropy but it is related to the deformation ability along different orientations (i.e.: kink band formation).

From nanoindentation tests, the elastic modulus of MAX phase thin films are in the

240-280GPa range[108,109]. This value is independent on the penetration depth of the indenter. Nevertheless, this value is lower than the bulk material one, measured by RUS technique.

Method	Sample	Grain size (µm)	Indenter	Elastic modulus (GPa)	reference
Nanoindentation tests	Ti_3SiC_2 bulk	50-200	Berkovich	Parallel basal plane: 346±10 Perpendicular basal plane: 302±5	[106]
	Ti_3SiC_2 bulk	1000-2000	Spherical	Parallel basal plane: 320 Perpendicular basal plane: 320	[107]
	Ti_3SiC_2 film	0.65	Beckovich	250-280	[108]
			Cube corner		
	Ti_3AlC_2 film	0.15	Berkovich	240	[109]
	Ti_2AlC film	0.15	Berkovich	240	[109]

Table 7: Elastic modulus (E) of some 312 MAX phases measured by nanoindentation test.

In summary, the elastic constants of MAX phases, measured by RUS technique, are temperature dependent. Elastic constants decrease linearly with increasing temperature. Elastic constants do not seem to depend on MAX phase grain size. The reported MAX phase RT values of E and G range from 245 to 347GPa and 105 to 145GPa, respectively. Compared to the 312 and 413 phases, the 211 phases are significantly less stiff due to the small fraction of M-X bonds in the structure. A solid solution strengthening is observed in the Ti-Al-C-N system but not in the Ti-Si-Al-C and Ti-Si-Ge-C systems. The MAX phase elastic modulus, measured by nanoindentation tests, does not depend on grain orientation and penetration depth of the indenter.

I-4.2. Hardness measured by microindentation and nanoindentation tests

MAX phases are relatively soft and anisotropic compared to their corresponding binary carbide or nitride phases MX. Tables 8 and 9 list hardness values of some typical MAX phases and related solid solutions measured by nanoindentation and microindentation tests respectively.

The hardness values measured by microindentation tests are distributed in the 2-8GPa range, and the highest value 8GPa, is measured on the new synthesized FG Ti_2SC sample[110]. Furthermore, MAX phases hardness is anisotropic. This was first reported by Nickl *et al.*[111] on Ti_3SiC_2 single crystals; the hardness values measured by microindentation tests normal to the basal planes are much higher (12-15GPa) than the ones parallel to the basal planes

(3-4GPa). Goto and Hirai *et al.*[112] confirmed this conclusion. Recently, nanoindentation tests performed on Ti_3SiC_2 also demonstrated the anisotropic behavior of the hardness[106,107]. Indeed, Kooi *et al.*[106] found that, using a Berkovich indenter, Ti_3SiC_2 hardness value measured parallel to basal plane is 4.9GPa whereas hardness value measured perpendicular to basal plane is 7.3GPa. With a spherical indenter, Murugaiah *et al.*[107] further confirmed the anisotropic behavior of Ti_3SiC_2 hardness. Otherwise, the hardness of MAX phase thin film, has been investigated by Emmerlich *et al.* [108] and Wilhelmsson *et al* [109] by nanoindentation tests. Wilhelmsson *et al.* found a much higher hardness value for Ti_3SiC_2 films (15-18GPa) as compared to the bulk one measured by nano[106, 107] and microindentation tests[30,114]. Nevertheless, these values are in good agreement with the ones measured by microindentation tests normal to basal plane by Nickl *et al.*[111].

Sample	Grain size (µm)	Load (mN)	Indenter	Hardness (GPa)	Reference
Ti_3SiC_2 bulk	50-200	500	Berkovich	Parallel basal plane: 4.9 Perpendicular basal plane: 7.3	[106]
Ti_3SiC_2 bulk	1000-2000	5-500	Spherical	Parallel basal plane: 4 Perpendicular basal plane: 4.5	[107]
Ti_3SiC_2 film on Al_2O_3 substrate	0.65	0.3-3	Berkovich	Normal to basal plane: 15-18	[108]
		0.1-3	Cube corner		
Ti_3AlC_2 film on Al_2O_3 substrate	0.15	-	Berkovich	14	[109]
Ti_2AlC film on Al_2O_3 substrate	0.15	-	Berkovich	15	[109]

Table 8: Hardness values of some MAX phases measured by nanoindentation tests.

Several key factors may affect the hardness measurements performed by microindentation and nanoindentation tests on MAX phases:

- ✧ ***Impurities.*** From Table 9, it can be seen that, some "harder" binary MX phase (TiC[30,57,96,114], TiN[34], NbC_x[85], Cr_3C_7[49], *etc*) and oxide (TiO_2[96,110] and Al_2O_3[31,36,85,116], *etc*) often coexist with the MAX phases. These "harder" impurities results in an increase of the hardness of as-synthesized MAX phase sample measured by microindentation tests.

- ✧ ***Grain orientation.*** MAX phase structure is anisotropic. As a consequence, the

hardness of MAX phases is strongly dependent on the grain orientation, especially for nanoindentation tests. When the indentation loads are parallel to the basal plane, MAX phases are "softer". In contrast, when the indentation loads are normal to basal plane, they are "harder".

- ***Grain size*.** The grain size effect does not seem very obvious in microindentation tests, especially for higher loads. One of the best evidence is that the hardness of FG and CG Ti_3SiC_2 measured at 100N are both 4 GPa[30]. However, in Ti_2SC[110], Cr_2AlC[116] , , V_2AlC[117] , a grain size effect is observed. The FG MAX phase is harder than the CG MAX one.

- ***Indentation Size Effect (ISE).*** Both for microindentation and nanoindention tests, an ISE is observed: hardness values decrease with increasing load. The ISE may be attributed to the critical load to initiate plastic deformation, i.e. by kink band formation in MAX phase[106]. Vickers indents realized at high load and large penetration depth introduce kink bands in several MAX phase grains, irrespective to their orientation; measured hardness value is likely affected by the presence of kink bands, but also by the presence of grain boundaries. Therefore, for high loads, the measured hardness is lower and probably underestimated[106].

- ***Solid solutions hardening effect*.** A solid solution hardening effect has been observed in the Ti-Al-C-N and V-Ti-Al-C systems. In the Ti-Al-C-N system[31], the hardness of $Ti_2AlC_{0.5}N_{0.5}$ (5.5 GPa) is higher than the ones of the end-members, Ti_2AlC (4.5GPa) and Ti_2AlN (4GPa); the hardness being measured in the same conditions. Such a kind of solid solution strengthening effect was further reported by Meng *et al.* in the V-Ti-Al-C system[86]. The measured hardness of the $(Ti_x,V_{1-x})_2AlC$ (x=0.05-0.2) is higher than the ones of Ti_2AlC[115] and V_2AlC[117] end-members for comparable conditions. However, in other solid solutions, such as in the Ti-Nb-Al-C[85], Ti-Si-Ge-C[96] and Ti-Si-Al-C[99] systems, no solid solution strengthening effect is observed.

Sample	Grain size (μm)	Impurities	Indentation load (N)	Hardness (GPa)	Reference
Ti_4AlN_3	20	1 vol.% TiN	3-100	2.5	[34]
Ti_3AlC_2	25	4 vol.% Al_2O_3	0.5-300	4.5	[36]
	FG: 5	TiC_x	10-100	FG: 6	[57]
	CG: 10-20			CG: 3.5	
	9.5	none	1-20	2.8	[113]
	Diameters:20-50, Thickness: 5-8	none	0.5-10	2.7	[53]
$Ti_3Al_{1-x}Si_xC_2$ ($x \leq 0.25$)	20	none	10	3-3.8	[99]
Ti_3SiC_2	FG: 3-5	3 vol.% TiC_x	0.5-100	FG: 4	[30]
	CG: 100-200			CG: 4	
	20	3 vol.% TiC_x	9.8-98	4	[114]
	10 Single grain	none	-	Normal to basal plane:12-15 Parallel to basal plane: 3-4	[111]
	40000×12000×400	none	9.8-98	Mean value: 6	[112]
$Ti_3Si_{0.5}Ge_{0.5}C_2$	40±30	2 vol.% TiC, 3 vol.% Si-Ti liquid phase	1-10	2.5±0.2	[96]
$Ti_3Si_{0.75}Ge_{0.25}C_2$	70±56	3 vol.% TiC	1-10	2.5±0.2	[96]
Ti_3GeC_2	46±15	3 vol.% TiO_2	1-10	2.2	[96]
Nb_2AlC	14±2	2 vol.% Al_2O_3, 1 vol.% Nb Carbides and aluminides	0.5-10	6.1	[85]
$(Ti_{0.5}Nb_{0.5})_2AlC$	45	< 1 vol.% Al_2O_3, ≈ 1 vol.% Nb-Ti carbides and aluminides	0.5-10	5.8	[85]
	15				
Ti_2AlN	100	10-20 vol.% Al_2O_3, Ti_3P and Ti_4AlN_3	0.5-10	4	[31]
$Ti_2AlC_{0.5}N_{0.5}$	25	4 vol.% Al_2O_3 and Ti_3P	0.5-10	5.5	[31]
Ti_2AlC	25	10-15% Al_2O_3 and Ti_3P	0.5-10	4.5	[31]
	L:20, W:5	none	10	2.8	[115]
	15	none	0.98	4.2-5.7	[50]
$(Ti_x,V_{1-x})_2AlC$ (x=0.05-0.2)	Diameter: 39 Thickness: 19	none	10	3.5-4.5	[86]
Cr_2AlC	10	none	1-10	5.5	[44]
	FG: 2	Al_2O_3	10-500	FG: 6.4	[116]
	CG: 35			CG: 3.5	
	5	3 wt.% Cr_3C_7	20	5.2	[49]
V_2AlC	L:49-405,W:19-106	none	5-100	1.9-2.9	[117]
Ti_2SC	FG: 2-4	6 vol.% TiO_2	2-300	FG: 7-8	[110]
	CG: 10-20			CG: 6-7	

Table 9: Hardness of selected MAX phases measured by microindentation tests (L: length of lamella, W: width of lamella).

I-4.3. Compressive behavior and deformation mechanisms at room temperature

I-4.3.1. Deformation of highly oriented quasi-single crystals of MAX phases[27,118]

Using a forging and grain-growth route, a high oriented Ti_3SiC_2 quasi-single crystal with a grain size of 1 to 2 mm has been fabricated at 1600°C for 24h by Barsoum *et al.*[27]. As shown schematically in Figure 12(a), the basal plane of the Ti_3SiC_2 macrograined is parallel to the x axis and it intercepts the x-y plane at an angle of 25°. The compressive stress-strain curves recorded along x and z axes at RT are shown in Figure 12(b). Barsoum and co-authors have shown that compression along different orientations is anisotropic:

- ✧ When the compression is performed along the z axis, the samples yield at 200±10MPa and they deformed plastically until the test was interrupted. *Barsoum et al.* demonstrated that it is possible to deform these samples in compression mode with strains exceeding 50%. In the z direction, the minimum critical resolved shear stress at RT is 36MPa. Two obvious intersecting shear bands are evidenced in the deformed microstructures. They are parallel to the basal plane. However, outside of these bands, the grains are intact.

- ✧ When the compression is performed along the x axis (parallel to basal plane), the yield stress is in the range 230-290MPa, which is higher than the one along the z axis. After the maximum stress, a strain softening effect is observed. Two intersected shear bands are observed from the deformed microstructure. However, a number of other features, such as delamination and kinking in individual grains are also detected. In this case, shear bands and kink band formation may explain the deformation mechanisms.

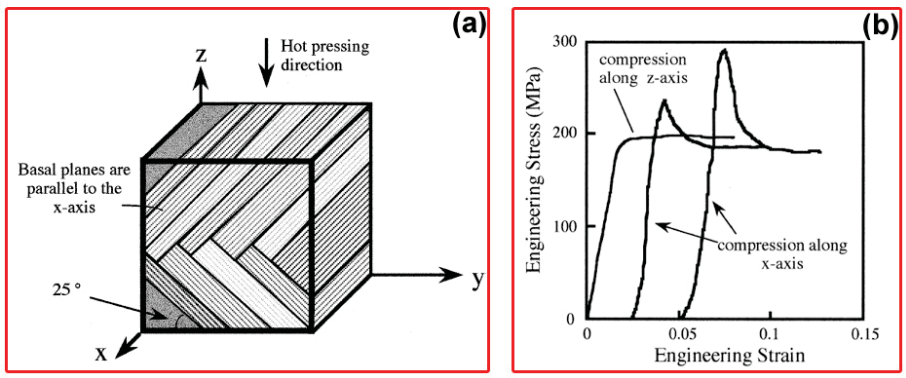

Figure 12 [27]*: (a) Schematic of grain orientation relative to loading directions. Basal planes are for the most part parallel to x axis. (b) Effect of Ti_3SiC_2 grain orientation on RT engineering stress-strain curves compressed in the z and x directions.*

I-4.3.2. The ultimate compressive strength

Table 10 lists the ultimate compressive strength of some typical MAX phases and related solid solutions. The ultimate compressive strength of MAX phases is in the 400-1400MPa range.

Sample	Grain size (μm)	Impurities	Strain rate (s^{-1})	Ultimate Stress (MPa)	Reference
Ti_4AlN_3	20	1 vol.% TiN	10^{-3}	476	[34]
Ti_3AlC_2	25	4 vol.% Al_2O_3	10^{-4}	560±20	[36]
	Diameters:20-50 Thickness: 5-8	None	10^{-4}	764	[53]
$Ti_3Al_{1-x}Si_xC_2$ ($x \leq 0.25$)	20	None	-	700-900	[99]
Ti_3SiC_2	FG: 3-5	3 vol.% TiC_x	10^{-3}	FG: 1050	[30]
	CG: 100-200			CG: 720	
$Ti_3Si_{0.5}Ge_{0.5}C_2$	40±30	2 vol.% TiC 3 vol.% Si-Ti liquid phase	-	538±8	[96]
$Ti_3Si_{0.75}Ge_{0.25}C_2$	70±56	3 vol.% TiC	-	668±10	[96]
Ti_3GeC_2	46±15	3 vol.% TiO_2	-	467±12	[96]
Nb_2AlC	14±2	2 vol.% Al_2O_3 1 vol.% Nb Carbides and aluminides	10^{-5}-10^{-3}	400-900	[85]
$(Ti_{0.5}Nb_{0.5})_2AlC$	45	< 1 vol.% Al_2O_3 ≈ 1 vol.% Nb-Ti carbides and aluminides	10^{-5}-10^{-3}	800	[85]
	15			900-1100	
Ti_2AlN	100	10-20 vol.% Al_2O_3, Ti_3P and Ti_4AlN_3	10^{-3}	470	[31]
$Ti_2AlC_{0.5}N_{0.5}$	25	4 vol.% Al_2O_3 and Ti_3P	10^{-3}	810±10	[31]
Ti_2AlC	25	10-15% Al_2O_3 and Ti_3P	10^{-3}	540±21	[31]
	L: 20, W: 5	None	10^{-4}	763	[120]
	Diameter: 41 Thickness: 16	None	10^{-4}	580	[115]
	15	None	-	670	[50]
$(Ti_{0.85}V_{0.15})_2AlC$	Diameter: 39 Thickness: 19	None	10^{-4}	660	[86]
Cr_2AlC	6.4±2.1	Cr_3C_7	10^{-3}-10^{-5}	997±29	[121]
	5	3 wt.% Cr_3C_7	-	1159±21	[49]
V_2AlC	L: 49, W: 19	None	-	742±89	[117]
	L: 108, W: 37	None		604±29	
	L: 119, W: 47	None		527±12	
	L: 405, W: 106	None		393±16	
Ti_2SC	FG: 2-4	6 vol.% TiO_2	-	1400	[110]

Table 10: Ultimate compressive strength of selected MAX phases.

And several factors are considered to affect the compressive strength according the previous studies:

- ✧ ***Grain size.*** The ultimate compressive strength of MAX phases is strongly dependent on the grain size and obeys the Hall-Petch effect[119]: the compressive strength increases with decreasing grain size. One of the best example is the V_2AlC MAX phase[117] shown in Table 10: the compressive strength decreases from 742±89MPa to 393±16MPa with the increasing grain size. In the smaller grained MAX phases, the ultimate compressive strength can be over 1GPa; the highest was measured in the FG-Ti_2SC samples (1.4GPa)[110] .

- ✧ ***Solid solution effects.*** Comparing the ultimate strength of the solid solutions to the ones of the end-members for similar grain size level, a solid solution strengthening is observed in the Ti-Al-C-N system[31]. However, for other solid solutions related to the Ti-Si-Al-C[99], Ti-Si-Ge-C[96], Ti-Nb-Al-C[85], Ti-V-Al-C[86] systems, the solid solution strengthening is not operative.

- ✧ ***Impurities.*** Another important factor that may affect the ultimate compressive strength is the presence of impurities in the MAX phase sample. Some of these impurities can act as reinforcement phase in the sample and enhance the compressive strength. However, up to now, no systematically work has been reported on such an effect.

I-4.3.3. Deformation mechanisms

The microstructures of as-grown and deformed MAX phases are characterized by two typical defects: dislocations and stacking faults. First, dislocations have been observed by TEM in as-grown and deformed samples [28,53,122-124]. Due to the very anisotropic structure, these dislocations are confined in the basal plane, their Burger vectors in MAX phases are 1/3<11-20> as far as being reported [28,106,122-124]. Another characteristic defect is stacking faults lying in the ab plane and corresponding to the insertion of extra MX planes [106,114,122,124].

It is well established that deformation of MAX phases is due to dislocation movement. The key for understanding the deformation mechanisms of MAX phases is described below[1,28,118,122,123] :

1. Only basal slip is operative at all temperatures. The Burgers vector in the basal plane

is 3.01Å. Any non-basal dislocation would have a Burgers vector higher than 17 Å [28,123]. MAX phases thus lack the five independent slip systems required for ductility.

2. Because of high c/a ratios, twinning is unlikely, and has never been observed in MAX phases. Instead, these compounds deform by the formation of kink bands within individual grains[27,28,30,123] .
3. Because they are confined into the basal planes, the dislocations arrange themselves either in arrays (pile-ups) on the same slip plane, or in walls normal to the arrays[28,123].

In such a case, it is important to understand the formation of kink bands in MAX phases; phenomena well investigated by Barsoum *et al.*[1,4,5,28,30,40,118,123]. The kink bands have been modeled [125] as thin infinite elliptic cylinders (with axes α and β such that α >> β, see Figure 13 (a)), whose sides comprise two dislocation walls of opposite sign, with Burgers vector **b** and spacing *D*. The precise mechanisms responsible for nucleation of kinks have not yet been identified. It is believed that once the kinks nucleate, they grow athermally until they meet the grain boundaries (interior grains) or free surfaces (exterior grains). At the grain boundaries, the opposite walls of the kink are held together giving the kink a lenticular shape (Figure 13(b)). At elevated temperatures, the dislocation walls bounding the kink separate (Figure 13(c)), and the coalescence of several walls eventually produces a kink band (Figure 13(d)). To avoid confusion, the term IKB denotes a kink band for which the dislocation walls remain attached at its ends, that is, one that remains lenticular in shape (Figure 13(a)); once the walls separate we will refer to them as kink bands. This distinction is important because the production and annihilation of IKBs is believed to be a reversible process, whereas that of the kink bands is an irreversible one.

Dislocation arrays also play a critical role [28,40,123]. At this stage their role is less clearly understood than that of the walls. However, delaminations are most likely to occur at the intersection of the dislocation walls and arrays [28,40,123,126,127], eliminating the latter and resulting in large strain energy releases. Note that the arrays are also inherent to the overall kinking process; without them, the various lamellas cannot shear relative to each other [28,40,123]. The stresses at the tips of arrays could also nucleate IKB in adjacent grains. It is also not

unreasonable to assume that, if present, ahead of an IKB, they would create a strong driving force for delaminations to occur at the plane in which they exist. Lastly, there is also little doubt that they are responsible for the large internal stresses that develop in these materials as a result of loading [118].

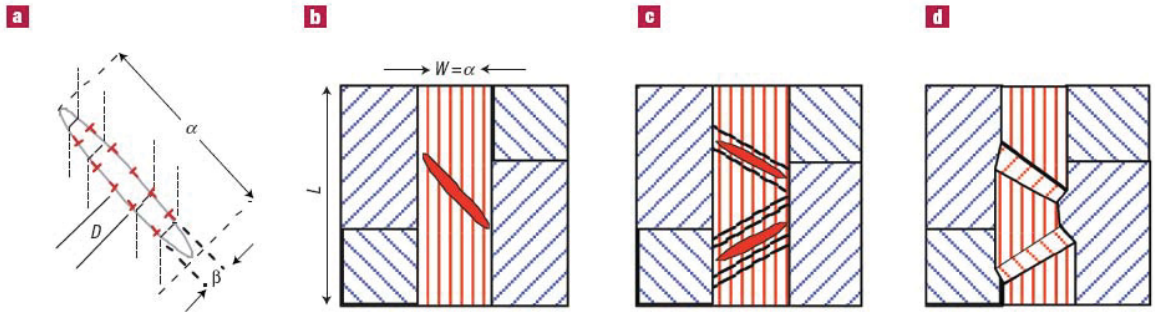

Figure 13 [40]: Kink-band formation. (a) Thin elliptic cylinder with axes α and β where α >> β. The sides are comprised of two dislocation walls (shown in red) of opposite sign, and a uniform spacing of D. (b) Formation of an IKB in hard (red) grains adjacent to soft (blue) grains. (c) Multiple pile-ups and kink bands in a large grain. (d) Same as (c) after removal of stress, emphasizing formation of grain boundaries (dark lines).

Kinking Nonlinear Elastic deformation of MAX phases *[4,5,40,118,125-137]*

Recently, Barsoum *et al.* identified and classified a class of solids as Kinking Nonlinear Elastic (KNE) because they deform by the formation of kink bands [4,5,40,118,128-133,135,136]. The loading-unloading stress-strain curves of KNE solids in the elastic regime outline nonlinear, fully reversible, reproducible, closed hysteresis loops whose shape and extent of energy dissipation are strongly impacted by grain size of the samples. A sufficient condition for a solid to be KNE is plastic anisotropy with the c/a ratio higher than 1.4 in hexagonal crystals. In this case, it has been found that most of MAX phases can be classified as KNE solids.

Kink Bands (KBs) were first found by Orowan[134] in single crystals of Cd and Zn loaded parallel to their basal planes. Kinking is distinct from slip or twinning in that it needs the generation of a succession of more or less regularly spaced dislocation pairs on many parallel slip planes [134] . Barsoum and co-workers emphasized that the formation of IKBs must precede the regular KB formation (Figure 13(b)). IKBs are comprised of near parallel walls of opposite sign dislocations (Figure 13(a)) that are un-dissociated (i.e.: still attached to each other at their ends). When the load is increased, IKBs grow whereas they shrink when it is

decreased. Mobile Dislocation Walls (MDWs) are formed when IKBs dissociate (Figure 13(c)). Thus, an irreversible or permanent deformation and/or damage, in the form of delamination, is produced (Figure 13(d)). The coalescence of mobile walls can result in kink boundaries that make up the kink bands, intensively discussed in literature [4,5,40,125,135,143,144].

KNE Microscale Model [4,5,40,118,125-137]

It has been demonstrated in 2003 that Ti_3SiC_2 samples do not have constant apparent modulus [4,5,40,118]. Indeed, the slope of its stress-strain curve changes with stress. Thus, deformation can not be calculated from stress by using Hooke's law[119]. When stress-strain curves are loaded cyclically on the samples, they show hysteretic loops. These hysteretic loops may dissipate up to 25% of the mechanical energy; loss factors being higher than most woods[138] and comparable to propylene and nylon[139-142]. The stress-strain loops are fully reversible, strain-rate independent and closed. The loop shape is strongly influenced by grain size, with energy dissipated per unit volume per cycle, W_d, being significantly larger in the coarse-grained solids. Barsoum and his group attribute this phenomenon to the reversible growth and shrinkage of Incipient Kink Bands (IKBs) [4,5,40,118], and refer to this new class of solids as KNE solids.

The deformation of KNE solids gives rise to stress-strain curves with large hysteretic loops as displayed schematically in Figure 14(d). A sample loaded to a stress σ will lead to a total strain, ε_{tot}. This strain, ε_{tot}, consists of two parts: non linear strain (ε_{nl}) and linear strain (ε_l). The latter can be calculated from Hooke's law[119] ($\varepsilon_l = \sigma/E$ where E is the Young's modulus of the material). Thus, ε_{tot} can be written as:

$$\varepsilon_{tot} = \frac{\sigma}{E} + \varepsilon_{IKB} + \varepsilon_{DP} \qquad (6)$$

In the most general case and in the absence of phase transitions and/or microcracking, the nonlinear fully reversible strain, ε_{nl}, can be divided into two components, the first, $\varepsilon_{IKB,}$ is due to IKBs; the second, ε_{DP}, is owing to basal slip that leads to dislocations pileups (DPs) . It is worth noting that because of the plastic anisotropy of KNE solids, both strains are fully reversible since the dislocation loops are confined to parallel planes. Barsoum *et al.* assume that ε_{DP}, if present, is small and increases linearly with stress [4,5]. In this case, only ε_{IKB} is

considered in the following.

Frank and Stroh [125] considered an elliptic KB with length 2α and width 2β, where α>>β (cf Figure 14(a)), and demonstrated that the remote critical axial stress (σ_t), at the polycrystal level, needed to cause such a subcritical KB unstable is given by [4,5] :

$$\tau > \tau_c \approx \frac{\sigma_t}{M} \approx \sqrt{\frac{4G^2 b\gamma_c}{2\alpha\pi^2} \ln(\frac{b}{\gamma_c w})} \tag{7}$$

where τ_c is the local critical shear stress, at the single grain level. M is the Taylor factor relating σ_t to τ_c, G is the shear modulus and b is the Burgers vector; w is associated to the dislocation core width [125]. For MAX phases, 2α can be considered as the grain dimension along the *c*-axis [4,5] (i.e.: normal to the direction of easy slip). Measuring the threshold stress (σ_t) and assuming M=3 [135], one can determine w, an important parameter that is otherwise quite difficult to measure.

γ_c is the critical kinking angle which can be calculated as following [125,130,144]:

$$\gamma_c = \frac{b}{D} \approx \frac{3\sqrt{3}(1-\nu)\tau_{loc}}{2G} \tag{8}$$

where ν is Poisson's ratio, τ_{loc} is the local shear stress required to nucleate a dislocation pair; D is the distance between dislocation loops along 2α (Figures 14 (a) and (c)).

The local shear stress, τ_{loc}, needed to form a dislocation loop is assumed to be given by [125]:

$$\tau_{loc} = \frac{G}{4\pi e} \bullet (\frac{b}{w}) \tag{9}$$

where e = 2.718. Equation (9) is only valid at an ideal condition, 0K. At RT, this equation is only roughly correct. Therefore, the dislocation core width, w, may change due to the test conditions. If one assumes $\tau_{loc} \approx G/30$, γ_c is of the order of 3.4^o [4,5]. Note that assuming G/30 implicitly assumes w=b. If, as assumed by Barsoum, w=5b, γ_c is of the order of 0.012 rad or 0.7^o.

An IKB consists of multiple parallel dislocation loops (Figure 14(a)). As a first approximation, Barsoum *et al.* assumed that each loop is comprised of two edge and two screw dislocation segments with lengths, $2\beta_x$ and $2\beta_y$, respectively (see Figure 14(c)). The latter are assocaited to the applied stress σ and 2α, assuming [125,130]:

$$2\beta_x \approx \frac{2\alpha(1-\nu)}{G\gamma_c}\frac{\sigma}{M} \qquad 2\beta_y \approx \frac{2\alpha}{G\gamma_c}\frac{\sigma}{M} \tag{10}$$

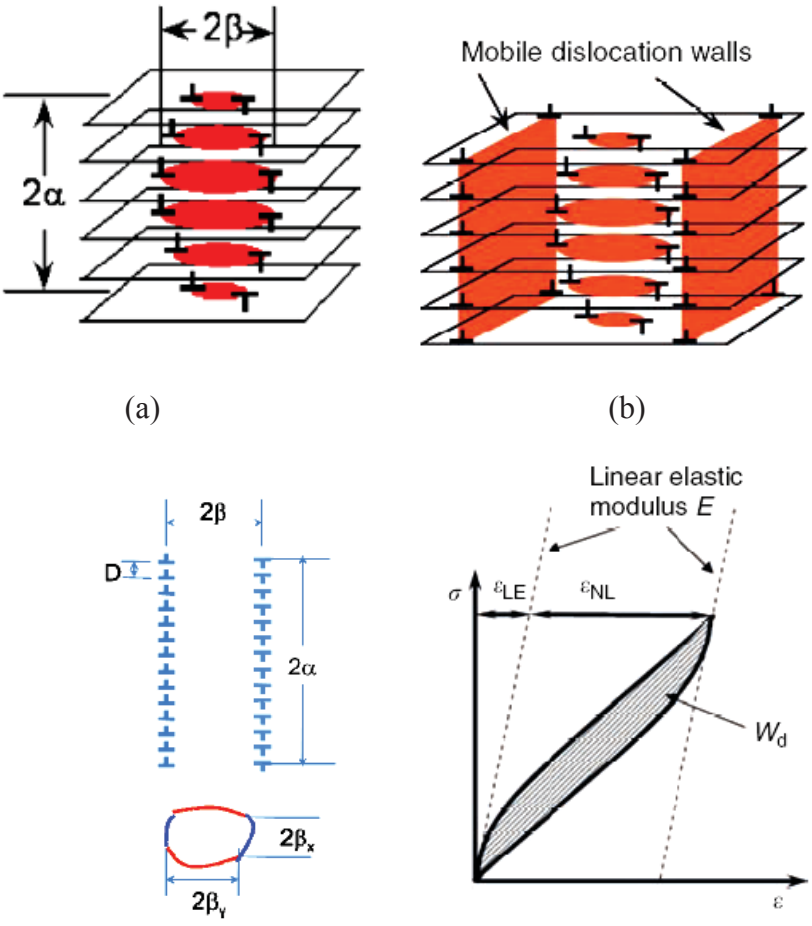

Figure 14: (a)[5] The schematic of an IKB in ellipsoid shape with the length 2α and diameter 2β. (b) [5] Same as (a), but showing MDWs. (c)[128] Dislocation walls and dislocation loops of an IKB. D is the distance of two dislocation loops, $2\beta_x$ is the length of the edge dislocation segment, $2\beta_y$ is the length of the screw dislocation segment. (d) [5]Typical stress-strain loop and definitions of nonlinear strain, ε_{NL}, and W_d.

The formation of an IKB can be separated into two stages: nucleation and growth [125]. As the former is not well understood, the model only concerns IKB growth from $2\beta_{xc}$ and $2\beta_{yc}$ to $2\beta_x$ and $2\beta_y$, respectively. The dislocation segment lengths of an IKB nucleus, $2\beta_{xc}$ and $2\beta_{yc}$ are assumed to either preexist, or to nucleate during pre-straining. It follows that, for $\sigma>\sigma_t$, the IKB nuclei grow. The IKB induced axial strain resulting from their growth is assumed to be given by [125]:

$$\varepsilon_{IKB} = \frac{\Delta V N_k \gamma_c}{k_1} = \frac{N_k \gamma_c 4\pi\alpha(\beta_x\beta_y - \beta_{cx}\beta_{cy})}{3k_1}$$
$$= \frac{4\pi(1-\nu)N_k\alpha^3}{3k_1 G^2 \gamma_c M^2}(\sigma^2 - \sigma_t^2) = m_1(\sigma^2 - \sigma_t^2) \quad (11)$$

where m_1 is the coefficient before the term in brackets in the fourth term, N_k is the number of IKBs per unit volume, ΔV is the IKB volume change (i.e.: its volume at σ minus its critical volume at σ_t). It follows that the product $V \times N_k$ is the volume fraction of the material that is kinked. The factor k_1 relates the volumetric strain due to the IKBs to the axial strain along the loading direction. The value of k_1 depends on the texture of the sample and ranges from 1 to 2. If there is no texture in the sample, k_1 can be assumed to be 2[137]. Once m_1 is determined experimentally, and since the other factors are known, N_k can be estimated from equation (11).

The energy dissipated per unit volume per cycle, W_d, caused by the growth of the IKBs from β_{ic} to β_i is given by [4,5,125]

$$W_d = \frac{4\Omega N_k \alpha}{D}(\beta_x\beta_y - \beta_{xc}\beta_{yc})$$
$$= \frac{4\pi(1-\nu)N_k\alpha^3}{G^2\gamma_c M^2}\frac{\Omega}{b}(\sigma^2 - \sigma_t^2) = m_2(\sigma^2 - \sigma_t^2) \quad (12)$$

where Ω is the energy dissipated by a dislocation line sweeping a unit area. It follows that Ω/b should be proportional, if not equal, to the Critical Resolved Shear Stress (CRSS) of an IKB dislocation loop. Combining equations (11) and (12) yields:

$$W_d = 3k_1\frac{\Omega}{b}\varepsilon_{IKB} = \frac{m_2}{m_1}\varepsilon_{IKB} \quad (13)$$

Assuming, for simplicity, that IKBs are cylinders with mean radius β_{av}, then the reversible dislocation density, ρ_{rev}, due to the IKBs is given by:

$$\rho_{rev} = \frac{2\pi N_k 2\alpha\beta_{av}}{D} = \frac{4\pi N_k \alpha\beta_{av}\gamma_c}{b} \quad (14)$$

Experimentally (see below) one can obtain m_1, m_2, σ_t, and $3k_1\Omega/b$. To estimate Ω/b only knowledge of k_1 in Equation (13) is required whereas N_k can be determined from Equation (11) provided k_1 and M are known .

Once the nested loops are obtained, m_1 and σ_t can be determined from the slopes of ε_{nl}

versus σ^2 plots. Similarly, m_2 and σ_t can be determined from W_d versus σ^2 plots and $3k_1\Omega/b$ can be determined from the plot of W_d versus ε_{nl}.

It follows that if assumptions are correct, and more importantly, if the micromechanism causing the dependence of ε_{nl} on σ is the same as the one responsible for W_d (Eq. 12), then the ratio m_2/m_1 should equal $3k_1\Omega/b$. In other words, if both expressions give the same values for Ω/b, the same micromechanism resulting in the parabolic dependence of σ on ε_{nl}, is the one responsible for W_d as well.

Chapter II

Experimental Details

II-1. Synthesis of MAX phases

II-1.1. Powder mixtures

In the present study, Ti, Al, Sn, C, TiC, $TiC_{0.66}$, and Fe were used as the starting materials to synthesize Ti_3AlC_2, Ti_3SnC_2 and $Ti_3Al_xSn_{(1-x)}C_2$ solid solutions. The characteristics of the powders are listed in Table 11. To prepare homogeneous mixtures corresponding to the desired stoichiometry, powders were dry ball-milled in a Turbula mixer (WAB, Basel, Switzerland). Due to the different sizes of designed green samples (see Figure 15), the initial reactant mixtures constituting small and big samples were milled for 1h with 1 steel ball and 4h with 6 steel balls, respectively.

Powders	Particle size (µm)	Purity (%)	Factory
Ti	150-250	99.5	Alfa Aesar
Al	45-150	99.5	Alfa Aesar
TiC	<45	98	Alfa Aesar
Sn	2-20	99	Alfa Aesar
C	<20	-	-
Fe	6-80	-	POUDMET
$TiC_{0.66}$	<10	-	PHYMAT Mechanical milling of Ti+0.66C Vibratory ball-mill[145,146] R_{bp}=10, t=3h

Table 11: Characteristics of the starting powders.

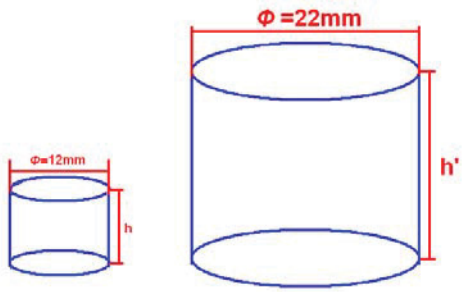

Figure 15: Schematic representation of (a) small (10<h<13mm) and (b) big (5<h'<35mm) green compacts.

II-1.2. Compacting procedure

The small cylindrical samples (diameter Φ=12mm, height 10<h<13mm) result from the cold-compaction of powders, into cylindrical steel dies, using an 810 Material Testing System

(MTS System Corp., USA) with a uniaxial pressure of 800MPa. The green density, evaluated from weight and geometric measurements, ranged from 75 to 85 % of the theoretical density.

To prepare big cylindrical samples (diameter Φ=22mm, height 5<h'<35mm), powders were enclosed in a rubber soft tube, and then placed in a Cold Isostatic Press (CIP) machine (ACB, Group ALSTHOM, France) pressurized to 300MPa with oil. After CIPing, the cylindrical green sample density is approximately 80% of the theoretical density.

II-1.3. Reactive hot isostatic pressing

Except for the 2Ti:Sn:C reactant samples, the other green samples were sealed under vacuum in a pyrex container; the use of a pyrex container allows, for temperatures higher than the vitreous transition temperature, applying the isostatic gas pressure to the reacting powder mixture. The top and bottom of the green body were covered with glass powder in order for the sample to be completely embedded in glass (Figure 16). In the case of 2Ti:Sn:C samples, the green body was placed in a stainless steel container. Thus, the container was sealed under high vacuum.

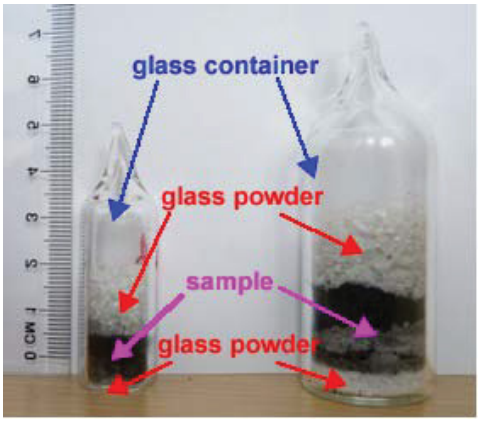

Figure 16: Photography of small and big green samples sealed under vaccum in pyrex containers.

Afterwards, the compacted reactant powder sealed in the glass container was placed in a graphite container sprayed with BN on the inner surface; the BN spray avoids sample sticking onto the graphite container. Stainless steel container was directly placed in the Hot Isostatic Press (HIP).

The reactive sintering procedure was performed in a HIP machine (Graphite furnace, T_{max}=2000°C, P_{max}=200MPa, GEC ALSTHOM, France). The green samples encapsulated in

pyrex were subjected to the following temperature and pressure cycles (Figure 17):

- The sample was heated in the 5-30°C/min heating rate range to reach the desired temperature, under an Ar atmospheric pressure.
- The HIP was pressurized at 0.5 MPa/min to the desired Ar pressure. The pressure increase is adjusted, in order to be relatively low (smaller than 10 MPa) at the vitreous transition temperature of the pyrex (cf Figure 16), to avoid glass fracture.
- Once the processing temperature and pressure were reached, the sample was held for 1 to 20h.
- Cooling the furnace to room temperature and decreasing the pressure to atmospheric pressure proceeds in 90min.

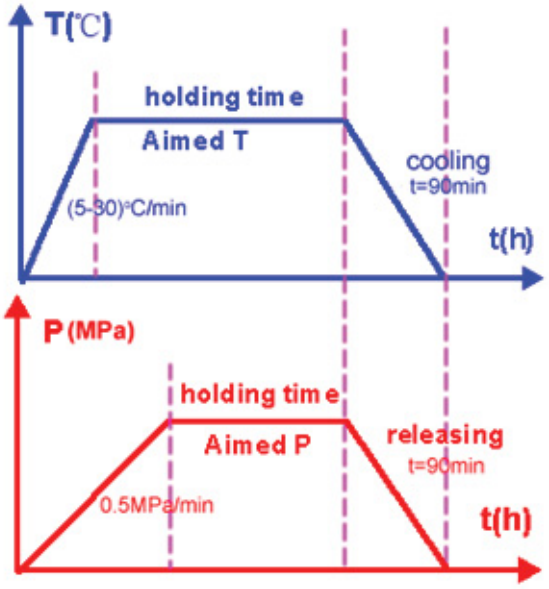

Figure 17: Typical pressure-temperature (P, T) cycle used in the HIP to synthesize MAX phases.

The (P, T) cycle used for the 2Ti:Sn:C green sample encapsulated in a stainless steel container is described in III-1.

After HIPing, samples were machined to remove the encapsulating glass or stainless steel container and sliced using a diamond wheel.

II-1.4. Thermal expansion curve measurement: study of the reaction mechanisms

Thermal expansion curve (TEC) measurement was performed in a high sensitivity (±0.5 µm) dilatometric system (SETSYS 16/18 type, SETARAM Instrumentation Regulation,

France) under high purity argon. Coupled with X-ray Diffraction (XRD), dilatometry was used in order to investigate the reaction mechanisms for the formation of Ti_3SnC_2 using Fe as additive. Powder compacts were heated to various temperatures, ranging from room temperature (RT) to 1200°C, for an isothermal holding time of 1 hour. Heating and cooling were performed at an identical rate of 10°C.min^{-1}. The dimensional changes of the compact (in the axial direction) were continuously recorded throughout the thermal cycle.

II-2. Microstructural Characterization

II-2.1. Structure and cell parameters

XRD diffractograms were acquired, using a Bruker D501 diffractometer with Cu-K_α radiation, to identify the different phases of the as-synthesized samples. The data were collected in the 2θ range 8-75°, with a step size of 0.04°, and duration of 4.2s per step. XRD data were also used for Rietveld refinement analysis using MAUD software[147] in order to extract the lattice parameters and the volume fraction of the different phases present in the as-synthesized samples. The refined parameters are listed in Table 12.

Background and scale parameters
Basic phase parameters
Microstructure parameters
Crystal structure parameters
Texture analysis
Sample displacement z
Volume fraction
Intensity (scale factors)
2-theta or d-spacing offset
Lattice parameters
Z position of C, Ti
B factors

Table 12: Parameters refined in the Maud software.

For the refinement models, the following original "cif" files were used:

- Ti_3AlC_2 (Hexagonal, P63/mmc, *a*= 3.0654 Å, *c*= 18.4870Å),
- Ti_2AlC (Hexagonal, P63/mmc, *a*=3.0400 Å, *c*= 13.6400 Å),
- Ti_2SnC (Hexagonal, P63/mmc, *a*=3.1630 Å, *c*= 13.6790Å),
- TiC (Cubic, Fm3m, *a*= 4.3176 Å),
- Sn (Tetragonal, I41, *a*=5.8318 Å, *c*=3.1819 Å).

II-2.2. Phase distribution, grain size and chemical composition

The microstructure of the sample, in terms of phase distribution and grain size, was observed by Scanning Electron Microscopy (SEM, JEOL 5600LV, Japan), coupled with Energy Dispersive X-ray Spectrometry (EDXS, Oxford Isis 300, UK) for the chemical analysis. For SEM observations, samples were prepared using the following steps: the sliced sample was first embedded in a phenolic conductive resin (Struers Labopress-1: 15kN/180°C/5min). The embedded sample was then grinded with silicon carbide papers and finely polished with a 0.25 µm diamond suspension. In order to produce a very flat surface and to avoid any work hardening due to conventional grinding, a chemo mechanical polishing has been performed using a suspension of alumina particles. At last, the sample was washed in acetone or ethanol, and dried with nitrogen.

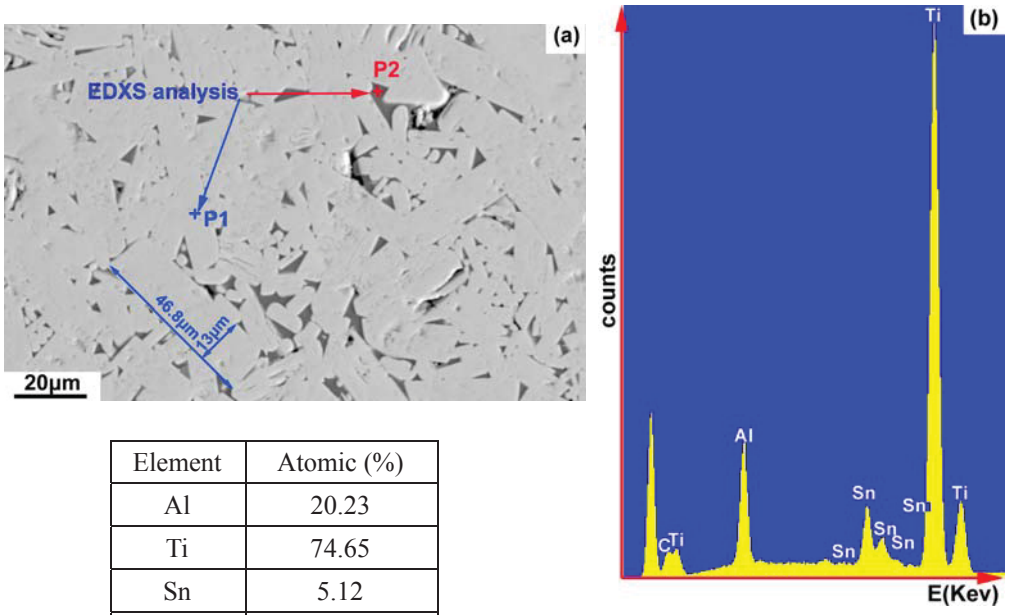

Element	Atomic (%)
Al	20.23
Ti	74.65
Sn	5.12
Total	100

Figure 18: (a) SEM micrograph (back-scattered electron mode) of a $Ti_3Al_xSn_{(1-x)}C_2$ solid solution sample showing grain size and phase distribution. (b) EDXS spectrum and related chemical composition of the point P1 in (a).

As shown, as an example, in Figure 18, one can extract some information about MAX phase's grain size and phases distribution from micrographs obtained in back-scattered electron mode. The resulting grain size and the different phase contents are thus measured using the Image J software[148]. Moreover, EDXS allows extracting the Ti/(Al+Sn) and Al/(Al+Sn) ratios in the case of solid solutions; in these conditions, one can get the

composition of the MAX phase solid solutions (i.e.: the nature (312 or 211) and the Sn content).

II-2.3. Microstructural defects

Weak beams and extinction diffraction conditions techniques, conducted on a Transmission Electron Microscope (TEM, JEOL 200CX, Japan) operating at 200kV, were used to characterize Stacking Faults (SFs) and dislocations in as-grown and deformed samples.

To prepare the sample for TEM observations, thin foils, from deformed samples, were cut at 45° degrees from the compression axis with a 2mm thick section, followed by a slow mechanical polishing down to 20µm with a tripod technique. For as grown samples, thin foils of 2 mm in thickness were cut perpendicular to the cylinder axis. During this mechanical polishing, the polished thin foil was carefully observed under the optical microscope (OPTIPHOT-2, NIKON and REICHERT, Japan) to roughly measure the thickness. After the mechanical polishing, the thin foil was further ion milled at 2.5keV/20mA using a precision ion-polishing system (PIPS, MODEL 691, Gatan, USA). After that, the thin foil was washed in acetone and dried at 60°C for 4h.

II-2.4. Density

The density of the synthesized samples was measured by helium (He) and mercury (Hg) pycnometry techniques which allow determining the closed porosity and total (closed+opened) porosity, respectively.

The He pycnometry was performed with an AccuPyc 1330 apparatus (Micromeritics, USA) using He as the displaced gas to measure the volume of the sample. The density of the sample is directly calculated from the formula:

$$\rho = \frac{m}{v} \tag{1}$$

where, m is the mass of the sample and v is the volume of the sample measured from the AccuPyc 1330.

The density measured by Hg pycnometry follows Archimedes' principle and it can be

calculated from the following formula:

$$\rho_{sample} = \frac{\rho_{Hg}(m_s - m_0)}{(m_l - m_0) - (m_{sl} - m_s)} \quad (2)$$

where,

ρ_{Hg} is the density of Hg,

m_0 is the mass of the pycnometer,

m_S is the mass of the pycnometer containing the sample,

m_l is the mass of the pycnometer full of Hg,

m_{Sl} is the mass of the pycnometer containing the sample and Hg.

II-3. Mechanical Properties

II-3.1. Nanohardness and Elastic modulus at room temperature

Nanoindentation tests have been performed in polycrystalline multi-phased $Ti_3Al_xSn_{(1-x)}C_2$ (x=0, 0.25, 0.5, 0.8 and 1) samples. Nanoindentation is particularly interesting with this kind of samples, since:

- the grain size is larger compared to the penetration depth and indents size,
- it is a suitable technique to determine the intrinsic hardness and the elastic modulus of the different phases constituting multi-phased materials,
- it allows deforming very small volume, much smaller than the grain, and even if polycrystalline samples are synthesized, nanoindentation allows studying plasticity in "single crystals".

The assessment of the hardness was implemented on a nanoindentation apparatus (Nano Hardness Tester) from CSM Instruments (Peseux, Switzerland) equipped with a Berkovich indenter (triangular base pyramid).

Nanoindentation tests have been performed on $Ti_3Al_xSn_{(1-x)}C_2$ (x=0, 0.25, 0.5, 0.8 and 1) samples. In order to study the hardness as a function of penetration depth, several loads have been used for each sample. For each load, more than 15 measurements have been performed for a good statistics. Note that at maximum load, a holding time of a few seconds is performed to let the system stabilize. The detailed number of indents with different loads for

the $Ti_3Al_xSn_{(1-x)}C_2$ solid solutions investigated are listed in Table 13.

In the multi-phased "Ti_3SnC_2" sample, hardness cartography and optical microscopy of the sample surface were used to correlate the hardness and the elastic modulus values to the sample phases, by using a deconvolution method. In the other samples, SEM observations were carried out to identify and to remove the indents that were not on a MAX phase grain.

The nanoindentation test consists in monitoring the penetration depth during a loading-unloading cycle. Figure 19 shows a typical load-penetration depth curve recorded from such a test.

	Number of indents for $Ti_3Al_xSn_{(1-x)}C_2$				
x value / Load (mN)	1	0.8	0.5	0.25	0
1	29	20	40	40	100
2	29	20	40	40	100
3	29	20	40	40	500
6	19	20	40	40	100
10	19	20	40	40	100
15	30	20	40	40	100
30	15	20	40	40	100
100		7	14	14	100
150					50
220			40	40	
250	7				
300					50

Table 13: Load values and corresponding number of indents used to perform nanoindentation tests on $Ti_3Al_xSn_{(1-x)}C_2$ solid solution samples.

The nanoindentaion hardness, H, can be determined by the following equation:

$$H = \frac{F}{A} \tag{3}$$

where, F is the maximum applied load and A is the projected contact area under maximum load. Nevertheless this projected contact area cannot be determined directly during the indentation test. Furthermore, due to the elastic recovery around and below the indenter, the shape of the indent evolves during unloading, so that A cannot be determined by further Atomic Force Microscopy (AFM) observation of the residual indent. The method consists

thus in determining, from an analysis of the unloading curve, the true penetration depth h_c, which corresponds to the penetration depth below the contact line at maximum load (see Figure 20). Thus, the projected contact area can be deduced from the true penetration depth provided that the indenter shape is perfectly known.

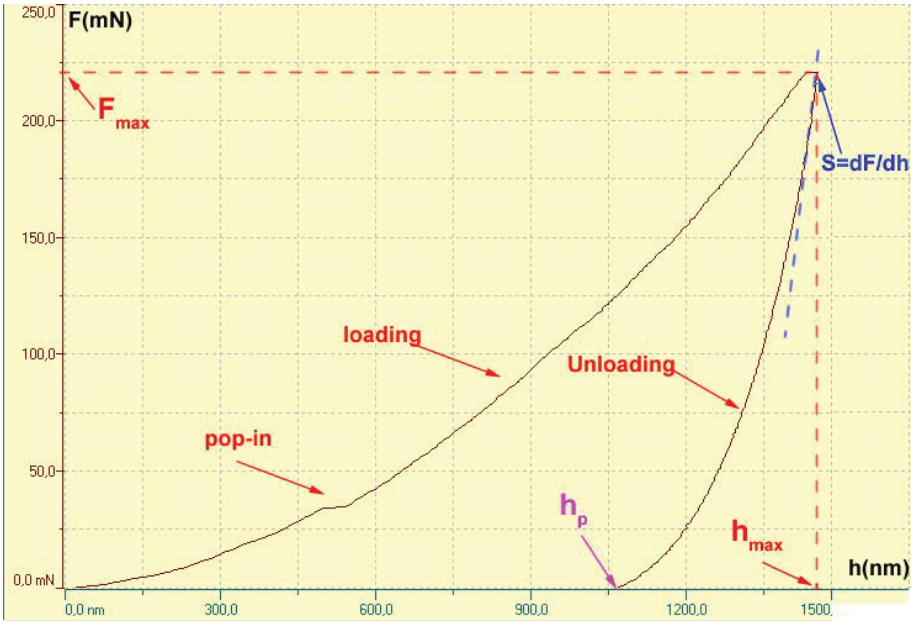

Figure 19: Typical load-penetration depth curve obtained from nanoindentation tests.

For a better understanding, a schematic of the surface of the material, under maximum load and after unloading, is shown in Figure 20.

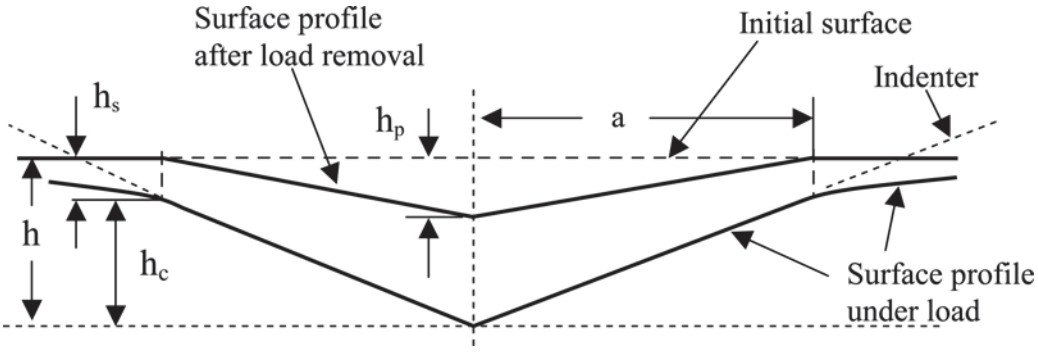

Figure 20[149]: Schematic of the surface of a solid while in contact with an indentation tip and after removing the loaded tip.

The most commonly used method for the determination of h_c is the Oliver and Pharr method[149]. The principle consists in assuming that the elastic contact of a conical indenter in

an imprint is equivalent to that of a paraboloid with a flat surface (see Figure 21).

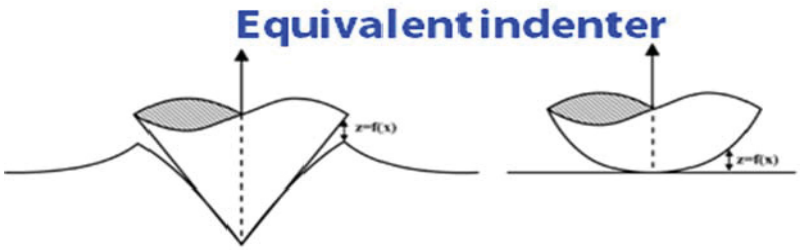

Figure 21[150] *: The equivalent tip model. True indenter tip pressed against a previously indented surface and equivalent tip pressed against a flat surface.*

By assuming a perfectly elastic behavior of the material during unloading, the true penetration depth is given by the following equation[151]:

$$h_c = h_p - \varepsilon \frac{F_{\max}}{S} \tag{4}$$

where ε is a constant equal to 0.75[151]

More recently, Woirgard and Dargenton[150], proposed to determine the exact shape of the equivalent indenter from the unloading curve. In this way, the true penetration depth is still determined by Equation (4), but the value of the ε coefficient is determined for each unloading curve. This is the method we used in this study.

In most materials, the unloading curve can be fitted by a power law [151,152]:

$$F = a(h - h_p)^m \tag{5}$$

with exponent m ranging between 1.2 and 1.7.

The stiffness (S) is given by [152]:

$$S = \frac{dF}{dh} = \frac{mF_{\max}}{h_{\max} - h_p} \tag{6}$$

And the value of ε is a function of the exponent of the unloading curve according to the following equation:

$$\varepsilon = m\left(1 - \frac{2(m-1)\Gamma\left(\frac{m}{2(m-1)}\right)}{\sqrt{\pi}\,\Gamma\left(\frac{1}{2(m-1)}\right)}\right) \tag{7}$$

The indentation elastic modulus E_r can be also obtained from the slope of the beginning of the unloading curve [149]:

$$E_r = \frac{\sqrt{\pi}}{2\beta\sqrt{A}} S = \frac{\sqrt{\pi}}{2\beta\sqrt{A}} \frac{mF_{\max}}{h_{\max} - h_p} \tag{8}$$

where,

β is a geometrical coefficient equal to 1.034 for a triangular Berkovich indenter[149,151,152],

E_r, the indentation modulus, is a balance between the Young's modulus of the sample, E_s, and the Young's modulus of the diamond indenter, E_i:

$$\frac{1}{E_r} = \frac{(1-\upsilon_s^{\,2})}{E_s} + \frac{(1-\upsilon_i^{\,2})}{E_i} \tag{9}$$

where,

ν_s is the Poisson's ratio of the sample (ν_s =0.2 for $Ti_3Al_xSn_{(1-x)}C_2$)[1]

ν_i is the Poisson's ratio of diamond (Berkovich indenter) (ν_i =0.07)[151]

E_i, the Young's modulus of diamond (Berkovich indenter), is set to 1141GPa[151]

For a perfect Berkovich indenter, the relation, between the true penetration depth h_c and the contact area (A) between the indenter tip and the sample follows the simple relation (as for a Vickers indenter):

$$A = 24.5\, h_c^{\,2} \tag{10}$$

However, the apex of the indenter is not perfectly sharp, and the true shape of the indenter must be calibrated, particularly for low load indentations. Calibration has been performed by direct AFM observation of the indenter (see Figure 22) and by indenting fused silica sample, a material of known Young's modulus (72 GPa). The contact area for each value of the contact penetration depth can be then described by a polynomial expression as proposed below:

$$A(h_c) = 21.1 \times h_c^{\,2} + (2.34 \times 10^3) \times h_c - (1.34 \times 10^4) \times h_c^{\,1/2} + (1.7 \times 10^4) \times h_c^{\,1/4} \tag{11}$$

The indenter has been regularly calibrated all along the experiments performed in this study in order to take into account the evolution of its shape.

Plastic deformation is induced by nanoindentation on a single crystal; this single grain

being embedded in MAX phase grains of the same material. Slip systems and individual dislocation behaviors are studied through the observation of surface slip lines by AFM (AFM, Dimension 3100 microscope, Veeco, USA). In AFM, tapping mode has been used and topographic and error signal mode images were recorded simultaneously. The first kind of picture provides quantitative information on the vertical direction while the second one enhances the contrast on abrupt topography variations such as slip lines. All the AFM images were processed with the WSxM software [153].

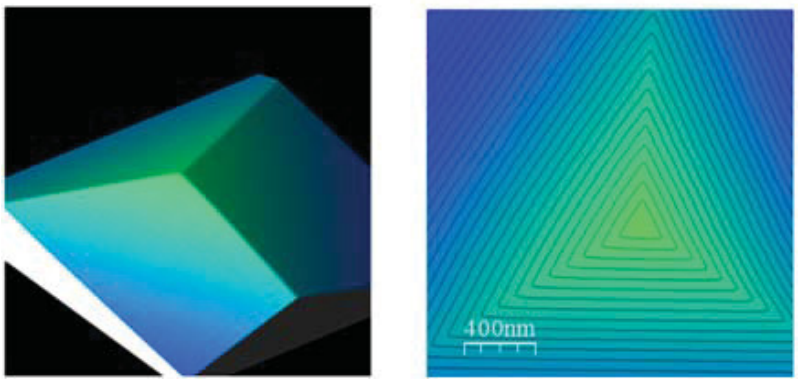

Figure 22: AFM observation of the indenter shape, for calibration purpose. The scale of the figure on the left is 2×2 μm².

II-3.2. Microhardness

Microindentation tests were performed on Ti_3AlC_2 samples by using the Shimadzu Micro Hardness tester (HMV-2000, Japan). 3 loads (0.5N, 1N and 20N) were investigated and a total of 50 indents were performed. Each indent was observed in the SEM. The diagonals of the indents (d) were accurately measured by the Image J software [148].

In Vickers Micro-hardness tests, micro-hardness value is defined as[151]:

$$H_v = \frac{m}{\frac{d^2}{1.854}} \tag{12}$$

where m is the applied load in kgf and $\frac{d^2}{1.854}$ is the total area of the indent. Such a definition is different from the one that is used in nanoinentation tests, where hardness is physically defined as the ratio between the applied force and the projected area of the indent at the maximum load; it corresponds to the contact pressure. In order to compare the hardness

values that we get from micro and nanoindentation tests, Vickers hardness has been calculated from the following formula:

$$H_v = \frac{F}{A_1} \tag{13}$$

$$A_1 = \frac{d^2}{2} \tag{14}$$

where, F is the applied load in N and A_1 is the projected contact area of the indent on the initial sample surface; d being the mean value of the diagonals of imprint indentation.

Thus, the main difference between the two techniques is that nanoindentation hardness values are calculated from the projected contact area at the maximum load (i.e.: at a h value of the penetration depth in Figure 20) whereas microindentation hardness values are determined from the projected contact area after unloading (i.e.: at a h_p value of the penetration depth in Figure 20)

Microindentation tests allow determining the hardness as a function of the load; these values will be compared to the ones obtained by nanoindentation tests which will be presented as a function of the plastic penetration depth (h_p, see Figure 20). Assuming a perfect Vickers indenter and based on the equation (10), the relation between the plastic penetration depth, h_p, and the projected contact area, A_1, of the indenter tip is given by:

$$A_1 = \frac{d^2}{2} = 24.5(h_p)^2 \tag{15}$$

Finally, it is important to notice that the section area of a Vickers or Berkovitch indenters is the same for a same penetration depth. Thus, hardness values obtained from micro and nanoindentation tests can be compared.

II-3.3. Young's modulus as a function of temperature

The Young's modulus has been determined, on Ti_3AlC_2 and $Ti_3Al_{0.8}Sn_{0.2}C_2$ samples, as a function of temperature, by means of the dynamic resonant method in bending mode on beam specimen. Experiments were performed at 1K/mn under high vacuum (10^{-4} Pa). In this technique, the sample is maintained horizontally, without any harmful contact, between steel

wires located at the vibration nodes. Excitation and detection are insured by an electrostatic device (capacitance created between the sample and a unique electrode).

The Young's modulus E of a bulk sample in bending mode is directly determined by the relation:

$$E = 0.9464 \rho f^2 \frac{L^4}{h^2} T(h/L, \nu) \quad (16)$$

where,

f is the resonance frequency,

ρ is the density,

ν is the Poisson's ratio,

h and L are respectively the beam thickness and span length,

T(h/L, ν) is a correcting factor close to 1.

The accuracy of the method is better than 1 % with regular specimen dimensions. The dimensions of our samples were 25 mm in length, 1.2 mm in thickness and 3 mm in width.

II-3.4. Kinking nonlinear elastic deformation at room temperature in a Instron machine

The kinking nonlinear elastic deformation process of MAX phases was performed in an Instron testing machine of 1114 type. Ti_3AlC_2 and $Ti_3Al_{0.8}Sn_{0.2}C_2$ samples used for compression tests have a parallelepiped shape (2.5mm×2.5mm×6mm). All faces of the samples were carefully mechanically polished. Three strain rates, 10^{-5}, 10^{-4} and 10^{-3} s^{-1}, were used for the load-unload compression tests. Compression tests allow studying two different processes:

- Cyclic compressive stress-strain curves (as shown in Figure 23) were recorded to study kinking non linear elastic deformation and to check the validity of the kinking non linear microscale model developped by Barsoum *et al.*[4,5].
- Compressive strain-stress curve was performed up to the sample failure in order to get some information on deformation and fracture mechanisms. Deformation mechanisms were investigated by SEM observations.

Figure 23 shows an example of the cyclic stress-strain curve recorded on a Ti_3AlC_2

sample. It is worth noting that the measured strain includes a contribution which results from the deformation of the machine. In order to analyze the results, it is thus mandatory to determine the stiffness of the compression machine and to remove the machine strain from the measured strain.

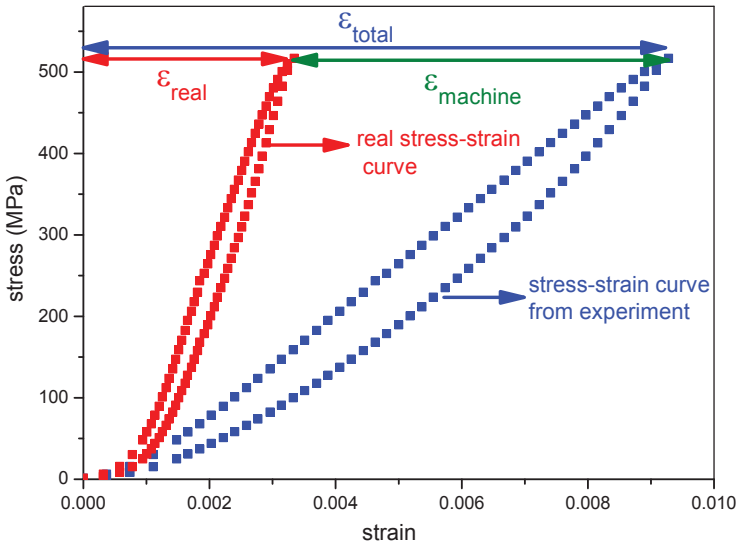

Figure 23: Typical stress-strain hysteresis loop recorded on a Ti_3AlC_2 sample. In blue: as recorded stress-strain curve. In red: stress-strain curve after removing the strain resulting from the machine stiffness.

The machine stiffness (R*) can be calculated from the following equations:

$$\frac{1}{E_{measure}} = \frac{1}{E_{material}} + \frac{1}{M} \tag{17}$$

$$M = \frac{R^* \times h}{S} \tag{18}$$

where,

$E_{measure}$ is the apparent Young's modulus determined from the experiment,

$E_{material}$ is the Young's modulus of the material (MAX phase),

M is the apparent Young's modulus of the machine,

R^* is the machine stiffness,

h and S are the height and cross section of the sample under study.

In order to experimentally determine the machine stiffness R*, and the corresponding

apparent Young's modulus of the machine M, 304L stainless steel samples, with different lengths and cross sections, were prepared. Stress-strain curves were recorded for the different samples. $E_{measure}$ is experimentally determined from the slope of the compressive stress-strain curve. A list of the samples' characteristics is given in Table 14.

304L stainless steel			
Sample ID	Sample dimensions		$E_{measure}$ (GPa)
	S (mm^2)	H (mm)	
1	4.01	1	18.9
2	4.01	1.33	23.7
3	4.01	2	35.6
4	4.01	4	67.7
5	5.60	1	16.1
6	5.60	2	31.4
7	5.60	3	46.6
8	5.60	4	65.9

Table 14: Characteristic parameters of the 304L stainless steel samples used to determine the machine stiffness R.*

Figure 24 shows the variation of the inverse of the measured Young's modulus ($E_{measure}$) as a function of the S/h ratio. As expected from Equations (17) and (18), a linear variation is observed. The slope of the straight line allows determining the machine stiffness R* whereas the intercept point allows determining the 304L stainless steel Young's modulus. The R^* value is 93 GPa/mm and the Young's modulus value of the 304L stainless steel is 207 GPa. Such a Young's modulus value is in very good agreement with the expected value (210 GPa) which gives confidence to the determined value of the machine stiffness.

Thus, the machine strain contribution to the total strain can be calculated, for a given sample (i.e.: for a known value of S/h), from the following equations:

$$\varepsilon_{machine} = \frac{\sigma}{M} \tag{19}$$

$$\varepsilon_{real} = \varepsilon_{total} - \varepsilon_{machine} \tag{20}$$

As a consequence, the blue stress-strain loop shown in Figure 23 can be corrected into the red one.

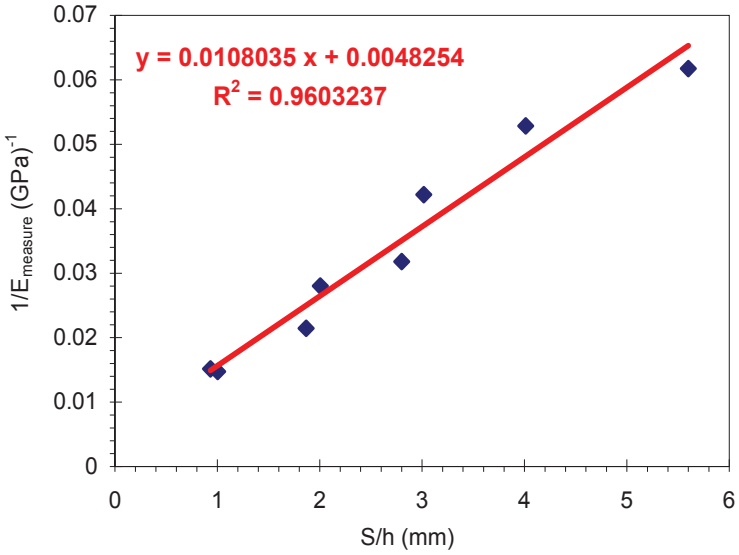

Figure 24: Inverse of the measured Young's modulus versus S/h ratio, for the different 304L stainless steel samples listed in Table 14.

II-3.5. Plastic deformation at room temperature using a Paterson machine

Ti_3AlC_2 and $Ti_3Al_{0.8}Sn_{0.2}C_2$ were chosen for the compression tests performed under hydrostatic pressure at RT in the Paterson press [154,155]. The Paterson machine allows deforming brittle materials at temperature lower than the brittle-ductile transition temperature (BDTT). It thus becomes possible to study deformation mechanisms of materials that are currently brittle at RT.

The MAX phase samples were cut into parallelepipeds with a dimension of 2.30mm×1.90mm×7.38mm for Ti_3AlC_2 and 2.44mm×1.90mm×7.30mm for $Ti_3Al_{0.8}Sn_{0.2}C_2$. All faces of the samples were carefully mechanically polished. As shown in Figure 25, the samples were inserted into fully annealed Al jackets to fit into the deformation assembly of the compression apparatus. Compression tests were performed, at RT, under an argon confining pressure of 350MPa and at a strain rate of 5.10^{-5} s^{-1}.

Due to the confining gas pressure, the MAX phases in the Paterson apparatus can be deformed plastically. Consequently, the RT engineering stress-strain curves for MAX phases were recorded. Because the samples are inserted in Al cylinders, the mechanical data that are recorded during the tests are the results from both sample and Al. To remove the contribution of the Al jacket, a procedure was developed that consists in preliminary tests on pure Al samples in identical conditions as the "sample+Al" tests. The obtained stress-strain Al curve

is then subtracted from the "sample+Al" mechanical data following a Rule Of Mixture (ROM) that takes into account the sample and Al volume fractions. The validity of the ROM law is conditioned to the fact that the two phases, sample and Al, are tested in parallel without interactions at interfaces and they obey to iso-strain conditions: the ROM validity has been verified by Finite Elements Modelling (FEM) of the compression tests under hydrostatic pressure[156].

After removal of the Al jacket and washing in ethanol, the macroscopic deformation imposed on a sample, by using the Paterson machine, is studied. Deformed samples were examined by SEM to get macroscopic information on the deformation processes (micro crack, grain buckling, intragranular fracture …) and TEM to observe dislocations. For Ti_3AlC_2, the deformed surfaces were further studied by AFM.

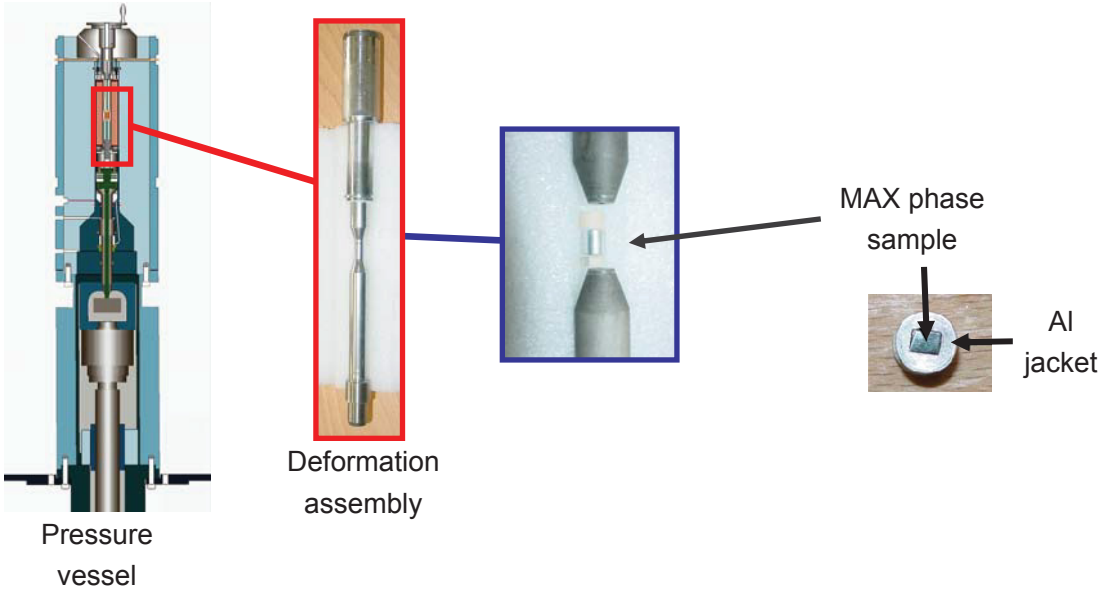

Figure 25: Deformed assembly of the Paterson machine.

Chapter III

Synthesis, Microstructural Characterization and Mechanical Properties of Ti_3SnC_2

III-1. Discovery of the new Ti_3SnC_2 MAX phase by HIPing process using a stainless steel container: synthesis and microstructural characterization

Powder mixtures of Ti, Sn and C were used to yield a final composition with the 2Ti:Sn:C (at.%) stoichiometry[15]. The powder characteristics are described in II-1.1. The powders were thoroughly ball-mixed in a turbula for 1 hour in order to ensure good mixing and to break up agglomerates. A stainless steel container was then filled with the reactant powder mixture. The extremity of the container was welded under high vacuum using electron beam. Then, the container was placed in the HIP and subjected to the following temperature and pressure cycle:

- heating at 850°C with a heating rate of 5°C/min under an Ar atmospheric pressure[157],
- heating at 850°C for 1h while Ar pressurization increases to 120 MPa,
- once pressurized, heating up to 1315°C with a heating rate of 25°C/min[157],
- holding at 1315°C and 120MPa for 4 hours before cooling to room temperature and atmospheric pressure.

A typical SEM micrograph of the HIPed sample is displayed in Figure 26. It shows that the material is not fully dense because of the presence of numerous pits and holes. Furthermore, a marked contrast can be observed between the core of the sample and its external part, which looks darker (see the dashed line which separates the different contrasted regions). This external ring extends between 200 and about 800μm depending on the observed area. At higher magnification (Figure 27), one observes black precipitates and elongated plates (light gray) embedded in a more uniform matrix (dark gray). From EDXS analyses, black precipitates are assigned to TiC while light gray elongated plates are enriched in Fe (mainly Fe_3Sn_2 from EDXS analyses). The composition of the dark gray areas varies from the core of the sample to its periphery: the ratio Ti/Sn is close to 2 in the first region and close to 3 in the second one.

The related XRD pattern is shown in Figure 28. The most striking point is to observe well defined diffraction peaks at $2\theta = 9.6°$ and 19.12° (diamonds in Figure 28) that look like replicates of the (0002) and (0004) reflections of the Ti_2SnC phase. From EDXS analyses, one can assume that it exists an unknown 312 MAX phase contributing to the measured XRD pattern. To assess this assumption, XRD data were refined using the MAUD software [147]

assuming the presence of a mixture of Ti_2SnC, TiC and of an hypothetic Ti_3SnC_2 MAX phase (space groupe $P6_3/mmc$).

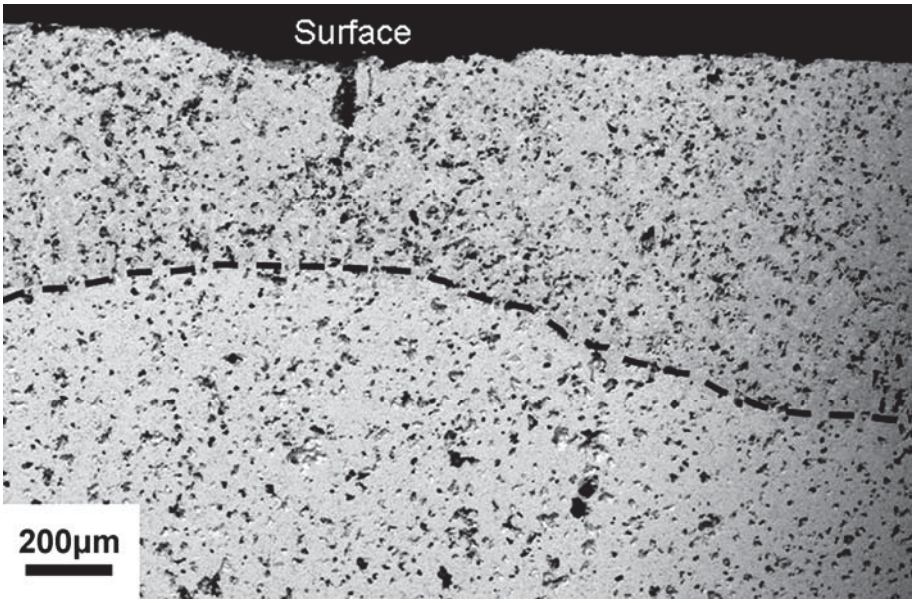

Figure 26: Back-scattered SEM micrograph of the cross section of the cylindrical HIPed sample. The dashed line is a guide for the eyes (see text).

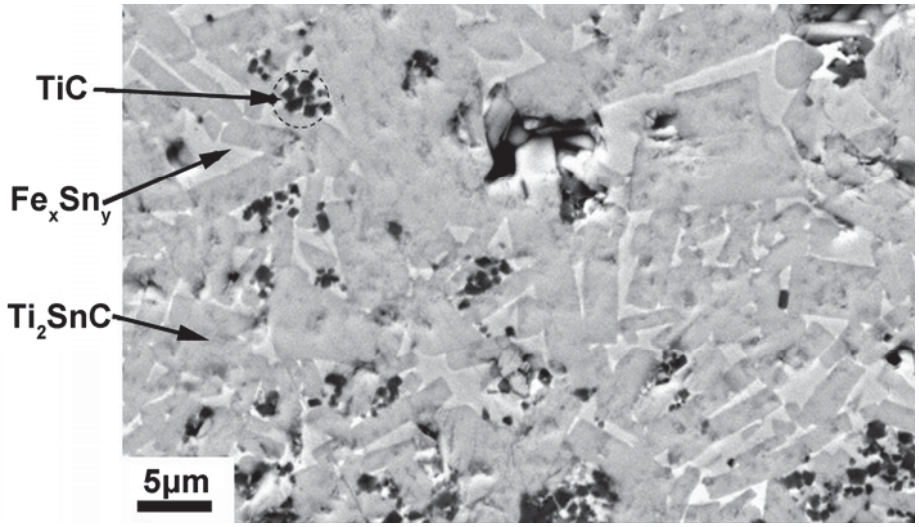

Figure 27: Back-scattered SEM micrograph of the core of the sample.

Despite the true conditions are not fulfilled to perform a Rietveld analysis (the sample is not milled to obtain a powder), the calculated pattern is in rather good agreement with the experiment (Figure 28). For the probed volume in the core of the sample, the analysis gives a composition of about 92 vol.% of Ti_2SnC, 5 vol.% of Ti_3SnC_2 and 3 vol.% of TiC. The lattice parameters of the 211 phase are a=0.31665±0.00001 nm and c=1.37123±0.00006 nm, values

slightly different from those reported by Jeitschko *et al.*[8](*a*=0.3186 nm, *c*=1.363 nm) and more recently by Vincent *et al.*[158] (*a*=0.316265±0.000009 nm, *c*=1.36789±0.00005 nm) and Barsoum *et al.*[157,159] (*a*=0.31635 nm and *c*=1.3675 nm). Concerning the new 312 MAX phase, Ti_3SnC_2, its lattice parameters are *a*=0.3136±0.0001 nm and *c*=1.866±0.001 nm. It should be pointed out here that impurities have been excluded from the Rietveld fit, the missing diffraction peaks being attributed to secondary phases (mainly Fe_3Sn_2 and Fe_2Sn).

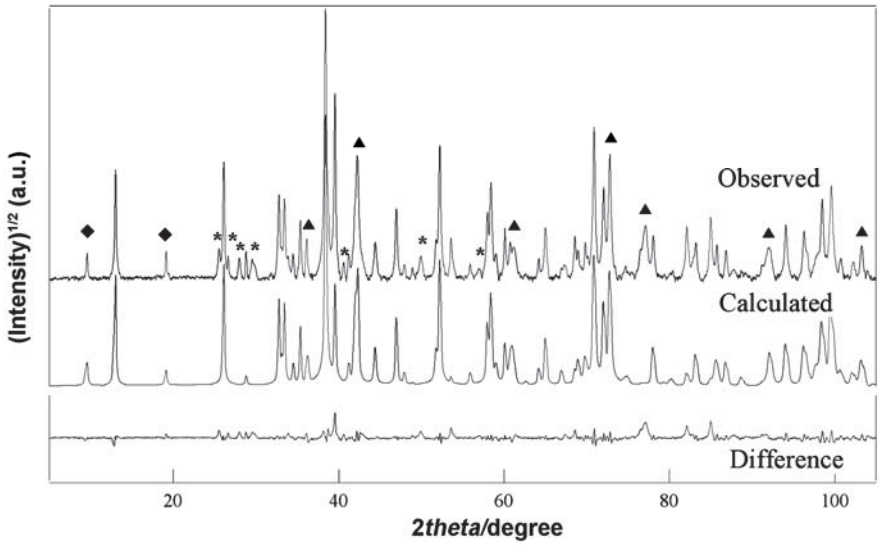

Figure 28: Observed/calculated/difference XRD Rietveld plots for Ti_2SnC (no symbol), Ti_3SnC_2 (♦), TiC (▲) and impurities (Fe_3Sn_2, Fe_2Sn) (*).

To have a better determination of the 312 MAX phase lattice parameters, an XRD experiment was performed illuminating the external part of the sample. Indeed, SEM observations and EDXS analyses have shown that such a region is nearly free of 211 phase. The related XRD pattern as well as its Rietveld fit is plotted in Figure 29. As the illuminated sample surface is not perfectly flat, the background is more important than in Figure 28, but the overall agreement between the experimental and calculated patterns is quite good. Here also, impurities that are at a quite low level are excluded from the fit. If one excludes these minority phases, the probed volume was found to be composed of Ti_3SnC_2 (78 vol.%) and TiC (22 vol.%) only. The 312 lattice parameters are found to be *a*=0.31366±0.00002 nm and *c*=1.8650±0.0002 nm, values that are, within the error bars, in agreement with those quoted above. In the Wycoff notations, it exists four inequivalent sites in the hexagonal $P6_3/mmc$ space group for 312 MAX phases: M_I in 2a, M_{II} in 4f, A in 2b and X in 4f. For the atoms in 4f

positions, the ideal values of the two internal dimensionless parameters z/c are 1/8 = 0.125 and 1/16 = 0.0625 for M_{II} and X respectively. From our analysis, Ti_3SnC_2 departs from the ideal stacking because we obtain z/c=0.1204±0.0003 for Ti_{II} and z/c=0.072±0.001 for C atoms, a behavior already observed in MAX phases [160,161]. Finally, the unexpected presence of Fe in our sample can be discussed. Its presence likely originates from the steel container used during the HIPing process. Nevertheless, it is surprising that this quite large amount of Fe (10 at.% from EDXS) does not forbid the MAX phases growth[162], a point which deserves to be further studied.

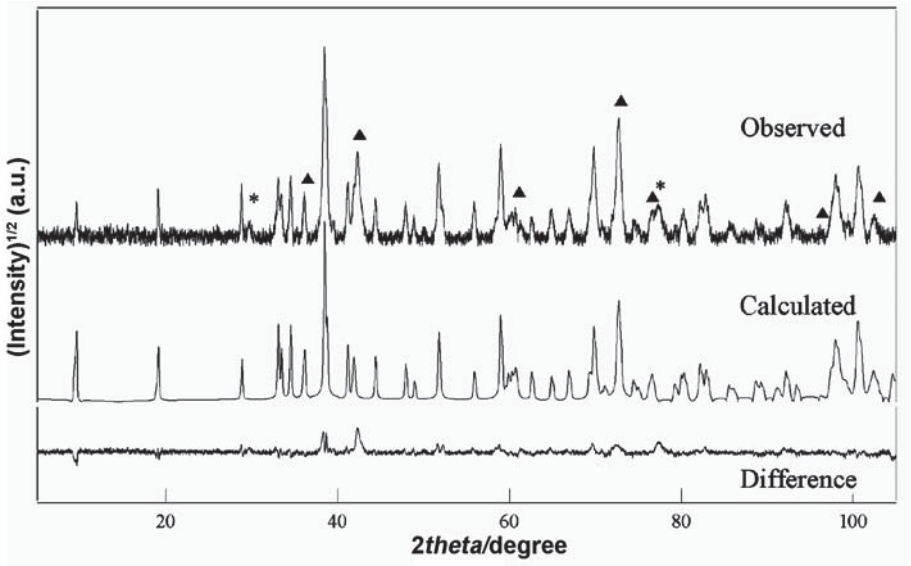

Figure 29: Observed/calculated/difference XRD Rietveld plots for Ti_3SnC_2 (no symbol), TiC (▲) and impurities (Fe_3Sn_2, Fe_2Sn) (*).

In summary, a new member of the 312 MAX phases family has been discovered. Its lattice parameters (a=0.31366±0.00002 nm and c=1.8650±0.0002 nm) have been determined from Rietveld refinement of the XRD data. It seems that Fe promotes the Ti_3SnC_2 formation.

III-2. Synthesis and microstructural characterization of a high Ti_3SnC_2 volume content material using Fe or Al as additive

III-2.1. Reaction mechanisms for the formation of Ti_3SnC_2 using Fe as additive

In III-1, it is shown that Fe may favor the formation of Ti_3SnC_2 MAX phase. In such a case, it is of interest to investigate the reaction mechanisms for the formation of Ti_3SnC_2 using Fe as additive.

3Ti:Sn:0.6Fe:2C and 3Ti:Sn:2C (at. %) reactant powder mixtures were investigated to study the effect of Fe as additive. Sintering of the compacts was carried out in a high sensitivity (±0.5 µm) dilatometric system under high purity argon. Compacts were heated to various temperatures, ranging from 510 to 1200°C, for an isothermal holding time of 1 hour. Heating and cooling were performed at an identical rate of 10°C.min^{-1}. The dimensional changes (in the axial direction) were continuously recorded throughout the thermal cycle.

Figure 30 shows the Thermal Expansion Curves (TEC) of the cold-compacted 3Ti:Sn:0.6Fe:2C and 3Ti:Sn:2C reactant powder mixtures heated at 1200°C for 1h. Indeed, sintering time is limited to 1h since it has been demonstrated in a previous work, by coupling dilatometry and XRD measurements, that Ti_3SnC_2 decomposes into TiC and Ti_2SnC at 1200°C for long holding time (t>8h).

From the TEC of 3Ti:Sn:2C (red one in Figure 30), one can observe that the sample length increases in the 230-310°C, 550-660°C, 710-730°C, 730-870°C and 920-1200°C temperature ranges. Those results are in good agreement with the ones obtained, for the formation of Ti_2SnC using 2Ti:Sn:C, by Bei *et al*. and Li *et al*.[163,164].

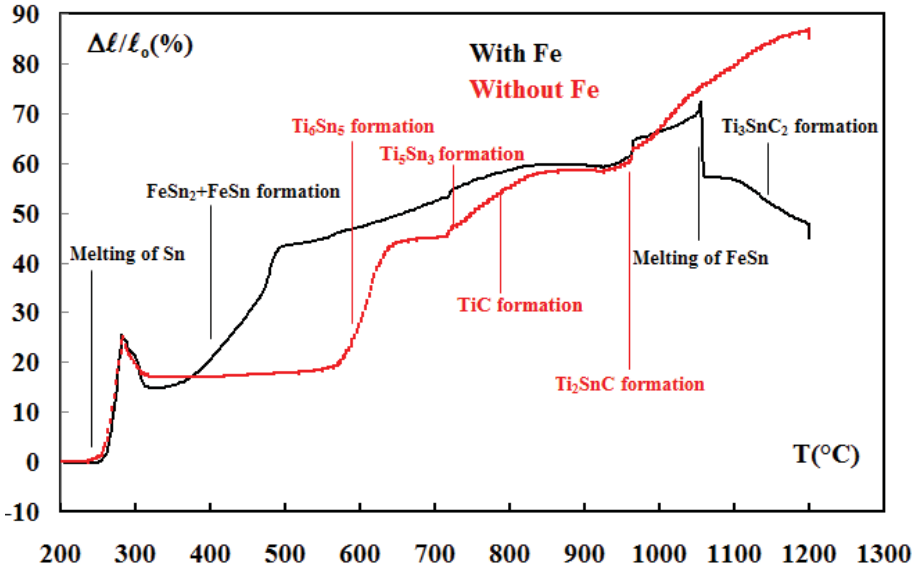

Figure 30: Thermal expansion Curves of cold-compacted 3Ti:Sn:2C (red curve) and 3Ti:Sn:0.6Fe:2C (black curve) samples heated at 1200°C for 1h.

XRD patterns of 3Ti:Sn:2C heated at 670°C, 780°C, 890°C, 1050°C and 1200°C for 1h

as well as the starting mixture milled for 1h are shown in Figure 31. Figures 30 and 31 allow correlating sample length changes and phase transformations. From the XRD pattern shown in Figure 31 (a), one can observe Ti and Sn diffraction peaks. C is not detected since it became nanostructured (or amorphous), and moreover, it is embedded in the soft metal during the milling process. The sample length increase, in the 230-310°C temperature range, is due to Sn melting. The sample length increase, as shown in Figure 31 (b), in the 550°C-660°C temperature range, is related to the Ti_6Sn_5 formation from Ti and Sn reactants. The inflection point at 717°C in the TEC may be attributed to the Ti_5Sn_3 formation which may result from Ti_6Sn_5 partial decomposition into Ti_5Sn_3, Ti and Sn.

Indeed, from Figure 31(c), one can notice that, a new Ti_5Sn_3 phase has been detected at 780°C, while the intensity of Ti_6Sn_5 decreases and the intensity of Ti XRD peaks increases. Moreover, XRD peaks of TiC are detected at T≥780°C (see Figures 31(c)-(f)), which confirm that the sample length change, in the 730-870°C temperature range, corresponds to TiC formation. The sample length change, above 960°C corresponds to Ti_2SnC MAX phase formation. Indeed, for T ≥1050°C, Ti_2SnC MAX phase is mainly observed in the XRD patterns recorded on the 3Ti:Sn:2C reactant powder mixtures heated for 1h (Figures 31(e) and (f)).Residual TiC, Ti_5Sn_3 and Sn (and Ti at 1050°C only) XRD peaks are also detected at T ≥1050°C. In such a case, it is reasonable to assume that Ti_2SnC formation results from Ti_xSn_y intermetallics and TiC reaction.

Hence, the reaction route of the 3Ti:Sn:2C, in the 20-1200°C temperature range, can be summarized as follows:

- At about 230°C: $Sn_{(S)} \longrightarrow Sn_{(L)}$
- In the temperature range 550-660°C: $6Ti + 5Sn \longrightarrow Ti_6Sn_5$
- In the temperature range 710-730°C: $Ti_6Sn_5 \longrightarrow Ti_5Sn_3 + Ti + 2Sn$
- In the temperature range 730-870°C: $Ti + C \longrightarrow TiC$
- At about 960°C: $Ti_xSn_y + TiC \longrightarrow Ti_2SnC$

Such a reaction route is moreover in good agreement with Bei's and Li's research work on the formation of Ti_2SnC using 2Ti:Sn:C as starting materials[163,164].

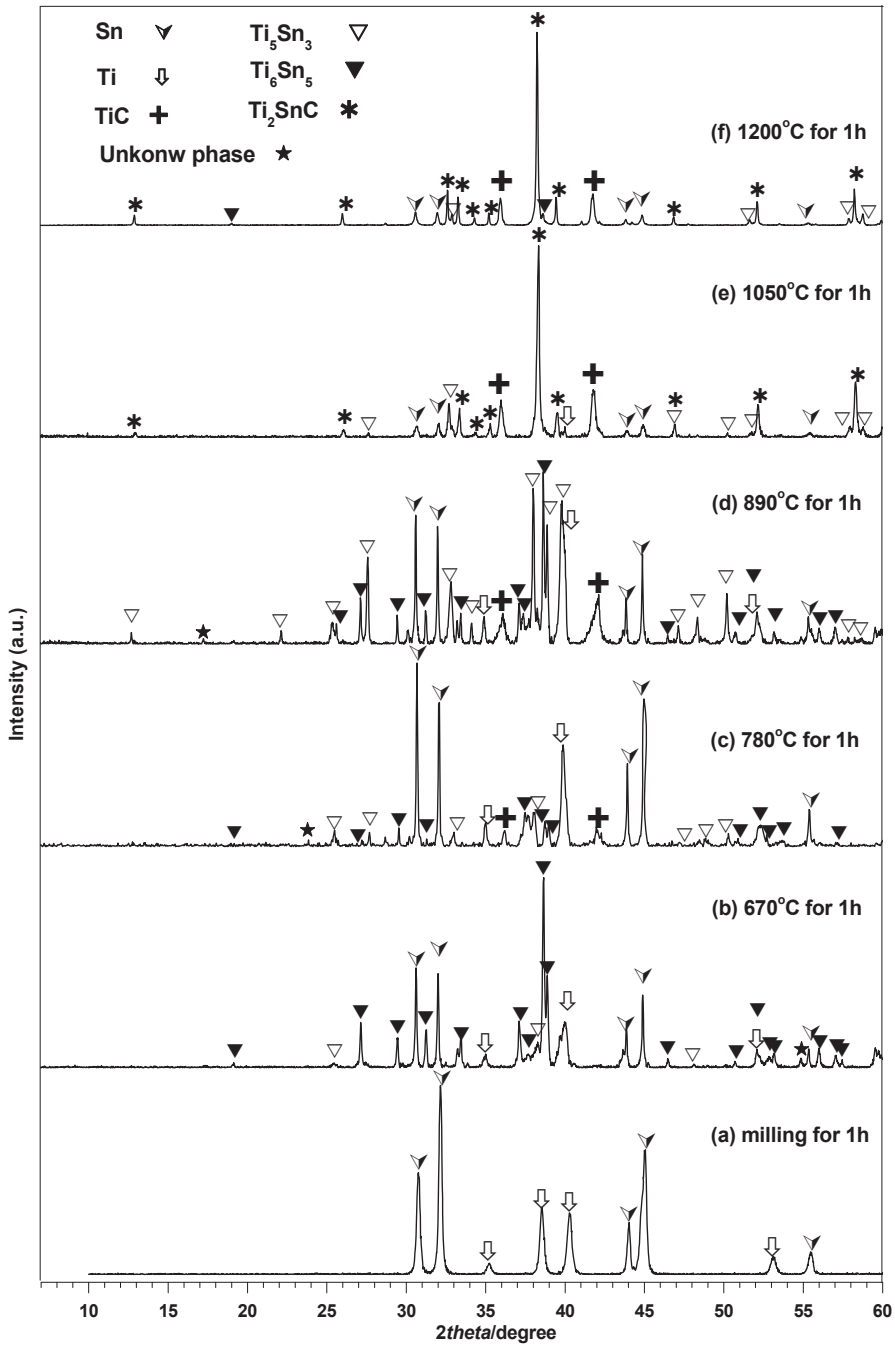

Figure 31: XRD patterns of a 3Ti:Sn:2C reactant mixture. (a) After milling. After 1h sintering at (b) 670°C, (c) 780°C, (d) 890°C, (e) 1050°C, (f) 1200°C.

The TEC of the 3Ti:Sn:0.6Fe:2C reactant powder mixture heated at 1200°C for 1h (black curve in Figure 30) is different from the one recorded on the 3Ti:Sn:2C reactant powder mixture. One can observe that, beside the same general shape of the TEC curve, some other characteristic sample length changes are observed in the 340-510°C, 990-1050°C, 1052-1068°C and 1100-1200°C temperature ranges.

To identify the corresponding phase transformations, XRD patterns have been recorded on 3Ti:Sn:0.6Fe:2C reactant powder mixtures after 1h milling and after heating at 510°C, 850°C, 1020°C, 1100°C and 1200°C for 1h (Figure 32). After milling, Ti and Sn diffraction peaks are observed. Because of its low content, Fe is not detected at the XRD detection limit. C is not detected for the reasons evoked previously for the 3Ti:Sn:2C mixture. In the XRD pattern of 3Ti:Sn:0.6Fe:2C heated at 510°C for 1h, Ti, Sn, FeSn, $FeSn_2$ and a small amount of Ti_6Sn_5 are detected. In such a case, the sample length change, in the 340-510°C temperature range, is attributed to the formation of $FeSn_2$ and FeSn. As the Gibbs energy of $FeSn_2$ is lower than the one of FeSn[165], in the 20-600°C temperature range, the reaction route between Fe and Sn can be interpreted by the following reactions:

$$Fe + 2Sn \longrightarrow FeSn_2$$

$$FeSn_2 \longrightarrow FeSn + Sn$$ [166]

The presence of a small amount of Ti_6Sn_5 also confirms the results that we get in the previous section with the 3Ti:Sn:2C reactant powder mixture as starting materials. Nevertheless, Ti_6Sn_5 seems to form at a lower temperature in the presence of iron. With increasing temperature, the sample length changes, recorded from 520°C to 1020°C, are due to the formation of Ti_6Sn_5, Ti_5Sn_3, TiC and Ti_2SnC phases, as observed in the previous section with a 3Ti:Sn:2C reactant powder mixture. Indeed, the XRD pattern of 3Ti:Sn:0.6Fe:2C heated at 850°C confirms the formation of Ti_6Sn_5, Ti_5Sn_3 and TiC.

At 1020°C, Ti_2SnC MAX phase is mainly observed while FeSn and Ti_6Sn_5 are no more detected at the XRD detection limit. Residual Ti and Sn are also detected. With further temperature increase, the fast sample length decrease, in the 1052-1068°C temperature range, is attributed to the Fe_xSn_y alloys melting[166]. In the 1100-1200°C temperature range, XRD patterns (see Figures 32 (e) and (f)) demonstrate that a large amount of Ti_3SnC_2 MAX phase is formed; the Ti_2SnC and Ti_5Sn_3 phases are no more present. In such a case, it is reasonable to believe that the Ti_3SnC_2 MAX phase is formed above 1100°C where a slight decrease of the sample length is observed in Figure 30. Moreover, in parallel, in the 1100-1200°C temperature range, TiC is formed as Ti peak intensity decreases.

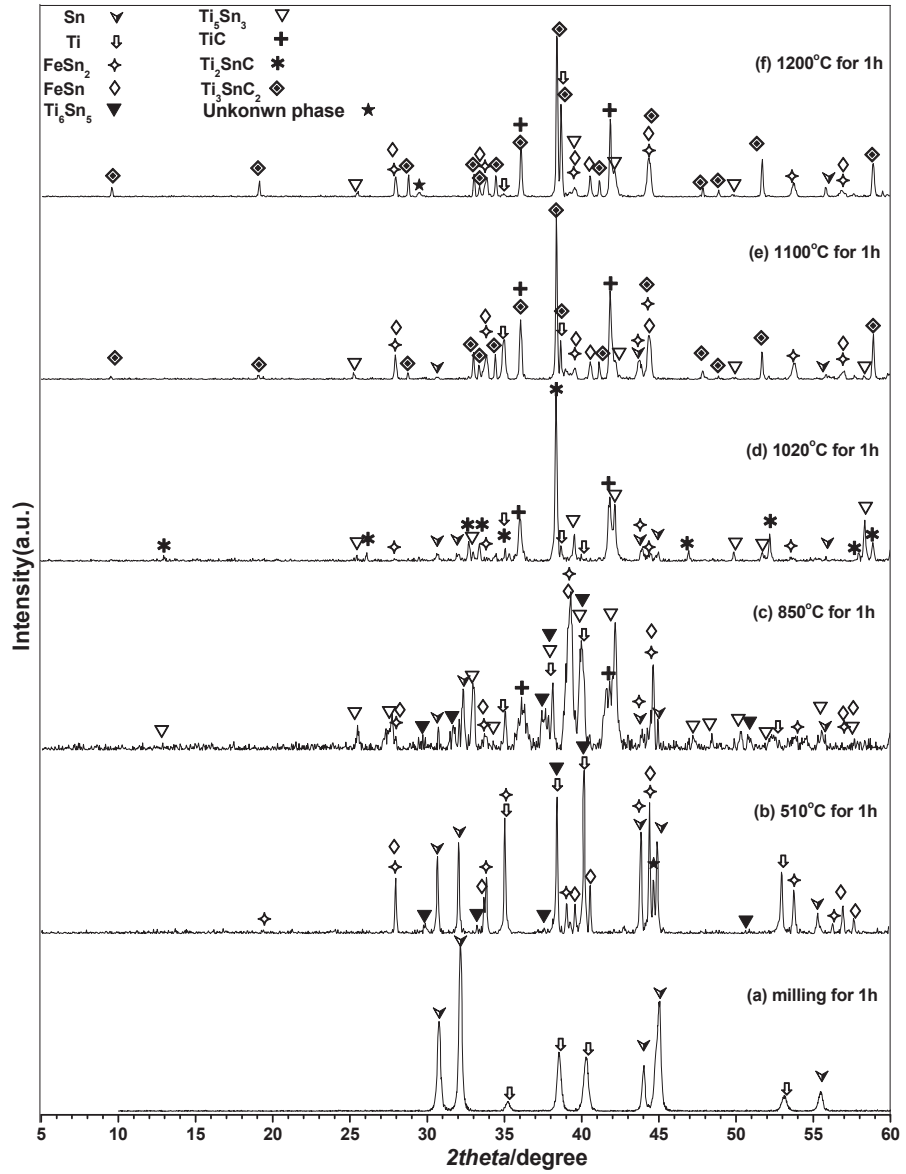

Figure 32: XRD patterns of a 3Ti:Sn:0.6Fe:2C reactant mixture. (a) After milling. After 1h sintering at (b) 510°C, (c) 850°C, (d) 1020°C, (e)1100°C, (f) 1200°C.

Hence, the different reactions evidenced, in the 20-1200°C temperature range, for the 3Ti:Sn:0.6Fe:2C reactant powder mixture can be summarized as follows:

- At about 230°C: $Sn_{(S)} \longrightarrow Sn_{(L)}$
- In the temperature range 340-510°C: $Fe + 2Sn \longrightarrow FeSn_2$

  and $FeSn_2 \longrightarrow FeSn + Sn$
- Above 510°C: $6Ti + 5Sn \longrightarrow Ti_6Sn_5$
- In the temperature range 710-730°C: one can suppose that Ti_5Sn_3 is formed from Ti and Ti_6Sn_5 as it is the case for the reactant mixture which does not contain Fe. Nevertheless, Ti_6Sn_5 peaks intensity increases from 510 to 850°C which suggest that

Ti_6Sn_5 content may increase, while Ti and Sn peaks intensity decrease. Thus, either Ti_6Sn_5 is decomposed into Ti_5Sn_3 and, at the same time, Ti_6Sn_5 is formed from Ti and Sn, or Ti and Sn react to from Ti_5Sn_3.

- At 730°C, TiC starts to form: $Ti + C \longrightarrow TiC$
- At about 960°C: $Ti_xSn_y + TiC \longrightarrow Ti_2SnC$
- In the temperature range 1052-1068°C: $Fe_xSn_{y(S)} \longrightarrow Fe_xSn_{y\,(L)}$
- At about 1100°C: Ti_3SnC_2 formation starts from Ti_5Sn_3 and TiC and/or from Ti_2SnC and TiC. The results also demonstrate that the presence of the liquid phase promotes the 312 phase formation which likely precipitates from the melt.

In summary, it has been demonstrated that the presence of Fe in the mixture promotes the Ti_3SnC_2 formation, since Ti_3SnC_2 is not formed by using a 3Ti:Sn:2C reactant powder mixture. The appearance of a liquid containing Fe and Sn at about 1060°C is demonstrated to favor the Ti_3SnC_2 phase formation from the melt. Ti_3SnC_2 very likely precipitates from the melt.

III-2.2. Optimization of the Fe content in the initial reactant mixtures

In order to optimize the Ti_3SnC_2 volume content in the produced material, 0.1Fe (1.6 at.%), 0.2Fe (3.2 at.%), 0.6Fe (9.1 at.%) and 1.2Fe (16.7 at.%) were added to the 3Ti:Sn:2C reactant powder mixture. The powders were thoroughly ball-mixed in a turbula@ mixer for 1 hour in order to ensure good mixing and to break up agglomerates. The different mixtures were cold-compacted into cylindrical steel dies using a uniaxial pressure of 800 MPa. The green bodies were then sealed under vacuum in a pyrex container. Then, the green bodies were placed in the HIP and subjected to the following temperature and pressure cycle:

- heating at 850°C with a heating rate of 5°C/min under an Ar atmospheric pressure[157],
- heating at 850°C for 1h while Ar pressurization increases to 50 MPa,
- once pressurized, heating up to 1150°C (T<1200°C since Ti_3SnC_2 decomposes after long duration at 1200°C) with a heating rate of 25°C/min,
- holding at 1150°C and 50MPa[157] (a lower pressure is applied in this case since we use a pyrex container) for 10 hours (long time to favor densification) before cooling to room temperature and atmospheric pressure.

After HIPing, the sample was machined to remove the encapsulating glass container and sliced using a diamond wheel. The polishing procedure is described in II.2.2..

XRD data were refined using the MAUD software[147] in order to determine the volume % of Ti_3SnC_2 in the produced material. Figure 33 shows the 312 volume content as a function of the Fe atomic content in the initial mixture. From this figure, it is shown that about 9 at.% of Fe (0.6Fe) leads to the highest volume content of Ti_3SnC_2 (80 vol.%) in the final product for the analyzed compositions.

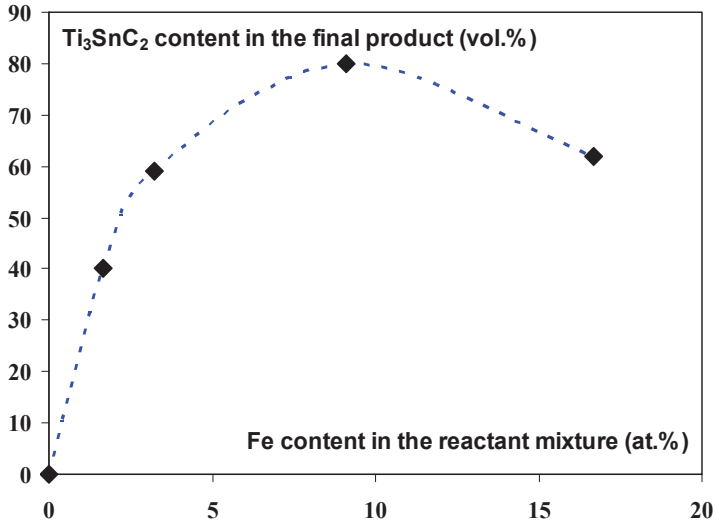

Figure 33: Ti_3SnC_2 volume content in the final product as a function of the Fe atomic content in the initial reactant mixture. Blue dotted line is only a guide for the eyes.

III-2.3. Characterization of the sample containing a high volume content of Ti_3SnC_2

Figure 34 shows the XRD pattern of the 3Ti:Sn:0.6Fe:2C reactant mixture sintered at 1150°C and 50MPa for 10h. One can notice that the main peaks belong to the Ti_3SnC_2 phase. Some TiC and small amounts of Sn, FeSn and $FeSn_2$ are also detected in the sample. XRD data were refined using the MAUD software [147] assuming the presence of a mixture of Ti_3SnC_2, TiC, FeSn, $FeSn_2$ and Sn. For the probed volume, the analysis gives a composition of about 80.5 vol.% of Ti_3SnC_2, 16.2 vol.% of TiC, 0.3 vol.% of FeSn, 0.8 vol.% of $FeSn_2$ and 2.2 vol.% of Sn.

Figure 35 shows the back-scattered SEM images of the as-synthesized sample. From Figure 35(a), one can observe that three contrasts (grey, black and white areas) can be

distinguished. More detailed information about the sample morphology and composition can be obtained from Figure 35(b). Grey areas observed in Figure 35(b) have a MAX phase characteristic shape, i.e. lamella shape (3-5µm in width and 10-15µm in length). EDXS results allow demonstrating that Ti, Sn Al are indeed detected in these grey areas. Moreover, the atomic ratio Ti/Sn is close to 3 which confirms that grey areas consists in Ti_3SnC_2. Furthermore, Fe is not detected in these lamellas. Black areas are assemblies of small round shape grains; EDXS analyses show that they contain Ti and C. As a result, one can deduce that these small grains consist in TiC. Finally, EDXS analyses show that white areas, located in the grain boundaries, mainly contain Sn and Fe. Hence, these white areas likely consist in a mixture of Sn, $FeSn_2$ and FeSn as referred to XRD results.

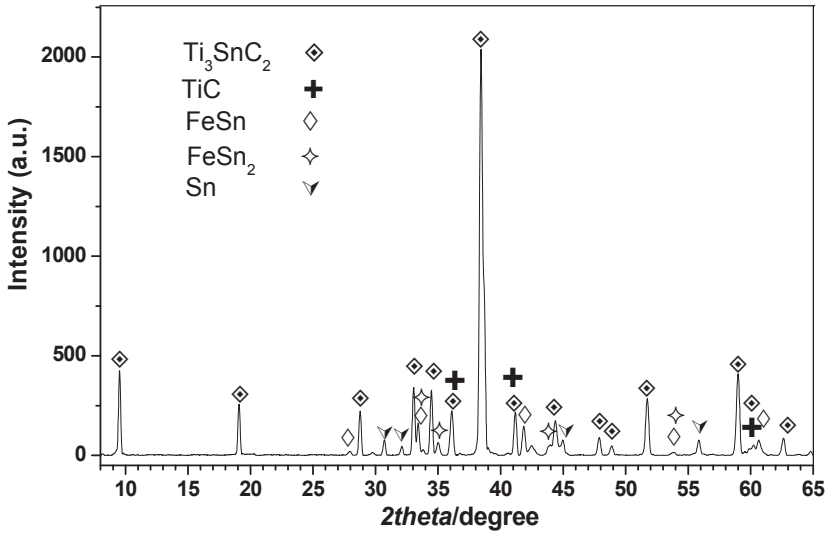

Figure 34: XRD pattern of a 3Ti:Sn:0.6Fe:2C reactant mixture sintered at 1150°C and 50MPa for 10h.

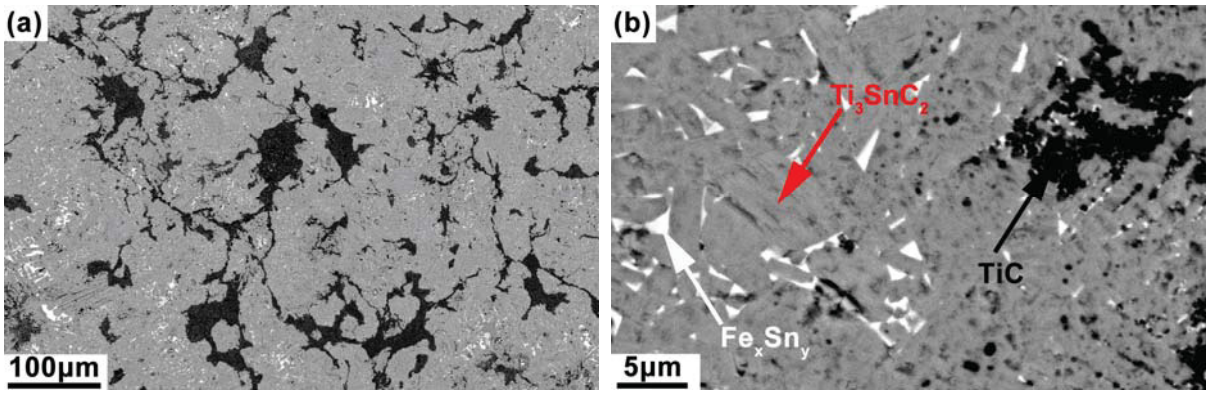

Figure 35: (a) Bak-scattered SEM micrographs of a 3Ti:Sn:0.6Fe:2C reactant mixture HIPed at 1200°C and 50MPa for 10h, (b) enlarged area in (a).

III-2.4. Synthesis and microstructural characterization of Ti_3SnC_2 samples using Al as additive

It has been shown in the previous section that Fe may be efficiently used as an additive to produce Ti_3SnC_2 MAX phase. On the other hand, Al or Sn is often used as additive to produce pure Ti_3SiC_2 or Ti_3AlC_2 MAX phase, respectively [2,3,55]. In such a context, it is of interest to use Al as an additive into the initial 3Ti:Sn:2C reactant powder mixture and to compare the results (volume content of the 312 phase, cell parameters …) with the ones obtained by using Fe as additive.

Thus, a 3Ti:Sn:0.6Al:2C reactant powder mixture has been prepared for that purpose. The preparation method used for this green body is the same as the one described in III.2.2.. The HIPing process of the 3Ti:Sn:0.6Al:2C reactant compact is slightly different as Ti_3AlC_2 is generally synthesized at higher temperature. The temperature and pressure cycles used are the following:

- heating at 30°C/min to 1450°C under an Ar atmospheric pressure,
- pressurization at 0.5 MPa/min to 100MPa,
- once the processing temperature (1450°C) and pressure (100MPa) are reached, holding at 1450°C for 4h and 100MPa for 90min, respectively, before cooling to room temperature and atmospheric pressure.

Figure 36 shows XRD patterns recorded on a 3Ti:Sn:0.6Al:2C reactant mixture HIPed at 1450°C for 4h and 100 MPa for 90min (Figure 36 (b)) and on a 3Ti:Sn:0.6Fe:2C reactant mixture HIPed at 1150°C and 50MPa for 10h (Figure 36 (a)). In Figure 36(b), only the 312 phase, TiC and pure Sn are detected. Compared to the XRD pattern recorded on the sample synthesized from 3Ti:Sn:0.6Fe:2C, one can notice that the 312 peaks are shifted towards smaller angles. Rietveld refinement of the XRD data, performed with MAUD software, shows that the sample contains about 94 vol.% of 312 phase, 4 vol.% of Sn and 2 vol.% of TiC. The lattice parameters of the 312 phase, as deduced from Rietveld refinement, are a=0.31054±0.00001 nm and c=1.8572±0.0001 nm. These values are in between the ones of Ti_3SnC_2 (a=0.31366 nm and c=1.8650 nm) and Ti_3AlC_2 (a=0.30779 nm and c=1.8579 nm) [17]. These results suggest that a $Ti_3Al_xSn_{(1-x)}C_2$ MAX phase solid solution may have been formed

by using Al as an additive in the reactant powder mixture.

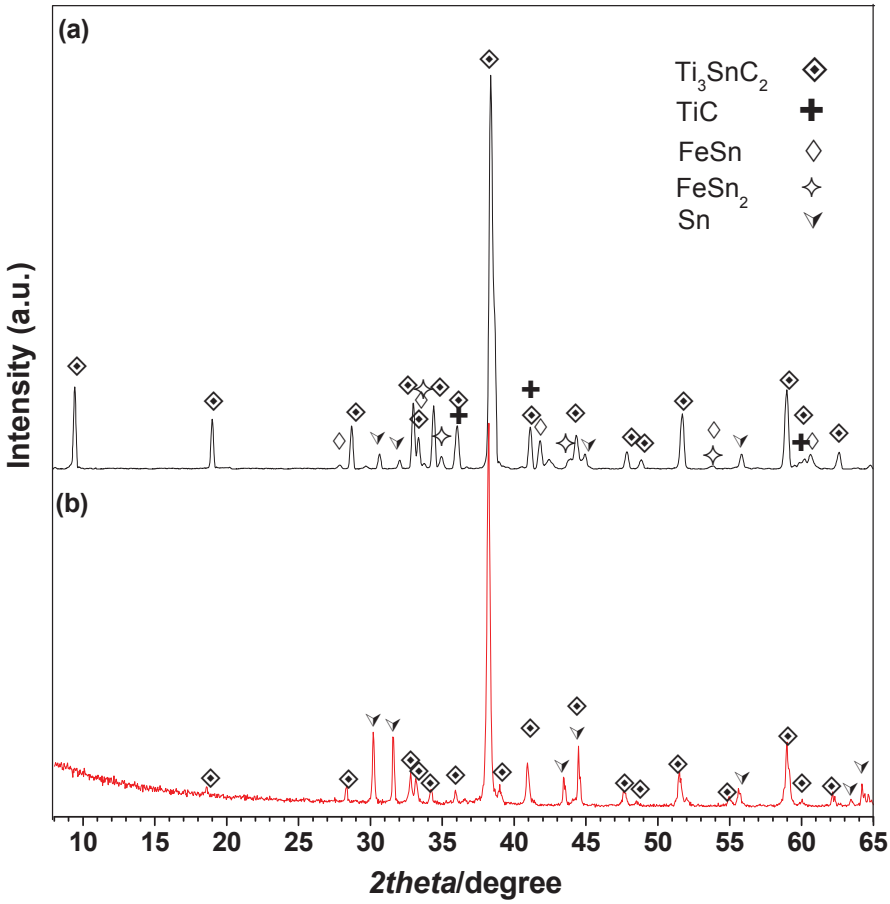

Figure 36: XRD patterns of (a) a 3Ti:Sn:0.6Fe:2C reactant mixture HIPed at 1150°C and 50MPa for 10h, (b) a 3Ti:Sn:0.6Al:2C reactant mixture HIPed at 1200°C for 4h and 100MPa for 90min.

Figure 37 shows the back-scattered SEM images and EDXS analyses of the as-synthesized sample. One can notice that three different contrasts (grey, black and white areas) are distinguished in the images. More detailed information about the sample morphology and composition can be obtained in Figure 37(b) which is an enlarged SEM image of the red rectangle drawn in Figure 37(a). Grey areas observed in Figure 37(b) have a MAX phase characteristic shape, i.e. lamella shape (1-3µm in width and 5-8µm in length). EDXS results of Figure 37(c) show that Ti, Sn Al are detected in these grey areas. Moreover, the atomic ratio Ti/(Sn+Al) is close to 3 which further confirms that these areas are $Ti_3Al_xSn_{(1-x)}C_2$ MAX phase solid solutions. Such a result demonstrates that $Ti_3Al_xSn_{(1-x)}C_2$ solid solutions can be formed by using Al as additive in the 3Ti:Sn:2C reactant powder mixture.

EDXS analyses performed in black areas (Figure 37(d)) show that they are rich in O and Al. Thus, these black areas likely consist in Al_2O_3 which is not detected by XRD, probably because of its too low volume fraction or amorphous state. Alumina may result from the oxidation of the Al reactant powders. Indeed, the EDXS spectrum of Figure 37(f) shows that the original Al powder contains small amount of oxygen. Finally, EDXS analyses (Figure 37(e)) carried out on white areas show that they contain nearly pure Sn.

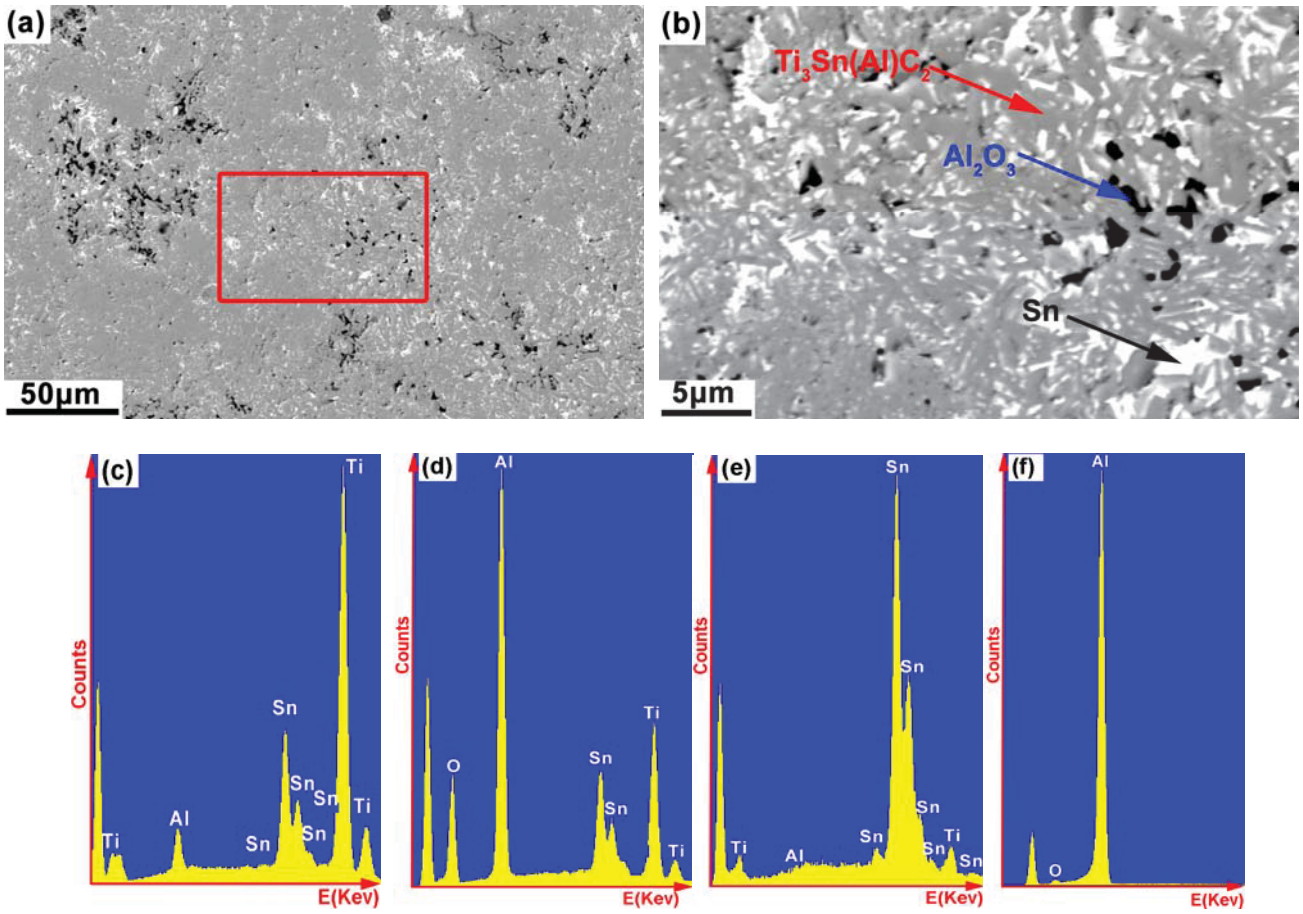

Figure 37: (a) Back-scattered SEM micrographs of a 3Ti:Sn:0.6Al:2C reactant mixture HIPed at 1200°C for 4h and 100MPa for 90min, (b) enlarge image of the red rectangle in (a), (c) EDXS analyses performed in the grey area, (d) in the black area, (e) in the white area, (f) EXDS analysis of original Al powders of the starting material.

In summary, it has been demonstrated that, using Al as additive in the 3Ti:Sn:2C reactant powder mixture, Al atoms can substitute Sn atoms in the Ti_3SnC_2 structure and thus form a $Ti_3Al_xSn_{(1-x)}C_2$ MAX phase solid solution. Such a result is of main importance as it will allow investigating the mechanical properties modifications in the $Ti_3Al_xSn_{(1-x)}C_2$ MAX phase solid solutions as a function of x. These results will be discussed in Chapter V.

III-3. Mechanical properties of Ti_3SnC_2 determined by nanohardness cartography

As discussed in sections III-1 and III-2, no pure Ti_3SnC_2 samples were obtained by using reactive HIPing process. Thus, hardness cartography and optical microscopy of the multi-phases sample can be used to correlate hardness values and phase nature[167]. In order to study hardness variation with penetration depth, 9 loads (1, 2, 3, 6, 10, 15, 30, 150 and 300 mN) have been used. As the sample is composed of five different phases (Ti_3SnC_2, TiC and small amounts of Sn, FeSn and $FeSn_2$), a statistical analysis has been performed, for each load, over 100 nanoindentations. The elastic modulus has been extracted from nanoindentation curves.

The analysis is here detailed for the 3 mN load indentations. In Figure 38, the elastic modulus histogram, determined from 500 indents, presents three peaks centered at 370, 245, and 177 GPa. The main peak, at 245 GPa, is unambiguously attributed to the Ti_3SnC_2 MAX phase. This value is moreover in good agreement with results obtained by nanoindentation in MAX phase thin films [108,109] or by ultrasound methods [46]. The peak at 370 GPa is ascribed to the TiC phase, and the peak at 177 GPa very likely results from the minority phases (i.e.: Sn, FeSn and $FeSn_2$), and from artifacts induced when the indent is localized in a grain boundary. The peak ascribed to TiC is centered at a lower value than those often reported for TiC[168] and presents a large full width at half maximum (90 GPa). Such an effect is likely related both to the presence, in the sample, of other phases, softer than TiC and thus elastically deformed below the TiC tested grains and to the small size of TiC grains that can furthermore be substoichiometric.

It must be noted that the Gaussian peak deconvolution, shown in Figure 38, gives area ratios of 74% for Ti_3SnC_2, 22% for TiC and 4% for the minority phases. These values are in reasonable agreement with the volume fractions determined by XRD (80 vol.% for the 312, 16 vol.% for the TiC and 4 vol.% for impurities). The histogram of hardness values, measured with the same load, is plotted in Figure 39(a), with a 500 MPa bin size. As for the elastic modulus, three main peaks are observed. The highest one, centered at 15.7GPa, is ascribed to Ti_3SnC_2. When this central peak is plotted with lower bin sizes of 200, 150 and 100MPa (See

Figures 39(b)-(d)), secondary hardness peaks ranging from 11 to 18 GPa are observed. Their position is the same for the different bin sizes and this substructure is thus relevant and not due to scattering in hardness measurement.

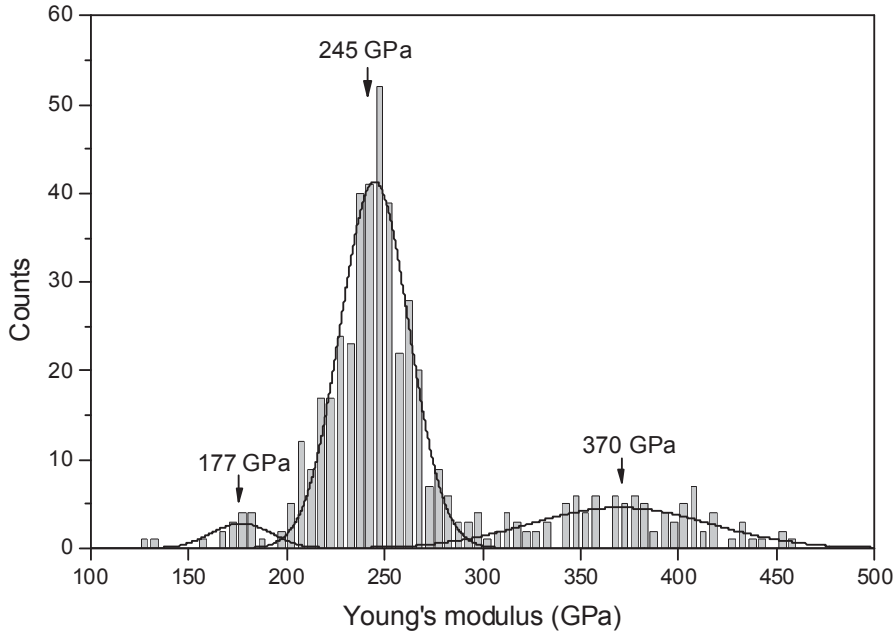

Figure 38: Histogram of elastic modulus determined from 500 indents performed with a 3 mN load.

Hardness and elastic modulus cartographies have been established for a better understanding of the hardness histogram. 400 of the studied 3 mN indents were organized in a regular square shaped network, with a 7 µm step size. These indents, as well as the sample surface morphology, have thus been observed by optical microscopy using polarized light. Hardness cartography, obtained from a bicubic interpolation in between measurement points, is shown in Figure 40 and superimposed to an optical microscopy image of the indented area. This cartography clearly demonstrates the correlation between hardness value and nature of the indented phase. Indeed, red, green and blue regions of the hardness cartography are unambigously respectively ascribed to TiC, Ti_3SnC_2 and impurity phases of the optical micrograph. It thus explains the 3 peaks observed in Figures 38 and 39(a).

For the MAX phase grains, the color distribution shows that hardness values are homogeneous for a given grain, but changes from one grain to another. This effect is emphasized in the inset of Figure 40, which is a magnification of the region marked by a white square. In this case, the actual hardness values have been indicated below each indent

for three large Ti_3SnC_2 grains. Two of them have a hardness value of about 17 GPa while the third one has a hardness value of about 14 GPa. Indeed, in such an anisotropic material, where the dislocation glide is supposed to be limited to basal planes[133], deformation mechanisms, involved during the indent formation, are supposed to be strongly related to the grain orientation. This grain orientation dependence for the hardness explains the discrete substructure observed in Figures 39(b)-(d). It should be emphasized that this method of nanohardness cartography is also of the highest interest to detect artifacts due to, for example, indents localized in a grain boundary (see white arrow in Figure 40).

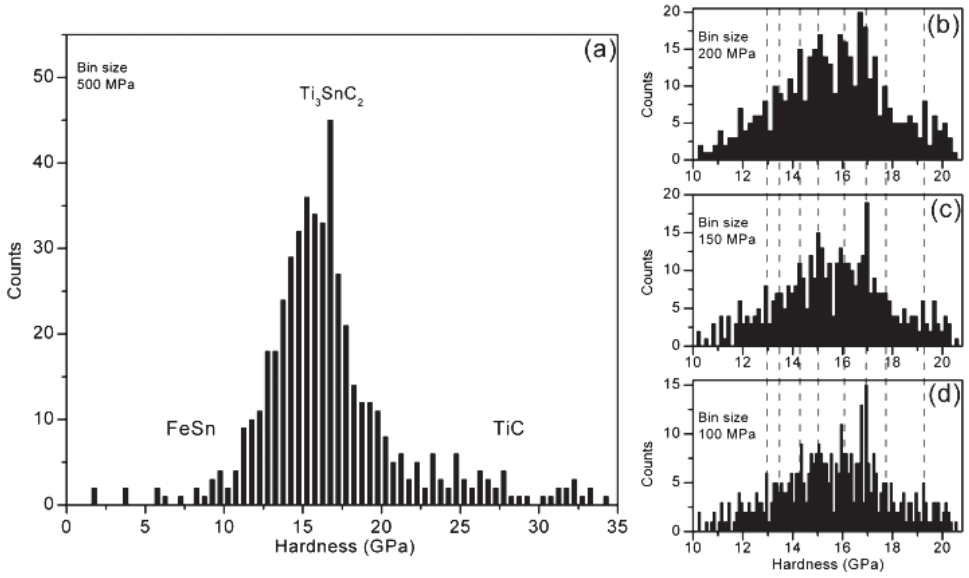

Figure 39: (a) Histogram of hardness values (bin size 500 MPa) determined from 500 indents performed with a 3 mN load. (b) to (d) Central hardness peak attributed to Ti_3SnC_2 plotted with bin size of respectively 200 MPa, 150 MPa and 100 MPa. A substructure is observed, independently of the histogram bin size.

For each indentation load, the same statistical analysis has been performed over 100 indents to identify the Ti_3SnC_2 peak on hardness and elastic modulus histograms and to extract a mean value. Corresponding hardness and modulus values are plotted in Figure 41 as a function of the penetration depth. The standard deviations, also shown on the graph, result from an average on different grain orientations. For the hardness, as reported previously in Ti_3SiC_2 samples[106], an Indentation Size Effect (ISE) is observed, that is an increase of the hardness value for the low penetration depth. This ISE is well fitted by the same function as the one proposed in the Nix and Gao model[169]. From this fit, one can deduce that the intrinsic hardness value of Ti_3SnC_2 is 9.3±0.5 GPa. Such a value is higher than some

previously measured hardness values of Ti_3SiC_2 MAX phases [106,107], although hardness values in the range 14-18 GPa have been measured by nanoindentation normal to the basal planes of MAX phase thin films[108,109]. The elastic modulus remains constant (245 GPa) whatever the penetration depth is. Such a result is in compatible agreement with an elastic properties and it attests that the ISE is not an artefact due to the indenter shape calibration.

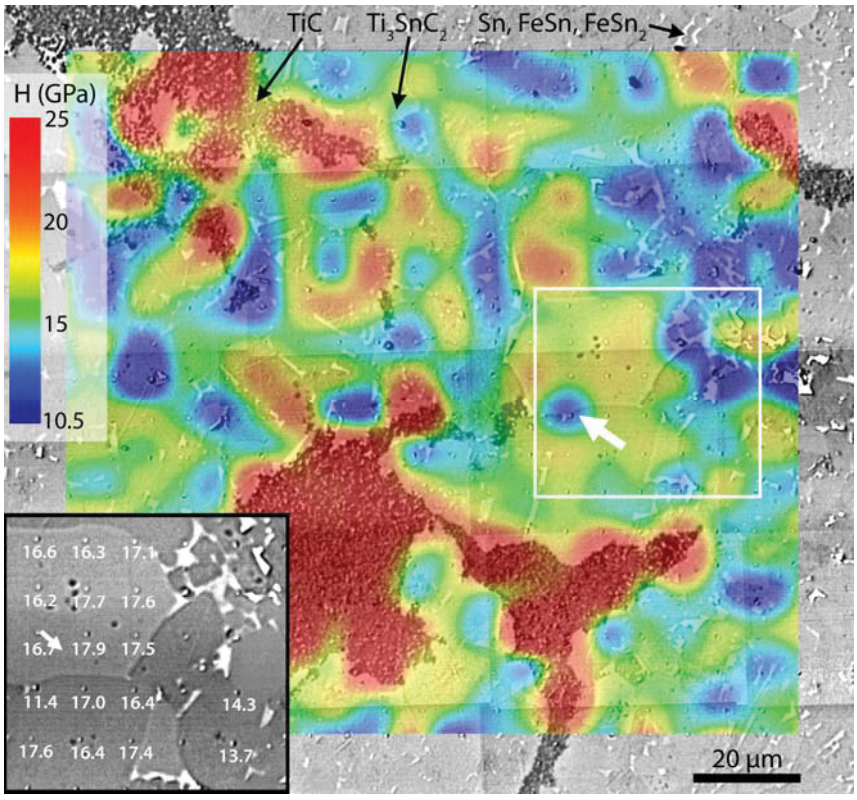

Figure 40: Hardness cartography superimposed to optical micrography of the sample surface. The 400 indents array is visible (step size: 7µm). The white arrow indicates an indent located on a grain boundary. In the inset (left corner): optical microscopy image of the indented area indicated by the white square. The indents are visible and the actual hardness values are given in GPa for three different large grains.

In the case of the 150 and 300 mN load indentations, the size of the indent is in the order of the mean grain size. In that case, as observed by AFM in Figure 42, several grains are involved in the deformation process and grain boundaries play an important role in macroscopic deformation. In particular, grain push-in and pull-outs, or grain boundary decohesion are observed near the indent. Slip lines, due to the emergence and propagation of dislocations, are also observed in several grains. It is worth noting that the most deformed grains are not necessarily the closest to the indent. In such a case, which is close to

microindentation test conditions, it is clear that intrinsic MAX phase hardness is underestimated.

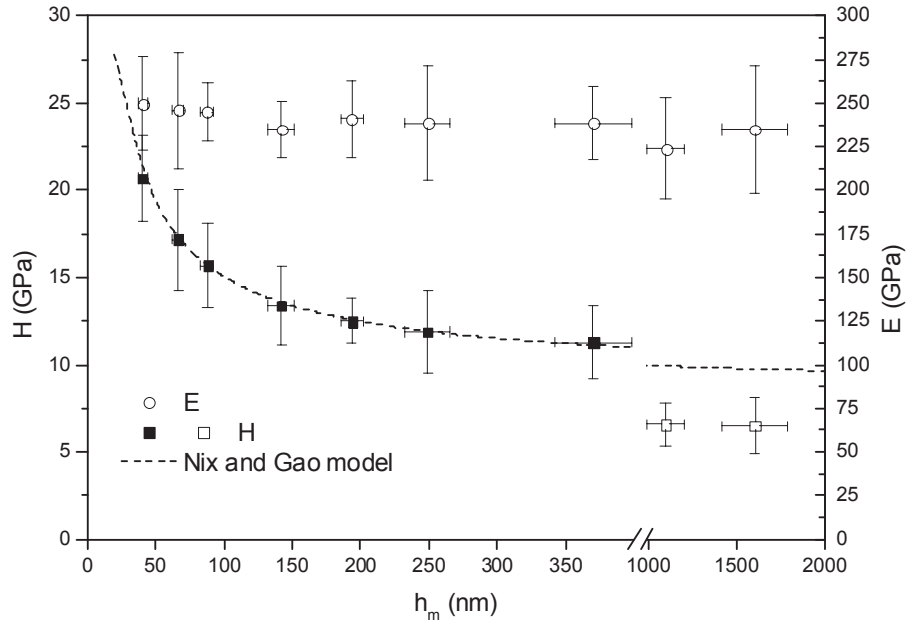

Figure 41: Ti_3SnC_2 elastic modulus (open circles) and Ti_3SnC_2 hardness (black squares) as a function of the indenter penetration depth. Dashed line: fit of the Indentation Size Effect using the Nix and Gao function [24].

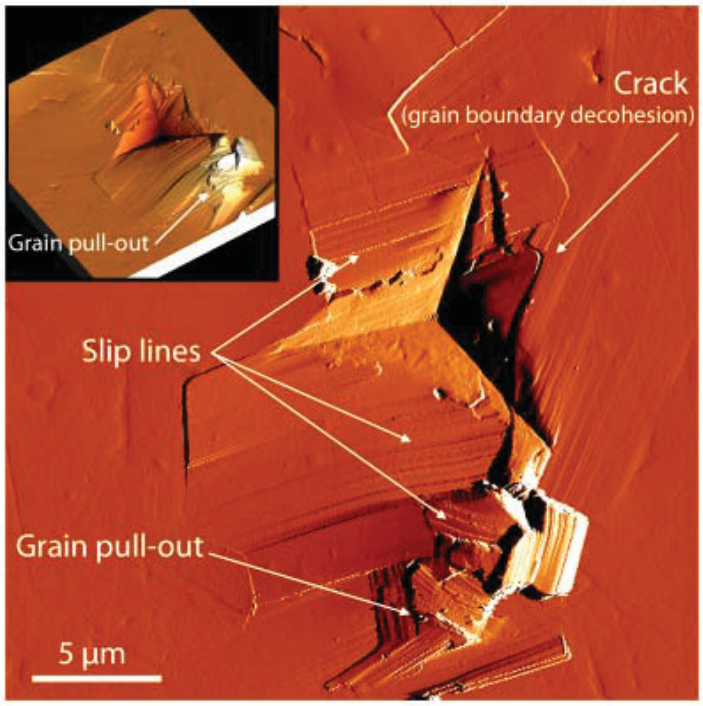

Figure 42: 300 mN indent in Ti_3SnC_2 observed by AFM (error signal mode image). A 3D representation of the corresponding topography image is shown in the inset. Slip lines are observed in several grains, as well as grain pull-outs near the indent.

In summary, nanoindentation has been used to characterize the mechanical properties of the recently synthesized Ti_3SnC_2 MAX phase. Hardness cartography has been established and compared with the nature of the different phases in the indented area. This method is very efficient to correlate hardness values and phase nature and to detect artifacts related to the presence of grain boundary during nanoindentation test. Moreover, the intrinsic hardness value of Ti_3SnC_2 (9.3 GPa) is shown to be higher than all previously measured hardness values of other MAX phases. It is demonstrated that hardness value is underestimated when several grains are involved in the deformation process, due to grains pull-outs and push-in or to cracks localized at grain boundaries. The elastic modulus value is 245 GPa.

III-4. Conclusions

A new member of the 312 MAX phase family has been discovered. Its lattice parameters (a=0.31366±0.00002 nm and c=1.8650±0.0002 nm) have been determined from Rietveld refinement of the XRD data. It has been demonstrated that the presence of Fe in the mixture promotes the Ti_3SnC_2 formation since Ti_3SnC_2 is not formed by using a 3Ti:Sn:2C reactant powder mixture. The appearance of a liquid containing Fe and Sn at about 1060°C favors Ti_3SnC_2 formation from the melt. The optimization of the iron content has demonstrated that 9 at.% of iron is the adequate amount to produce a high content of Ti_3SnC_2. Concerning the processing temperature, it has been shown in a previous work, coupling dilatometric and XRD measurements that the Ti_3SnC_2 MAX phase decomposes at 1200°C for long holding time. Thus, samples containing about 80 vol.% of Ti_3SnC_2 have been synthesized using 9 at.% of Fe as additive during reactive sintering at 1150°C and 50MPa for 10h. Using Al as additive in the 3Ti:Sn:2C reactant powder mixture, it has been demonstrated that one can synthesize $Ti_3Al_xSn_{(1-x)}C_2$ MAX phase solid solutions.

Nanoindentation has been used to characterize the mechanical properties of the synthesized Ti_3SnC_2 MAX phase. The intrinsic hardness value of Ti_3SnC_2 (9.3 GPa) is shown to be higher than all previously measured hardness values of other MAX phases. It has been shown that hardness value is underestimated when several grains are involved in the deformation process, due to grains pull-outs and push-in or to cracks localized at grain boundaries. The elastic modulus value of Ti_3SnC_2 is 245 GPa.

Chapter IV

Synthesis, Microstructural Characterization and Mechanical Properties of Ti_3AlC_2

IV-1. Synthesis and microstructural characterization of Ti_3AlC_2

Powders of Ti, Al, TiC were selected as the starting materials to synthesize Ti_3AlC_2 samples. The powder characteristics are described in II-1.1. To obtain highly pure Ti_3AlC_2 samples, a Ti:Al:1.9TiC reactant mixture was used. Indeed, previous experiments performed using the Ti:Al:2TiC reactant mixture have shown that some Al vaporizes during the HIPing process since TiC is always present in the end-products; as a consequence, either (Ti+C) substoichiometry or Al over-stoichiometry is investigated in this study. However, when the TiC content is 1.8 moles in the starting material, Ti_2AlC is detected in the final products. Only the samples resulting from the Ti:Al:1.9TiC reactant mixture leads to highly pure Ti_3AlC_2 samples. Thus, this reactant mixture was ball-milled in a Turbula mixer to obtain a homogenous powder mixture and cold-compacted using a uniaxial press. The resulting cylindrical green samples (12 mm in diameter and 10 mm in height) were encapsulated into glass containers under vacuum[36]. For the reactive sintering procedure, the samples were placed in a HIP machine and subjected to the following temperature and pressure cycle:

- Heating at 1450°C with a heating rate of 30°C/min under an Ar atmospheric pressure,
- Pressurization at 0.5 MPa/min to 50MPa,
- Once the processing temperature and pressure are reached, holding at 1450°C for 2h and 50MPa for 1 h before cooling to room temperature and atmospheric pressure.

After HIPing, the samples were machined to remove the glass container and sliced using a diamond wheel. The polishing procedure is described in II.2.2..

Figure 43 shows the XRD pattern of the Ti:Al:1.9TiC reactant mixture sintered at 1450°C for 2h and 50MPa for 1h. One can notice that only Ti_3AlC_2 peaks are observed and no other peaks such as TiC, Ti_xAl_y intermetallics or Ti_2AlC are detected. Moreover, the refining of XRD data using MAUD software demonstrates the presence of Ti_3AlC_2 single phase at the XRD detection limit. Ti_3AlC_2 lattice parameters are a=3.0786±0.0001Å and c=18.589±0.001Å. Figure 44 shows a typical SEM image in back-scattered mode of the as-produced Ti_3AlC_2 sample. One can observe the lamellar nature of Ti_3AlC_2 grains with an average dimension in the range 60-100 μm in length and 10-40 μm in width. Al_2O_3 and TiC

are not detected in the sample but a small amount of Ti_xAl_y intermetallics (<1 vol.%) is present at the grain boundaries. EDXS analyses performed on lamellas displayed in Figure 44 show that the mean Ti/Al mole ratio is 2.96 which confirm the composition of the Ti_3AlC_2 MAX phase. Image analysis, performed using the image J software, gives a volume content of Ti_3AlC_2 higher than 99%. The density of as-synthesized Ti_3AlC_2 samples, measured from He pycnometry, is about 100%.

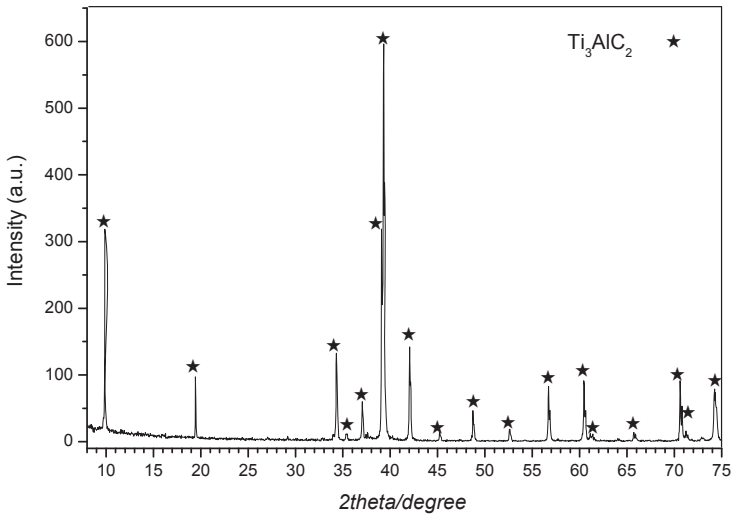

Figure 43: XRD pattern of Ti:Al:1.9TiC cold-compacted mixture sintered at 1450°C for 2h and 50MPa for 1h using HIPing process.

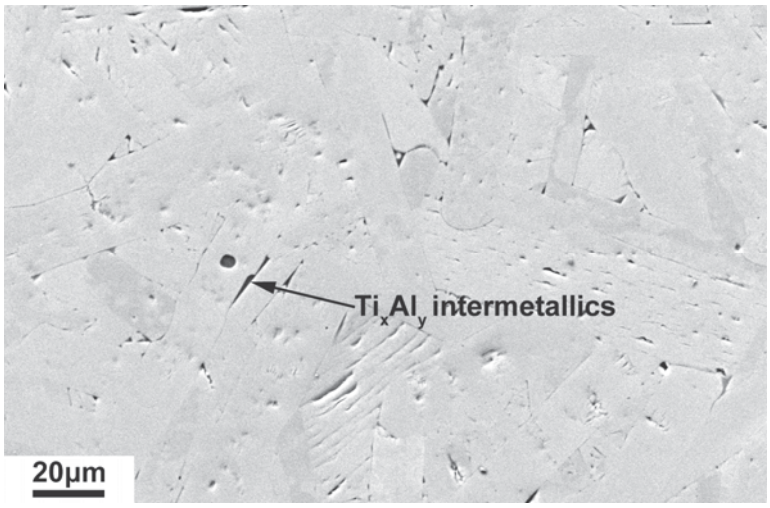

Figure 44: Back-scattered SEM micrograph of the Ti:Al:1.9TiC cold-compacted sample sintered at 1450°C for 2h and 50MPa for 1h using the HIPing process.

In summary, fully dense, nearly pure Ti_3AlC_2 sample is obtained by HIPing Ti:Al:1.9TiC powder mixture at 1450°C for 2h and 50 MPa for 1h. Ti_3AlC_2 grains have a lamellar shape, 60-100 µm in length and 10-40 µm in width. From an industrial point of view, it is worth

noting that, compared to the HIPing process used by Barsoum et al. for the preparation of predominately pure Ti_3AlC_2 dense sample[36], the HIPing cycle used in this study is optimized. Indeed, a lower pressure and a shorter time allow producing dense and highly pure Ti_3AlC_2 sample with comparable size.

IV-2. Mechanical properties of polycrystalline Ti_3AlC_2

IV-2.1. Elastic modulus and intrinsic hardness of polycrystalline Ti_3AlC_2 sample determined by nanoindentation tests

As described in Chapter II, a nanoindentation map with 8 loads (1, 2, 3, 6, 10, 15, 30, 250 mN) and a total of 177 indents was performed on the Ti_3AlC_2 sample. For the low loads (in the range 1-30mN), nanoindentations were performed on a single Ti_3AlC_2 lamella. Ti_3AlC_2 hardness and elastic modulus are plotted as a function of the indenter penetration depth in Figure 45.

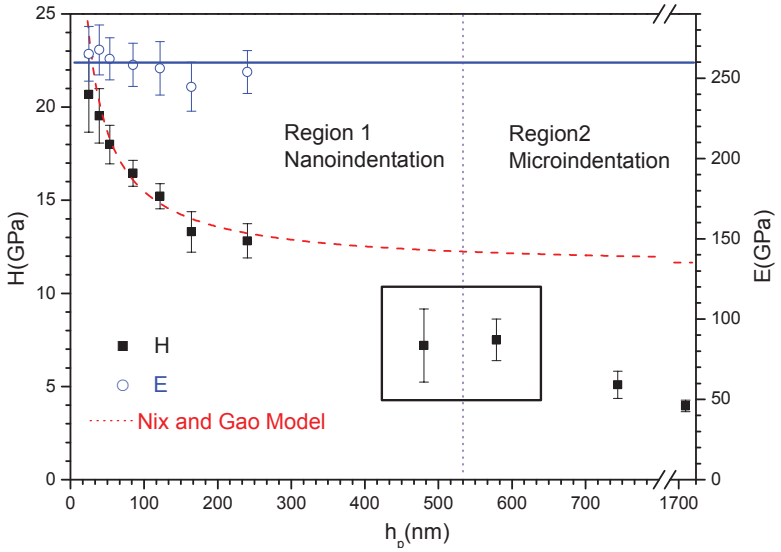

Figure 45: Hardness (squares) and elastic modulus (circles) of Ti_3AlC_2 as a function of the indenter penetration depth. Region 1: Hardness and elastic modulus values measured by nanoindentation tests. Red dot line is a fit with the function of the Nix and Gao model. Region 2: hardness values measured by microindentation tests.

From the nanoindentation tests performed in region 1, the Ti_3AlC_2 elastic modulus is 260±10GPa, which is lower than the one measured by RUS technique [32,36,46], but comparable with the one determined by nanoindention tests for Ti_3AlC_2 thin film (240GPa)[109]. Moreover, elastic modulus is nearly constant whatever the penetration depth. For the hardness, as

reported previously in Ti_3SiC_2[106] and Ti_3SnC_2 samples in previous chapter, an ISE is observed. This increase of the hardness value for the low penetration depth, as shown in the case of Ti_3SnC_2, is well fitted by the same function as the one proposed in the Nix and Gao model[169]. From this fit, one can deduce that the intrinsic hardness value of Ti_3AlC_2 is 11.4±0.7GPa. This value is lower than the one measured by nanoindentation on Ti_3AlC_2 thin films (14 GPa)[109]. The higher hardness value for such thin films may result from the Al_2O_3 substrate. Nevertheless, the value measured by nanoindentaion on bulk Ti_3AlC_2 samples is higher than the ones measured by microindentation tests (2.7-3.5GPa)[36,53].

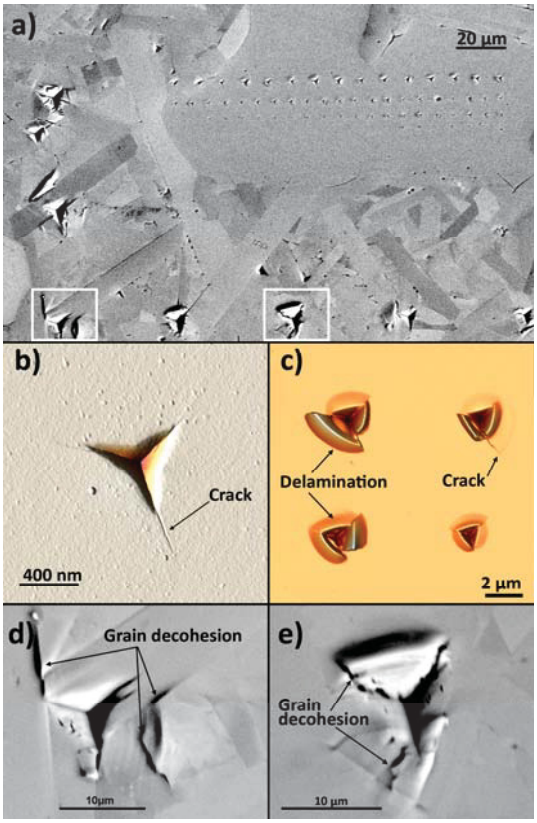

Figure 46: Array of indents performed on Ti_3AlC_2 sample. (a) indent array, (b) and (c) AFM topography images (3D top view) of low load indents, (d) and (e) enlarged micrographs of the 250 mN load indents localized in the white rectangle in (a).

The array of indent is shown in Figure 46(a). Around the indents obtained with low loads (in the range 1-30 mN), the deformation process leads to crack at the corner of the indent (Figure 46(b)) and to delamination (Figure 46(c)). However, around the indents obtained with the larger load (250mN), deformation process leads to quite different observations. As shown in Figures 46(d) and 46(e), grain decohesion is observed near the indents. Cracks are also evidenced at the corner of the indents. More importantly, several grains are involved in the

deformation process. Such kind of deformed microstructures are very similar to the ones observed from microindentation tests. Therefore, it is interesting to perform microindentation tests on the same sample in order to compare hardness values and deformation microstructures with the ones obtained from nanoindentation tests.

IV-2.2. Comparison of nano and microindentation tests

In region 2 of Figure 45, hardness values measured by microindentation tests are plotted as a function of the penetration depth. It can be seen that hardness values also decrease with increasing penetration depth. It is interesting to notice that nanoindentation and microindentation tests result in a single hardness value (about 7 GPa) provided that penetration depth of the indenter is in the same range (about 500 nm, see black rectangle in Figure 45).

In Figure 47, showing SEM observations of an indent obtained by microindentation test performed with a 1N load, several grains are involved in the deformation process. Hardness values measured by microindentation are in the range 4-7 GPa which is in correct agreement with previous microindentation tests for which hardness is in the 2.7-6 GPa range [36,53,57,113]. However, those values are very small compared to the intrinsic hardness value determined by nanoindentation tests (11.4±0.7GPa).

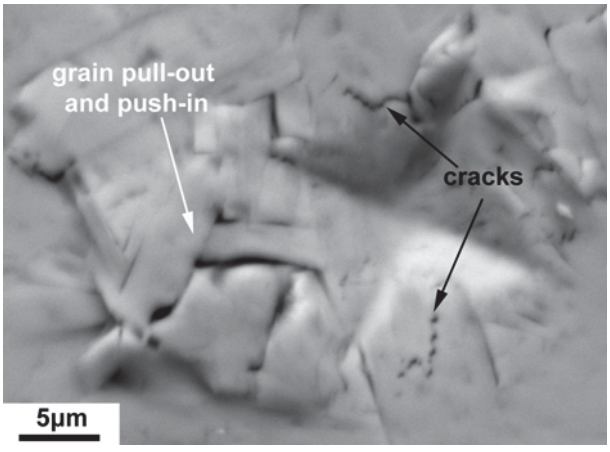

Figure 47: Indent obtained by microindentation with a 1N load. Grain pull-out and push-in as well as cracks are observed by SEM.

Indeed, for large load and whatever micro or nanoindentation is used, several grains are involved in the deformation process. Thus, grain boundaries and impurities affect the

measured hardness value which is underestimated. In this case, the measured hardness value thus gives the mean hardness of a bulk polycrystalline sample.

In summary, the elastic modulus of Ti_3AlC_2 deduced from nanoindentation is 260±10GPa which is lower than the one reported by Tzenov et al.[1]. The intrinsic hardness of Ti_3AlC_2 measured by nanoindentation, 11.4±0.7GPa, is higher than the hardness value determined by microindentation tests, 4-7GPa. It is demonstrated that MAX phases hardness values measured by microindentation are underestimated provided that grain boundaries and impurities are involved in the deformation.

IV-2.3. Kinking nonlinear elastic deformation of Ti_3AlC_2 at room temperature

IV-2.3.1. Cyclic compression tests

Typical stress-strain curves – progressively shifted to the right for clarity and corrected from the machine stiffness (see chapter II) – recorded at room temperature (RT) on the Ti_3AlC_2 sample are shown in Figure 48. Strain rate is 10^{-4} s^{-1}. At stress levels below 150 MPa (not shown in Figure 48), the response of the sample is linear elastic with a Young's modulus of about 280 MPa, which is in quite good agreement with the value that we get from nanoindentation (260 GPa). Hysteretic and fully reversible stress-strain loops are observed for stresses in the range 200-500 MPa, as it is the case for other MAX phases and for MAX phase solid solutions [4,5,40,128,131,136]. One can notice that, at 200MPa stress level, the hysteretic loop is small. However, larger hysteretic loops are observed with increasing stress.

Figure 49 shows compressive stress-strain loops recorded at 200MPa and 400MPa with three different strain rates (10^{-3}, 10^{-4} and 10^{-5} s^{-1}). Figure 49 allows demonstrating that the hysteretic, fully reversible strain-stress loops, do not depend on strain rate. Indeed, within the resolution of the measurement, these hysteretic fully reversible strain-stress loops are indistinguishable, at least in the 10^{-5}-10^{-3} s^{-1} strain rate range. These results are in good agreement with the ones obtained on Ti_3SiC_2 by Barsoum *et al*. [4,40] and Zhen *et al*.[131].

Finally, from the orange curve shown in Figure 48, one can observe that plastic deformation is unambiguous at 500MPa. Failure is observed at a 545MPa stress level and for a plastic deformation of about 0.6%. Such a result is in good agreement with the one reported

by Tzenov *et al.*[36] (560MPa, grain size about 20-30 µm in length and <10 µm in width), but different from the one given by Wang *et al.* [53] (764MPa, grain size about 20-50 µm in diameter and 5-8 µm in thickness) at RT. The grain size is likely not the only parameter at the origin of such a difference. The texture and porosity may play an important role in the measure of the stress level at failure.

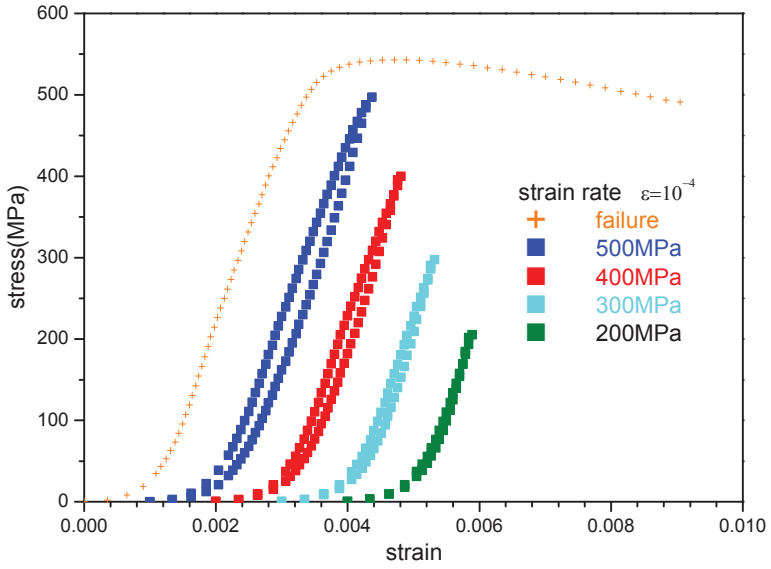

Figure 48: Typical stress-strain curves - progressively shifted to the right for clarity – recorded at 500, 400, 300, and 200MPa. Orange curve (cross symbols): stress-strain curve recorded up to failure.

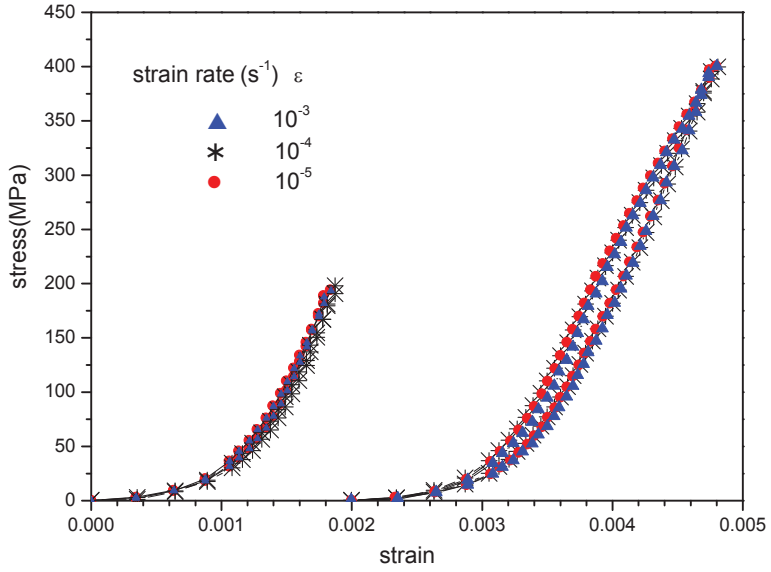

Figure 49: Compressive stress-strain loops recorded at 200MPa and 400MPa with three different strain rates (10^{-3}, 10^{-4} and 10^{-5} s^{-1}).

IV-2.3.2. Application of KNE model

The three parameters, stress (σ), non-linear strain (ε_{nl}), and dissipated energy (W_d), defined in the KNE model established by Barsoum *et al.* [4,5] (see I-4.3.3.), can be obtained from compressive stress-strain loops recorded on Ti_3AlC_2 samples. Indeed, ε_{nl} can be determined experimentally from Equation (1) and Figure 48 or calculated from Equation (11) of Chapter I.

$$\varepsilon_{nl} = \varepsilon_{tot} - \frac{\sigma}{E} \quad (1)$$

W_d is the gray surface area schematically shown in Figure 50.

The calculated parameters, stress (σ), non-linear strain (ε_{nl}), and dissipated energy (W_d), are listed in Table 15. Plots of ε_{nl} vs σ^2, W_d vs σ^2 and W_d vs ε_{nl} are shown in Figures 51(a), 51(b) and 51(c), respectively. Based on the KNE model established by Barsoum *et al.*[4,5], ε_{nl} and W_d should vary linearly with σ^2 and W_d should vary linearly with ε_{nl}. Indeed, one can notice that all plots exhibit a linear variation; the lowest correlation coefficient (R^2) value being larger than 0.987.

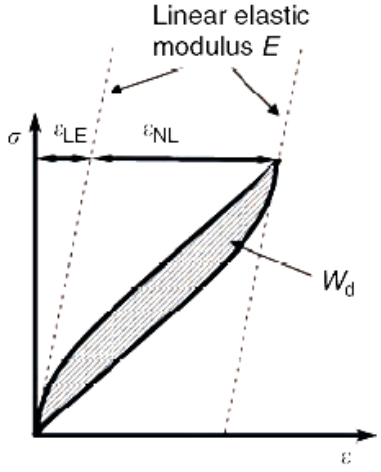

Figure 50 [5]: Typical stress-strain loop and definitions of nonlinear strain, ε_{NL}, and dissipated energy, W_d.

Thus, the slopes of the ε_{nl} vs σ^2 (m_1), W_d vs σ^2 (m_2) and W_d vs ε_{nl} (m_3) linear variations can be experimentally determined. These values are given in Table 15. Moreover, non-linear strain (ε_{nl}) values, determined from Equation (1) of KNE model, are listed for different stress values in Table 15. It is worth noting that, at low stress level (σ<250 MPa), experimental and calculated non-linear strains are a bit different. Such a result likely comes from the

measurement uncertainty. However, for high stress level (σ>250 MPa), the experimental and calculated non-linear strains are in good agreement.

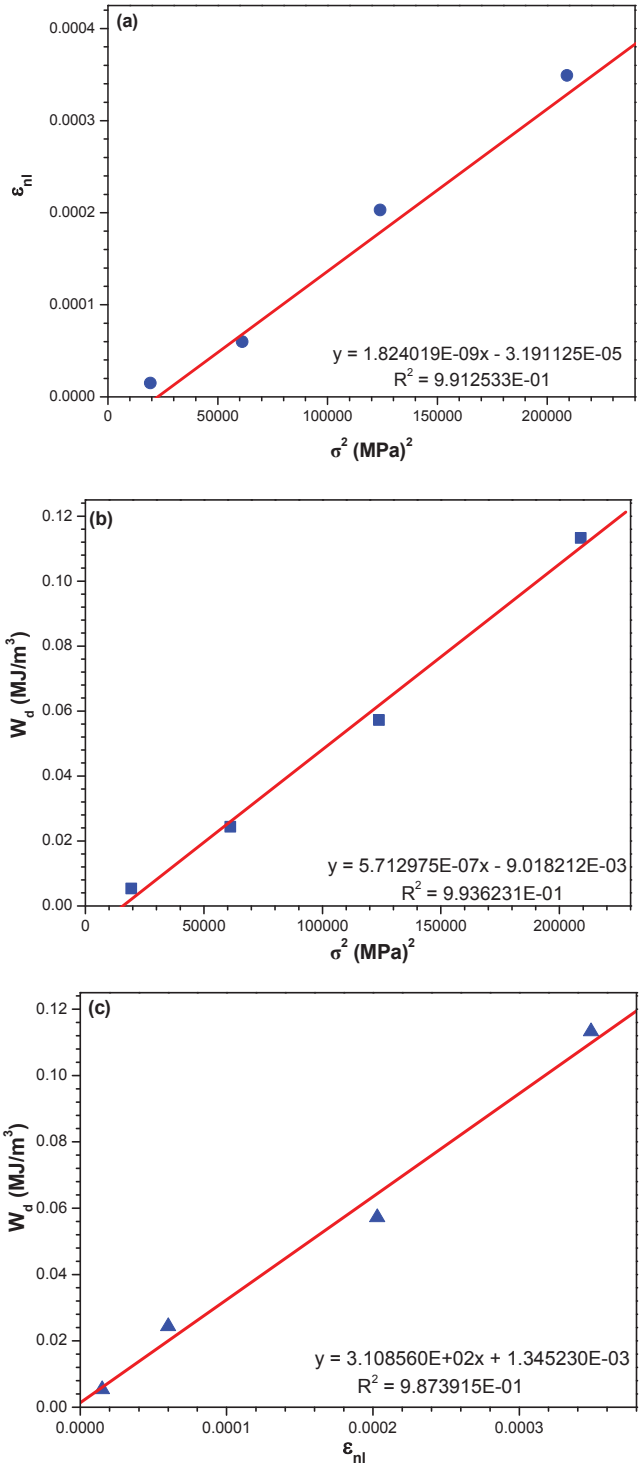

Figure 51: (a) ε_{nl} vs σ^2, (b) W_d vs σ^2, (c) W_d vs ε_{nl} plots determined from the stress-strain curves recorded on Ti_3AlC_2 sample.

The Ti_3AlC_2 physical parameters used in the KNE model are given in Table 16. It is worth noting, herein, that the elastic modulus of Ti_3AlC_2, E, determined from our nanoindentation

test, is smaller than the one used by Zhou *et al.*[136] and Barsoum *et al.*[5] (about 300 GPa). Thus, the shear modulus G is also smaller, since G=E/(2(1+ ν)). However, the other parameters, k_1, b, *w* and γ_c are the ones used by Zhou *et al.*[136]and Barsoum *et al.*[5]. Moreover, the threshold stress, σ_t, is directly calculated from the intercept of the W_d vs σ^2 straight line with the W_d axis. After σ_t determination, 2α can be calculated from Equation (7) of Chapter I.

sample	σ (MPa)	$\varepsilon_{nl\ exp}$	$\varepsilon_{nl\ cal}$	W_d (MJ/m^3)	m_1 (MPa)$^{-2}$	m_2 (MPa)$^{-1}$	$m_3=m_2/m_1$ (MPa)
Ti_3AlC_2	139	0.000015	0.000006	0.005360	1.824×10^{-9}	5.713×10^{-7}	313■ 311◈
	247	0.000060	0.000082	0.024378			
	352	0.000203	0.000198	0.057186			
	457	0.000349	0.000352	0.113298			

Table 15: Stress (σ), non-linear strain ($\varepsilon_{nl\ exp}$) and dissipated energy (W_d) extracted from compressive stress-strain curves shown in Figure 48. Slopes (m_1, m_2 and m_3, see text) of the different straight lines shown in Figure 51. $\varepsilon_{nl\ cal}$ is calculated from Equation (11) of KNE model in Chapter I, ■ m_2/m_1, ◈ m_3, slope of Figure 51(c).

Sample	E [a] (GPa)	G (GPa)	ν	k_1	b (Å)	*w* (Å)	M	γ_c (rad)	2α [b] (μm)	σ_t [c] (MPa)
Ti_3AlC_2	260	108.3	0.2	2	3	15	3	0.01	25	125

Table 16: Physical parameters of Ti_3AlC_2 used for calculations in the KNE model. [a] Obtained from nanoindentaion test; [b] Calculated from Equation (7) of Chapter I; [c] Calculated from W_d vs σ^2.

The kink band length 2α, which is supposed to be equal to the grain size along the *c* axis [5], is 25 μm. It is in compatible agreement with grain sizes observed by SEM in section IV-1.. Indeed, kink band length (2α=25 μm) has to be compared to the lamella width (10-40 μm) since Electron Back-Scattered Diffraction (P. Villechaise, PPRIME Institute) allows demonstrating that lamellas are observed if basal planes lie almost perpendicular to the observed surface. Such a 2α value (25 μm) is larger than the one deduced by Zhou *et al.*[136] (10 μm) using the KNE model. Thus, for comparison, one can define the Zhou's samples as fine-grained Ti_3AlC_2 samples, and our samples, as coarse-grained Ti_3AlC_2 samples.

In the KNE model, IKBs nucleation occurs at lower stresses in larger grains. Threshold stress determined in our experiments (125 MPa) and threshold stress determined in the

experiments performed by Zhou *et al.*[136] (205 MPa) on Ti_3AlC_2 are in compatible agreement with such a statement.

The dissipated energy (W_d) is an increasing function of grain size (see Equation (12) of KNE model in Chapter I). Indeed, for similar stress level, the dissipated energy calculated from our experiments is larger than the one obtained by Zhou *et al.*[136] on fine-grained Ti_3AlC_2 samples. Moreover, our values are of the same order as the ones obtained on coarse-grained Ti_3SiC_2 samples [5,40].

	σ (MPa)	Ω/b (MPa)	N_k (m^{-3})	$(1/N_k)^{1/3}$ (μm)	$2\beta_{av.c}$ (μm)	$2\beta_{av}$ (μm)	ρ_{rev} (m^{-2})
Ti_3AlC_2	139	52★ 52□	5.9×10^{14}	11	0.9	1	1.5×10^{12}
	247					1.7	2.7×10^{12}
	352					2.4	3.8×10^{12}
	457					3.2	4.9×10^{12}

Table 17: List of parameters calculated from KNE model described in Chapter I. N_k calculated from Equation (11) of Chapter I, $2\beta_{av.c}$ and $2\beta_{av}$ calculated from Equation (10) of Chapter I, σ listed in Table 15, ρ_{rev} calculated from Equation (14) of Chapter I, ★ and □ calculated from Equations (12) and (13) of Chapter I, respectively.

From Equation (12) of Chapter I and plots of ε_{nl} vs σ^2 and W_d vs σ^2, or from Equation (13) of Chapter I and plot of W_d vs ε_{nl}, the Ω/b value (which is equal to the Critical Resolved Shear Stress (CRSS) [130]) can be determined. The Ω/b value deduced from our experiments is 52MPa, whatever is the determination method (See Table 17). As both expressions give the same Ω/b value, one can conclude that the same micromechanism is responsible for the parabolic dependence of non-linear strain (ε_{nl}) and dissipated energy (W_d) on stress (σ). The determined Ω/b value (52 MPa) is moreover in reasonable agreement with the only reported value of a CRSS in a MAX phase, i.e.: 36 MPa for Ti_3SiC_2[27]. However, our Ω/b value (52 MPa) seems to be large compared to the Ω/b values reported previously by Barsoum *et al.* for fine and coarse-grained Ti_3SiC_2, 39 and 9.3 MPa, respectively[5]. Indeed, it has been shown that Ω/b, a measure of "yield", essentially follows a Hall-Petch effect[170]. Nevertheless, it is important to point out that, the elastic modulus that we use (260 GPa) is smaller than the one used by Zhou *et al.* (298 GPa). As a result, for a given stress level, non linear strain is

smaller in our calculation than the one determined in the fine-grained sample studied by Zhou *et al.*[136]. As a consequence, the slope of the straight lines shown in Figure 51(c) should decrease by using a larger elastic modulus. Hence, the Ω/b value would be smaller.

The IKBs number per unit volume (N_k) and the reversible dislocation density (ρ_{rev}) have reasonable values given the applied stress. These values are moreover comparable to the ones obtained by Barsoum *et al.* in coarse-grained Ti_3SiC_2 sample [4,40]. With increasing stress, IKBs out of the basal plane (β_{av}) grow from about $2\beta_{av.c}$=0.9 to $2\beta_{av}$=3.2 μm and the reversible dislocation density (ρ_{rev}) increases from about 1.5×10^{12} to 4.9×10^{12} m^{-2}. Compared to fine-grained Ti_3AlC_2 sample deformed at comparable stress level[136], IKBs are larger (3.2 μm compared to 1 μm) and reversible dislocation density is smaller ($4.9\times10^{+12}$ m^{-2} compared to $4.3\times10^{+13}$ m^{-2}) in our coarse-grained Ti_3AlC_2 sample. These results are nevertheless comparable to the ones obtained on coarse-grained Ti_3SiC_2 sample[4,40].

IV-2.3.3. Microstructural characterization of the sample deformed up to failure

Figure 52(a) shows a SEM image of the Ti_3AlC_2 sample deformed up to failure (see stress-strain curve in Figure 48). It can be observed that the angle between main fatal crack propagation path (at the bottom in the right corner of Figure 52(a)) and compression axis is roughly 34°. Another crack (at the top in the right corner of Figure 52(a)), appearing at about 45° from the compression axis, is also observed. The typical deformation microstructures near the fatal crack and fracture surface are displayed in Figures 52(b) and 52(c), respectively. One can notice that different energy dissipation mechanisms are observed which is not surprising for MAX phase materials [1,27,36,118]. Indeed, grain bending, grain pull-out and push-in (red arrows), transgranular fracture (black arrows), grain decohesion and crack deflection around the grain boundaries (white arrows), kink bands and delaminations (blue arrows) are observed on the surface near the fatal cracks. It is worth noting that for some individual grains, for example the crack features marked with black arrows in Figure 52 (b), lamellas are exhibiting brittle nature. On the other hand, some other lamellas are bending and forming kink bands (red and blue arrows and the inset in the left corner). As shown in Figures 52 (c) to (e), a large number of kink bands and delaminations are observed in the fracture surface of Ti_3AlC_2 sample. As schematically shown in Figure 52 (d), kink band formation is explained by the

regular glide of dislocations. Such a kind of kink bands can be continuously formed in one lamella (Figure 52 (e)).

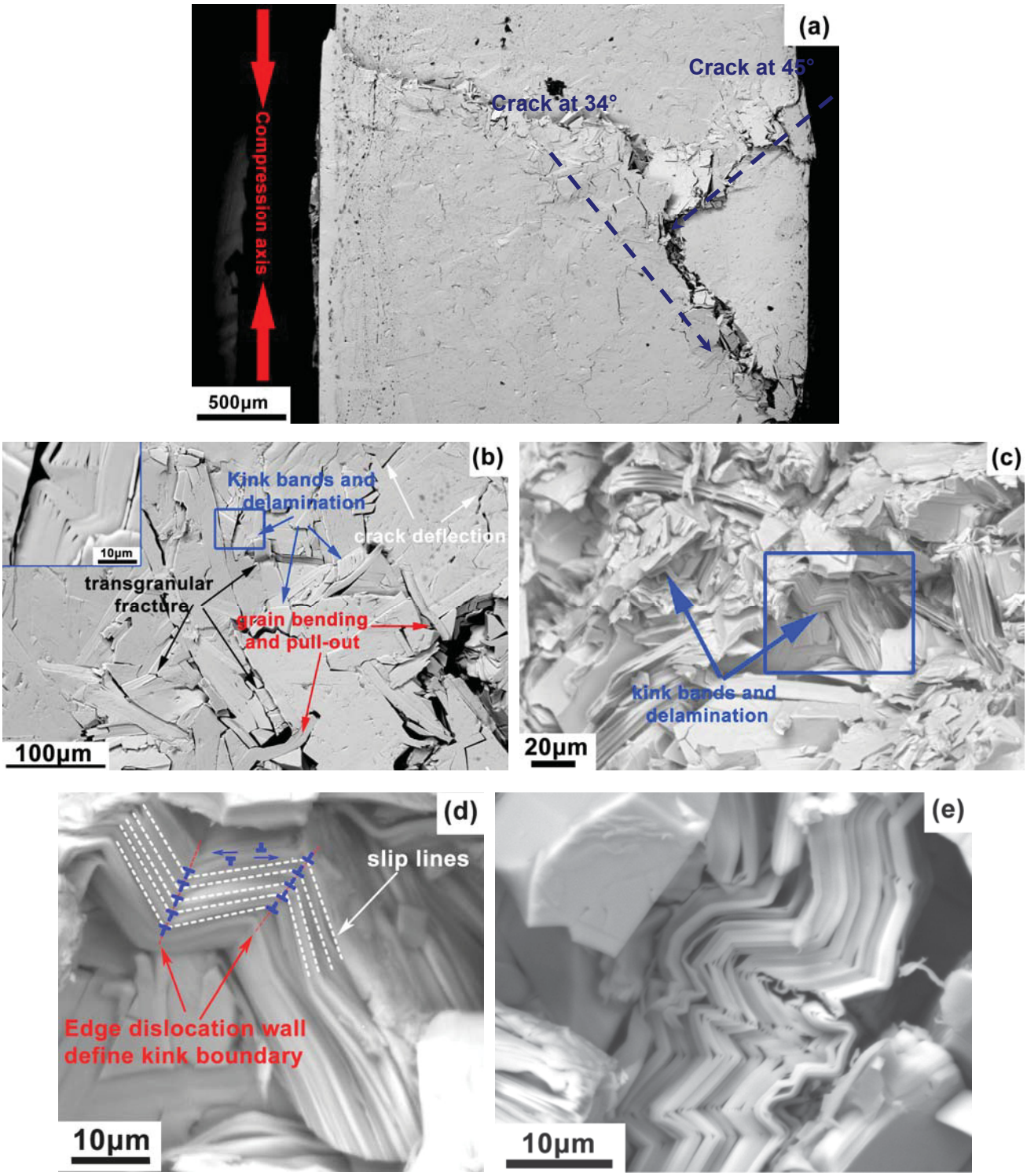

Figure 52: SEM images of the microstructure of Ti_3AlC_2 sample deformed up to failure at RT. (a) fatal cracks after compression, (b) deformation microstructures near the fatal cracks, the inset at the left corner is an enlarged image of the blue rectangle, (c) the fracture surface after deformation, (d) enlarged image of the blue rectangle in (c), kink bands with scheme of kink boundary and dislocation walls, (e) continuous formation of kink band.

After failure, it is noticed that Ti_3AlC_2 specimen fractured in a shear mode (cf Figure 52(a)). The fracture surface makes an angle α_c=34° with the compression axis ; such a value deviates from the maximum shear stress plane (45°) but it is in reasonable agreement with results obtained by Zhang *et al.*[171] for Ti_3SiC_2 (α_c=23° at RT and α_c =30° at 900°C) and Bao *et al.*[172] for Ti_3AlC_2 (α_c=26 and 38° at RT). This macro-scale shear fracture behavior has been widely observed in some brittle materials, such as polycrystalline ice [173-179] and bulk metallic glasses (BMG) [180-187]. Meanwhile, it is noticed that the shearing does not penetrate through the whole Ti_3AlC_2 sample at RT but it changes its path. Observed damages are strongly localized near the main fatal crack. Deformation and damage at RT mainly consist in intergranular and transgranular cracks, but kink bands and delamination are also frequently observed. Nevertheless, there is little contribution to plasticity during compressive deformation at RT. This is consistent with previous reports related to compression tests on MAX phases[30,114,188]. As the shear fracture surface deviates from the maximum shear stress plane, as in polycrystalline ice and in BMG, the macro-shear fracture mechanisms for the brittle Ti_3AlC_2 material, should, to some extent, be quite similar and should be described using a Mohr-Coulomb criterion [186]:

$$\tau_n + \mu \cdot \sigma_n \geq \tau_c \quad (2)$$

where,

μ is a constant for a brittle material,

τ_c is the critical shear fracture stress,

τ_n and σ_n are shear stress and normal stress respectively on any shear plane.

$$\sigma_n = -\sigma \cdot \sin^2\alpha \quad (3)$$

$$\tau_n = \sigma \cdot \sin\alpha \cdot \cos\alpha \quad (4)$$

where,

σ is the applied compression stress,

α is the angle between the compression axis and the considered shear plane.

Substituting τ_n and σ_n into Eq (3) yields the critical fracture condition for Ti_3AlC_2 as

$$\sigma_f = \tau_c / [\sin\alpha \cdot (\cos\alpha - \mu \cdot \sin\alpha)] \quad (5)$$

where σ_f is the applied compressive stress at shear fracture.

A specimen must fracture along a favourable shear plane at the minimum fracture stress σ_f, which corresponds to an angle α_c can thus be extracted from:

$$d(1/\sigma_f)/d\alpha = 1/2\tau_c \cdot [\cos(2\alpha_c) - \mu.\sin(2\alpha_c)] \quad (6)$$

therefore, the critical shear fracture condition can be expressed as

$$\mu = \cot g 2\alpha_c \quad (7)$$

Furthermore, from Eq. (5) to (8), τ_c can be calculated by the following equation:

$$\tau_c = \sigma_f \cdot \sin\alpha_c \cdot (\cos\alpha_c - \mu.\sin\alpha_c) \quad (8)$$

The macro-shear fracture stress, τ_c, represents the average resistance to break a polycrystalline Ti_3AlC_2 sample through intergranular cracking and fracture of grains. According to our results, μ=0.40 and τ_c =185 MPa. It means that the Ti_3AlC_2 sample can be sheared to fracture by a constant pure shear stress of about 185 MPa. Such a value is obviously higher than the CRSS of 36 MPa on basal plane of coarse-grained (1-2 mm) Ti_3SiC_2 specimens[27]; CRSS being the shear stress needed to initiate slip in the basal plane of a single grain. The measured macro-shear fracture stress is very large compared to the CRSS due to the smaller grain size of our Ti_3AlC_2 sample. Our τ_c value is moreover in the same range as the one (195 MPa) determined by Zhang *et al*.[171] in a Ti_3SiC_2 sample whose grain size is in the range 20-50 μm. It is well-known that grain size and grain size distribution can strongly affect the orientation of the shear fracture plane in brittle polycrystalline materials.

In summary, the coarse-grained Ti_3AlC_2 sample tested here can be classified as KNE solids. The cyclic compressive stress-strain loops are hysteretic and fully spontaneously reversible. Based on KNE model, the parameters obtained here can make great contributions for MAX phase KNE solids. Multiply energy dissipation mechanisms such as formation of kink bands, delamination, crack deflection, grain buckling, grain pull-out and push-in etc are observed. At failure, Ti_3AlC_2 specimen fractured in a shear mode. The fracture surface of Ti_3AlC_2 samples makes an angle α_c =34° with the compression axis and Ti_3AlC_2 can be sheared to fracture by a constant pure shear stress of about 185 MPa.

IV-2.4 Plastic deformation of Ti_3AlC_2 at room temperature under confining gas pressure

IV-2.4.1. Stress-strain curve

After removing the mechanical contribution of Al jacket, the engineering compressive stress-strain curve of Ti_3AlC_2 sample obtained at RT in the Paterson apparatus is shown in Figure 53. The compression test has been performed at a low strain rate of 5×10^{-5} s^{-1} with a confining pressure of 350MPa.The presented curve exhibits some noise that is due to the very low strain rate used.

From the stress-strain curve shown in Figure 53, one can notice that large plastic strain is achieved under the confining pressure. The curve presents typical features with a linear elastic regime followed by a hardening regime leading to the presence of a stress peak followed by a softening leading to a zero hardening regime. As discussed in IV-2.3-1, without confining pressure, only 0.6% plastic strain could be reached followed by sudden brittle rupture at a stress of 545MPa. It is a typical feature for samples deformed at RT, where massive cracking is usually observed when trying to reach large strain [1,171]. Here, under confining pressure, the plastic strain attains almost 6% without reaching the sample ruin. Such a result is due to the effect of the imposed hydrostatic confining pressure that artificially closes cracks to the favor of plasticity during uniaxial compression. Without this pressure, all the samples would exhibit progressive cracking, if not sudden brittle rupture, at stresses lower that the ones reached here.

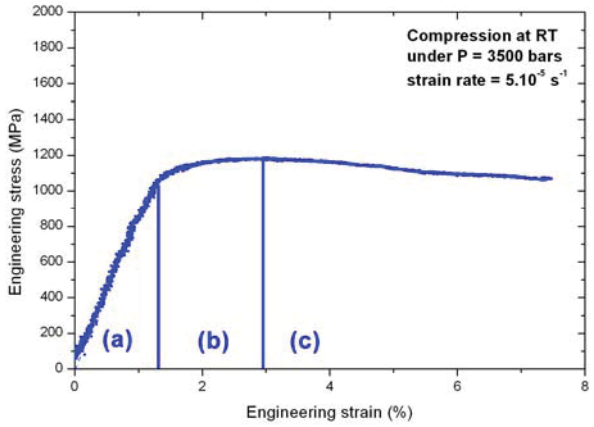

Figure 53: The engineering stress-strain curve obtained from the compression of polycrystalline Ti_3AlC_2 sample at RT in the Paterson apparatus exhibiting (a) an elastic regime, (b) a strain hardening regime and (c) a softening regime.

The maximum RT compressive stress for the Ti_3AlC_2 sample tested here is 1180MPa, which is much higher than the value measured in IV-2.3.1. and the ones reported by Tzenov *et al.* (560MPa)[36] and Wang *et al.* (764MPa)[53]. It should be pointed out that room pressure

compression tests are associated to early brittle failure predominantly characterized by intergranular cracking. Therefore, it is meaningless to compare the literature data with the present results where the confining pressure suppresses the brittle failure at RT to the profit of plasticity.

IV-2.4.2. Characterization of deformed Ti_3AlC_2 microstructures by SEM observation

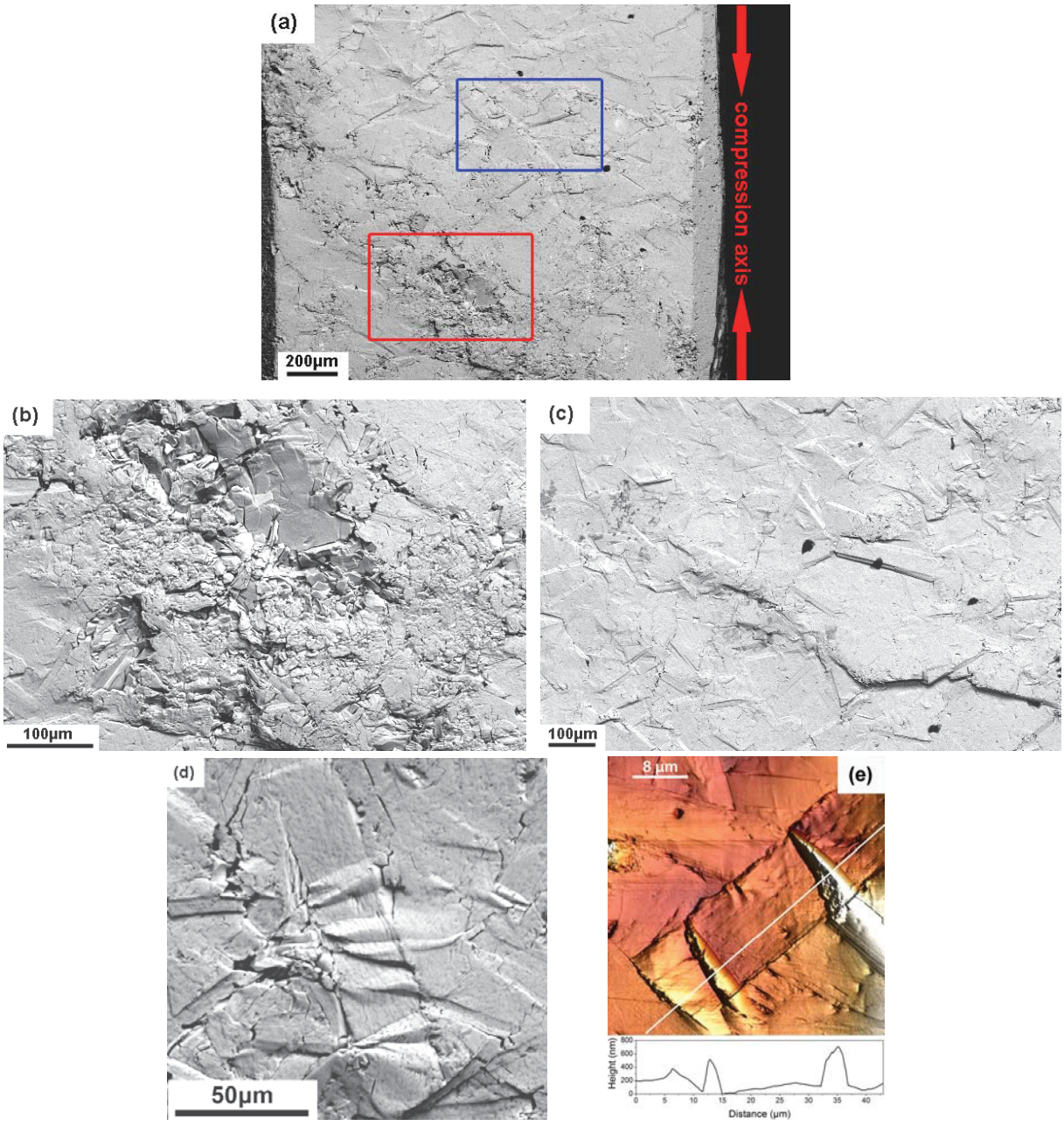

Figure 54: (a) General features of deformed Ti_3AlC_2 sample using the Paterson apparatus, the most damage area is marked with the red rectangle; (b) enlarged SEM image of the most damage area, (c) enlarged SEM image of the less damaged area in the blue rectangle in (a), (d) a series of kink bands in one lamellar grain; (e) AFM image of kink bands.

Figure 54(a) shows the external features of the Ti_3AlC_2 sample after the deformation in the Paterson apparatus. One can notice that the whole Ti_3AlC_2 sample is plastically deformed, but some areas are more damaged than others: the "most" damaged area is in the red rectangle. Various deformation mechanisms can be observed in the deformed Ti_3AlC_2 sample. As shown in Figure 54(b), corresponding to the "most" damaged area, Ti_3AlC_2 exhibits brittle fracture. Indeed, during the deformation process, the crack propagation breaks the individual grains or leads to grain boundary delamination. However, in the "less damaged" areas (the blue rectangle in Figure 54(a)), grain pull-out and push-in are observed as shown in Figure 54(c). Moreover, crack propagation is mainly along the grain boundaries. Kink bands are also observed: indeed, in Figures 54(d) and (e), some lamellar grains are severely deformed by a series of kink bands.

IV-2.4.3. Characterization of deformed Ti_3AlC_2 microstructures by TEM observation

Figures 55 and 56 show the deformed Ti_3AlC_2 microstructure analyzed by TEM using two beams technique. First of all, the deformed Ti_3AlC_2 microstructure is characterized by high density of dislocations. All dislocations lie in the basal plane.

Figure 55 shows a grain where dislocations present characteristic organization in walls or piles-up. Different configurations are also observed like in Figures 56(a) and (b) showing a grain where the basal plane is parallel to or near the thin foil that is cut at 45^o from the compression axis. In this grain, some very long isolated dislocations are observed without any obvious organization. Dislocation density may become very high (see Figure 56(b)) and form a dense dislocation network with dislocation interactions. However, the very large density does not allow determining the exact nature of the dislocation interactions.

Plastic deformation in MAX phases is generally attributed to dislocation movement in the basal plane organized in stable configuration like pile-ups or walls[28,118,122,123]. Our observations confirm that, in Ti_3AlC_2, plastic deformation at RT is associated to a high dislocation density, dislocations being confined in the basal plane. According to the orientation of the grain relative to the compression axis, dislocations are arranged, or not, in specific configurations. When the *ab* plane is in a favorable orientation, that is at 45° from the

compression axis, no specific orientation of the dislocations is observed. In some grains with different orientations, dislocations exhibit specific configuration: piles-up or walls. Since shear bands and kink bands have been observed in our deformed Ti_3AlC_2 sample by SEM and AFM, the formation of the dislocation walls probably obeys the same mechanisms as the one of the Ti_3SiC_2 deformed sample reported by Barsoum *et al.*[28]. If the dislocation pile-ups probably play a role in the deformation by shear, when the orientation is favorable, plastic deformation is due to dislocation movement without implying piles-up or walls.

In addition, in the deformed Ti_3AlC_2, areas with very high dislocation density are observed. As the dislocations are expected to glide in the basal plane only at low temperature, such entanglement may lead to hardening of soft grains. These observations questioned the role of such hardening in the polycrystalline MAX phase during macroscopic deformation tests; such hardening has to be deeper analyzed.

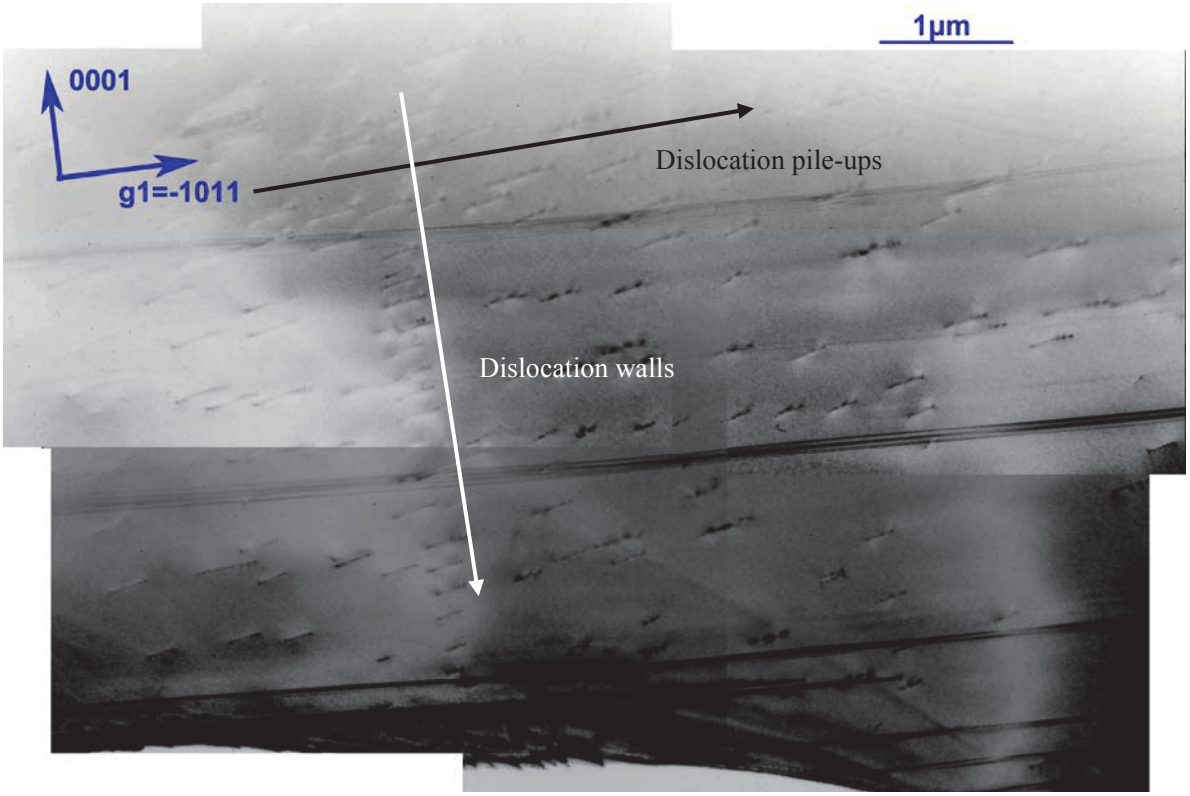

Figure 55: TEM observations of dislocation walls and pile-ups in the deformed Ti_3AlC_2 at room temperature under confining gas pressure.

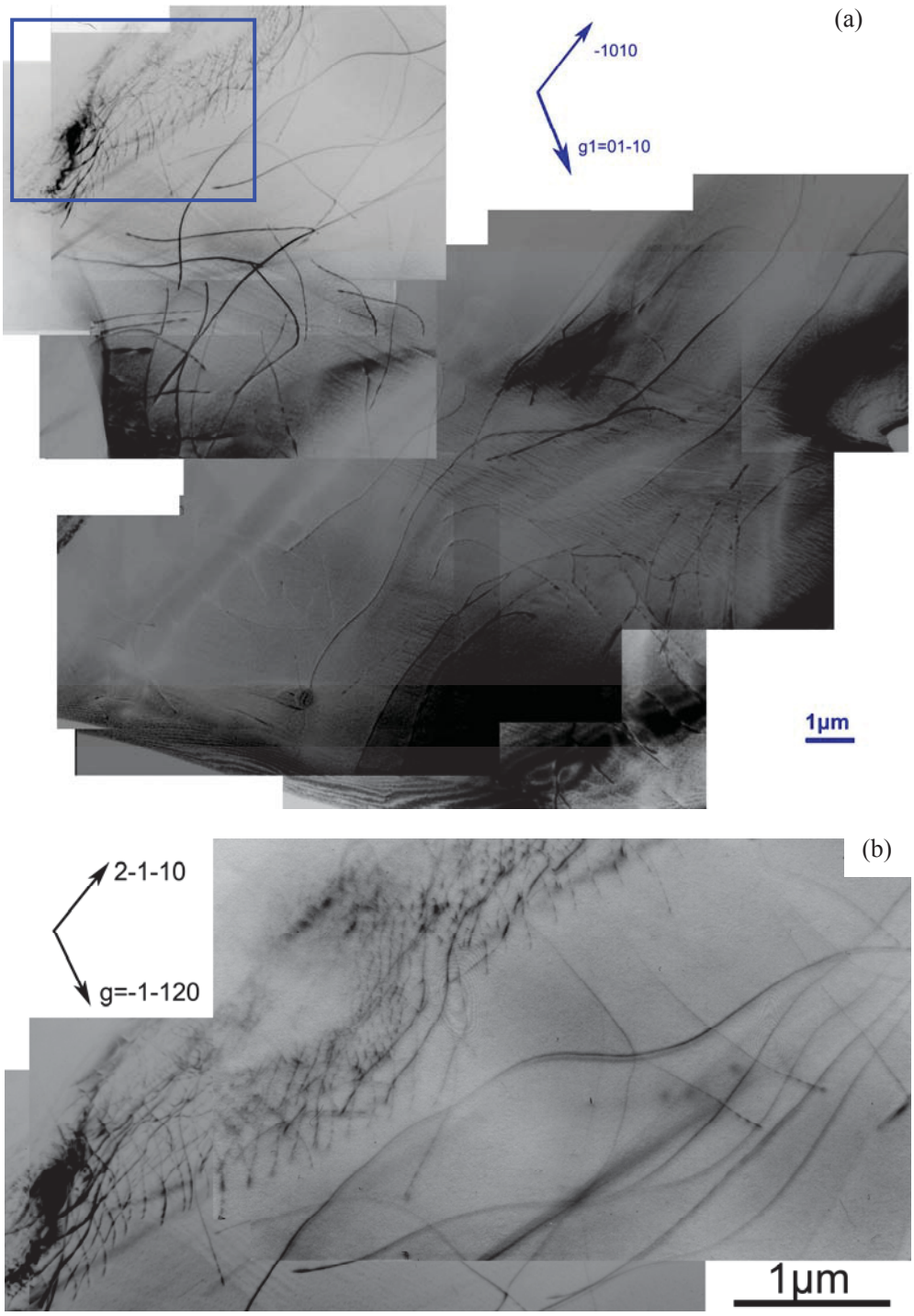

Figure 56: (a):TEM observations of high density dislocations without any orientations in the deformed Ti_3AlC_2 at room temperature under confining gas pressure. (b) Enlarged image of extremely high density of dislocations in the blue rectangle of (a)

In summary, the microstructures of Ti_3AlC_2 deformed samples were investigated by SEM and TEM observations. From SEM observations of the sample surface, a combination of deformation mechanisms such as intra-granular fracture, delamination of individual grains, grain pull-out, grain push-in, and grain kinking are evidenced. By TEM observations, high

density of dislocations such as, dislocation walls, dislocation pile-ups and dislocation networks etc, were observed in the deformed sample; these dislocations lying in the basal plane. This high density of dislocations likely plays an important role in the deformation process. It probably results in grain hardening whose influence on the macroscopic deformation has to be deeper analyzed.

IV-3. Conclusions

In this chapter, fully dense, nearly pure Ti_3AlC_2 sample were prepared by a optimized HIPing process, with shorter time and lower pressure compared to the one used by Barsoum *et al.*[36]. As-synthesized Ti_3AlC_2 samples owned large grains: about 60-100 μm in length and 10-40 μm in width.

Nanoindentation tests were used to measure the elastic modulus and intrinsic hardness of Ti_3AlC_2. The elastic modulus is 260±10GPa whatever is the penetration depth. Ti_3AlC_2 hardness value measured by nanoindentation is 11.4±0.7GPa. This value can be considered as Ti_3AlC_2 intrinsic hardness since deformation process is recorded at the single crystal level. It has been shown that hardness value measured by microindentation tests is underestimated as several grains are involved in the deformation process.

Compressive cyclic stress-strain curves allow testing the KNE deformation of Ti_3AlC_2 at RT. Results demonstrate that Ti_3AlC_2 is a member of KNE solids. Based on KNE model, the parameters obtained for our coarse-grained Ti_3AlC_2 sample can be added to previous contributions on MAX phase KNE solids. Different energy dissipation mechanisms such as formation of kink bands, delamination, crack deflection, grain buckling, grain pull-out and push-in *etc* are observed in the deformed Ti_3AlC_2 samples. At failure, Ti_3AlC_2 specimen fractured in a shear mode. The fracture surface of Ti_3AlC_2 sample made an angle α_c=34° with the compression axis and Ti_3AlC_2 sample can be sheared to fracture by a constant pure shear stress of about 185 MPa.

Ti_3AlC_2 can be plastically deformed at RT in a Paterson machine using a confining gas pressure. The stress-strain curve of Ti_3AlC_2 obtained from the Paterson machine exhibit three

regimes: 1) elastic regime, 2) hardening regime and 3) softening regime. Plastic strain of Ti_3AlC_2 samples deformed in the Paterson machine can reach values as large as 6% with a maximum stress of 1180MPa (compared to about 0.6% and 545 MPa for stress-strain curves recorded at RT without confining gas pressure). Microstructures of Ti_3AlC_2 sample deformed in the Paterson machine were investigated by SEM and TEM observations. With SEM, a combination of deformation mechanisms such as intergranular fracture, delamination of individual grains, grain pull-out, grain push-in and grain buckling can be observed during the deformation process. According to TEM observation, high density of dislocations such as dislocation networks, dislocations pile-ups and walls are observed. This high density of dislocations plays an important role in the plastic deformation of Ti_3AlC_2. Dislocation network should contribute to grain hardening whose influence has to be deeper analyzed.

Chapter V

Synthesis, Microstructral Characterization and Mechanical Properties of $Ti_3Al_xSn_{(1-x)}C_2$ Solid Solutions

V-1. Synthesis and microstructural characterization of $Ti_3Al_xSn_{(1-x)}C_2$ solid solutions[189]

V-1.1. Synthesis of $Ti_3Al_xSn_{(1-x)}C_2$ solid solutions

As demonstrated in section III-2.4., using Al as additive in the 3Ti:Sn:2C reactant powder mixture, Al atoms can substitute Sn atoms in the Ti_3SnC_2 structure and thus form a $Ti_3Al_xSn_{(1-x)}C_2$ MAX phase solid solution. Such a result is of main importance as it will allow investigating the mechanical property modifications in the $Ti_3Al_xSn_{(1-x)}C_2$ solid solutions as a function of x. Different Ti:Sn:Al:C, Ti:Sn:Al:TiC or $TiC_{0.66}$:Sn:Al ratios were selected in order to produce different $Ti_3Al_xSn_{(1-x)}C_2$ solid solutions. It is well-known that some A element is lost during powder metallurgy processing (Hot Isostatic Pressing, Hot Pressing or reactive sintering) of the reactant mixture[2,3,36,52,54,57,102]; as a consequence either (Ti+C) sub-stoechiometry or (Sn+Al) over-stoechiometry were used in this study. By using these different reactant mixtures, our goal is to synthesize a large set of $Ti_3Al_xSn_{(1-x)}C_2$ solid solutions (i.e.: with different x values), but not to investigate the reaction mechanisms.

Table 18 summarizes the initial reactant powder mixtures and HIP conditions used to synthesize $Ti_3Al_xSn_{(1-x)}C_2$ solid solutions.

Initial reactant mixture	HIP conditions	$Ti_3Al_xSn_{(1-x)}C_2$ lattice parameters	Position of Ti atoms Rietveld refinement	Phase content (vol %) Rietveld refinement	x value EDXS
3Ti + Sn + 2C + 0.6 Fe	1150°C-10h 50MPa-10h Ar	*a* = 3.1366 Å *c* = 18.650 Å	Z_{TiII} = 0.1197	80.5 % of 312 16.2 % of TiC 3.3 % of impurities	Sample a 0
3Ti + 0.8Sn + 0.3Al + 2C	1200°C-4h 50MPa-3h Ar	*a* = 3.1227 Å *c* = 18.613 Å	Z_{TiII} = 0.1297	57.6 % of 312 33.7 % of 211 8.7 % of TiC	Sample b 0.25
3Ti + 0.6Sn + 0.6Al + 2C	1200°C-2h 50MPa-1h Ar	*a* = 3.1052 Å *c* = 18.604 Å	Z_{TiII} = 0.1297	97 % of 312 3 % of 211	Sample c 0.38
$2.8TiC_{0.66}$ + 0.8Sn + 0.4Al	1200°C-4h 100MPa-90min Ar	*a* = 3.1114 Å *c* = 18.598 Å	Z_{TiII} = 0.1267	41.8 % of 312 43.5 % of 211 14.7 % of TiC	Sample d 0.40
1.8TiC + 0.6Sn + 0.6Al + Ti	1500°C-8h 50MPa-7h Ar	*a* = 3.1053 Å *c* = 18.579 Å	Z_{TiII} = 0.1317	96 % of 312 3 % of 211 1 % of Sn	Sample e 0.50
1.8TiC + 0.2Sn + Al + Ti	1450°C-2h 50MPa-1h Ar	*a* = 3.0891 Å *c* = 18.603 Å	Z_{TiII} = 0.1315	98 % of 312 2 % of impurities	Sample f 0.80
1.9TiC + Al + Ti	1450°C-2h 50MPa-1h Ar	*a* = 3.0779 Å *c* = 18.579 Å	Z_{TiII} = 0.1326	100% of 312	Sample g 1

Table 18: Initial reactant mixture and HIP conditions, lattice parameters, position of Ti atoms, composition and Al content (x) of the different $Ti_3Al_xSn_{(1-x)}C_2$ solid solutions.

V-1.2. Microstructural characterization of $Ti_3Al_xSn_{(1-x)}C_2$ solid solutions

V-1.2.1. SEM observations and chemical composition by EDXS

Figure 57 shows scanning electron micrographs obtained, in back-scattered mode, on samples (b) (Figure 57(a)), (c) (Figure 57(b)) (e) (Figure 57(c)) and (f) (Figure 57(d)) (see Table 18 which gives the relationship between sample name and initial reactant mixtures). In Figures 57(a) and 57(b), corresponding to the samples synthesized from (3Ti + 0.8Sn + 0.3Al + 2C) and ($2.8TiC_{0.66}$ + 0.8Sn + 0.4Al) reactant mixtures respectively, $Ti_3Al_xSn_{(1-x)}C_2$ (grey) phase always appears in between $Ti_2Al_xSn_{(1-x)}C$ (light grey) and TiC (dark grey) phases. Such a result strongly suggests that the 211 and TiC phases react to form the 312 solid solution[65]. SEM results demonstrate that TiC, $Ti_2Al_xSn_{(1-x)}C$ and $Ti_3Al_xSn_{(1-x)}C_2$ are prone to co-exist. Such a feature is not surprising since close structural relationships between Ti_3AlC_2, Ti_2AlC and TiC[190]; Ti_3SiC_2, Ti_5Si_3 and TiC[191] and Ti_2AlN and TiN[192] have been demonstrated by using HRTEM and Selected-Area Electron Diffraction (SAED). Nevertheless, it has been shown that, depending on the composition of the reactant mixture, the reaction mechanisms of Ti_3AlC_2 formation are different [54,57,69,190]. In Figure 57(c) and (d), related to the samples synthesized from (1.8TiC + 0.6Sn + 0.6Al + Ti) and (1.8TiC + 0.2Sn + Al + Ti) reactant mixtures respectively, MAX phase lamellas are obvious. In the sample (e), the EDXS analysis showns that the dark grey area is $Ti_3Al_{0.5}Sn_{0.5}C_2$ and light grey area is the corresponding to the 211 solid solution, $Ti_2Al_{0.5}Sn_{0.5}C$. Futhermore, some Al_2O_3 (black points) and Sn (white points) are also detected in this solid solution. However, in the sample (f) , the BSC image has less contrasts. The lamellas have a dimension in the range 10-80 µm in length and 2-15 µm in width. In addition, it is worth noting that some smaller MAX phase lamellas and Ti_xAl_y intermetallics are also detected in the grain boundaries. From $\frac{Ti}{Al+Sn} = 3.01$ and $\frac{Al}{Sn} = 3.94$ mean mole ratios determined by EDXS on different lamellas, one can deduce that the chemical composition of the solid solution is $Ti_3Al_{0.8}Sn_{0.2}C_2$.

Table 18 lists the x value from EDXS analyses for the different $Ti_3Al_xSn_{(1-x)}C_2$ solid solutions. In such a context, our experiments, whose goal consists in the synthesis of a large set of different $Ti_3Al_xSn_{(1-x)}C_2$ solid solutions, do not allow to get the reaction mechanisms of $Ti_3Al_xSn_{(1-x)}C_2$ formation and the influence of the reactant mixture composition.

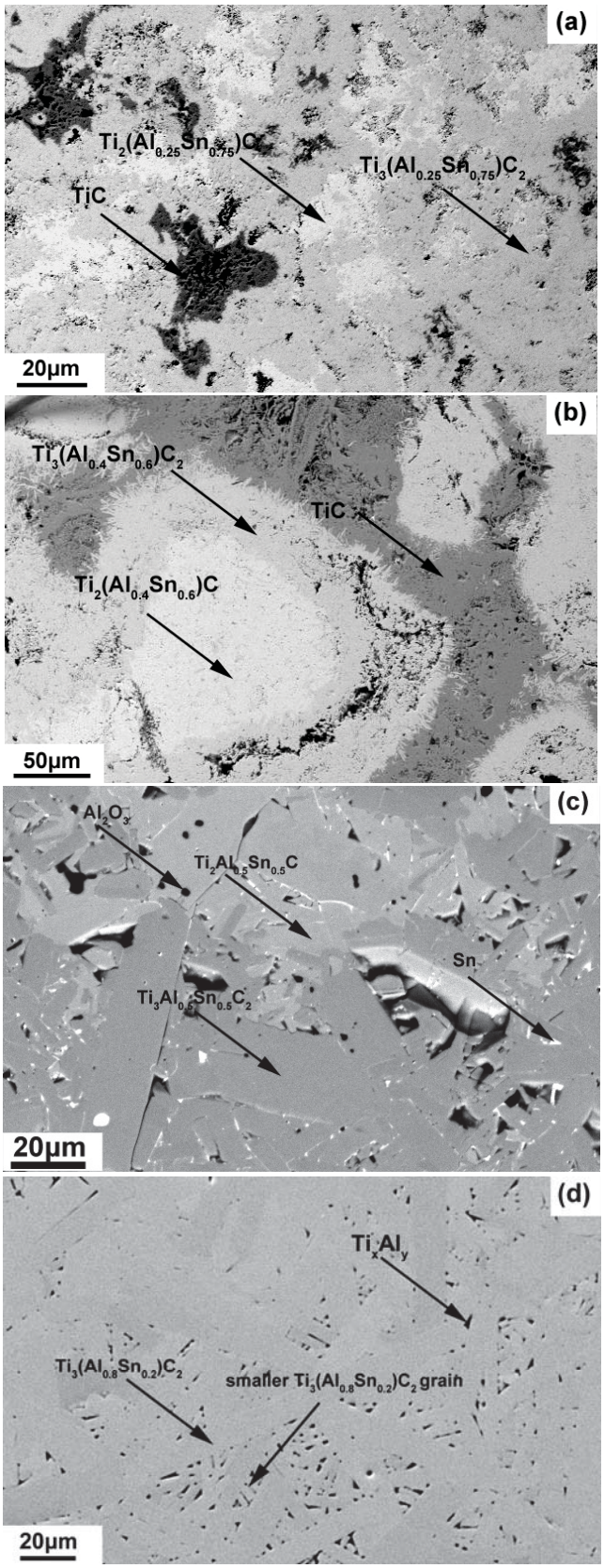

Figure 57: Scanning electron images recorded in back-scattered mode on (a) sample (b), (b) sample (d), (c) sample (e) and (d) sample (f).

V-1.2.2. Composition of the HIPed end-products and lattice parameters of the $Ti_3Al_xSn_{(1-x)}C_2$ solid solutions from Rietveld refinement[189]

Table 18 lists the lattice parameters of the $Ti_3Al_xSn_{(1-x)}C_2$ solid solutions and the volume content of the end-products resulting from Rietveld refinement. To compare the results with the two end members, Ti_3AlC_2 and Ti_3SnC_2, which have been discussed in chapters III and IV, some results of this two MAX phases are also described in this table.

As an example, the Rietveld refined pattern obtained on sample (e) is shown in Figure 58, the weighted reliability factor is 11.7%.

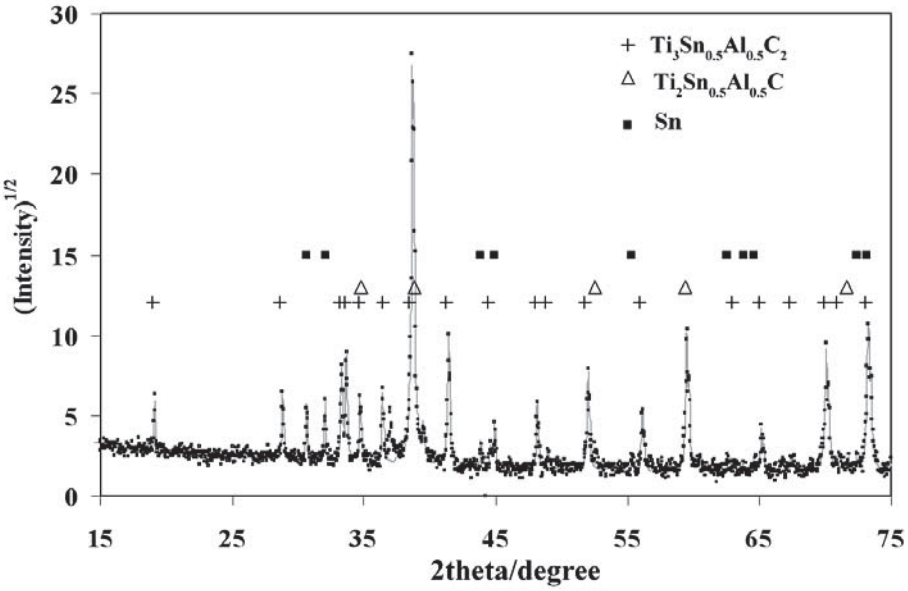

Figure 58: Rietveld refined pattern obtained on sample (e). Black squares: experimental data, full line: Rietveld refinement.

It can be noticed, in Table 18, that only samples (c), (e), (f) and (g) contain more than 95 vol. % of $Ti_3Al_xSn_{(1-x)}C_2$ solid solutions. Samples (f) and (g), which contain 80 and 100 at. % of Al as A element respectively, appear as pure samples at the XRD detection limit. Thus, the formation mechanism of $Ti_3Al_xSn_{(1-x)}C_2$, with x=0.8, is very likely the same as the formation mechanism of Ti_3AlC_2 from TiC, Al and Ti[54,65]. TiC reacts with Al, Ti and Sn to form either $Ti_3Al_{0.8}Sn_{0.2}C_2$ or $Ti_2Al_{0.8}Sn_{0.2}C$[54]. At high enough temperature, $Ti_2Al_{0.8}Sn_{0.2}C$ can react with TiC to form $Ti_3Al_{0.8}Sn_{0.2}C_2$.

Figure 59 exhibits the variation of the c/a ratio as a function of the Al content in $Ti_3Al_xSn_{(1-x)}C_2$ solid solutions. It shows that the lattice contraction of $Ti_3Al_xSn_{(1-x)}C_2$ is

strongly anisotropic, namely, much more reduction along the a axis than along the c axis. c/a variation is consistent with the formation of an ideal solid solution and follows the Vegard's law[193]. Indeed, according to this law, unit cell parameters vary linearly with composition for a continuous substitutional solid solution in which atoms that substitute for each other are randomly distributed. This law is valid for ideal solid solutions when the lattice parameters of the pure components differ by less than 5% which is the case for Ti_3AlC_2 and Ti_3SnC_2 MAX phases. Moreover, as in $V_2Ga_{(1-x)}Al_xC$[194], the z-parameter of Ti_{II} (Z_{Ti-II}) follows Vegard's law (not shown).

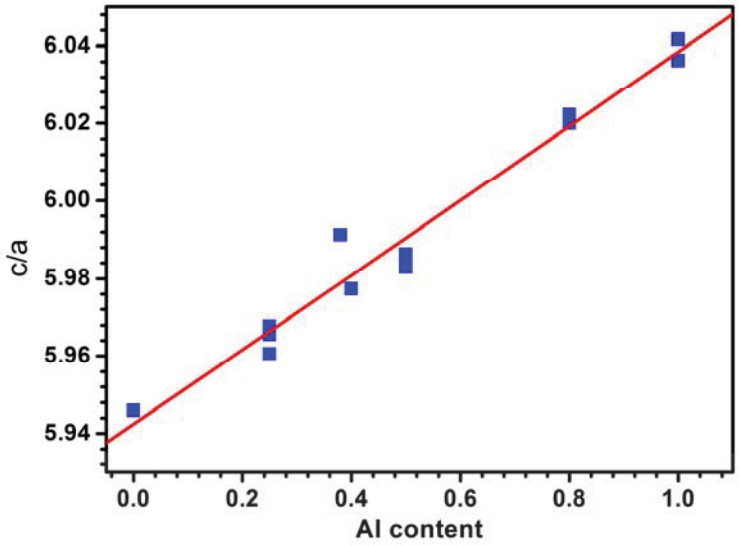

Figure 59: c/a ratio versus Al content in $Ti_3Al_xSn_{(1-x)}C_2$ solid solutions.

V-1.2.3. Distortion parameters of octahedrons and trigonal prisms in the $Ti_3Al_xSn_{(1-x)}C_2$ solid solutions[189]

According to previous studies[160,161], the MAX crystal unit cell can be considered as constituted of $[M_6X]$ octahedrons and $[M_6A]$ trigonal prisms. Figure 60 shows that the stacking of two octahedrons and one trigonal prism allows describing the 312 MAX phases[195]. A cubic octahedron is the unit block of the binary MX but it loses its fourfold axis in ternary MAX and it results in a relaxation owing to this reduced symmetry. The parameter O_d, defined as the ratio of the distances between two faces not in the basal planes (d_1) and two opposite faces contained in the basal planes (d_2)[160], allows estimating the non cubic distortion of the octahedron. It is given, in a 312 MAX phase, by:

$$O_d = \frac{d_1}{d_2} = \frac{\sqrt{3}}{2\sqrt{Z_{Ti}^2\left(\frac{c}{a}\right)^2 + \frac{1}{12}}} \quad (1)$$

The distortion parameter P_d, defined as the ratio of the M-M distance and the M-A distance[161], allows estimating the distortion of the trigonal prism. It is given, in either a 211 or 312 MAX phase, by:

$$P_d = \frac{1}{2\sqrt{\left(\frac{1}{4} - Z_{Ti}\right)^2\left(\frac{c}{a}\right)^2 + \frac{1}{3}}} \quad (2)$$

For 312 MAX phases, an ideal packing of hard spheres of equal diameter leads to a ratio $c/a = 8\sqrt{\frac{2}{3}} \approx 6.532$ and $O_d = P_d = 1$ for ideal octahedron (cubic) and trigonal prism. From the position of Ti atoms (Z_{Ti}), and a and c lattice parameters given in Table 18, one can easily determine the O_d and P_d distortion parameters.

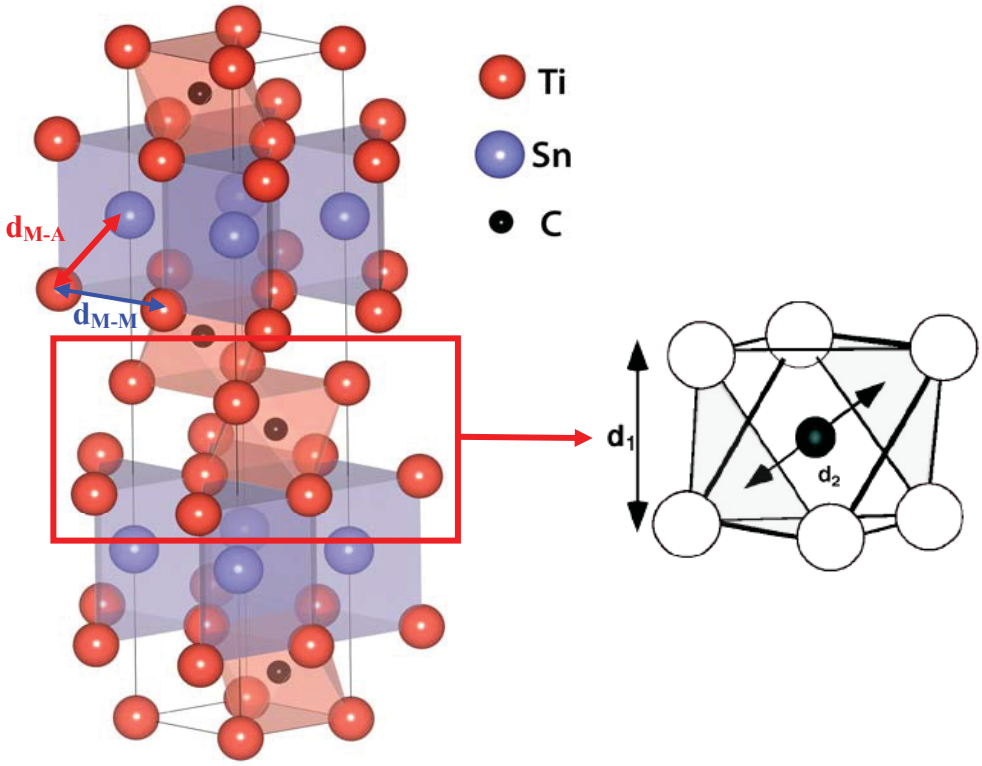

Figure 60: Unit cell of the Ti_3SnC_2 phase. [Ti_6C] octahedrons and [Ti_6Sn] trigonal prisms are represented. Drawn with VESTA [195].

Figure 61 shows the O_d and P_d variations as a function of the Al content in the $Ti_3Al_xSn_{(1-x)}C_2$ solid solutions. For the solid solutions investigated, different (P,T) cycles were used in the HIP to optimize the amount of solid solutions in the final products. This is the reason why, for each x value, at least two different O_d and P_d distortion parameters are calculated, after refining the lattice parameters and Ti positions in the MAUD software using the XRD data. As expected, it can be concluded that both polyhedrons are distorted whatever the Al content in the $Ti_3Al_xSn_{(1-x)}C_2$ MAX phase. Ti_3SnC_2 shows strong distortion of the octahedron; however, Ti_3AlC_2 shows small distortion of the octahedron. The trigonal prism distortion does not seem to change a lot with the Al content of the solid solution, when x is in the range 0.25-1. No $Ti_3Al_xSn_{(1-x)}C_2$ solid solutions have been synthesized for $x<0.25$; thus for such compositions, different tendency can be suggested for the trigonal prism distortion parameters. The dashed line used to show the evolution of the octahedron distortion parameters as a function of the Al content is a guide for the eyes. Finally, the octahedron and trigonal prism distortion are quite similar for Al content in the range 0.4-0.5 (the ratio O_d/P_d departs from unity by 4×10^{-4}). As previously shown[8], anisotropic deformation, i.e. much more reduction along the a axis than along the c axis of the $[Ti_6C]$ octahedrons occurs in ternary compounds. O_d is larger in Ti_3SnC_2 than in Ti_3SiC_2[8] and Ti_3AlC_2.

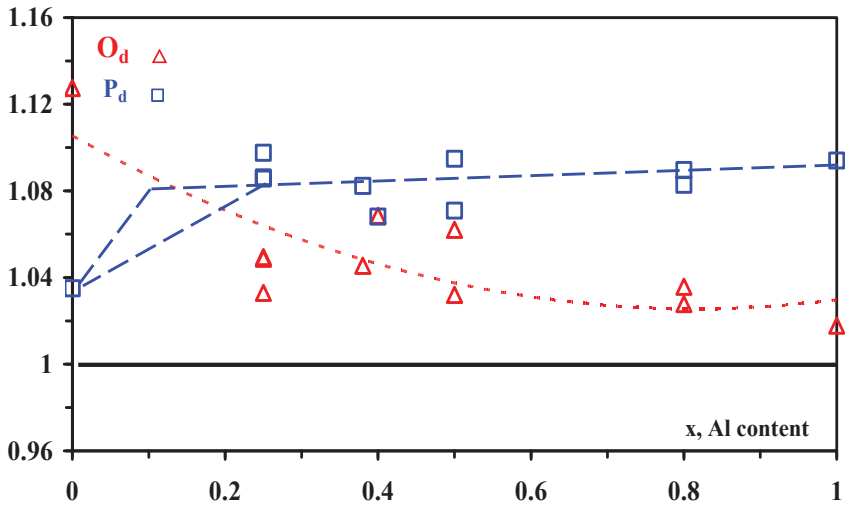

Figure 61: Octahedron (O_d, open triangles) and trigonal prism (P_d, open squares) distortion parameters versus Al content in $Ti_3Al_xSn_{(1-x)}C_2$ solid solutions.

Figure 62 shows the variation of the Ti-C-Ti (Figure 62(a)) and Ti-A (Figure 62(b)) distances as a function of the Al content. The Ti-C-Ti distance monotonically increases with

the Al content. These distances are moreover strongly modified compared with those in TiC (4.3247Å). However, the Ti-A distance decreases with the Al content increase. These results indicate that the distortion is accommodated by shrinking of the Ti-C bonds in the $[Ti_6C]$ octahedrons and it differs from the one obtained by Gamarnik *et al.* who mentioned that accommodation occurs by Ti-C bond rotation[196]. Such a shrinking of the Ti-C-Ti distances will affect the Ti-C bond stiffness and may thus modify the elastic properties of the ternary compounds. The small Ti-Ti spacing, observed in Ti_3SnC_2, would increase direct bonding between Ti sheets whereas higher values, observed in Ti_3AlC_2, would favour the formation of C 2p-Ti ds bonds.

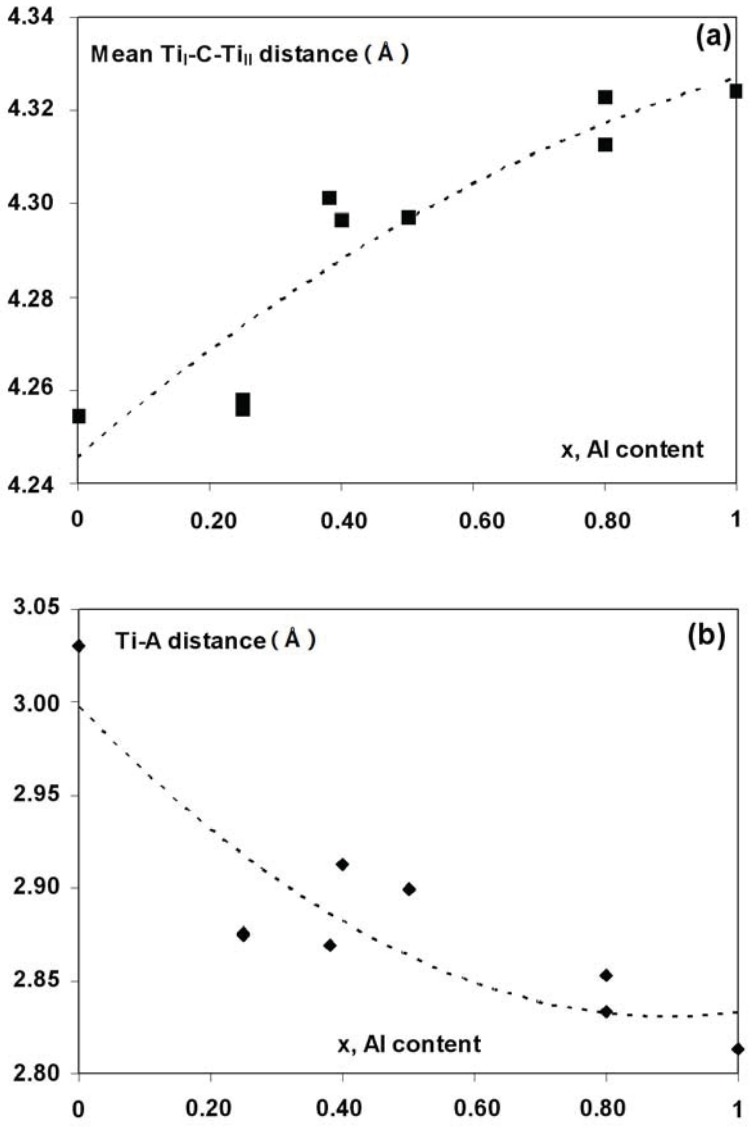

Figure 62: (a) Mean Ti_I-C-Ti_{II} and (b) Ti-A distances versus Al content in $Ti_3Al_xSn_{(1-x)}C_2$ solid solutions.

V-2. Mechanical properties of $Ti_3Al_xSn_{(1-x)}C_2$ solid solutions

V-2.1. $Ti_3Al_xSn_{(1-x)}C_2$ solid solution hardness and elastic modulus variations determined by nanoindentation tests

The intrinsic hardness and elastic modulus of the $Ti_3Al_xSn_{(1-x)}C_2$ solid solutions (x=0.25, 0.5, 0.8) were determined by nanoindentation tests. To measure these parameters, a statistical analysis of the hardness values chosen after phase identification by using SEM coupled with EDXS was performed.

In the present section, experimental details of the different analyses concern sample (f) which contains 98 vol.% of $Ti_3Al_{0.8}Sn_{0.2}C_2$ and about 2 vol.% of Ti_xAl_y intermetallics (see Table 18). As mentioned in section II-3.1., a network of indents of 8 loads (1 to 100 mN) and a total of 147 indents were performed on the surface of this sample; such an indent network is shown, as an example, in Figure 63(a). SEM observation of the indent network allows checking that indents are performed inside a $Ti_3Al_{0.8}Sn_{0.2}C_2$ single grain, inside grain boundaries or inside impurities (Ti_xAl_y, …). Figure 63(b), which is an enlarge view of a part of the network presented in Figure 63(a), shows, as an example, that indents 1, 2, 4 and 5 can be considered as not being performed in a single grain. Indent 3 is carried out in a Ti_xAl_y region. However, indents 6 and 7 are performed in a $Ti_3Al_{0.8}Sn_{0.2}C_2$ single grain. In this case, only hardness and elastic modulus values extracted from indents 6 and 7 are considered in the statistics. From hardness and elastic modulus values measured on $Ti_3Al_{0.8}Sn_{0.2}C_2$ single grain, one can get a mean value for intrinsic hardness and elastic modulus of the MAX phase solid solution. For each indentation load, the same analysis has been performed over 20 indents (except for 100 mN, 7 indents) to measure the $Ti_3Al_{0.8}Sn_{0.2}C_2$ intrinsic hardness and elastic modulus values and to extract, for each property, a mean value.

Hardness and elastic modulus values are plotted in Figure 64(a) as a function of the tip penetration depth for $Ti_3Al_{0.8}Sn_{0.2}C_2$ MAX phase solid solution. The Indentation Size Effect (ISE) observed on the hardness vs penetration depth curves is well fitted by the same function as the one used in the Nix and Gao model[169]. This model leads to the intrinsic hardness value (H_o=10.2GPa) of the $Ti_3Al_{0.8}Sn_{0.2}C_2$ solid solution.

One can notice that a deviation from the function of Nix and Gao model is observed for the largest penetration depth. Like for Ti_3AlC_2 and Ti_3SnC_2, for such high loads, several grains are involved in the deformation process during the indent formation. In such a situation, which is close to microindentation test conditions, grain boundaries play an important role in macroscopic deformation, and MAX phases hardness is underestimated. The elastic modulus remains constant whatever the penetration depth (E=250 GPa). Such a result attests that the ISE is not an artefact due to the indenter shape calibration.

For each indentation load and each $Ti_3Al_xSn_{(1-x)}C_2$ solid solution, the same analysis as the one described above has been performed, to measure the $Ti_3Al_xSn_{(1-x)}C_2$ intrinsic hardness and elastic modulus values and to extract, for each property, a mean value as a function of the Al content. Hardness and elastic modulus values are plotted in Figures 64(b) and 64(c) as a function of the tip penetration depth for $Ti_3Al_xSn_{(1-x)}C_2$ MAX phase solid solutions with x=0.5 and x=0.25 respectively.

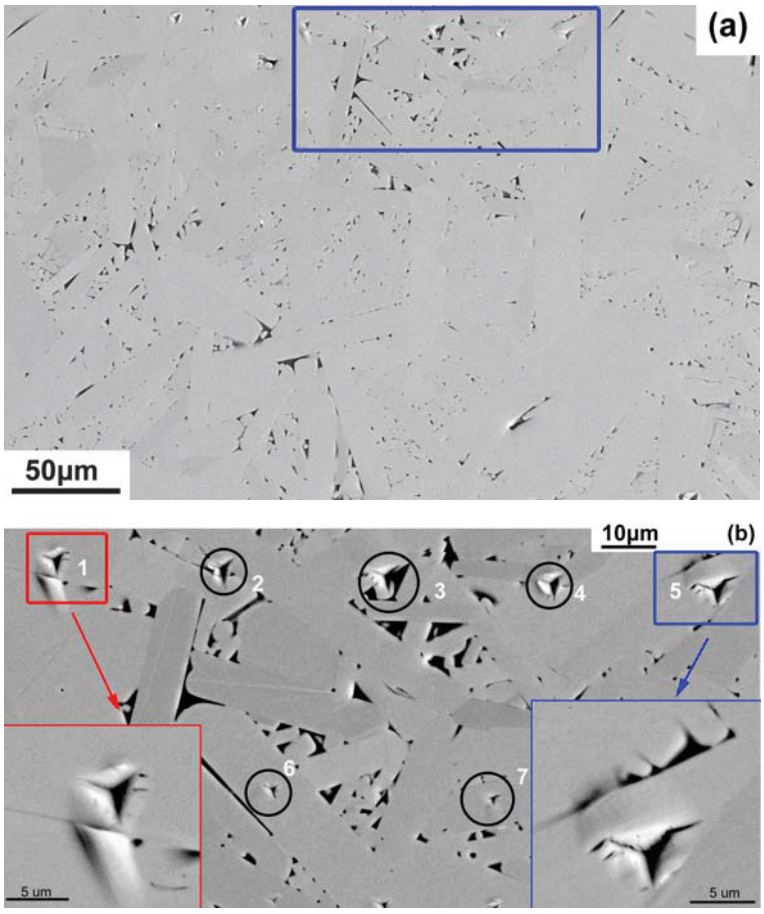

Figure 63: (a) SEM image of the indent network performed on $Ti_3Al_{0.8}Sn_{0.2}C_2$ (sample f), (b) enlarged view of the indents shown in the rectangle presented in (a).

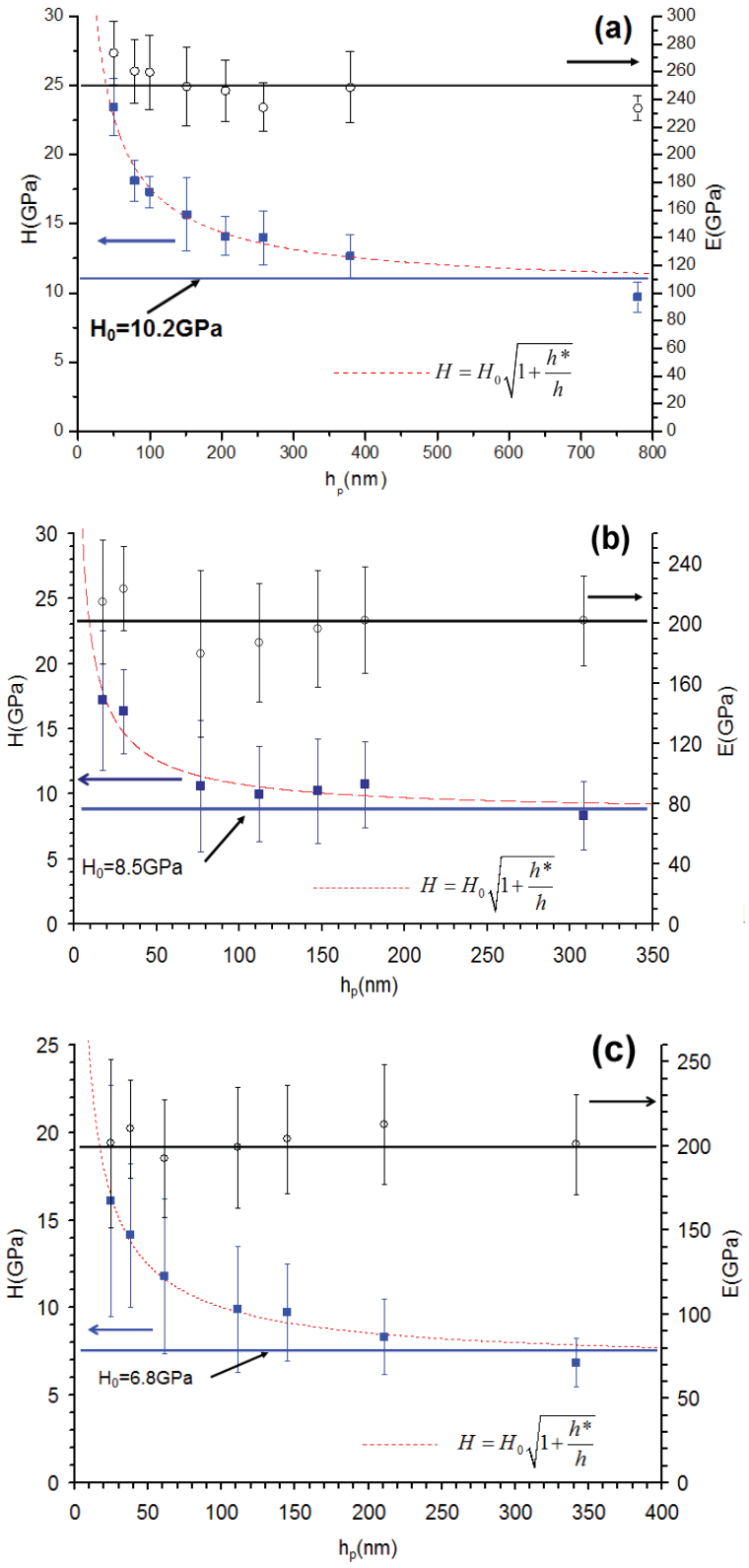

Figure 64: (a) $Ti_3Al_{0.8}Sn_{0.2}C_2$, (b) $Ti_3Al_{0.5}Sn_{0.5}C_2$, (c), $Ti_3Al_{0.25}Sn_{0.75}C_2$ elastic modulus (open circle) and hardness (closed squares) as a function of the plastic penetration depth. Dashed lines: fit of the ISE (function of Nix and Gao model, where h is the plastic penetration, h is a characteristic of length that depends on the indenter shape)*

Figure 65 shows the hardness and elastic modulus variations as a function of the Al content in the $Ti_3Al_xSn_{(1-x)}C_2$ solid solutions. First of all, one can notice that intrinsic hardness values (in the range 7-11 GPa), deduced from nanoindentation experiments performed as a function of load, are larger than the currently determined microhardness values (in the range 2.7-6 GPa for Ti_3AlC_2 and $Ti_3Al_xSi_{(1-x)}C_2$ solid solution[36,53,57,99]). Nevertheless, our values are in compatible agreement with the ones determined by nanoindentation performed on Ti_3AlC_2 thin films[109] or on Ti_3SiC_2 thin film[108]. It is also shown, in Figure 65, that hardness and elastic modulus do not vary monotonically with Al content; they first slightly decrease until x=0.25 and then increase up to x=1. Thus, solid solution hardening effect is not operative in this system. The same kind of results has been obtained by Ganguly *et al.*[96] in $Ti_3Si_{(1-x)}Ge_xC_2$ and by Zhou *et al.*[99] in $Ti_3Al_{1-x}Si_xC_2$ solid solutions. Based on a quite limited set of data, it seems that only substitutions on the X sites lead to solid solution hardening [31,84]; those on the M sites[77,85] and A sites[53,96,99], do not.

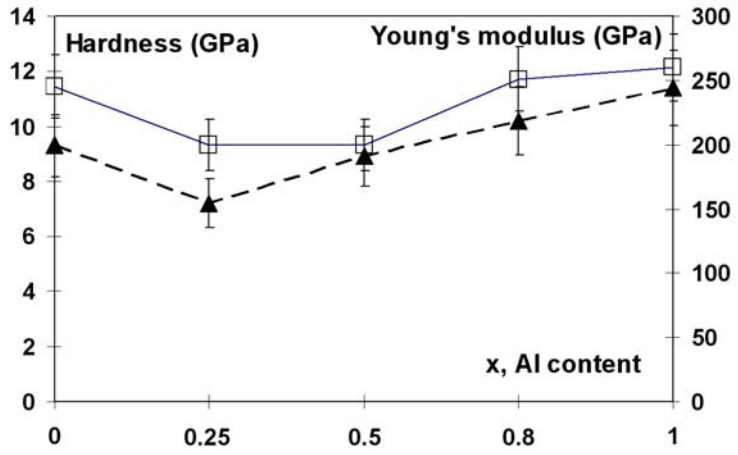

Figure 65: Hardness (closed triangles) and elastic modulus (open squares) versus Al content in $Ti_3Al_xSn_{(1-x)}C_2$ solid solutions.

As MAX phases consist of "soft" M-A and "hard" M-X bonds, it is reasonable that the strengthening of the softer bond leads to an increase of the elastic modulus. The effect of intercalation of a weak M-A bond is twofold: first, enhancement of room temperature ductility, toughness and damage tolerance, and second, degradation of strength and hardness. Therefore, optimizations of elastic stiffness and strength of MAX phases have to focus on properly strengthening of the M-A bonds by tuning the chemical composition and the valence electron

concentration [1,75,77,161,197,198]. It has been shown theoretically that the increase of p electrons from A atoms when moving rightward along the periodic table results in an increase of the bulk modulus up to s^2p^3 column[85]. The shift of the Ti d-A p hybrid to lower energy and its higher filling leads to stronger bonds. Nevertheless, Al ($3s^23p$) and Sn ($5s^25p^2$) do not lie in the same period of the Mendeleiëv's periodic table. Hug shows that Ti-Sn (2.975 Å) and Ti-Al (2.898 Å) bonds have about the same bond stiffness in Ti_2AlC and Ti_2SnC MAX phases[161]. In $Ti_3Al_xSn_{(1-x)}C_2$, Ti-A bond lengths differ more significantly and so Ti-A bond stiffness may also differs. As a consequence, the slight difference observed in the elastic modulus of the $Ti_3Al_xSn_{(1-x)}C_2$ solid solutions may likely be explained by the strength of the Ti-A bonds but more work is needed to confirm such hypothesis.

V-2.2. $Ti_3Sn_{0.2}Al_{0.8}C_2$ Young's modulus variations with temperature

Figure 66 shows the temperature variation of the $Ti_3Al_{0.8}Sn_{0.2}C_2$ Young's modulus. In the temperature range investigated (20-450°C), the Young's modulus decreases slowly and almost linearly with increasing temperature. The loss rate of Young's modulus, in this temperature range, is about 30.8 MPa.°C^{-1} which is much lower than that of $Ti_3Al_xSi_{(1-x)}C_2$ (49 MPa.°C^{-1})[199]. The RT Young's modulus is 268 GPa which corresponds to a 6% difference with the elastic modulus that we get from nanoindentation experiments. Such a slight difference is within the standard deviation of the nanoindentation experiments.

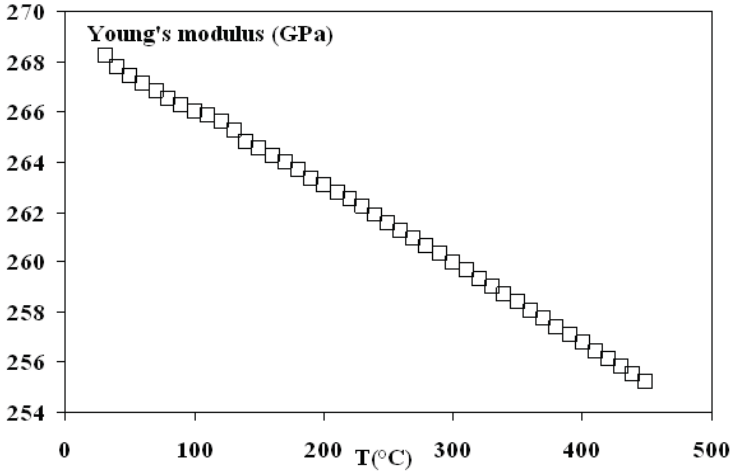

Figure 66: $Ti_3Al_{0.8}Sn_{0.2}C_2$ Young's modulus, measured by means of dynamic resonant method in bending mode, as a function of temperature.

Indeed, a single oriented grain is under study during nanoindentation experiments and

even if about 20 values have been extracted to get a mean value among the different orientations, it is possible that the statistics is not high enough to recover the mean Young's modulus along all crystallographic orientations. As shown previously for Ti_3AlC_2, Ti_3SiC_2[200], Nb_2AlC and Nb_4AlC_3[201], the $Ti_3Al_{0.8}Sn_{0.2}C_2$ Young's modulus does not vary significantly with temperature in the temperature range under study. Radovic *et al.*[46] suggested that the critical temperature for the accelerated decrement of the elastic modulus is close to the BDTT for Ti_3SiC_2 and Ti_2AlC. For most MAX phases, such a BDTT is about 1000°C.

V-2.3. Kinking nonlinear elastic deformation of $Ti_3Al_{0.8}Sn_{0.2}C_2$ at room temperature

V-2.3.1. Cyclic compression tests

Typical cyclic compressive stress-strain loops – progressively shifted to the right for clarity and corrected from the machine stiffness (see chapter II) – recorded at RT on the $Ti_3Al_{0.8}Sn_{0.2}C_2$ sample are shown in Figure 67. Strain rate is 10^{-4} s^{-1}. At stress levels below 200 MPa, the response of the sample is linear elastic with a Young's modulus of about 250 MPa. This value exactly corresponds to the one that we get from nanoindentation tests. As for other MAX phases and for MAX phase solid solutions [4,5,136], hysteretic and fully reversible stress-strain loops are observed for stresses in the range 300-750 MPa. One can notice that, at 300MPa stress level, the hysteretic loop is small. However, larger hysteretic loops are observed with increasing stress. Comparing these results with the ones that we get on Ti_3AlC_2, cyclic compressive stress-strain loops can be obtained up to 750 MPa for the $Ti_3Al_{0.8}Sn_{0.2}C_2$ sample whereas the Ti_3AlC_2 sample breaks at 545 MPa.

Figure 68 shows compressive stress-strain loops - progressively shifted to the right for clarity and corrected from the machine stiffness (see chapter II) - recorded at RT on Ti_3AlC_2 and $Ti_3Al_{0.8}Sn_{0.2}C_2$ samples at 400MPa with three different strain rates (10^{-3}, 10^{-4} and 10^{-5} s^{-1}). Figure 68 allows demonstrating that the hysteretic, fully reversible strain-stress loops, do not depend on strain rate, both for $Ti_3Al_{0.8}Sn_{0.2}C_2$ and Ti_3AlC_2 samples. It also demonstrates that the closed hysteretic stress-strain loops for $Ti_3Al_{0.8}Sn_{0.2}C_2$ are smaller than the ones for Ti_3AlC_2. The dissipated energy (W_d) is thus smaller in the case of the $Ti_3Al_{0.8}Sn_{0.2}C_2$ sample; such an observation likely results from the $Ti_3Al_{0.8}Sn_{0.2}C_2$ smaller grain size.

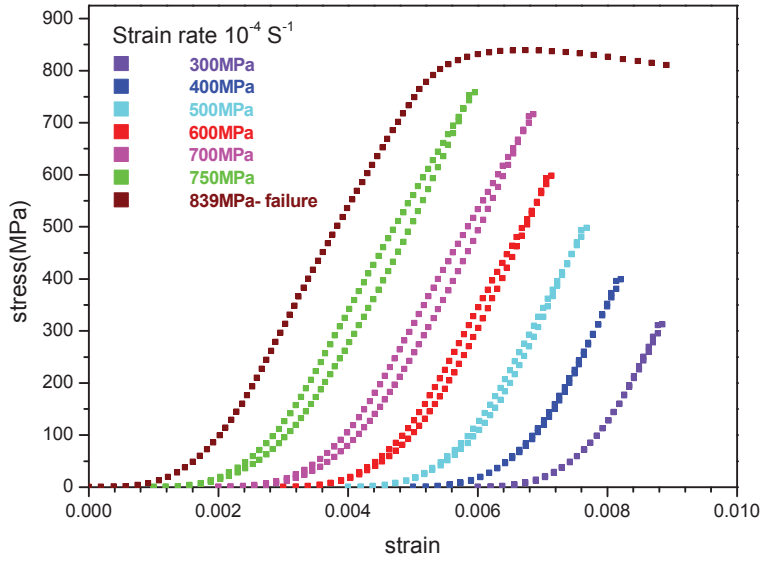

Figure 67: Typical cyclic compressive reversible stress-strain loops recorded on $Ti_3Al_{0.8}Sn_{0.2}C_2$ at different stress level. Brown curve: compressive stress-strain curve recorded up to failure - curves shifted to the right for clarity.

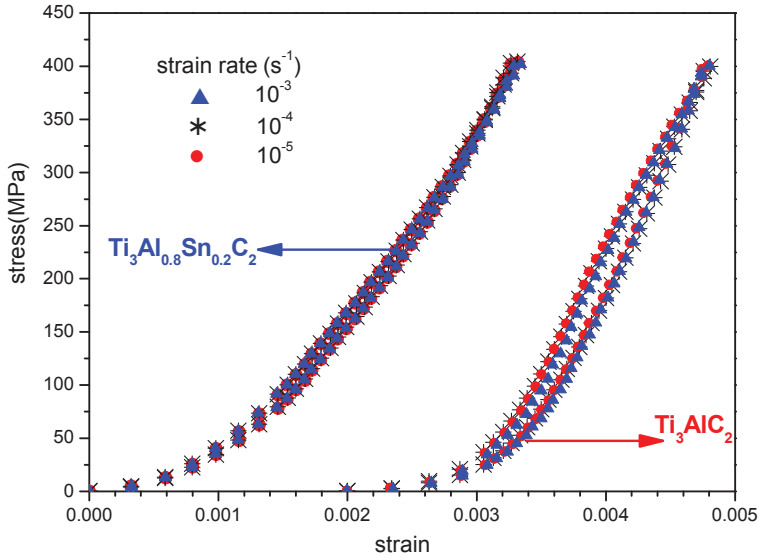

Figure 68: Cyclic compressive reversible stress-strain loops recorded on $Ti_3Al_{0.8}Sn_{0.2}C_2$ and Ti_3AlC_2 at 400MPa with different strain rates.

In addition, the brown stress-strain curve shown in Figure 67 demonstrates that the RT-failure of $Ti_3Al_{0.8}Sn_{0.2}C_2$ sample is also brittle. The maximum stress can reach a value as high as 839 MPa which is very high compared to the one obtained on Ti_3AlC_2 (545 MPa). Solid solution strengthening has been observed in $(Ti_{0.8}V_{0.2})_2AlC$[86], $Ti_3Al_{0.75}Si_{0.25}C_2$[99] and $Ti_2AlC_{0.5}N_{0.5}$[31]. However, as discussed in previous section, solid solution strengthening is not operative by substituting Al by Sn. Hence, the compressive strength enhancement of $Ti_3Al_{0.8}Sn_{0.2}C_2$ sample may be related either to grain size effects or to the presence of Ti_xAl_y

intermetallics located at the $Ti_3Al_{0.8}Sn_{0.2}C_2$ grain boundaries. From SEM observations, $Ti_3Al_{0.8}Sn_{0.2}C_2$ grain size (10-80 μm in length and 2-15 μm in width) is indeed smaller than the Ti_3AlC_2 grain size (60-100 μm in length and 10-40 μm in width). Moreover, about 2-3 vol.% of Ti_xAl_y intermetallics are homogenously distributed at the grain boundaries of the $Ti_3Al_{0.8}Sn_{0.2}C_2$ lamellas. The Ti_xAl_y intermetallics play the role of a second phase at the grain boundaries of $Ti_3Al_{0.8}Sn_{0.2}C_2$ skeleton; such a ductile phase may accommodate the deformation and improve the compressive stress of the sample.

V-2.3.2. Application of KNE model

According to KNE model[4,5], the three parameters, stress (σ), nonlinear strain (ε_{nl}) and dissipated energy (W_d) can be obtained from compressive, closed, hysteretic stress-strain loops recorded on $Ti_3Al_{0.8}Sn_{0.2}C_2$ sample. Those parameters are listed in Table 19; for comparison, the same parameters, determined on Ti_3AlC_2, are also given in the Table 19. Plots of ε_{nl} vs σ^2, W_d vs σ^2 and W_d vs ε_{nl} are shown in Figure 69.

Based on the KNE model established by Barsoum *et al.* [4,5], ε_{nl} and W_d should vary linearly with σ^2 and W_d should vary linearly with ε_{nl}. Indeed, one can notice that all plots exhibit a linear variation; the lowest correlation coefficient value, R^2, being larger than 0.99. Thus, the slopes of the three straight lines, respectively m_1, m_2 and m_3 are calculated and given in Table 19. In addition, experimental nonlinear strains ($\varepsilon_{nl\ exp}$), determined at different stress levels, from Equation (1) of Chapter IV and Figure 67, are listed in Table 19. As in the case of Ti_3AlC_2 sample, ε_{nl} value experimentally determined at low stress is larger than the one obtained from calculation. Such a result is likely due to the measurement uncertainty. For high stress level, the experimental and calculated nonlinear strains are in good agreement.

The Ti_3AlC_2 and $Ti_3Al_{0.8}Sn_{0.2}C_2$ physical parameters that have been used in KNE model are given in Table 20. The $Ti_3Al_{0.8}Sn_{0.2}C_2$ Young's modulus results from nanoindentation test (see V-2.1). The other parameters, k_1, b, ω and γ_c are the ones used for Ti_3AlC_2.

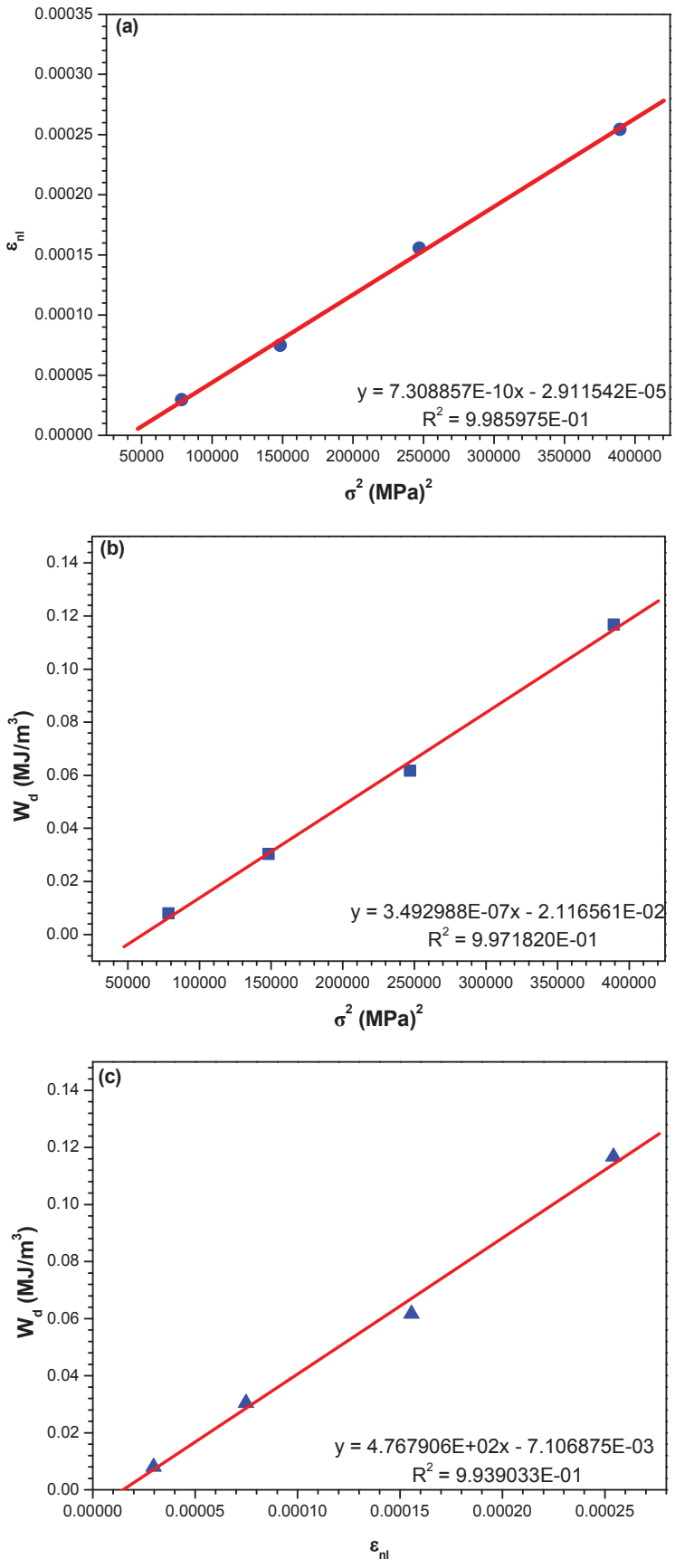

Figure 69: (a) plot of ε_{nl} vs σ^2, (b) plot of W_d vs σ^2, (c) plot of W_d vs ε_{nl} determined from the stress-strain curves recorded on $Ti_3Al_{0.8}Sn_{0.2}C_2$ sample.

	σ (MPa)	$\varepsilon_{nl\ exp}$	$\varepsilon_{nl\ cal}$	W_d (MJ/m^3)	m_1 (MPa)$^{-2}$	m_2 (MPa)$^{-1}$	$m_3=m_2/m_1$ (MPa)
Ti_3AlC_2	139	0.000015	0.000006	0.005360	1.824×10^{-9}	5.713×10^{-7}	313■ 311◈
	247	0.000060	0.000082	0.024378			
	352	0.000203	0.000198	0.057186			
	457	0.000349	0.000352	0.113298			
$Ti_3Al_{0.8}Sn_{0.2}C_2$	280	0.0000297	0.000013	0.007986	0.731×10^{-9}	3.493×10^{-7}	477.9■ 476.7◈
	376	0.0000748	0.000064	0.030370			
	500	0.0001556	0.000136	0.061662			
	621	0.0002542	0.000240	0.116769			

Table 19: Stress (σ), nonlinear strain (ε_{nl}) and dissipated energy (W_d) extracted from compressive stress-strain curves shown in Figure 67. Slopes (m_1, m_2 and m_3, see text) of the different straight lines shown in Figure 69. $\varepsilon_{nl\ cal}$ is calculated from Equation (11) of KNE model in Chapter I, ■ m_2/m_1 ◈ Slope of Figure 69(c).

	E[a] (GPa)	G (GPa)	ν	b (Å)	ω (Å)	k_1	M	γ_c (rad)	2α [b] (μm)	σ_t [c] (MPa)
Ti_3AlC_2	260	108.3	0.2	3	15	2	3	0.01	25	125
$Ti_3Al_{0.8}Sn_{0.2}C_2$	250	104.1	0.2	3	15	2	3	0.01	6	246

Table 20: Ti_3AlC_2 and $Ti_3Al_{0.8}Sn_{0.2}C_2$ physical parameters used for calculation in the KNE model. [a] Obtained from nanoindentaion test; [b] Calculated from Equation (7) of chapter I; [c] Calculated from W_d vs σ^2.

The threshold stress, σ_t, is calculated from the intercept of the W_d vs σ^2 straight line with the W_d axis. The threshold stress value determined for $Ti_3Al_{0.8}Sn_{0.2}C_2$ sample is larger (246 MPa) than the one determined for Ti_3AlC_2 sample (125 MPa). Subsequently, the grain size of $Ti_3Al_{0.8}Sn_{0.2}C_2$, along the c-axis (2α), is smaller (6 μm) than the one of Ti_3AlC_2 (25 μm). From SEM image of as-synthesized $Ti_3Al_{0.8}Sn_{0.2}C_2$ sample (see Figure 57(d)), $Ti_3Al_{0.8}Sn_{0.2}C_2$ grains are indeed smaller than Ti_3AlC_2 grains; however, the distribution of grain size is larger for the solid solution. It is consequently quite difficult to give a mean grain size. Nevertheless, the increase in σ_t is in qualitative agreement with the decrease in grain size.

The dissipated energy (W_d) strongly depends on the grain size, W_d decreases with decreasing grain size (see Equation (12) of chapter I). Thus, it is not surprising to observe that, at the same stress level, the $Ti_3Al_{0.8}Sn_{0.2}C_2$ solid solution dissipates less energy per cycle than the Ti_3AlC_2. Moreover, comparable dissipated energy values are obtained by Zhou *et al.* [136] on un-annealed Ti_3AlCN solid solution with 2α in the same range (7 μm).

As shown in Table 21, the Ω/b value, calculated for $Ti_3Al_{0.8}Sn_{0.2}C_2$ from Equation (13) of Chapter I and plot of W_d vs ε_{nl}, is 79 MPa which means that, like Ti_3AlC_2, the same micromechanism is responsible for the parabolic dependence of non-linear strain (ε_{nl}) and dissipated energy (W_d) on the stress (σ). Furthermore, the Ω/b value calculated for $Ti_3Al_{0.8}Sn_{0.2}C_2$ is the highest among the ones reported on MAX phases [4,5,136,202]. Since there is no other work that has reported the KNE deformation of $Ti_3Al_{0.8}Sn_{0.2}C_2$, such kind of high Ω/b value may be attributed to two points: 1) grain size; according to KNE model [4,5,136,202], Ω/b is strongly dependent on the grain size and follows Hall–Petch effect. 2) the Young's modulus; like in Ti_3AlC_2, the Young's modulus (E=250GPa) used here is smaller than other MAX phase used [4,5,136,202] which will lead to smaller non-linear strain (ε_{nl}). As a result, the slope of the straight line shown in Figure 69(c) will increase and result in an increase of Ω/b value.

	σ (MPa)	Ω/b (MPa)	N_k (m^{-3})	$(1/N_k)^{1/3}$(μm)	$2\beta_{av.c}$(μm)	$2\beta_{av}$ (μm)	ρ_{rev} (m^{-2})
Ti_3AlC_2	139	52★ 52□	5.9×10^{14}	11	0.9	1	1.5×10^{12}
	247					1.7	2.7×10^{12}
	352					2.4	3.8×10^{12}
	457					3.2	4.9×10^{12}
$Ti_3Al_{0.8}Sn_{0.2}C_2$	280	79★ 79□	1.6×10^{16}	4	0.4	0.5	5.2×10^{12}
	385					0.7	7.2×10^{12}
	497					0.9	9.3×10^{12}
	624					1.2	1.2×10^{13}

Table 21: List of parameters calculated for $Ti_3Al_{0.8}Sn_{0.2}C_2$ from KNE model. N_k calculated from Equation (11) of Chapter I, $2\beta_{av.c}$ and $2\beta_{av}$ calculated from Equation (10) of Chapter I, σ_t listed in Table 19 and σ listed in Table 20. ρ_{rev} calculated from Equation (14) of Chapter I, ★ and □ determined from m_2/m_1 and m_3, respectively.

The IKBs number per unit volume (N_k) and the reversible dislocation density (ρ_{rev}) take reasonable values given the applied stress. These values are moreover comparable to the ones obtained by Barsoum et al. in fine-grained un-annealed Ti_3AlCN and Ti_3AlC_2 samples [5,136]. With increasing stress, IKBs size in the basal plane ($2\beta_{av}$) grows from about 0.5 to 1.2 μm and the reversible dislocation density (ρ_{rev}) increases from about 5.2×10^{12} to 1.2×10^{13} m^{-2}. Compared to fine-grained Ti_3AlC_2 sample (10μm) deformed at comparable stress level[5,136], IKBs have about the same size (0.95 μm compared to 0.9 μm) and reversible dislocation

density is a little bit smaller in our coarse grained Ti_3AlC_2 sample at the same stress level.

V-2.3.3. Microstructural characterization of the sample deformed up to failure

Figure 70 shows SEM images of the $Ti_3Al_{0.8}Sn_{0.2}C_2$ sample deformed up to failure (see stress-strain curve in Figure 67). It can be observed, in Figure 70(a), that the angle between main fatal crack propagation path and compression axis is roughly 30°. The typical deformation microstructures near the fatal crack are displayed in Figure 70(b) (magnification of the blue rectangle shown in 70(a)). One can notice that most of the deformation microstructures near the fatal cracks of the $Ti_3Al_{0.8}Sn_{0.2}C_2$ sample are different than the ones observed for Ti_3AlC_2. Indeed, the main energy dissipation mechanisms are crack deflections along the grain boundaries. Figures 70(c) to 70(e) show the deformation microstructures of the fracture surface. In this case, the deformation microstructures look like the ones observed in Ti_3AlC_2. Indeed, intergranular fractures, kink bands and delaminations (white arrows in Figure 70(c)) are observed in the fracture surface. As it is the case for Ti_3AlC_2, kink bands, in some grains, can be continuously formed (see Figure 70(e)). In addition, careful observation of Figures 70(b) and 70(c) lead to the conclusion that $Ti_3Al_{0.8}Sn_{0.2}C_2$ grains embedded in Ti_xAl_y intermetallics are well protected. Indeed, no damage is observed in these areas. Such a result further confirms that ductile Ti_xAl_y intermetallics play an important role in the enhancement of the compressive strength of the material. As it is the case for Ti_3AlC_2, it is noticed that $Ti_3Al_{0.8}Sn_{0.2}C_2$ specimen fractured in a shear mode (see Figure 70(a)). The fracture surface made an angle α_c=30° with the compression axis; such a value deviates from the maximum shear stress plane (45°), but it is in reasonable agreement (α_c=23° at RT and α_c =30° at 900°C) with results obtained by Zhang and Sun[171].

The same analysis as the one performed on the Ti_3AlC_2 sample leads to μ=0.6 and τ_c=242 MPa for the $Ti_3Al_{0.8}Sn_{0.2}C_2$ polycrystalline material. The increase in τ_c may result from the smaller grain size of our $Ti_3Al_{0.8}Sn_{0.2}C_2$ sample (10-80 μm in length and 2-15 μm in width, τ_c=242 MPa) compared to our fine-grained Ti_3AlC_2 (60-100 μm in length and 10-40 μm in width, τ_c=185 MPa) samples. Nevertheless, one can not rule out the enhancement of the compressive strength which may be due to the presence of Ti_xAl_y intermetallics. Such an enhancement results in an intrinsic raise of τ_c.

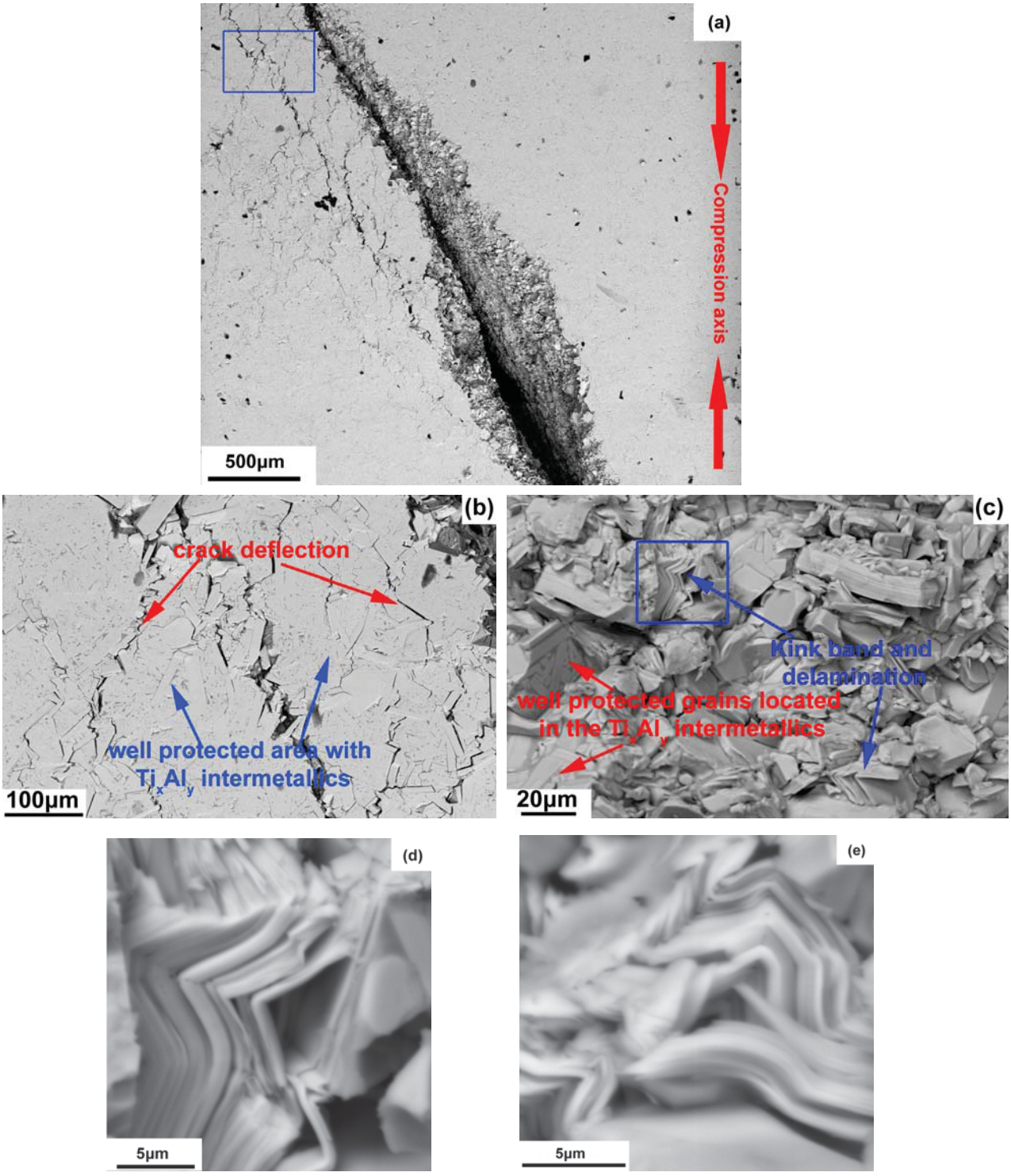

Figure 70: SEM images of deformation microstructures of $Ti_3Al_{0.8}Sn_{0.2}C_2$ sample deformed up to failure at RT. (a) fatal crack after compression, (b) magnification of the blue rectangle shown in (a), (c) fracture surface, (d) magnification of the blue rectangle shown in (c), (e) continuous kink band formation in one grain.

In summary, like most of the MAX phases, $Ti_3Al_{0.8}Sn_{0.2}C_2$ solid solution belongs to KNE solids. The cyclic compressive stress-strain loops for $Ti_3Al_{0.8}Sn_{0.2}C_2$ are typical hysteretic and fully reversible. The maximum stress for $Ti_3Al_{0.8}Sn_{0.2}C_2$ is higher than the one of Ti_3AlC_2 due to

the grain size effect and to the presence of ductile Ti_xAl_y intermetallics distributed in the grain boundaries. The deformation mechanisms for $Ti_3Al_{0.8}Sn_{0.2}C_2$ are mainly crack deflections, intragranular fractures, kink bands and delaminations etc.. No damage is detected in the areas where $Ti_3Al_{0.8}Sn_{0.2}C_2$ grains are embedded into Ti_xAl_y intermetallics.

V-2.4. Plastic deformation of $Ti_3Al_{0.8}Sn_{0.2}C_2$ sample at room temperature under confining gaseous pressure using a Paterson apparatus

V-2.4.1. Stress-strain curve of $Ti_3Al_{0.8}Sn_{0.2}C_2$

Figure 71 provides the engineering stress-strain curves of $Ti_3Al_{0.8}Sn_{0.2}C_2$ and Ti_3AlC_2 samples obtained from the compression tests in the Paterson machine at RT after removing the mechanical contribution of Al jacket. The characteristics of the compressive stress-strain curve of $Ti_3Al_{0.8}Sn_{0.2}C_2$ solid solution are similar to the one of Ti_3AlC_2, with three regimes: (a) an elastic regime, (b) a strain hardening regime, and (c) a softening regime. For the solid solution sample, a plastic strain of 3% could be reached without brittle rupture. Nevertheless, the strain hardening and maximum stress of $Ti_3Al_{0.8}Sn_{0.2}C_2$ are higher than those of Ti_3AlC_2 despite identical deformation conditions. The mechanisms for the enhancement of the maximum stress are similar with the ones discussed in sectionV-2.3: since the solid solution strengthening is not operative by incorporation of Al into the Ti_3SnC_2 structure, the grain size effect and the presence of the ductile Ti_xAl_y intermetallics distributed in the grain boundaries are the main contributors to the observed enhancement of compressive strength.

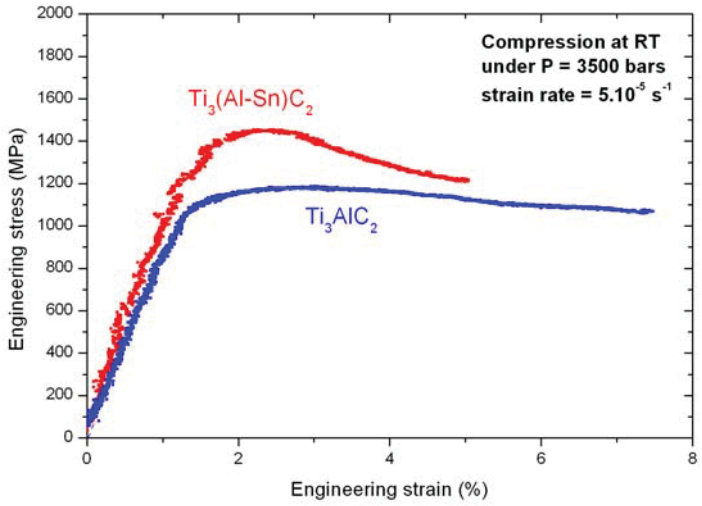

Figure 71: The engineering stress-strain curves obtained from the compression of polycrystalline $Ti_3Al_{0.8}Sn_{0.2}C_2$ and Ti_3AlC_2 samples at RT in a Paterson press.

V-2.4.2. Characterization of deformed $Ti_3Al_{0.8}Sn_{0.2}C_2$ microstructures by SEM observations

Herein, like in Ti_3AlC_2, we also define two different regions at the surface of the deformed sample: 1) one "most damaged" area and 2) "less damaged" areas. Figures 72(a) and 72(b) show the surfaces of $Ti_3Al_{0.8}Sn_{0.2}C_2$ after deformation in the damaged area and "less damaged" areas, respectively.

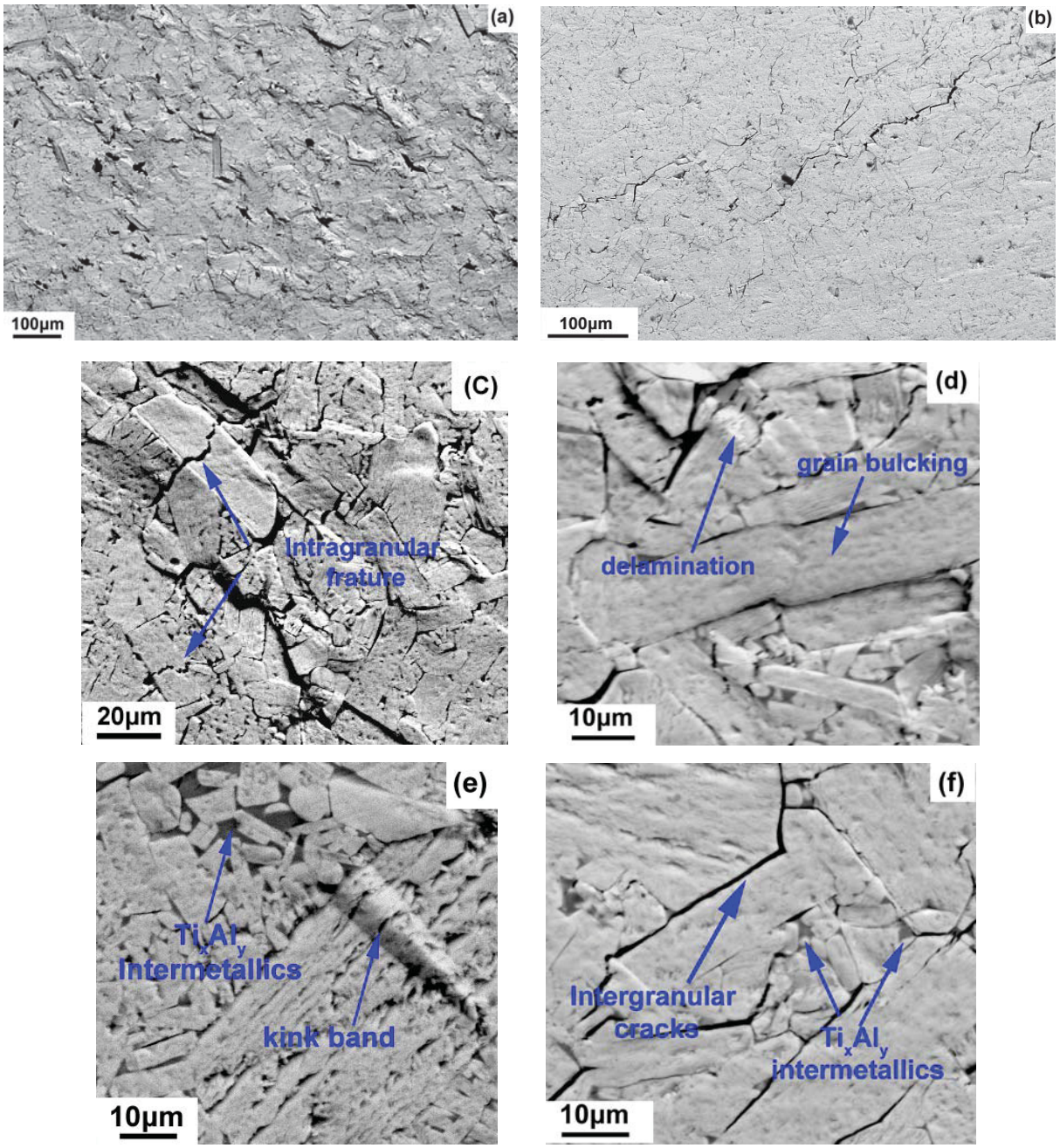

Figure 72: SEM images of the deformed surface microstructure of $Ti_3Al_{0.8}Sn_{0.2}C_2$, (a) most damaged area, (b) less damaged area, (c) intra-granular fracture, (d) grain buckling and delamination, (e) kink band, (f) grain boundary cracks.

As shown in Figure 72(a), the microstructure of the surface in the damage area is not as catastrophic as in Ti_3AlC_2. The main deformation mechanisms are grain pull-out, push-in, intergranular and intragranular cracks. In the "less damaged" area shown in the Figure 72(b), one can see only grain boundary cracks. More information about the deformation mechanisms are shown in Figures 72(c)-(f). Figures 72(c)-(e) show microstructures in the "most damaged" area. From Figure 72(c), intra-granular fracture, grain pull-out and push-in are observed. As already observed in Ti_3AlC_2, grain buckling and delamination of individual grains are evidenced in Figures 72(d) and 72(e). Furthermore, in the "less damaged" areas, as shown in Figure 72(f), the crack propagation mainly occurs along grain boundaries. From Figures 72(e) and (f), one can notice that no cracks are observed within the Ti_xAl_y intermetallics present in the grain boundaries. In such case, it is reasonable to believe that the Ti_xAl_y intermetallics can inhibit the crack propagation and play an important role in the enhancement of strain hardening and maximum stress compared to Ti_3AlC_2.

Therefore, from SEM observations, the deformed microstructure of $Ti_3Al_{0.8}Sn_{0.2}C_2$ is not as catastrophic as the one observed in Ti_3AlC_2. Compared to Ti_3AlC_2, besides the multiple deformation mechanisms such as intra-granular failure, delamination of individual grains, grain pull-out, grain push-in, grain boundary cracks and grain buckling, the ductile Ti_xAl_y intermetallics also play an important role to accommodate the deformation during the compression test in the Paterson press.

V-2.4.3. Characterization of deformation mechanisms for $Ti_3Al_{0.8}Sn_{0.2}C_2$ by TEM observations

V-2.4.3.1. TEM observations of as-grown $Ti_3Al_{0.8}Sn_{0.2}C_2$ sample

Before going into the deformed $Ti_3Al_{0.8}Sn_{0.2}C_2$ solid solution, the microstructures of the as-grown sample were examined by TEM observations. As shown in Figure 73, two major features, dislocations and stacking faults (SF), are present in the as-grown $Ti_3Al_{0.8}Sn_{0.2}C_2$ solid solution. These two features have already been reported in other as-grown MAX phases such as Ti_4AlN_3[124], Ti_3SiC_2[114,122,203] and Ti_3AlC_2[53] *etc.*. The defect density is quite low and dislocations as well as stacking faults are not homogenously distributed among the grains, large areas being free of defects.

As reported by Joulain *et al.* [124], some dislocations are out of basal plane in the as-grown Ti_4AlN_3. It is not the case of $Ti_3Al_{0.8}Sn_{0.2}C_2$ solid solution, all the dislocations observed here lie in the basal plane and are organised in specific configurations. For instance, Figure 73(a) shows a characteristic dislocation arrangement and some isolated dislocations in the as-grown $Ti_3Al_{0.8}Sn_{0.2}C_2$ solid solution In Figure 73(b), long basal plane SFs crossing the whole grain in $Ti_3Al_{0.8}Sn_{0.2}C_2$ are observed in two beams condition. In present diffraction condition, all SFs do not present the same contrast: some are in contrast when some are out. Furthermore, the contrast of dislocation "in contrast" is more or less strong (white arrow in Figure 73(b)). Partial dislocations separating the different SFs with different contrasts are observed. Such characteristics are exactly the same as those analyzed in details in as-grown Ti_4AlN_3[124]. Joulain *et al.* gave evidence that SFs of MAX phases, corresponding to insertion of MX planes [114,124,203], lead to different fault vectors, depending of the number of inserted planes. These fault vectors present a dilatation component parallel to the *c*-axis but also a shear component in the basal plane. The contrast obtained in two beam conditions varies according to the fault vector. This shear component implies that the stacking fault may have a role in the plastic deformation especially at high temperature where diffusion is easy.

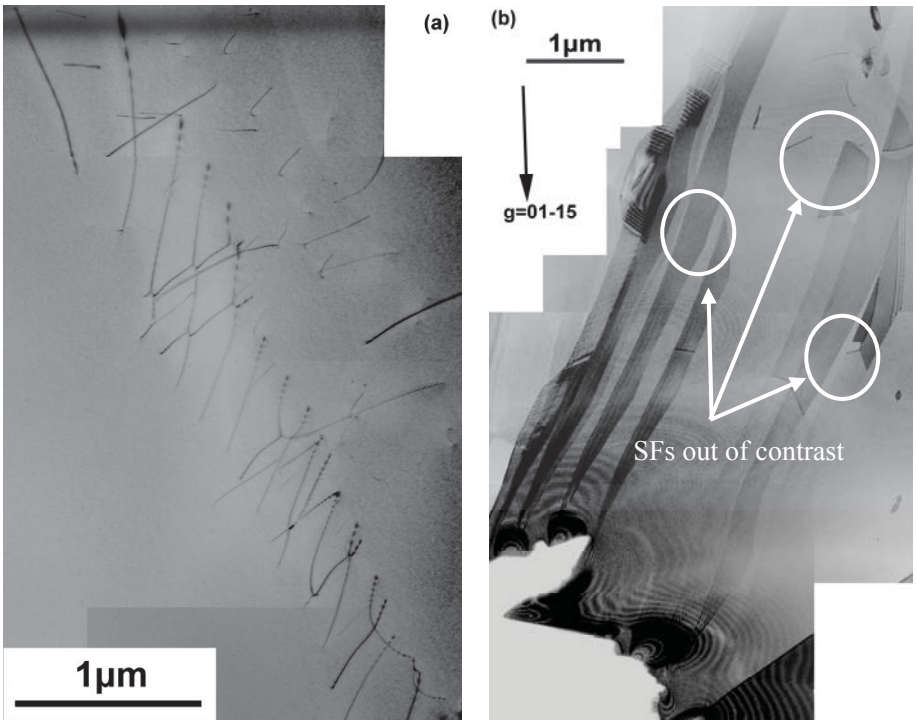

Figure 73: Dislocations and stacking faults in as-grown $Ti_3Al_{0.8}Sn_{0.2}C_2$ sample characterized by TEM observation, (a): dislocations, (b): stacking faults.

V-2.4.3.2.TEM observations of deformed $Ti_3Al_{0.8}Sn_{0.2}C_2$ sample

Figure 74 shows a characteristic example of the microstructure of $Ti_3Al_{0.8}Sn_{0.2}C_2$ deformed at RT. For the observed grain of $Ti_3Al_{0.8}Sn_{0.2}C_2$ solid solution, the basal plane is at 40° from the thin foil plane that was cut at 45° from the compression axis.

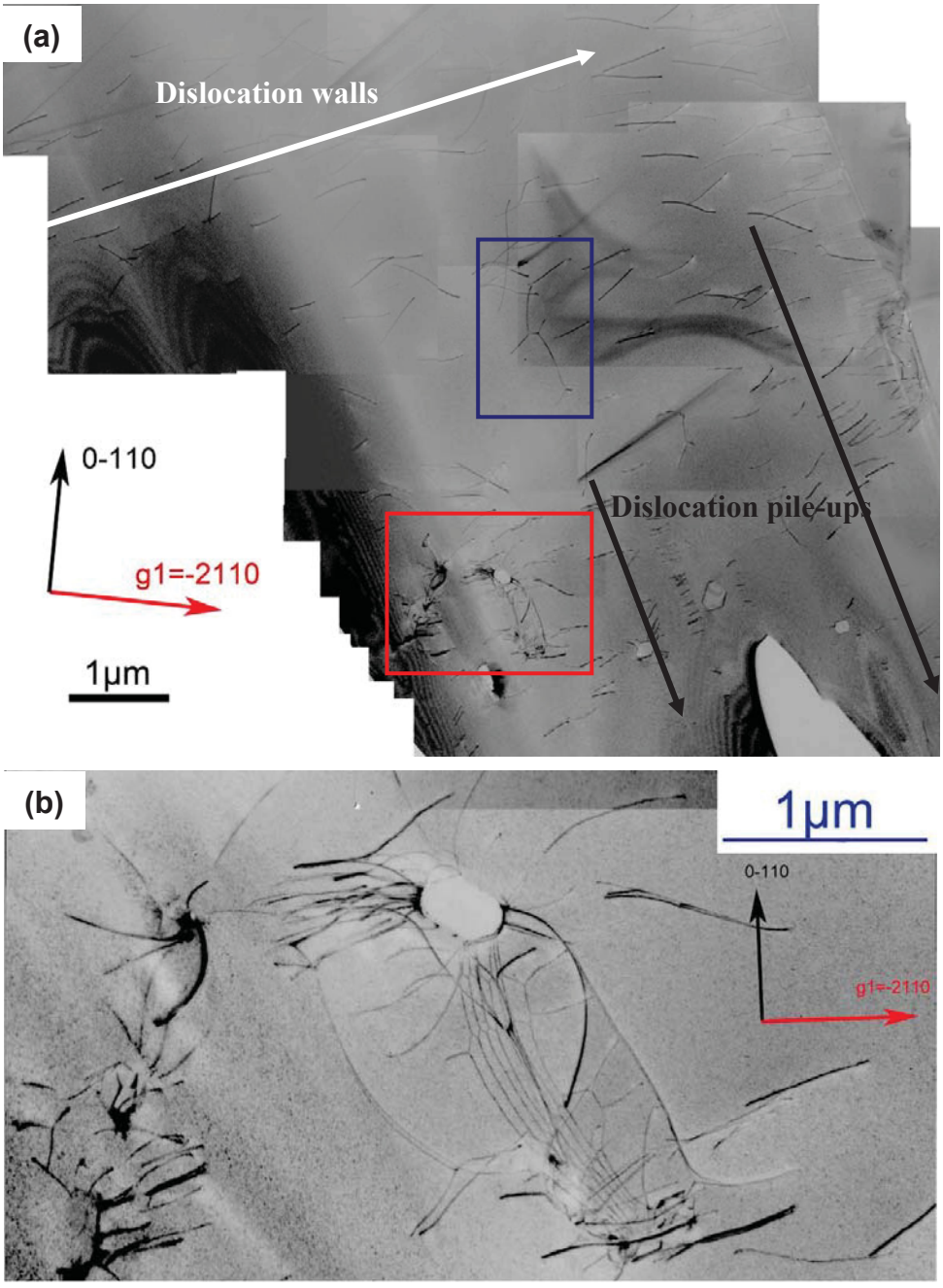

Figure 74: (a) High density of dislocations in the deformed $Ti_3Al_{0.8}Sn_{0.2}C_2$ solid solution. In the used diffraction condition, the basal plane is perpendicular to the electron beam. (b) enlarged image of the dislocation network in the red rectangle in (a).

Compared to the as-grown sample, the dislocation density is unambiguously increased after deformation. All the dislocations lie in the basal plane and they are arranged in pile-ups.

In this deformed material, dislocation walls are also observed but without any evidence of increase of their density compared to the as-grown samples. Figure 74(b) shows dislocations nucleated at the interface between $Ti_3Al_{0.8}Sn_{0.2}C_2$ solid solution and an inclusion. The dislocations form a net. However, it is not possible to determine the exact nature of the dislocation interactions.

Figure 75 shows a dislocation configuration imaged with two different diffraction g vectors, g_1=-2110, g_2=–g_1=2-1-10, respectively. Comparing the two images, we clearly observe different distances between the dislocation contrasts. Such a feature is characteristic of dislocation dipoles. Actually, dislocation dipoles are observed in many grains of $Ti_3Al_{0.8}Sn_{0.2}C_2$ as well as in Ti_2AlN[204] or Ti_4AlN_3[204]. Dislocation dipoles appear then to be a characteristic microstructure of, at least, Ti-Al-N and Ti-Al-C MAX phases and may be of all MAX phases. The presence of these dipoles is consistent with the difficulty to glide in plane different from the basal plane in these very anisotropic structures. However, further TEM investigations are necessary to determine the characteristics of these dipoles and their role in the deformation mechanism.

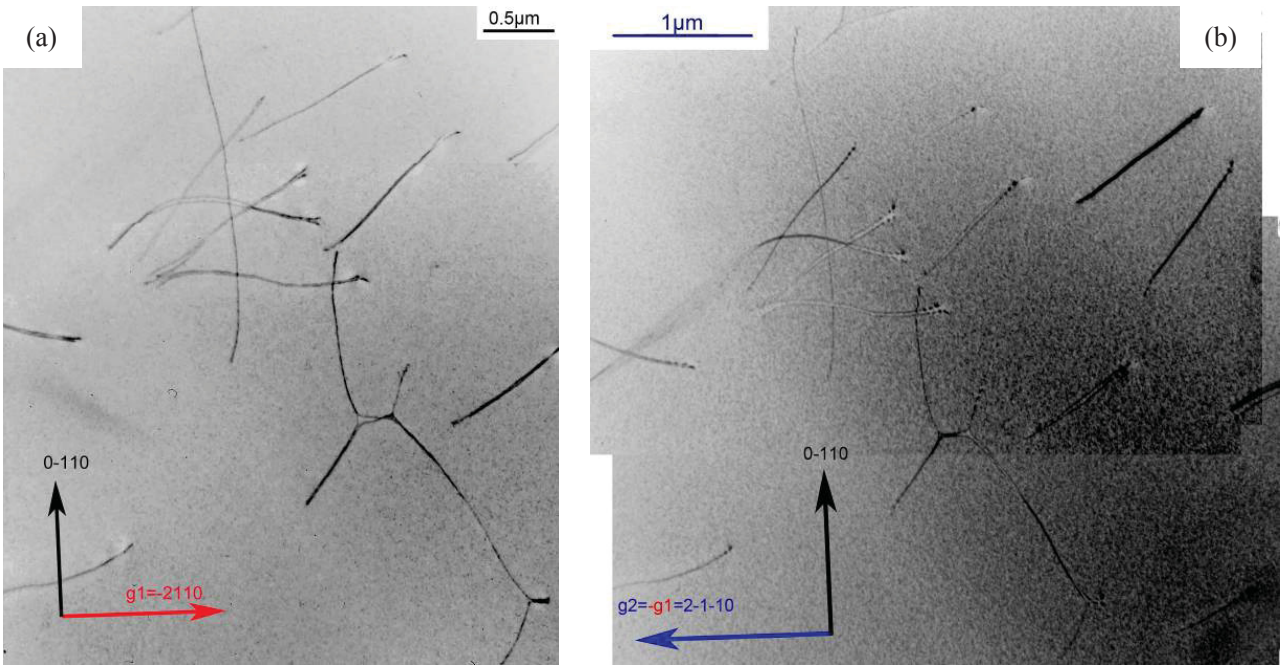

Figure 75: Dislocation dipoles (enlarged image of the blue rectangle in Figure74 (a)) in deformed $Ti_3Al_{0.8}Sn_{0.2}C_2$ solid solution characterized by different g diffraction vectors, (a) g_1=-2110, (b) g_2=-g_1=2-1-10.

In summary, polycrystalline $Ti_3Al_{0.8}Sn_{0.2}C_2$ solid solution can be plastically deformed with a confining gas pressure at room temperature in the Paterson machine. The strain hardening and maximum stress of $Ti_3Al_{0.8}Sn_{0.2}C_2$ solid solution is higher than the one for the Ti_3AlC_2 under the same compression condition. Such kind of enhancement of the compressive strength is mainly attributed to the grain size effect and the Ti_xAl_y intermetallics located in the grain boundaries. From SEM observations, the deformed microstructure of $Ti_3Al_{0.8}Sn_{0.2}C_2$ is not as catastrophic as Ti_3AlC_2 and multiple deformation mechanisms such as intra-granular crack, delamination of individual grains, grain pull-out, grain push-in, grain boundary cracks and grain buckling are observed. The TEM observations of the as-grown $Ti_3Al_{0.8}Sn_{0.2}C_2$ sample show that low density of dislocations and stacking faults lie in the basal plane. With the further investigations on the deformed $Ti_3Al_{0.8}Sn_{0.2}C_2$ microstructure, high density of dislocations is observed. Besides dislocation pile-ups, dislocation walls and, new features, dislocation dipoles and dislocation entanglements, are observed in the deformed samples. All these features play important roles in the deformation process.

V-3. Conclusions

In this Chapter, a set of $Ti_3Al_xSn_{(1-x)}C_2$ MAX phase solid solutions have been successfully synthesized from different reactant mixtures by HIPing process. The microstructures of these solid solutions are characterized by SEM coupled with EDXS and Rietveld refinements of XRD data. It is shown that 312 solid solutions are likely formed from reaction between TiC and 211 solid solutions. The c/a ratio changes linearly with the Al content in the solid solution which is consistent with the formation of an ideal solid solution and follows the Vegard's law [193]. Moreover, it has been shown that in Ti_3SnC_2 and Ti_3AlC_2, hexagonal unit cell is strongly distorted: [Ti_6C] octahedra are mainly distorted in Ti_3SnC_2 whereas [Ti_6Al] trigonal prisms are mainly distorted in Ti_3AlC_2.

Nanoindentation tests are used to measure the intrinsic hardness and elastic modulus of $Ti_3Al_xSn_{(1-x)}C_2$ (x=0, 0.25, 0.5, 0.8, 1) solid solutions. The intrinsic hardness and elastic modulus of $Ti_3Al_xSn_{(1-x)}C_2$ solid solutions are in the 7-11GPa range and 200-260GPa range, respectively. Elastic modulus and hardness values of $Ti_3Al_xSn_{(1-x)}C_2$ solid solutions do not

vary monotonically with the Al content and are smaller than the ones of end-members. Thus, it can be concluded that no solid solution strengthening effect occurs in the Ti-Al-Sn-C system. With the dynamic resonant method, the measured Young's modulus of $Ti_3Al_{0.8}Sn_{0.2}C_2$ slightly varies with temperature in the 20-450°C temperature range and the measured RT Young's modulus is in good agreement with the one determined by nanoindentation tests.

Like most of the MAX phases, $Ti_3Al_{0.8}Sn_{0.2}C_2$ solid solution belongs to KNE solids. The cyclic compressive stress-strain loops for $Ti_3Al_{0.8}Sn_{0.2}C_2$ are typical hysteretic and fully reversible. As for Ti_3AlC_2, $Ti_3Al_{0.8}Sn_{0.2}C_2$ solid solution fractured in shear mode and the maximum stress of $Ti_3Al_{0.8}Sn_{0.2}C_2$ is higher than the one of Ti_3AlC_2 at RT. The enhancement of the maximum stress in $Ti_3Al_{0.8}Sn_{0.2}C_2$ is mainly attributed to grain size effect and to the presence of Ti_xAl_y intermetallics distributed in the grain boundaries. By SEM observations, the main deformation mechanisms of $Ti_3Al_{0.8}Sn_{0.2}C_2$ are crack deflection, delamination and kink bands formation.

Polycrystalline $Ti_3Al_{0.8}Sn_{0.2}C_2$ solid solution can be plastically deformed under a confining gas pressure at RT in the Paterson machine. Due to the grain size effect and to the presence of Ti_xAl_y intermetallics distributed in the grain boundaries, the strain hardening and maximum stress of $Ti_3Al_{0.8}Sn_{0.2}C_2$ solid solution are higher than the ones of Ti_3AlC_2 under the similar compression condition. From SEM observations, the deformed microstructure of $Ti_3Al_{0.8}Sn_{0.2}C_2$ is not as catastrophic as the one of Ti_3AlC_2; intragranular cracks, delamination of individual grains, grain pull-out, grain push-in, grain boundary cracks and grain buckling *etc.* are observed in the deformed microstructures. TEM investigations on the as-grown $Ti_3Al_{0.8}Sn_{0.2}C_2$ solid solution show stacking faults and low density of dislocations, when for deformed sample, a significant increase of the dislocation density is observed. The dislocations in the deformed sample are mainly dislocation pile-ups and walls. In addition, two new features, dislocation dipoles and interactions, are observed in the deformed MAX phase sample for the first time. These defects need to be further investigated for a better understanding of the deformation mechanisms of MAX phases.

Conclusions and Perspectives

In this work, Ti_3SnC_2 and Ti_3AlC_2 as well as $Ti_3Al_xSn_{(1-x)}C_2$ solid solutions have been successfully synthesized using HIPing technique. The microstructures and some of the mechanical properties of these ternary carbides have been investigated by various methods. The main highlights of this thesis are summarized as follows:

A new 312 MAX phase, Ti_3SnC_2, has been discovered in the Ti-Sn-C system. The unit cell of Ti_3SnC_2 is isostructural with Ti_3SiC_2 with lattice parameters a=0.31366±0.00002 nm and c=1.8650±0.0002 nm. It has been shown that Fe is an efficient additive to promote Ti_3SnC_2 formation. Indeed, bulk samples with high Ti_3SnC_2 content (about 80 vol.%) are obtained by HIPing a 3Ti:Sn:2C:0.6Fe (at.%) reactant mixture at 1150°C and 50MPa for 10h. The study of the Ti_3SnC_2 reaction mechanisms using Fe as additive suggests that the MAX phase formation starts, at about 1100°C, from Ti_5Sn_3 and TiC and/or from Ti_2SnC and TiC intermediate products; the presence of the Fe_xSn_y liquid phase promotes the 312 phase formation which likely precipitates from the melt.

Highly pure and dense Ti_3AlC_2 samples have been produced by sintering a Ti:Al:1.9TiC reactant mixture at 1450°C for 2h and 50MPa for 1h using HIPing technique. Compared to the results reported in the literature on the synthesis of Ti_3AlC_2 using HIPing technique [36], the (P,T) cycle used in the frame of this thesis is optimized (shorter holding time and lower pressure). The grains of the as-synthesized Ti_3AlC_2 MAX phase have a typical lamellar shape (60-100 μm in length and 10-40 μm in width).

A set of $Ti_3Al_xSn_{(1-x)}C_2$ solid solutions have been successfully synthesized from different reactant mixtures by HIPing process. It has been demonstrated that $Ti_3Al_xSn_{(1-x)}C_2$ are ideal solid solutions obeying to the Vegard's law since the c/a ratio varies linearly with the Al content. Moreover, it has been shown that the lattice contraction of $Ti_3Al_xSn_{(1-x)}C_2$ is strongly anisotropic. Further investigations on the distortion parameters of octahedrons and trigonal prisms in the $Ti_3Al_xSn_{(1-x)}C_2$ solid solutions show that both polyhedrons are distorted whatever is the Al content. Ti_3SnC_2 shows strong distortion of the octahedron contrary to Ti_3AlC_2.

The intrinsic hardness of Ti_3SnC_2, Ti_3AlC_2 and $Ti_3Al_xSn_{(1-x)}C_2$ (x=0.25, 0.5, 0.8) solid

solutions has been measured by nanoindentation tests. The as-measured intrinsic hardness, in the 7-11GPa range, does not vary monotonically with the Al content; the highest value being obtained for Ti_3AlC_2 and the lowest for $Ti_3Al_{0.25}Sn_{0.75}C_2$ solid solution. Consequently, it has been demonstrated that there is no solid solution hardening in the Ti-Al-Sn-C system, but a solid solution softening. Moreover, from a comparison of the hardness measured by micro and nanoindentation tests, it has been shown that the hardness of MAX phase evaluated by microindentation tests is underestimated. Since several grains are involved in the deformation process, grain boundaries and impurities affect the measured hardness value which is indeed the mean hardness of a bulk polycrystalline sample.

The elastic modulus of Ti_3SnC_2, Ti_3AlC_2 as well as $Ti_3Al_xSn_{(1-x)}C_2$(x=0.25, 0.5, 0.8) solid solutions has been determined by nanoindentation tests. The elastic modulus, in the 200-260GPa range, does not vary linearly with the Al content in the solid solutions. As it is the case for hardness measurements, the highest elastic modulus value is related to Ti_3AlC_2 and the lowest to $Ti_3Al_{0.25}Sn_{0.75}C_2$ solid solution. It can be further concluded that no solid solution strengthening is operative in the Ti-Al-Sn-C system.

The temperature dependency of $Ti_3Al_{0.8}Sn_{0.2}C_2$ Young's modulus has been studied in the 20-450°C temperature range by dynamic resonant method. The measured Young's modulus of $Ti_3Al_{0.8}Sn_{0.2}C_2$ slightly varies with temperature and the measured RT Young's modulus is in good agreement with the one determined by nanoindentation tests.

The loading-unloading compressive stress-strain curves of Ti_3AlC_2 and $Ti_3Al_{0.8}Sn_{0.2}C_2$ solid solution obtained at RT from the Instron uniaxial compression machine are typically hysteretic and fully reversible. This demonstrates that, like other MAX phases and MAX phase solid solutions, Ti_3AlC_2 and $Ti_3Al_{0.8}Sn_{0.2}C_2$ belong to KNE solids. At failure, both Ti_3AlC_2 and $Ti_3Al_{0.8}Sn_{0.2}C_2$ solid solution fracture in a shear mode. The maximum stress of $Ti_3Al_{0.8}Sn_{0.2}C_2$ solid solution (839MPa, 0.5% plastic strain) is higher that the one of Ti_3AlC_2 (545MPa, 0.6% plastic strain) due to the grain size effect and to the presence of ductile Ti_xAl_y intermetallics in the grain boundaries. Kink bands and delaminations, crack deflections, grain bending, grain pull-out and push-out, grain decohesion, intergranular fracture are observed

near the fatal cracks on the surface of the deformed Ti_3AlC_2 sample. For $Ti_3Al_{0.8}Sn_{0.2}C_2$ solid solution, the main energy dissipation mechanisms near the fatal cracks are crack deflections along the grain boundaries.

Ti_3AlC_2 and $Ti_3Al_{0.8}Sn_{0.2}C_2$ solid solution have been successfully plastically deformed under a confining gas pressure at RT in the Paterson machine. The compressive stress-strain curves of these two carbides exhibit three regimes: 1) elastic regime, 2) hardening regime and 3) softening regime. Under a confining pressure, the maximum stress and plastic strains are much higher than the ones resulting from uniaxial compression tests. Indeed, under confining pressure, the plastic strain attains almost 6% without reaching the Ti_3AlC_2 sample ruin and the maximum RT compressive stress is 1180MPa. For the solid solution sample, a plastic strain of 3% can be reached without brittle rupture. The strain hardening and maximum stress of $Ti_3Al_{0.8}Sn_{0.2}C_2$ are higher than those of Ti_3AlC_2 despite identical deformation conditions. As evoked above, this may be attributed to the grain size effect and to the presence of ductile Ti_xAl_y intermetallics in the grain boundaries of the solid solution. The deformed microstructure of $Ti_3Al_{0.8}Sn_{0.2}C_2$ is not as catastrophic as the one observed in Ti_3AlC_2. Compared to Ti_3AlC_2, besides the multiple deformation mechanisms such as intra-granular failure, delamination of individual grains, grain pull-out, grain push-out, grain boundary cracks and grain buckling, Ti_xAl_y intermetallics also play an important role to accommodate the deformation during the compression test in the Paterson press. In Ti_3AlC_2 and $Ti_3Al_{0.8}Sn_{0.2}C_2$ solid solution, plastic deformation at RT is associated to a high density of dislocations, such as, dislocation walls, dislocation pile-ups and dislocation networks; dislocations being confined in the basal plane. New features, such as dislocation dipoles and dislocations interactions, are observed in the deformed $Ti_3Al_{0.8}Sn_{0.2}C_2$ samples.

This PhD thesis opens some prospects:

- *ab-initio* calculations should allow to better understand the influence of M-A and M-X bond stiffness of the octahedrons and trigonal prism distortion on the elastic properties of solid solutions.
- Hardness and elastic modulus values determined from nanoindentation tests seem to

be anisotropic (which is indeed expected due to the structure anisotropy of MAX phases). Such a feature is studied in the PPRIME Institute by C. Tromas et al. by coupling nanoindentation tests and EBSD. The anisotropy of the electrical transport properties are also currently studied by S. Dubois and V. Mauchamp et al.

- Dislocation dipoles observed in all Ti-A-C and Ti-A-N systems have to be studied in details to reach a better understanding of their role in the deformation mechanisms.
- Although the KNE model seems to work for Ti_3AlC_2 and $Ti_3Al_{0.8}Sn_{0.2}C_2$ MAX phases, the existence of Incipient Kink Bands has never been demonstrated experimentally. MAX phase micro-pillars have recently been deformed in Switzerland under a neutron microdiffraction line. IKB may be evidenced with this kind of experiment.

References

1 M. W. Barsoum, The $M_{N+1}AX_N$ phases: A new class of solids thermodynamically stable nanolaminates, *Progress in Solid State Chemistry*, 28 (1-4), 201-281, 2000.

2 M. X. Ai, H. X. Zhai, Y. Zhou, Z. Y. Tao, Z. Y. Huang, Z. L. Zhang and S. B. Li, Synthesis of Ti_3AlC_2 powders using Sn as an additive, *Journal of the American Ceramic Society*, 89 (3), 1114-1117, 2006.

3 S. B. Li, W. H. Xiang, H. X. Zhai, Y. Zhou, C. W. Li and Z. L. Zhang, Formation of a single-phase Ti_3AlC_2 from a mixture of Ti, Al and TiC powders with Sn as an additive, *Materials Research Bulletin*, 43 (8-9), 2092-2099, 2008.

4 M. W. Barsoum, T. Zhen, A. Zhou, S. Basu and S. R. Kalidindi, Microscale modeling of kinking nonlinear elastic solids, *Physical Review B - Condensed Matter and Materials Physics*, 71 (13), 1-8, 2005.

5 M. W. Barsoum and S.Basu, Kinking Nonlinear Elastic Solids, *Encyclopedia of Materials: Science and Technology*, Elsevier, Oxford, 1-23, 2010.

6 W. Jeitschko, H. Nowotny and F. Benesovsky, Kohlen-stoffhaltige ternare Verbindungen (H-Phase), *Monatshefte für Chemie*, 94 (4), 672-676, 1963.

7 W. Jeitschko, H. Nowotny and F. Benesovsky, Die H-phasen Ti_2TlC, Ti_2PbC, Nb_2InC, Nb_2SnC und Ta_2GaC, *Monatshefte für Chemie*, 95 (2), 431-435 1964.

8 W. Jeitschko and H. Nowotny, Die Kristallstructur von Ti_3SiC_2-Ein Neuer Komplxcarbid-Typ, *Monatshefte für Chemie*, 98 (2), 329-337, 1967.

9 H. Wolfsgruber, H. Nowotny and F. Benesovsky, Die Kristallstuktur von Ti_3GeC_2, *Monatshefte für Chemie*, 98 (6), 2401-2405, 1967.

10 V. H. Nowotny, Strukturchemie einiger Verbindungen der Übergangsmetalle mit den elementen C, Si, Ge, Sn, *Progress in Solid State Chemistry*, 5 (C), 27-70, 1971.

11 M. W. Barsoum and T. El-Taghy, The MAX phases: Unique new carbide and nitride materials, *American Scientist*, 89 (4), 334-343, 2001.

12 Z. J. Lin, M. J. Zhuo, Y. C. Zhou, M. S. Li and J. Y. Wang, Microstructures and theoretical bulk modulus of layered ternary tantalum aluminum carbides, *Journal of the American Ceramic Society*, 89 (12), 3765-3769, 2006.

13 J. Etzkorn, M. Ade and H. Hillebrecht, Ta_3AlC_2 and Ta_4AlC_3-single crystal investigation of two new ternary carbides of tantalum synthesized by the molten metal technique, *Inorganic Chemistry*, 46 (4), 1410-1418, 2007.

14 H. Hillebrecht and D. Kotzott, Ternary Carbides Ti_3MC_2 (M = Al, Si, Ga, Ge) -Synthesis, Crystal Growth, Solid Solutions and Micro-Hardness Measurements, *Proceedings of the Materials Science and Technology Conference*, Pittsburgh, USA, 2009.

15 S. Dubois, T. Cabioc'h, P. Chartier, V. Gauthier and M. Jaouen, A new ternary nanolaminate carbide: Ti_3SnC_2, *Journal of the American Ceramic Society*, 98 (8), 2642-2644, 2007.

16 Z. J. Lin, M. J. Zhuo, Y. C. Zhou, M. S. Li and J. Y. Wang, Structural characterization of a new layered-ternary Ta_4AlC_3 ceramic, *Journal of Materials Research*, 21 (10), 2587-2592, 2006.

17 P. Eklund, J.-P. Palmquist, J. Höwing, D. H. Trinh, T. El-Raghy and L. H. H. Högberg, Ta_4AlC_3: Phase determination, polymorphism and deformation, *Acta Materialia*, 55 (14), 4723-4729, 2007.

18 C. Hu, Z. J. Lin, L. He, Y. Bao, J. Y. Wang, M. S. Li and Y. C. Zhou, Physical and mechanical properties of bulk Ta_4AlC_3 ceramic prepared by an in situ reaction synthesis/hot-pressing method,

Journal of the American Ceramic Society, 90 (8), 2542-2548, 2007.

19 C. Hu, F. Li, J. Zhang, J. Y. Wang and Y. C. Zhou, Nb_4AlC_3: A new compound belonging to the MAX phases, *Scripta Materialia*, 57 (10), 893-896, 2007.

20 H. Högberg, L. Hultman, J. Emmerlich, T. Joelsson, P. Eklund, J. M. M.Aldareguia, J. P. Palmquist and U. Jansson, Growth and characterization of MAX-phase thin films, *Surface and Coatings Technology*, 193 (1-3 SPEC. ISS.), 6-10, 2005.

21 H. Högberg, P. Eklund, J. Emmerlich, J. Birch and L. Hultman, Epitaxial Ti_2GeC, Ti_3GeC_2, and Ti_4GeC_3 MAX-phase thin films grown by magnetron sputtering, *Journal of Materials Research*, 20 (4), 779-782, 2005.

22 J. Etzkorn, M. Ade, D. Kotzott, M. Kleczek and H. Hillebrecht, Ti_2GaC, Ti_4GaC_3 and Cr_2GaC-Synthesis, crystal growth and structure analysis of Ga-containing MAX-phases $M_{n+1}GaC_n$ with M=Ti, Cr and n=1, 3, *Journal of Solid State Chemistry*, 182 (5), 995-1002, 2009.

23 C. Hu, J. Zhang, J. Wang, F. Li, J. Wang and Y. C. Zhou, Crystal structure of V_4AlC_3: A new layered ternary carbide, *Journal of the American Ceramic Society*, 91 (2), 636-639, 2008.

24 M. W. Barsoum and T. El-Raghy, Synthesis and characterization of a remarkable ceramic: Ti_3SiC_2, *Journal of the American Ceramic Society*, 79 (7), 1953-1956, 1996.

25 M. W. Barsoum, D. Brodkin and T. El-Raghy, Layered machinable ceramics for high temperature applications, *Scripta Materialia*, 36 (5), 535-541, 1997.

26 T. El-Raghy, A. Zavaliangos, M. W. Barsoum and S. Kalidindi, Damage mechanisms around hardness indentations in Ti_3SiC_2, *Journal of the American Ceramic Society*, 80 (2), 513–516, 1997.

27 M. W. Barsoum and T. El-Raghy, Room temperature ductile carbides, *Metallurgical and Materials Transactions A*, 30 (2), 363-369, 1999.

28 M. W. Barsoum, L. Farber and T. El-Raghy, Dislocations, kink bands and room temperature plasticity of Ti_3SiC_2, *Metallurgical and Materials Transactions A*, 30 (7), 1727-1738, 1999.

29 T. El-Raghy and M. W. Barsoum, Processing and mechanical properties of Ti_3SiC_2: Part I. Reaction path and microstructure evolution, *Journal of the American Ceramic Society*, 82 (10), 2849-2854, 1999.

30 T. El-Raghy, M. W. Barsoum, A. Zavaliangos and S. Kalidindi, Processing and mechanical properties of Ti_3SiC_2: Part II. Mechanical properties, *Journal of the American Ceramic Society*, 82 (10), 2855–2860, 1999.

31 M. W. Barsoum, M. Ali and T. El-Raghy, Processing and characterization of Ti_2AlC, Ti_2AlN and $Ti_2AlC_{0.5}N_{0.5}$, *Metallurgical and Materials Transactions A*, 31 (7), 1857-1865, 2000.

32 P. Finkel, M. W. Barsoum and T. El-Raghy, Low temperature dependencies of the elastic properties of Ti_4AlN_3, $Ti_3Al_{1.1}C_{1.8}$, and Ti_3SiC_2, *Journal of Applied Physics*, 87 (4), 1701-1703, 2000.

33 J. Gilbert, D. R. Bloyer, M. W. Barsoum, T. El-Raghy, A. P. Tomsia and R. O. Ritchie, Fatigue-crack growth and fracture properties of coarse and fine-grained Ti_3SiC_2, *Scripta Materialia*, 42 (8), 761-767, 2000.

34 A. T. Procopio, M. W. Barsoum and T. El-Raghy, Characterization of Ti_4AlN_3, *Metallurgical and materials transactions. A*, 31 (2), 333-337, 2000.

35 M. Radovic, M. W. Barsoum, T. El-Raghy, J. Seidensticker and S. Wiederhorn, Tensile properties of Ti_3SiC_2 in the 25-1300^oC temperature range, *Acta Materialia*, 48 (2), 453-459, 2000.

36 N. V. Tzenov and M. W. Barsoum, Synthesis and characterization of Ti_3AlC_2, *Journal of the American Ceramic Society*, 83 (4), 825-832, 2000.

37 I. Chen, K. Shirato, M. W. Barsoum, T. El-Raghy and R. O. Ritchie, Crack Growth and Fracture

Properties in Ti_3SiC_2 Ceramics at Elevated Temperatures, *Journal of the American Ceramic Society*, 84 (12), 2914-2920, 2001.

38 M. Radovic, M. W. Barsoum, T. El-Raghy and S. Wiederhorn, Tensile creep of fine-grained (3-5 mm) Ti_3SiC_2 in the 1000-1200^{o}C temperature range, *Acta Materialia*, 49 (19), 4103-4112 2001.

39 M. Radovic, M. W. Barsoum, T. El-Raghy, S. M. Wiederhorn and W. E. Luecke, Effect of temperature, strain rate and grain size on the mechanical response of Ti_3SiC_2 in tension, *Acta Materialia*, 50 (6), 1297-1306, 2002.

40 M. W. Barsoum, T. Zhen, S. Kalidindi, M. Radovic and A. Murugaiah, Fully reversible, dislocation-based compressive deformation of Ti_3SiC_2 up to 1 GPa, *Nature Materials*, 2, 107 - 111, 2003.

41 M. Radovic, M. W. Barsoum, T. El-Raghy and S. M. Wiederhorn, Tensile creep of coarse-grained Ti_3SiC_2 in the 1000–1200°C temperature range, *Journal of Alloys and Compounds*, 361 (1-2), 299-312, 2003.

42 Z. Sun, S. Li, R. Ahuja and J. M. Schneider, Calculated elastic properties of M_2AlC (M = Ti, V, Cr, Nb and Ta), *Solid State Communications*, 129 (9), 589-592, 2004.

43 J. D. Hettinger, S. E. Lofland, P. Finkel, T. Meehan, J. Palma, K. Harrell, S. Gupta, A. Ganguly, T. El-Raghy and M. W. Barsoum, Electrical transport, thermal transport, and elastic properties of M_2AlC (M=Ti, Cr, Nb, and V), *Physical Review B - Condensed Matter and Materials Physics*, 72 (11), 1-6, 2005.

44 Z. Lin, Y. Zhou, M. Li and J. Wang, In-situ hot pressing/solid-liquid reaction synthesis of bulk Cr 2AlC, *Zeitschrift fuer Metallkunde/Materials Research and Advanced Techniques*, 96 (3), 291-296, 2005.

45 M. W. Barsoum and M. Radovic, Physical properties of the MAX phases, *Encyclopedia of Materials: Science and Technology*, 2006.

46 M. Radovic, M. W. Barsoum, A. Ganguly, T. Zhen, P. Finkel, S. R. Kalidindi and E. Lara-Curzio, On the elastic properties and mechanical damping of Ti_3SiC_2, Ti_3GeC_2, $Ti_3Si_{0.5}Al_{0.5}C_2$ and Ti_2AlC in the 300-1573 K temperature range, *Acta Materialia*, 54 (10), 2757-2767, 2006.

47 W. Tian, P. Wang, G. Zhang, Y. Kan, Y. Li and D. Yan, Synthesis and thermal and electrical properties of bulk Cr_2AlC, *Scripta Materialia*, 54 (5), 841-846, 2006.

48 Z. J. Lin, M. S. Li, J. Y. Wang and Y. C. Zhou, High-temperature oxidation and hot corrosion of Cr_2AlC, *Acta Materialia*, 55 (18), 6182-6191, 2007.

49 W. B. Tian, P. L. Wang, G. J. Zhang, Y. M. Kan and Y. X. Li, Mechanical properties of Cr_2AlC ceramics, *Journal of the American Ceramic Society*, 90 (5), 1663-1666, 2007.

50 P. Wang, B. C. Mei, X. L. Hong and W. B. Zhou, Synthesis of Ti_2AlC by hot pressing and its mechanical and electrical properties, *Transactions of Nonferrous Metals Society of China (English Edition)*, 17 (5), 1001-1004, 2007.

51 M. A. Pietzka and J. C. Schuster, Summary of constitutional data on the Aluminum-Carbon-Titanium system, *Journal of Phase Equilibria*, 15 (4), 392-400, 1994.

52 X. Wang and Y. Zhou, Solid-liquid reaction synthesis of layered machinable Ti_3AlC_2 ceramic, *Journal of Materials Chemistry*, 12 (3), 455-460, 2002.

53 X. H. Wang and Y. C. Zhou, Microstructure and properties of Ti_3AlC_2 prepared by the solid-liquid reaction synthesis and simultaneous in-situ hot pressing process, *Acta Materialia*, 50 (12), 3141-3149, 2002.

54 A. Zhou, C. A. Wang and Y. Huang, A possible mechanism on synthesis of Ti_3AlC_2, *Materials*

Science and Engineering A, 352 (1-2), 333-339, 2003.

55 J. Zhu, B. Mei, X. Xu and J. Liu, Synthesis of single-phase polycrystalline Ti_3SiC_2 and Ti_3AlC_2 by hot pressing with the assistance of metallic Al or Si, *Materials Letters*, 58 (5), 588-592, 2004.

56 H. Zhai, Z. Huang, M. Ai, Y. Zhou, Z. Zhang and S. Li, Tribophysical properties of polycrystalline bulk Ti_3AlC_2, *Journal of the American Ceramic Society*, 88 (11), 3270-3274, 2005.

57 J. H. Han, S. S. Hwang, D. Lee and S. W. Park, Synthesis and mechanical properties of Ti_3AlC_2 by hot pressing TiC_x/Al powder mixture, *Journal of the European Ceramic Society*, 28 (5), 979-988, 2008.

58 A. Zhou, C. A. Wang and Y. Hunag, Synthesis and mechanical properties of Ti_3AlC_2 by spark plasma sintering, *Journal of Materials Science*, 38 (14), 3111-3115, 2003.

59 W. Zhou, B. Mei, J. Zhu and X. Hong, Synthesis of high-purity Ti_3SiC_2 and Ti_3AlC_2 by spark plasma sintering (SPS) technique, *Journal of Materials Science*, 40 (8), 2099-2100, 2005.

60 Y. Zou, Z. Sun, H. Hashimoto and S. Tada, Low temperature synthesis of single-phase Ti_3AlC_2 through reactive sintering Ti/Al/C powders, *Materials Science and Engineering A*, 473 (1-2), 90-95, 2008.

61 Y. Zou, Z. Sun, H. Hashimoto and S. Tada, Synthesis of high-purity polycrystalline Ti_3AlC_2 through pulse discharge sintering Ti/Al/TiC powders, *Journal of Alloys and Compounds*, 456 (1-2), 456-460, 2008.

62 Y. Zou, Z. Sun, S. Tada and H. Hashimoto, Synthesis reactions for Ti_3AlC_2 through pulse discharge sintering Ti/Al_4C_3/TiC powder mixture, *Scripta Materialia*, 55 (9), 767-770, 2006.

63 Y. Zou, Z. Sun, S. Tada and H. Hashimoto, Rapid synthesis of single-phase Ti_3AlC_2 through pulse discharge sintering a TiH_2/Al/TiC powder mixture, *Scripta Materialia*, 56 (9), 725-728, 2007.

64 Y. Zou, Z. M. Sun, H. Hashimoto and L. Cheng, Synthesis reactions for Ti_3AlC_2 through pulse discharge sintering TiH_2/Al/C powder mixture, *Journal of Alloys and Compounds*, 468 (1-2), 217-221, 2009.

65 C. Peng, C. A. Wang, Y. Song and Y. Huang, A novel simple method to stably synthesize Ti_3AlC_2 powder with high purity, *Materials Science and Engineering A*, 428 (1-2), 54-58, 2006.

66 S. B. Li, H. X. Zhai, G. P. Bei, Y. Zhou and Z. L. Zhang, Synthesis and microstructure of Ti_3AlC_2 by mechanically activated sintering of elemental powders, *Ceramics International*, 33 (2), 169-173, 2007.

67 A. Zhou, C. A. Wang, Z. Ge and L. Wu, Preparation of Ti_3AlC_2 and Ti_2AlC by self-propagating high-temperature synthesis, *Journal of Materials Science Letters*, 20 (21), 1971-1973, 2001.

68 M. Łopacinski, J. Puszynski and J. Lis, Synthesis of Ternary Titanium Aluminum Carbides Using Self-Propagating High-Temperature Synthesis Technique, *Journal of the American Ceramic Society*, 84 (3-12), 3051-3053, 2001.

69 Z. Ge, K. Chen, J. Guo, H. Zhou and J. M. F. Ferreira, Combustion synthesis of ternary carbide Ti_3AlC_2 in Ti-Al-C system, *Journal of the European Ceramic Society*, 23 (3), 567-574, 2003.

70 G. Liu, K. Chen, H. Zhou, J. Guo, K. Ren and J. M. F. Ferreira, Layered growth of Ti_2AlC and Ti_3AlC_2 in combustion synthesis, *Materials Letters*, 61 (3), 779-784, 2007.

71 C. L. Yeh and Y. G. Shen, Combustion synthesis of Ti_3AlC_2 from Ti/Al/C/TiC powder compacts, *Journal of Alloys and Compounds*, 466 (1-2), 308-313, 2008.

72 B. Holm, R. Ahuja and B. Johansson, Ab initio calculations of the mechanical properties of Ti_3SiC_2, *Applied Physics Letters*, 79 (10), 1450-1452, 2001.

73 J. Y. Wang and Y. C. Zhou, Ab initio investigation of the electronic structure and bonding properties

of the layered ternary compound Ti_3SiC_2 at high pressure, *Journal of Physics Condensed Matter*, 15 (12), 1983-1991, 2003.

74 Y. C. Zhou, X. H. Wang, Z. M. Sun and S. Q. Chen, Electronic and structural properties of the layered ternary carbide Ti_3AlC_2, *Journal of Materials Chemistry*, 11 (9), 2335-2339, 2001.

75 Z. Sun, R.Ahuja and J. M. Schneider, Theoretical investigation of the solubility in $(M_xM'^{2-x})AlC$ (M and M'=Ti, V and Cr), *Physical Review B - Condensed Matter and Materials Physics*, 68 (22), 224112.224111-224112.224114, 2003.

76 H. Nowotny, P. Rogl and J. C. Schuster, Structural chemistry of complex carbides and related compounds, *Journal of Solid State Chemistry*, 44 (1), 126-133, 1982.

77 J. Y. Wang and Y. C. Zhou, Ab initio elastic stiffness of nano-laminate $(M_xM'_{2-x})AlC$(M and M' = Ti, V and Cr) solid solution, *Journal of Physics Condensed Matter*, 16 (16), 2819-2827, 2004.

78 S. H. Jhi, J. Ihm, S. G. Loule and M. L. Cohen, Electronic mechanism of hardness enhancement in transition-metal carbonitrides, *Nature*, 399 (6732), 132-134, 1999.

79 J. Y. Wang and Y. C. Zhou, First-principles study of equilibrium properties and electronic structure of $Ti_3Si_{0.75}Al_{0.25}C_2$ solid solution, *Journal of Physics Condensed Matter*, 15 (35), 5959-5968, 2003.

80 X. Xu, E. Wu, X. Du, Y. Tian and J. He, First-principle study of electronic properties of $Ti_3Si_{1-x}Al_xC_2$ solid solutions, *Journal of Physics and Chemistry of Solids*, 69 (5-6), 1356-1361, 2008.

81 H. B. Zhang, Y. C. Zhou, Y. W. Bao and M. S. Li, Improving the oxidation resistance of Ti_3SiC_2 by forming a $Ti_3Si_{0.9}Al_{0.1}C_2$ solid solution, *Acta Materialia*, 52 (12), 3631-3637, 2004.

82 Y. L. Du, Z. M. Sun, H. Hashimoto and M. W. Barsoum, Theoretical investigations on the elastic and thermodynamic properties of $Ti_2AlC_{0.5}N_{0.5}$ solid solution, *Physics Letters, Section A: General, Atomic and Solid State Physics*, 374 (1), 78-82, 2009.

83 P. Blaha, K. Schwarz, G. K. H. Madsen, D. Kvasnicka and J. Luitz, WIEN2k, An Augmented Plane Wave plus Local Orbitals Program for Calculating Crystal Properties, *Techn. Universität Wien, Austria*, Vienna, 2007.

84 M. Radovic, A. Ganguly and M. W. Barsoum, Elastic properties and phonon conductivities of $Ti_3Al(C_{0.5},N_{0.5})_2$ and $Ti_2Al(C_{0.5},N_{0.5})$ solid solutions, *Journal of Materials Research*, 23 (6), 1517-1521, 2008.

85 I. Salama, T. El-Raghy and M. W. Barsoum, Synthesis and mechanical properties of Nb_2AlC and $(Ti,Nb)_2AlC$, *Journal of Alloys and Compounds*, 347 (1-2), 271-278, 2002.

86 F. L. Meng, Y. C. Zhou and J. Y. Wang, Strengthening of Ti_2AlC by substituting Ti with V, *Scripta Materialia*, 53 (12), 1369-1372, 2005.

87 N. A. Phatak, S. K. Saxena, Y. W. Fei and J. Z. Hu, Synthesis of a new MAX compound $(Cr_{0.5}V_{0.5})_2GeC$ and its compressive behavior up to 49GPa, *Journal of Alloys and Compounds*, 475 (1-2), 629-634 2009.

88 Y. Zhou, F. Meng and J. Zhang, New MAX-phase compounds in the V-Cr-Al-C system, *Journal of the American Ceramic Society*, 91 (4), 1357-1360, 2008.

89 I. Salama, T. El-Raghy and M. W. Barsoum, Oxidation of Nb_2AlC and $(Ti,Nb)_2AlC$ in air, *Journal of the Electrochemical Society*, 150 (3), C152-C158, 2003.

90 M. W. Barsoum, I. Salama, T. El-Raghy, J. Golczewski, W. D. Porter, H. Wang, H. J. Seifert and F. Aldinger, Thermal and electrical properties of Nb_2AlC, $(Ti, Nb)_2AlC$ and Ti_2AlC, *Metallurgical and Materials Transactions A: Physical Metallurgy and Materials Science*, 33 (9), 2775-2779, 2002.

91 B. Manoun, F. Zhang, S. K. Saxena, S. Gupta and M. W. Barsoum, On the compression behaviour of $(Ti_{0.5},V_{0.5})_2AlC$ and $(Ti_{0.5},Nb_{0.5})_2AlC$ to quasi-hydrostatic pressures above 50 GPa, *Journal of*

Physics Condensed Matter, 19 (24) 2007.

92 S. Gupta and M. W. Barsoum, Synthesis and Oxidation of V_2AlC and $(Ti_{0.5}, V_{0.5})_2AlC$ in Air, *Journal of the Electrochemical Society*, 151 (2), D24-D29, 2004.

93 S. Gupta, E. N. Hoffman and M. W. Barsoum, Synthesis and oxidation of Ti_2InC, Zr_2InC, $(Ti_{0.5},Zr_{0.5})_2InC$ and $(Ti_{0.5},Hf_{0.5})_2InC$ in air, *Journal of Alloys and Compounds*, 426 (1-2), 168-175, 2006.

94 B. Manoun, O. D. Leaffer, S. Gupta, E. N. Hoffman, S. K. Saxena, J. E. Spainer and M. W. Barsoum, On the compression behavior of Ti_2InC, $(Ti_{0.5}, Zr_{0.5})InC$, and M_2SnC(M=Ti, Nb, Hf) to quasi-hydrostatic pressures up to 50GPa, *Solid state communications*, 149 (43-44), 1978-1983, 2009.

95 M. W. Barsoum, J. Golczewski, H. J. Seifert and F. Aldinger, Fabrication and electrical and thermal properties of Ti_2InC, Hf_2InC and $(Ti,Hf)_2InC$, *Journal of Alloys and Compounds*, 340 (1-2), 173-179, 2002.

96 A. Ganguly, T. Zhen and M. W. Barsoum, Synthesis and mechanical properties of Ti_3GeC_2 and $Ti_3(Si_xGe_{1-x})C_2$ (x = 0.5, 0.75) solid solutions, *Journal of Alloys and Compounds*, 376 (1-2), 287-295, 2004.

97 B. Manoun, H. P. Hermann, R. P. Gulve, S. K. Saxena, A. Ganguly, M. W. Barsoum and C. S. Zha, Compression of $Ti_3Si_{0.5}Ge_{0.5}C_2$ to 53 GPa, *Applied Physics Letters*, 84 (15), 2799-2801, 2004.

98 P. Finkel, B. Seaman, K. Harrell, J. Palma, J. D. Hettinger, S. E. Lofland, A. Ganguly, M. W. Barsoum, Z. Sun, S. Li and R. Ahuja, Electronic, thermal, and elastic properties of $Ti_3Si_{1-x}Ge_xC_2$ solid solutions, *Physical Review B - Condensed Matter and Materials Physics*, 70 (8), 085104-085101-085104-085106, 2004.

99 Y. C. Zhou, J. X. Chen and J. Y. Wang, Strengthening of Ti_3AlC_2 by incorporation of Si to form $Ti_3Al_{1-X}Si_xC_2$ solid solutions, *Acta Materialia*, 54 (5), 1317-1322, 2006.

100 J. X. Chen and Y. C. Zhou, Effect of Si content on the oxidation resistance of $Ti_3Al_{1-x}Si_x C_2$ ($x \leq 0.25$) solid solutions at 1000-1400^{o}C in air, *Oxidation of Metals*, 65 (1-2), 123-135, 2006.

101 J. X. Chen, Y. C. Zhou and J. Zhang, Abnormal thermal expansion and thermal stability of $Ti_3Al_{1-x}Si_xC_2$ solid solutions, *Scripta Materialia*, 55 (8), 675-678, 2006.

102 Y. Zhou, H. Zhang, M. Liu, J. Wang and Y. Bao, Preparation of TiC free Ti_3SiC_2 with improved oxidation resistance by substitution of Si with Al, *Materials Research Innovations*, 8 (2), 97-102, 2004.

103 B. Manoun, S. K. Saxena, G. Hu, A. Ganguly, E. N. Hoffman and M. W. Barsoum, Synthesis and compressibility of $Ti_3(Al,Sn_{0.2})C_2$ and $Ti_3Al(C_{0.5}N_{0.5})_2$, *Journal of Applied Physics*, 101 (11), 135231-135237, 2007.

104 P. Finkel, M. W. Barsoum and T. El-Raghy, Low temperature dependence of the elastic properties of Ti_3SiC_2, *Journal of Applied Physics*, 85 (10), 7123-7126, 1999.

105 T. H. Scabarozi, S. Amini, P. Finkel, O. D. Leaffer, J. E. Spanier, M. W. Barsoum, M. Drulis, H. Drulis, W. M. Tambussi, J. D. Hettinger and S. E. Lofland, Electrical, thermal, and elastic properties of the MAX-phase Ti_2SC, *Journal of Applied Physics*, 104 (3) 2008.

106 B. J. Kooi, R. J. Poppen, N. J. M. Carvalho, J. T. M. De Hosson and M. W. Barsoum, Ti_3SiC_2: A damage tolerant ceramic studied with nano-indentations and transmission electron microscopy, *Acta Materialia*, 51 (10), 2859-2872, 2003.

107 A. Murugaiah, M. W. Barsoum, S. R. Kalidindi and T. Zhen, Spherical nanoindentations and kink bands in Ti_3SiC_2, *Journal of Materials Research*, 19 (7), 2194-2203, 2004.

108 J. Emmerlich, H. Högberg, S. Sasvári, P. O. A. Persson, L. Hultman, J. P. Palmquist, U. Jansson, J. M.

Molina-Aldareguia and Z. Czigány, Growth of Ti_3SiC_2 thin films by elemental target magnetron sputtering, *Journal of Applied Physics*, 96 (9), 4817-4826, 2004.

109 O. Wilhelmsson, J. P. Palmquist, E. Lewin, J. Emmerlich, P. Eklund, P. O. A. Persson, H. Hogberg, S. Li, R. Ahuja, O. Eriksson, L. Hultman and U. Jansson, Deposition and characterization of ternary thin films within the Ti-Al-C system by DC magnetron sputtering, *Journal of Crystal Growth*, 291 (1), 290-300, 2006.

110 S. Amini, M. W. Barsoum and T. El-Raghy, Synthesis and mechanical properties of fully dense Ti_2SC, *Journal of the American Ceramic Society*, 90 (12), 3953-3958, 2007.

111 J. J. Nickl, K. K. Schweitzer and P. Luxenberg, Gasphasenabscheidung im system TiSiC, *Journal of The Less-Common Metals*, 26 (3), 335-353, 1972.

112 T. Goto and T. Hirai, Chemically vapor deposited Ti_3SiC_2, *Materials Research Bulletin*, 22 (9), 1195-1201, 1987.

113 Y. Zou, Z. Sun, H. Hashimoto and S. Tada, Mechanical behavior of Ti_3AlC_2 prepared by pulse discharge sintering method, *Materials Transactions*, 48 (9), 2432-2435, 2007.

114 N. F. Gao, Y. Miyamoto and D. Zhang, Dense Ti_3SiC_2 prepared by reactive HIP, *Journal of Materials Science*, 34 (18), 4385-4392, 1999.

115 X. Wang and Y. Zhou, Solid-liquid reaction synthesis and simultaneous densification of polycrystalline Ti_2AlC, *Zeitschrift fuer Metallkunde/Materials Research and Advanced Techniques*, 93 (1), 66-71, 2002.

116 S. B. Li, W. B. Yu, H. X. Zhai, G. M. Song, W. G. Sloof and S. van der Zwaag, Mechanical properties of low temperature synthesized dense and fine-grained Cr_2AlC ceramics, *Journal of the European Ceramic Society*, 31 (1-2), 217-224, 2010.

117 C. Hu, L. He, M. Liu, X. Wang, J. Wang, M. Li, Y. Bao and Y. Zhou, In situ reaction synthesis and mechanical properties of V_2AlC, *Journal of the American Ceramic Society*, 91 (12), 4029-4035, 2008.

118 M. W. Barsoum and M. Radovic, Mechanical properties of the MAX phases, *Encyclopedia of Materials: Science and Technology*, ISBN:0-08-043152-6, 1-16, 2004.

119 W. D. Callister, Fundamentals of Materials Science and Engineering, *Wiley & Sons*, 7 edition 2006.

120 Y. C. Zhou and X. H. Wang, Deformation of polycrystalline Ti_2AlC under compression *Materials Research Innovations*, 5 (2), 87-93, 2001.

121 W. Tian, Z. Sun, H. Hashimoto and Y. Du, Compressive deformation behavior of ternary compound Cr_2AlC, *Journal of Materials Science*, 44 (1), 102-107, 2009.

122 L. Farber, M. W. Barsoum, A. Zavaliangos, T. El-Raghy and I. Levin, Dislocations and stacking faults in Ti_3SiC_2, *Journal of the American Ceramic Society*, 81 (6), 1677-1681, 1998.

123 L. Farber, I. Levin and M. W. Barsoum, High-resolution transmission electron microscopy study of a low-angle boundary in plastically deformed Ti_3SiC_2, *Philosophical Magazine Letters*, 79 (4), 163-170, 1999.

124 A. Joulain, L. Thilly and J. Rabier, Revisiting the defect structure of MAX phases: The case of Ti_4AlN_3, *Philosophical Magazine*, 88 (9), 1307-1320, 2008.

125 F. C. Frank and A. N. Stroh, On the theory of kinking, *Proceedings of the Physical Society. Section B*, 65 (10), 811-821, 1952.

126 A. N. Stroh, The formation of cracks as a result of plastic flow, *Proc. Roy. Soc. Lond. A* 223 (1154), 404-414, 1954.

127 A. N. Stroh, The cleavage of metal single crystal, *Philosophical Magazine*, 3 (30), 597 - 606 1958.

128 A. G. Zhou, Kinking Nonlinear Elastic Solids: Theory and Experiments, *doctor thesis of Drexel University*, 2008.

129 M. Fraczkiewicz, A. G. Zhou and M. W. Barsoum, Mechanical damping in porous Ti_3SiC_2, *Acta Materialia*, 54 (19), 5261-5270, 2006.

130 A. G. Zhou, S. Basu and M. W. Barsoum, Kinking nonlinear elasticity, damping and microyielding of hexagonal close-packed metals, *Acta Materialia*, 56 (1), 60-67, 2008.

131 T. Zhen, M. W. Barsoum and S. R. Kalidindi, Effects of temperature, strain rate and grain size on the compressive properties of Ti_3SiC_2, *Acta Materialia*, 53 (15), 4163-4171, 2005.

132 M. W. Barsoum, A. Murugaiah, S. R. Kalidindi, T. Zhen and Y. Gogotsi, Kink bands, nonlinear elasticity and nanoindentations in graphite, *Carbon*, 42 (8-9), 1435-1445, 2004.

133 M. W. Barsoum, A. Murugaiah, S. R. Kalidindi and T. Zhen, Kinking nonlinear elastic solids, nanoindentations, and geology, *Physical Review Letters*, 92 (25 I), 255508-255501, 2004.

134 E. Orowan, A type of plastic deformation new in metals, *Nature*, 149 (3788), 643-644, 1942.

135 S. Amini and M. W. Barsoum, On the effect of texture on the mechanical and damping properties of nanocrystalline Mg-matrix composites reinforced with MAX phases, *Materials Science and Engineering A*, 527 (16-17), 3707-3718, 2010.

136 A. G. Zhou and M. W. Barsoum, Kinking nonlinear elastic deformation of Ti_3AlC_2, Ti_2AlC, $Ti_3Al(C_{0.5},N_{0.5})_2$ and $Ti_2Al(C_{0.5},N_{0.5})$, *Journal of Alloys and Compounds*, 498 (1), 62-70, 2010.

137 R. E. Reed-Hill, E. P. Dahlberg and W. A. S. jr, Some anelastic effects in Zirconium at room temperature resulting from prestrain at 77 K, *Transactions of the Metallurgical Society of Aime*, 233, 1766-1771, 1965.

138 C. T. Keith and W. A. J. Cote, Microscopic characterization of slip lines and compression failures in wood cell walls, *Forest Prod. J.*, 18 (3), 67-74, 1968.

139 G. E. Attenburrow and D. C. Bassett, Compliances and failure modes of oriented chain-extended polyethylene, *Journal of Materials Science*, 14 (11), 2679-2687, 1979.

140 A. Keller and J. G. Rider, On the tensile behaviour of oriented polyethylene, *Journal of Materials Science*, 1 (4), 389-398, 1966.

141 R. E. Robertson, FORMATION OF KINK BANDS IN ORIENTED POLYMERS, *J Polymer Science-Polymer Physics*, 7 (8 Pt A-2), 1315-1328, 1969.

142 D. A. Zaukelies, Observation of slip in nylon 66 and 610 and its interpretation in terms of a new model, *Journal of Applied Physics*, 33 (9), 2797-2803, 1962.

143 J. B. Hess and C. S. Barrett, Structure and nature of kink bands in zinc, *Trans.Am. Inst.Min. Eng.*, 185, 599-606, 1949.

144 D. Hull, Introduction to Dislocation, *Pergamon Press*, Oxford 1965.

145 Z. G. Liu, J. T. Guo, L. L. Ye, G. S. Li and Z. Q. Hu, Formation mechanism of TiC by mechanical alloying, *Applied Physics Letters*, 65 (21), 2666-2668, 1994.

146 S. Dubois, E. Heian, N. Karnatak, M. F. Beaufort and D. Vrel, "Synthesis of TiC/Ni cermets via mechanically activated self-propagating high-temperature synthesis", in *Materials Science Forum*, 426-432, 2033-2038, 2003.

147 L. Lutterotti, S. Matthies and H. R. Wenk, MAUD: a friendly Java program for material analysis using diffraction, *IUCr: Newsletter of the CPD*, 21 (14--15) 1999.

148 T. Ferreira and W. Rasband, The image J user guide, http://imagej.nih.gov/ij/docs/, 2011.

149 W. C. Oliver and G. M. Pharr, Improved technique for determining hardness and elastic modulus using load and displacement sensing indentation experiments, *Journal of Materials Research*, 7 (6),

1564-1580, 1992.

150 J. Woirgard and J. C. Dargenton, An alternative method for penetration depth determination in nanoindentation measurements, *Journal of Materials Research*, 12 (9), 2455-2458, 1997.

151 D. F. Bahr and D. J. Morris, Nanoindentation: Localized Probes of Mechanical Behavior of Materials, *Springer Handbook of Experimental Solid Mechanics Part B*, 389-408, 2008.

152 J. Woirgard, C. Tromas, J. C. Girard and V. Audurier, Study of the Mechanical Properties of Ceramic Materials by the Nanoindentation Technique, *Journal of the European Ceramic Society*, 18 (15), 2297-XI, 1998.

153 I.Horcas, R. Fernández, J. M. Gómez-Rodríguez, J. Colchero., J. Gómez-Herrero and A. M. Baro, WSXM: A software for scanning probe microscopy and a tool for nanotechnology, *Review of Scientific Instruments*, 78 (1) 2007.

154 M. S. Paterson, HIGH-PRESSURE, HIGH- TEMPERATURE APPARATUS FOR ROCK DEFORMATION, *International Journal of Rock Mechanics and Mining Sciences*, 7 (5), 517-526, 1970.

155 M. S. Paterson and D. L. Olgaard, Rock deformation tests to large shear strains in torsion, *Journal of Structural Geology*, 22 (9), 1341-1358, 2000.

156 A. Mussi, L. Thilly, J. Rabier and J. L. Demenet, Determination of mechanical properties of parallelepiped materials embedded in solid medium and deformed under confining pressure, *Materials Science and Engineering A*, 478 (1-2), 140-146, 2008.

157 M. W. Barsoum, G. Yaroschuk and S. Tyagi, Fabrication and characterization of M_2SnC (M = Ti, Zr, Hf and Nb), *Scripta Materialia*, 37 (10), 1583-1591, 1997.

158 H. Vincent, C. Vincent, B. F. Mentzen, S. Pastor and J. Bouix, Chemical interaction between carbon and titanium dissolved in liquid tin: Crystal structure and reactivity of Ti_2SnC with Al, *Materials Science and Engineering A*, 256 (1-2), 83-91, 1998.

159 T. El-Raghy, S. Chakraborty and M. W. Barsoum, Synthesis and characterization of Hf_2PbC, Zr_2PbC and M_2SnC (M = Ti, Hf, Nb or Zr), *Journal of the European Ceramic Society*, 20 (14-15), 2619-2625, 2000.

160 G. Hug, M. Jaouen and M. W. Barsoum, X-ray absorption spectroscopy, EELS, and full-potential augmented plane wave study of the electronic structure of Ti_2AlC, Ti_2AlN, Nb_2AlC, and $(Ti_{0.5}Nb_{0.5})_2AlC$, *Physical Review B - Condensed Matter and Materials Physics*, 71 (2), 024105-024101-024105-024112, 2005.

161 G. Hug, Electronic structures of and composition gaps among the ternary carbides Ti_2MC, *Physical Review B - Condensed Matter and Materials Physics*, 74 (18) 2006.

162 M. W. Barsoum, Private Communication.

163 G. P. Bei, Research on the synthesis of Ti_2SnC and the oriented growth of Ti_2SnC grains, *Master thesis of Beijing Jiaotong University*, 2007.

164 S. B. Li, G. P. Bei, H. X. Zhai and Y. Zhou, Bimodal microstructure and reaction mechanism of Ti_2SnC synthesized by a high-temperature reaction using Ti/Sn/C and Ti/Sn/TiC powder compacts, *Journal of the American Ceramic Society*, 89 (12), 3617-3623, 2006.

165 M. Singh and S. Bhan, Contribution to the Fe-Sn system, *Journal of Materials Science Letters*, 5 (7), 733-735, 1986.

166 K. C. Hari Kumar, P. Wollants and L. Delaey, Thermodynamic evaluation of Fe-Sn phase diagram, *Calphad: Computer Coupling of Phase Diagrams and Thermochemistry*, 20 (2), 139-145, 1996.

167 C. Tromas, N. Ouabadi, V. Gauthier-Brunet, M. Jaouen and S. Dubois, Mechanical properties of

nanolaminate Ti_3SnC_2 carbide determined by nanohardness cartography, *Journal of the American Ceramic Society*, 93 (2), 330-333, 2010.

168 C. Kral, W. Lengauer, D. Rafaja and P. Ettmayer, Critical review on the elastic properties of transition metal carbides, nitrides and carbonitrides, *Journal of Alloys and Compounds*, 265 (1-2), 215-233, 1998.

169 W. D. Nix and H. Gao, Indentation size effects in crystalline materials: A law for strain gradient plasticity, *Journal of the Mechanics and Physics of Solids*, 46 (3), 411-425, 1998.

170 W. F. Smith and J. Hashemi, Foundations of Materials Science and Engineering (4th ed.), *McGraw-Hill, ISBN 0-07-295358-6*, 2006.

171 Z. F. Zhang and Z. M. Sun, Shear fracture behavior of Ti_3SiC_2 induced by compression at temperatures below 1000°C, *Materials Science and Engineering A*, 408 (1-2), 64-71, 2005.

172 Y. W. Bao, J. X. Chen, X. H. Wang and Y. C. Zhou, Shear strength and shear failure of layered machinable Ti_3AlC_2 ceramics, *Journal of the European Ceramic Society*, 24 (5), 855-860, 2004.

173 E. M. Schulson, The brittle compressive fracture of ice, *Acta Metallurgica Et Materialia*, 38 (10), 1963-1976, 1990.

174 T. R. Smith and E. M. Schulson, The brittle compressive failure of fresh-water columnar ice under biaxial loading, *Acta Metallurgica Et Materialia*, 41 (1), 153-163, 1993.

175 D. Iliescu and E. M. Schulson, Brittle compressive failure of ice: Monotonic versus cyclic loading, *Acta Materialia*, 50 (8), 2163-2172, 2002.

176 E. M. Schulson, Compressive shear faults in ice: Plastic vs. Coulombic faults, *Acta Materialia*, 50 (13), 3415-3424, 2002.

177 E. M. Schulson, Brittle failure of ice, *Engineering Fracture Mechanics*, 68 (17-18), 1839-1887, 2001.

178 C. E. Renshaw and E. M. Schulson, Universal behaviour in compressive failure of brittle materials [5], *Nature*, 412 (6850), 897-900, 2001.

179 H. O. K. Kirchner, G. Michot, H. Narita and T. Suzuki, Snow as a foam of ice: Plasticity, fracture and the brittle-to-ductile transition, *Philosophical Magazine A: Physics of Condensed Matter, Structure, Defects and Mechanical Properties*, 81 (9), 2161-2181, 2001.

180 P. E. Donovan, A yield criterion for $Pd_{40}Ni_{40}P_{20}$ metallic glass, *Acta Metallurgica*, 37 (2), 445-456, 1989.

181 P. Lowhaphandu, L. A. Ludrosky, S. L. Montgomery and J. J. Lewandowski, Deformation and fracture toughness of a bulk amorphous Zr-Ti-Ni-Cu-Be alloy, *Intermetallics*, 8 (5-6), 487-492, 2000.

182 G. He, J. Lu, Z. Bian, D. Chen, G. Chen and G. Tu, Fracture morphology and quenched-in precipitates induced embrittlement in a Zr-base bulk glass, *Materials Transactions*, 42 (2), 356-364, 2001.

183 W. J. Wright, R. Saha and W. D. Nix, Deformation mechanisms of the $Zr_{40}Ti_{14}Ni_{10}Cu_{12}Be_{24}$ bulk metallic glass, *Materials Transactions*, 42 (4), 642-649, 2001.

184 G. He, Z. F. Zhang, W. Löser, J. Eckert and L. Schultz, Effect of Ta on glass formation, thermal stability and mechanical properties of a $Zr_{52.25}Cu_{28.5}Ni_{4.75}Al_{9.5}Ta_5$ bulk metallic glass, *Acta Materialia*, 51 (8), 2383-2395, 2003.

185 Z. F. Zhang, J. Eckert and L. Schultz, Difference in compressive and tensile fracture mechanisms of $Zr_{59}Cu_{20}Al_{10}Ni_8Ti_3$ bulk metallic glass, *Acta Materialia*, 51 (4), 1167-1179, 2003.

186 Z. F. Zhang, G. He, J. Eckert and L. Schultz, Fracture mechanisms in bulk metallic glassy materials, *Physical Review Letters*, 91 (4), 045505/045501-045505/045504, 2003.

187 Z. F. Zhang, G. He and J. Eckert, Shear and distensile fracture behaviour of Ti-based composites with ductile dendrites, *Philosophical Magazine*, 85 (9), 897-915, 2005.

188 Y. Zhou and Z. Sun, Micro-scale plastic deformation of polycrystalline Ti_3SiC_2 under room-temperature compression, *Journal of the European Ceramic Society*, 21 (8), 1007-1011, 2001.

189 S. Dubois, G. P. Bei, C. Tromas, V. Gauthier-Brunet and P. Gadaud, Synthesis, microstructure, and mechanical properties of $Ti_3Sn_{(1-x)}Al_xC_2$ MAX phase solid solutions, *International Journal of Applied Ceramic Technology*, 7 (6), 719-729, 2010.

190 Z. J. Lin, M. J. Zhuo, Y. C. Zhou, M. S. Li and J. Y. Wang, Microstructural characterization of layered ternary Ti_2AlC, *Acta Materialia*, 54 (4), 1009-1015, 2006.

191 Z. J. Lin, M. J. Zhuo, Y. C. Zhou, M. S. Li and J. Y. Wang, Microstructural relationships between compounds in the Ti-Si-C system, *Scripta Materialia*, 55 (5), 445-448, 2006.

192 Z. J. Lin, M. J. Zhuo, M. S. Li, J. Y. Wang and Y. C. Zhou, Synthesis and microstructure of layered-ternary Ti_2AlN ceramic, *Scripta Materialia*, 56 (12), 1115-1118, 2007.

193 K. T. Jacob, S. Raj and L. Rannesh, Vegard's law: A fundamental relation or an approximation, *International Journal of Materials Research*, 98 (9), 776-779, 2007.

194 J. Etzkorn, M. Ade and H. Hillebrecht, V_2AlC, V_4AlC_{3-x} (x =0.31), and $V_{12}Al_3C_8$: Synthesis, crystal growth, structure, and superstructure, *Inorganic Chemistry*, 46 (18), 7646-7653, 2007.

195 K. Momma and F. Izumi, VESTA: A three-dimensional visualization system for electronic and structural analysis, *Journal of Applied Crystallography*, 41 (3), 653-658, 2008.

196 M. Y. Gamarnik and M. W. Barsoum, Bond lengths in the ternary compounds Ti_3SiC_2, Ti_3GeC_2 and Ti_2GeC, *Journal of Materials Science*, 34 (1), 169-174, 1999.

197 R. S. Kumar, S. Rekhi, A. L. Cornelius and M. W. Barsoum, Compressibility of Nb_2AsC to 41 GPa, *Applied Physics Letters*, 86 (11), 1-3, 2005.

198 T. Liao, J. Wang and Y. Zhou, Superior mechanical properties of Nb_2AsC to those of other layered ternary carbides: A first-principles study, *Journal of Physics Condensed Matter*, 18 (41), L527-L533, 2006.

199 Y. C. Zhou, D. T. Wan, Y. W. Bao and J. Y. Wang, In situ processing and high-temperature properties of $Ti_3Si(Al)C_2$/SiC composites, *International Journal of Applied Ceramic Technology*, 3 (1), 47-54, 2006.

200 Y. W. Bao and Y. C. Zhou, Evaluating high-temperature modulus and elastic recovery of Ti_3SiC_2 and Ti_3AlC_2 ceramics, *Materials Letters*, 57 (24-25), 4018-4022, 2003.

201 J. Wang and Y. Zhou, "Recent progress in theoretical prediction, preparation, and characterization of layered ternary transition-metal carbides", in *Annual Review of Materials Research*, 39, 415-443, 2009.

202 A. G. Zhou, M. W. Barsoum, S. Basu, S. R. Kalidindi and T. El-Raghy, Incipient and regular kink bands in fully dense and 10 vol.% porous Ti_2AlC, *Acta Materialia*, 54 (6), 1631-1639, 2006.

203 R. Yu, Q. Zhan, L. L. He, Y. C. Zhou and H. Q. Ye, Stacking faults and grain boundaries of Ti_3SiC_2, *Philosophical Magazine Letters*, 83 (5), 325-331, 2003.

204 A. Joulain, Private communications.

Acknowledgements

At this moment, it is difficult to find appropriate words to express my gratitude to my advisors **Prof. Sylvain Dubois and Dr. Véronique Brunet** for their encouragement, continuous support, great teaching, and friendly advice during my Ph.D study in France. Thus, I can simply say: **THANK YOU**. I have been very fortunate to have such good advisors.

I consider myself lucky and honored for having an opportunity to collaborate with a lot of wonderful people during my Ph.D thesis in Institute Pprime. Among all of them, I would like specially to thanks:

- **Dr. C. Tromas**, for the help of nanoindentation tests, inspiriting discussions, great suggestions and participating in my defense committee.
- **Dr. A. Joulain**, for the help of TEM training and interpreting experimental results, inspiriting discussions.
- **Prof. L. Thilly,** for the help of the compression tests in the Paterson machine and interpreting experimental results, inspiriting discussions.
- **Prof. J. Bonneville** and **Mr. G. Laplache**, for the help of the compression tests in the Intron machine and interpreting experimental results, inspiriting discussions.
- **Prof. T. Cabioc'h**, for the help of TEC measurement, Rietveld Refinement, inspiriting discussions.
- **Prof. M. Jaouen,** for the help of training in Rietveld Refinement with MAUD software.
- **Prof. P. Gadaud,** for the help of Young's modulus measurement.
- **Dr. D. Eyidi** and **Dr. F. Pailloux**, for their great help of XRD and SEM microscope.
- **The group of technical assistance: Mr. A. Baudet, Mrs. A. Archambault, Mr. F. Berneau, Mr. P. Tanguy, Mr. Y. Diot, Mr. B. Lamongie and many others.**
- **My fellow colleagues and friends in Institute Pprime,** for making this work an enjoyable and unforgettable experience. Sincere thanks are given to: **Mr. V. Antad, Mr. E. Dion, Mr. M. Bugnet, MS. T. Pham Thi Huven, Dr. J.B. Dubois, Dr. C. Dupeyrat, Dr. B. Lacroix, Mr. G. B. Chen, G.D. Wang, Dr. X. Y. Li, W.B. Yu and many others**.
- All **Faculty** and **Staff members** of Institute Pprime;

I also would like to give my sincere thanks to the jury:

- **Prof. G. Dirras**, LSPM, Paris XIII, for participating in my defense committee and giving the report.
- **Prof. F. Berbard,** ICB, Dijon, for participating in my defense committee and giving the report.
- **Prof. D. Vrel,** LSPM, Paris XIII, for participating in my defense committee

Finally, I would like to thank my parents, **Sen-Lin Bei** and **Gen-Mei Jin,** my wife **Wen Juan Wang** my uncle and aunty**, Xue-Qi Bei** and **Lei Wang** for their comprehension, help and relentless support through all these years. Without their help, this work would not have been possible.

Guo-Ping Bei

Poitiers, 19/7/2011

RESUME

Les travaux exposés dans cet ouvrage portent sur l'élaboration, la caractérisation microstructurale et les propriétés mécaniques de solutions solides nanolamellaires de phases dites MAX. Les phases MAX représentent une classe exceptionnellement étendue de céramiques. Elles répondent à une formule générale du type $M_{n+1}AX_n$ (n=1, 2 ou 3) où M est un métal de transition, A est un métal des groupes IIIA ou IVA, et X est un métalloïde (C ou N).
Nous avons dans un premier temps réalisé l'optimisation de la synthèse, par métallurgie des poudres, de Ti_3AlC_2 pur. Une nouvelle phase, Ti_3SnC_2, ayant été découverte au laboratoire en 2007, les travaux se sont alors focalisés sur la synthèse de solutions solides du type $Ti_3Al_xSn_{(1-x)}C_2$ par pressage isostatique à chaud. Nous nous sommes, par la suite, attachés à la caractérisation microstructurale de ces solutions solides en étudiant notamment les variations du paramètre de maille, du taux de distorsion des octaèdres [Ti_6C] et des prismes trigonaux [$Ti_6Al_xSn_{(1-x)}$]. Enfin, nous avons déterminé la dureté intrinsèque et le module d'élasticité des différentes solutions solides en fonction du taux de substitution en utilisant la nanoindentation. Par ailleurs, des essais de compression, uniaxiale et sous confinement de gaz, ont été réalisés à température ambiante, afin d'étudier et de comparer les mécanismes de déformation de Ti_3AlC_2 et de la solution solide $Ti_3Al_{0.8}Sn_{0.2}C_2$. Les relations entre modifications microstructurales et propriétés mécaniques sont discutées. Nous montrons notamment que Ti_3AlC_2 et $Ti_3Al_{0.8}Sn_{0.2}C_2$ peuvent être considérés comme des matériaux "Kinking Non-linear Elastic".

Mots Clés : phases MAX, solutions solides, compression isostatique à chaud, microstructure, nanoindentation, module d'élasticité, dureté, déformation plastique.

ABSTRACT

The work described in this thesis concerns the elaboration, the microstructural characterization and the mechanical properties of nanolaminated MAX phases solid solutions. The MAX phases represent a large class of ceramics. They are a family of ternary nitrides and carbides, with the general formula $M_{n+1}AX_n$ (n=1, 2 or 3), where M is an early transition metal, A is a metal of the groups IIIA or IVA, and X is either carbon or nitrogen.
We performed at first the optimization of the synthesis, by powder metallurgy, of highly pure Ti_3AlC_2. Since a new MAX phase, Ti_3SnC_2, has been discovered in the laboratory in 2007, the study has been further focused on the synthesis of $Ti_3Al_xSn_{(1-x)}C_2$ solid solutions by hot isostatic pressing. In a second step, the microstructural characterization of these solid solutions has been carried out, by studying, in particular, the variation of the cell parameters, the distortion rates of [Ti_6C] octahedrons and [$Ti_6Al_xSn_{(1-x)}$] trigonal prisms. Finally, we have determined the intrinsic hardness and the elastic modulus of the various solid solutions as a function of the Al content by using the nanoindentation. Besides, uniaxial and gas confining compression tests were realized at room temperature, to study and compare the deformation mechanisms of Ti_3AlC_2 and $Ti_3Al_{0.8}Sn_{0.2}C_2$. The relationship between microstructural modifications and mechanical properties are discussed. We show in particular that Ti_3AlC_2 and $Ti_3Al_{0.8}Sn_{0.2}C_2$ can be considered as "Kinking Non-linear Elastic" materials.

Key words: MAX phases, solid solutions, hot isostatic pressing, microstructure, nanoindentation, elastic modulus, hardness, plastic deformation.